Advances in Monte Carlo simulations for the design of X-ray phase contrast imaging systems

Jonathan Sanctorum

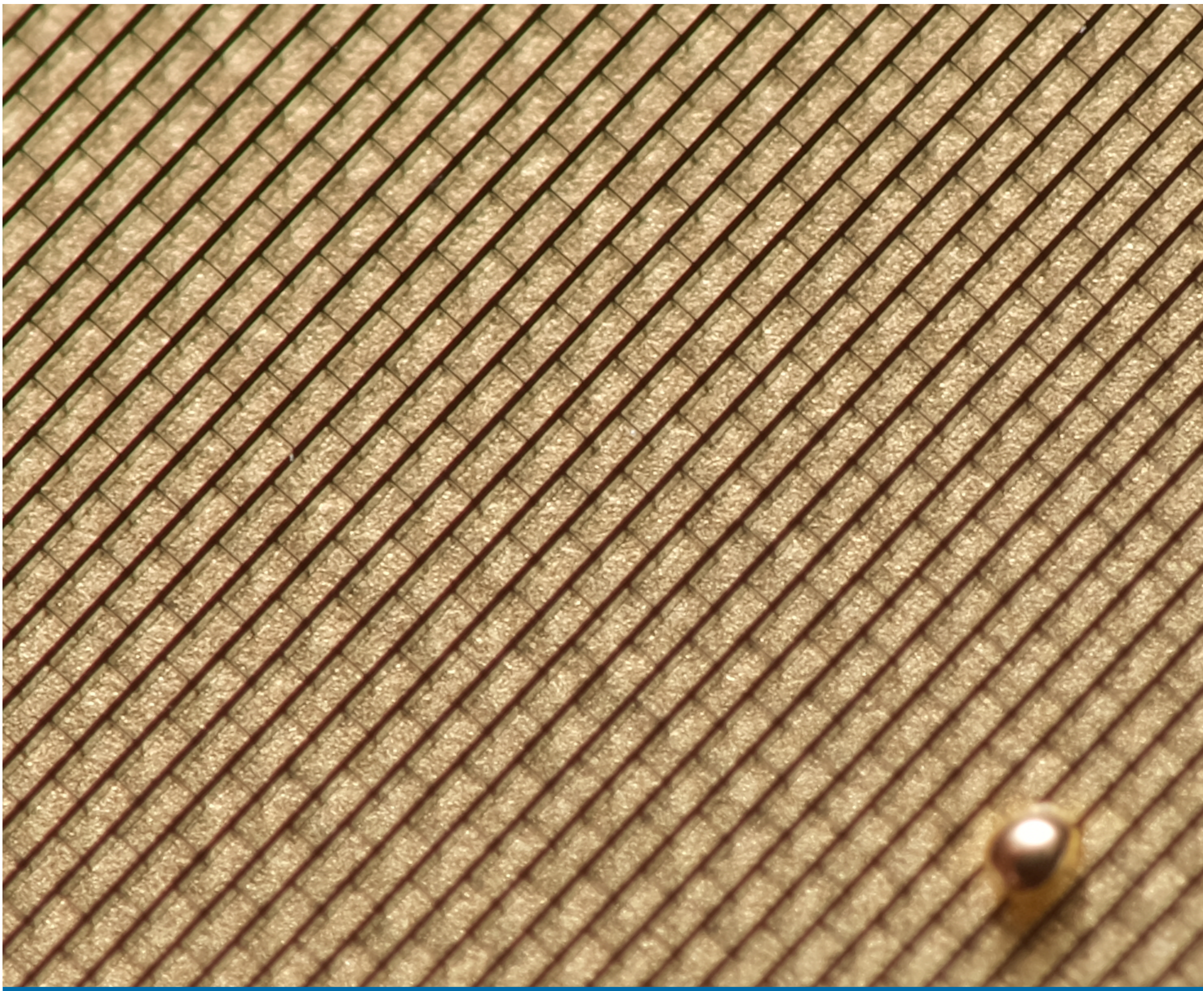

Supervisors **Prof. dr. Jan Sijbers** | **Prof. dr. ir. Jan De Beenhouwer**

Thesis submitted for the degree of Doctor of Science: Physics
Faculty of Science | **Antwerpen, 2026**

University of Antwerp

University of Antwerp

Faculty of Science

Advances in Monte Carlo simulations for the design of X-ray phase contrast imaging systems

Thesis submitted for the degree of
Doctor of Science: Physics
at the University of Antwerp to be defended by

Jonathan Sanctorum

Supervisors
Prof. dr. Jan Sijbers
Prof. dr. ir. Jan De Beenhouwer

Antwerpen, 2026

Jury

Chair
Prof. dr. Joris Dirckx, University of Antwerp, Belgium

Supervisors
Prof. dr. Jan Sijbers, University of Antwerp, Belgium
Prof. dr. ir. Jan De Beenhouwer, University of Antwerp, Belgium

Members
Prof. dr. Sandra Van Aert, University of Antwerp, Belgium
Prof. dr. Alessandro Olivo, University College London, UK
Prof. dr. Christoph Heinzl, University of Passau, Germany
Dr. Paul Leblans, Agfa-Gevaert Group, Belgium

Contact

Jonathan Sanctorum

University of Antwerp
Faculty of Science - Department of Physics
imec-Vision Lab
Universiteitsplein 1, 2610 Antwerp, Belgium
email: jonathan.sanctorum@uantwerpen.be

The PhD researcher and supervisor(s) declare that the PhD research was conducted according to the principles of scientific integrity, as mentioned in the general PhD regulations and charter for PhD researchers of UAntwerp and the integrity charter for PhD researchers and supervisors affiliated with the University of Antwerp.

Copyright disclaimer

Declaration of integrity

The PhD researcher and supervisor(s) declare that the PhD research was conducted according to the principles of scientific integrity, as mentioned in the general PhD regulations and charter for PhD researchers of UAntwerp and the integrity charter for PhD researchers and supervisors affiliated with the University of Antwerp.

Statement on the use of generative AI

No data or images in this thesis were generated with AI. The cover image shows a zoomed-in photograph of an edge illumination mask made of gold, which was designed for the FleXCT-system using the simulation framework presented in this dissertation. Image courtesy by Falk Mielke from imec-Vision Lab.

Titel in het Nederlands

Vorderingen op het gebied van Monte Carlo-simulaties voor het ontwerp van Röntgenfasecontrastbeeldvormingssystemen

Dankwoord

Should I write this page in Dutch or in English?

It would be a lie to state that this was the most difficult question that occurred to me during my PhD, but it was certainly not an easy one knowing that this is probably the only page most people will ever read. In the end, I decided that this is my page and that I can do whatever I want with it, so a combination of Dutch and English it will be.

Okay, let's go.

Many will agree that completing a PhD is not an easy task. It's like a walk in the park, but there's a storm and the park is on fire. Jokes aside, doing a PhD is indeed a sometimes hard but often rewarding journey. It still feels somewhat strange to type these words, since the fact that I am typing them implies that I actually completed the PhD. But did *I*, meaning just me, myself, and I, really do it? Obviously, I did do a couple of things, otherwise this would be an empty booklet. Yes, it was me who wrote the thesis and the papers. Yes, it was me who prepared for the presentations and the conferences. Yes, it was me who spent countless sleepless nights trying to figure out how to fix a problem or wondering why this or that idea did not work, and it was me who quietly but victoriously whispered ”Yes!” at my computer screen when an error in the code was finally discovered after hours of searching, or when a paper was finally accepted for publication many months after submission.

However, the truth is that all of this would never have been possible without the support I have received in various ways from many different people. Although I will never be able to thank all of you enough, I will try my best. First, I would like to thank my supervisors, Jan and Jan, for their endless support. They tirelessly spent countless hours giving feedback on ideas, papers, and presentations. Jan and Jan never stopped believing in my ability to finish this PhD, even at times when I started losing faith myself. I have learned so much from both of you, thank you for everything. In addition, I would like to thank all the members of the jury, who are all absolute experts in their fields and are therefore always overburdened with work, but still invested their precious time in carefully reading my work.

Although doing the research for a PhD is mostly a solitary endeavor, I have never felt alone at the lab. I have always enjoyed the atmosphere at Vision Lab, and for that I have to thank all my Vision Lab mates. Thank you Femke, Pavel, Bikram, Vincent, Björn, Michele, Alice, Arpad, and so many others for the chats and the laughs. I consider myself lucky for having been part of a journey where X-ray phase contrast imaging evolved from a single project within the lab to a broader research topic involving multiple people. Thank you Nathanaël, Ben, Nicholas, Pieter-Jan, and others for making this journey possible. I have also always greatly enjoyed the teaching hours during my PhD, in part due to the presence of fantastic fellow teaching assistants. Thank you Femke, Eline, Piet, Jan, Quinten, Jeroen, Annelinde, Nathanaël, Daniel, Jens, Lars-Paul, Pieter-Jan, Ben, Jannes, Caroline, and all others I might have accidentally overlooked in this long list that grew over the years.

There's a special class of lab mates, also known as office mates, consisting of the people with whom you share your daily sorrows, PhD frustrations, and laughs. I would like to explicitly thank dr. Tim Elberfeld for existing, and for replacing the emptiness in my office by a top tier German quality colleague. I would also like to thank Van Nguyen for the time we spent together at the office, I will forever cherish our little chats about all the important and unimportant things in life. Thank you Jens for the jokes and the tenfold increase in IQ points you brought to the office every day. Thank you Jian for being such a kind and supportive colleague. Ja, Joaquim, jij bent ook een office mate, maar jij bent vooral ook zoveel meer dan dat. Dus later meer daarover.

There's also life outside the lab. Ik wil heel graag mijn familie en vrienden bedanken voor de steun en broodnodige afleiding gedurende de afgelopen jaren, ook zonder jullie was het niet gelukt. Ik koester voor altijd de fijne herinneringen die gemaakt werden met mijn klasgenoten van 6WeWiB en mijn studiegenoten in de opleiding Fysica. Bedankt Jonathan en Nick voor de vele surfer rosa's in Vrij België na de werkuren. Ook de boskes wil ik bedanken voor de jarenlange kamaraderie en de vele onvergetelijke momenten in binnen- en buitenland. Ik denk uiteraard ook aan mijn jeugdvrienden Kilian en Kiara, hoewel we ondertussen al lang elkaars buren niet meer zijn, is de afstand tussen ons nooit echt groter geworden en daar ben ik dankbaar voor. Bedankt Laura en Cyrelle voor jullie licht op de donkerste dagen, de wereld is een betere plek met jullie erin. En lieve, lieve Charline. Ik weet dat jij weet dat het mij gelukt is. Ik koester voor altijd ieder moment.

Zonder de nooit aflatende steun van mijn ouders, onder wiens dak ik heb gewoond tot in de eerste jaren van mijn doctoraat, zou ik niet staan waar ik vandaag sta. Ik heb heel veel aan jullie te danken, meer dan ik met woorden kan uitdrukken. Ook de rol van mijn grote kleine broer Joaquim valt niet te overschatten. Weet dat ik elke dag trots ben jouw broer te zijn en dat ik mij geen betere peter kan inbeelden voor ons zoontje. Bedankt om samen met je geweldige vrouw Audrey jullie prachtige dochter Donna op de wereld te zetten. Al vanaf haar geboorte is Donna een wonderlijk lichtpuntje in mijn leven.

Tenslotte wil ik Merel bedanken, mijn lieve Merel. Bij de start van mijn doctoraat al mijn vriendin en ondertussen al ruim anderhalf jaar mijn vrouw. Bedankt om deze onwaarschijnlijke rollercoaster ride samen met mij uit te zitten en om mij mee over de finishlijn te trekken toen deze eindelijk binnen handbereik kwam. Je bent de beste, ik zie je graag.

Dag en bedankt he!

Jonathan Sanctorum
13 januari 2026

P.S.: I would also like to sincerely thank my chickens, Mambo, Tango, Hix, and Fix for the mental support and for simply being the utterly fantastic animals they always were.

Voor Charline
I won’t let you fade

Questions of science,
science and progress
Do not speak as loud as my heart
- The Scientist, Coldplay

Summary

Über eine neue Art von Strahlen, or *On a new kind of rays*. With this compelling manuscript title, Röntgen introduced his newly discovered rays to the scientific community. More than a century has passed, and today these once mysterious rays can no longer be described as new or unknown. Nowadays, the applications of X-rays extend far beyond frightening Röntgen's wife. X-rays are found in airports for luggage screening, hospitals for medical imaging, research labs for material characterization, and so on. It goes without saying that X-rays left an impact on our society that cannot be overestimated. The existence of dozens of impressively large and impressively expensive synchrotrons all around the world, whose main purpose is simply to generate high-quality X-ray beams, is just one indication of the importance of X-rays. Therefore, it can be be considered symbolic today that the first Nobel prize in physics was awarded to Röntgen for the discovery of the X-ray.

In fact, X-rays later turned out to show a lot of similarities with the visible light rays we are all so familiar with. Just like visible light, X-rays are essentially traveling photons, illuminating their environment. X-ray photons, however, carry much more energy than their visible counterparts, allowing them to penetrate many materials, especially soft tissue, in contrast to visible light. Although their high energy makes X-rays invisible to the human eye, their invisibility does not mean that they are harmless. In the early days after the discovery of the X-ray, little to nothing was known about the hazard associated with long or repeated exposure to X-rays or other types of ionizing radiation. Today, it is well-known that ionizing radiation poses a health risk. Nonetheless, if used with caution, the diagnostic value of X-rays often largely outweighs the risks. As such, strict safety regulations keep the radiation dose administered to patients and staff as low as possible. In addition, there are numerous nonmedical applications as well, particularly in the fields of nondestructive testing and materials science.

Similar to how visible light is refracted by a prism or deformed by a glass of water, X-rays will also refract when passing through a material. In conventional X-ray images, the contrast relies on local differences in absorption of the X-rays. Interestingly, X-ray refraction yields information about the object as well. It has been shown that this refraction, or in more general terms, phase contrast, can provide improved contrast in certain materials compared to conventional absorption contrast, without necessarily increasing the radiation dose. Unfortunately, the magnitude of X-ray refraction is many orders of magnitude smaller compared to visible light, making it much harder to detect. Typically,

this requires advanced, dedicated imaging systems, be it coherent synchrotron sources or modified lab-based systems with dedicated X-ray optics. Due to the convenience of such modified lab-based systems, lab-based X-ray phase contrast imaging is becoming increasingly popular.

More recently, a third type of contrast gained increasing interest as well. This contrast type, associated with phase contrast, is known as dark field contrast. Refraction is an important underlying contribution to dark field contrast, but in this case results from unresolved microstructures. Such unresolved interactions result in an increased angular spread of the X-rays, providing sensitivity to the presence of otherwise undetectable microscopic features. These effects are often subtle, and typically require dedicated setups as well. The design and development of such dedicated imaging system requires the determination of its specifications in function of its envisaged purpose. This is especially true for the parameters of the X-ray components required for X-ray phase contrast imaging. To this end, it is common practice to perform (sometimes extensive) parameter studies using computer simulations.

In this dissertation, a collection of tools is presented that aim to meet the often challenging requirements associated with simulations for the design of X-ray phase contrast imaging systems. Two types of X-ray phase contrast imaging methods will be of particular interest, namely grating-based interferometry and edge illumination.

The first chapter of this thesis, aptly named Chapter 1, provides a concise introduction to the most important aspects of X-rays, describing interactions between X-rays and matter and how these interactions can be exploited for imaging purposes in 2D and 3D. In addition, the concept of Monte Carlo simulations is introduced, and it is explained how it is used for X-ray imaging simulations.

Chapter 2 introduces the fundamentals of X-ray phase contrast imaging and builds up to the practical realization of a number of popular phase contrast imaging setups and the concepts of wave optics simulations. In this chapter, special attention is given to grating-based interferometry and edge illumination.

Chapter 3 is dedicated to the realization of X-ray phase contrast imaging simulations for grating-based interferometry using the GATE Monte Carlo framework, hereby relying on a hybrid simulation approach combining Monte Carlo simulations with wave optics. This includes the implementation of both X-ray refraction and the construction of X-ray wavefronts from photons in GATE. Subsequent propagation of this wavefront by means of wave optics calculations then results in the generation of simulated grating-based phase contrast images. The separation of the Monte Carlo and the wave optics part allows for changes in the grating parameters and propagation distance without having to repeat the time-consuming Monte Carlo calculations. The framework is validated by comparison to theoretical expectations, and its functionalities are demonstrated for both 2D imaging and computed tomography of microstructured digital phantoms.

The presented simulation framework can be used for edge illumination simulations as well, where in most cases the memory-intensive wave optics calculations can be safely omitted. This implies that the gratings are in this case directly modeled as objects in GATE. However, Monte Carlo simulations are known to be very time-consuming, especially when performing grating parameter studies. In Chapter 4, it is demonstrated that the total computation time required for edge illumination grating parameter studies can be reduced by introducing the concept of virtual gratings. In the virtual gratings approach, the explicitly modeled gratings in GATE are replaced by virtual volumes that do not interact with the simulation, but track the position and direction of intersecting photons, which allows for a post-simulation definition of the grating geometry. As such, a single Monte Carlo simulation can serve as a basis for a multitude of different grating designs. The validity of the virtual gratings approximation is checked by means of comparison to explicit grating simulations and the effectiveness of the method is demonstrated for 2D imaging applications.

In Chapter 5, the virtual gratings approach is used for the design of edge illumination gratings to augment the flexible FleXCT micro-CT scanner of imec-Vision Lab with phase contrast imaging capabilities. The system magnification, the desired phase sensitive field of view, and the source voltage are fixed by the envisaged application, which is phase contrast imaging of apple-sized fruits. The tunable grating parameters, being the aperture size and the material thickness, are determined through a parameter study including different focal spot sizes. For the grating thickness, the trade-off between grating bar transmission and shadowing effects is taken into account, whereas for determining the aperture size the peak-to-peak contrast-to-noise ratio is considered. At the time of the writing of this thesis, the designed gratings have been manufactured and installed in the FleXCT system.

Chapter 6 addresses the benchmarking of multi-contrast simulation results in GATE. This is done by using the virtual gratings approach to determine the reference values required for benchmarking. By tracking and storing the trajectories of the individual simulated photons, which is the main functionality of the virtual gratings approach, the transmission, refraction, and local beam broadening can be estimated directly from the photon tracks using straightforward calculations, without intermediate contrast retrieval steps. In this way, a full set of reference values becomes available for benchmarking the simulation results without requiring additional Monte Carlo simulations. The interpretation of the reference values is discussed in detail and a set of examples of benchmarking simulation results is shown.

The thesis is concluded with a general conclusion of the research presented in the preceding chapters, as well as an outlook on possible future work based on the results presented in this work.

Samenvatting

Über eine neue Art von Strahlen, of *Over een nieuw soort stralen*. Met deze gevatte titel presenteerde Röntgen zijn net ontdekte stralen aan de wetenschappelijke gemeenschap. Meer dan een eeuw is inmiddels verstreken, en intussen kunnen deze eens zo mysterieuze stralen al lang niet meer omschreven worden als nieuw of onbekend. Vandaag de dag reiken de toepassingen van Röntgenstralen veel verder dan het louter angst aanjagen van Röntgens echtgenote. Röntgenstraling wordt gebruikt in luchthavens voor bagagecontrole, in ziekenhuizen voor medische beeldvorming, in onderzoekslaboratoria voor het bepalen van materiaaleigenschappen, enzovoort. Het spreekt voor zich dat de maatschappelijke impact van Röntgenstraling nauwelijks te overschatten is. Enkel en alleen al het bestaan van tientallen, indrukwekkend grote (en indrukwekkend prijzige) synchrotrons wereldwijd, met als enige doel het opwekken van kwalitatieve Röntgenstraling, vormt een bewijs van het belang ervan. De ontdekking van de Röntgenstraling is dus zonder twijfel een zeer symbolische eerste Nobelprijs in de fysica.

Later werd duidelijk dat Röntgenstraling in essentie niet zozeer verschilt van het zichtbare licht waarmee we allen zo vertrouwd zijn. Net zoals zichtbaar licht bestaat Röntgenstraling uit fotonen die de wereld rondom belichten. Röntgenfotonen zijn echter vele malen energetischer dan hun zichtbare tegenhangers, waardoor ze met veel gemak door velerlij materialen kunnen dringen, dit in tegenstelling tot zichtbaar licht. Hoewel hun hoge energie de Röntgenstraling onzichtbaar maakt voor het menselijk oog, wil dat niet zeggen dat deze straling niet schadelijk kan zijn. In de periode kort na de ontdekking van de Röntgenstralen was er weinig tot niets geweten over de risico's die verbonden zijn aan Röntgenstraling en andere soorten ioniserende straling. Vandaag is men zich zeer goed bewust van het feit dat ioniserende straling bepaalde gezondheidsrisico's inhoudt. Desalniettemin wegen de risico's in vele gevallen niet op tegen de diagnostische waarde wanneer Röntgenstraling op verstandige wijze gebruikt wordt. Strikte veiligheidsvoorschriften waken erover dat de stralingsdosis toegediend aan patiënten en personeel zo laag mogelijk wordt gehouden. Bovendien bestaan er ook veel niet-medische toepassingen, met name binnen de materiaalwetenschappen en het niet-destructief onderzoek.

Vergelijkbaar met hoe zichtbaar licht wordt gebroken door een prisma of vervormd door een glas water, zullen Röntgenstralen ook breking ondergaan wanneer ze van een materiaal overgaan naar een ander. In conventionele Röntgenfoto's wordt het contrast bepaald door lokale verschillen in de absorptie van Röntgenstraling. Interessant genoeg kan de breking van Röntgenstraling ons ook iets leren over voorwerpen. Het is aangetoond dat deze breking, of algemener gesteld, fasecontrast, tot een sterk verbeterd contrast kan leiden in vergelijking met conventionele Röntgenfoto's, zonder een verhoogde stralingsdosis. De breking van Röntgenstralen is echter vele malen zwakker dan de breking van zichtbaar licht, waardoor het een moeilijker te detecteren effect is. Dit vereist typisch het gebruik van geavanceerde beeldvormingsapparatuur, hetzij coherente synchrotronbronnen, hetzij labsystemen met speciaal daarvoor ontworpen optische componenten. Het hoeft niet te verbazen dat de tweede optie in veel gevallen de meest praktische is, waardoor de populariteit van labgebaseerde Röntgenfasecontrastbeeldvorming nog steeds toeneemt.

Sinds kort kan ook een derde type contrast, dat gelieerd is aan fasecontrast, rekenen op een toenemende mate van interesse. Dit type contrast staat bekend als donkerveldcontrast. Breking van Röntgenstraling is opnieuw een belangrijk onderliggend effect voor dit type contrast, zij het in dit geval veroorzaakt door ononderscheidbare microstructuren. Dit effect resulteert in een lokale verbreding van de Röntgenstralenbundel, wat een signaal oplevert dat een gevolg is van de aanwezigheid van anders ondetecteerbare microscopische structuren. Aangezien deze effecten vaak subtiel zijn, vereisen ze ook het gebruik van speciaal ontworpen beeldvormingssystemen. De ontwikkeling en het ontwerp van dergelijke speciale beeldvormingssystemen vereisen op hun beurt het bepalen van de juiste specificaties in het licht van de beoogde toepassing. Dit is in het bijzonder zo voor de parameters van de specifieke componenten die nodig zijn voor Röntgenfasecontrastbeeldvorming. Doorgaans worden hiervoor parameterstudies uitgevoerd met behulp van computersimulaties.

In dit werk worden een aantal hulpmiddelen ontwikkeld om het ontwerp van Röntgenfasecontrastbeeldvormingssystemen via Monte Carlo-simulaties te faciliteren. Twee types van dergelijke systemen zijn hierin in het bijzonder van belang, namelijk roosterinterferometrie en randbelichting.

Het eerste hoofdstuk van deze thesis, toepasselijk Hoofdstuk 1 genoemd, geeft een beknopt overzicht van de belangrijkste eigenschappen van Röntgenstraling. Hierbij is er aandacht voor de interacties met materie en hoe deze aan de basis liggen van Röntgenbeeldvorming in 2D en 3D. Verder wordt ook het concept van Monte Carlo-simulaties uitgelegd, alsook hoe deze gebruikt kunnen worden voor het simuleren van Röntgenbeeldvorming.

In Hoofdstuk 2 worden de fundamenten van Röntgenfasecontrastbeeldvorming uit de doeken gedaan en wordt opbouwend toegewerkt naar de praktische realisatie van fasecontrastbeeldvormingssystemen. Het concept van fasecontrastsimulaties gebaseerd op fysische optica komt ook aan bod. Er is in dit hoofdstuk speciale aandacht voor roosterinterferometrie en randbelichting.

Hoofdstuk 3 behandelt het mogelijk maken van Röntgenfasecontrastsimulaties voor roosterinterferometrie met het Monte Carlo-simulatieraamwerk GATE, steunend op een hybride aanpak die Monte Carlo-simulaties combineert met fysische optica. Dit omvat zowel de implementatie van refractie van Röntgenstralen als het opbouwen van een golffront uit de bijdragen van afzonderlijke Röntgenfotonen in GATE. De propagatie van dit golffront door middel van golfoptische berekeningen laat vervolgens het genereren van fasecontrastbeelden toe. Het feit dat in dit raamwerk de Monte Carlo-simulaties en de golfpropagatie gescheiden onderdelen zijn, laat toe om de roosterparameters en de propagatieafstand aan te passen zonder dat er een nieuwe Monte Carlo-simulatie nodig is. De simulator wordt gevalideerd via vergelijking met theoretische verwachtingen en gedemonstreerd aan de hand van de simulatie van 2D beeldvorming en computertomografie van digitale fantomen met microstructuren.

Het voorgestelde simulatieraamwerk kan eveneens gebruikt worden voor de simulatie van randbelichting, waarbij doorgaans de geheugenintensieve golfoptische berekeningen achterwege kunnen worden gelaten. In dat geval moeten de roosters evenwel expliciet als objecten in GATE gemodelleerd worden. Monte Carlo-simulaties staan echter bekend als zeer tijdrovend, zeker voor het uitvoeren van parameterstudies. In Hoofdstuk 4 wordt aangetoond dat de totale simulatietijd voor parameterstudies voor randbelichtingsroosters kan worden ingekort door het invoeren van het concept van virtuele roosters. Bij deze methode worden de expliciet gemodelleerde roosters in GATE vervangen door virtuele roosters, die niet interageren met de simulatie maar wel de positie en richting bijhouden van de voorbijkomende fotonen. Dit laat toe om de parameters van de roosters achteraf te bepalen, zodat een enkele Monte Carlo-simulatie volstaat als basis voor een groot aantal roosterconfiguraties. De virtuele roosterbenadering wordt gevalideerd via vergelijking met simulaties met expliciete roosters en de methode wordt vervolgens gedemonstreerd aan de hand van 2D beeldvormingstoepassingen.

In Hoofdstuk 5 wordt de methode van de virtuele roosters toegepast om randbelichtingsroosters te ontwerpen voor de FleXCT micro-CT-scanner van Visielab, teneinde deze uit te breiden met fasecontrastbeeldvormingsmogelijkheden. De vergroting van het systeem, de grootte van de fasegevoelige zone in het beeld en de bronspanning worden vastgelegd door de beoogde toepassing, namelijk fasecontrastbeeldvorming van vruchten ter grootte van een appel. De aanpasbare roosterparameters, met name de apertuurgrootte en de dikte van het materiaal, worden bepaald via een parameterstudie die verschillende brandpuntgroottes in rekening brengt. De materiaaldikte wordt gekozen aan de hand van een afweging tussen het blokkeren van voldoende fotonen en het beperken van schaduweffecten, terwijl er voor de apertuurgrootte wordt gekeken naar de piek-tot-piek contrastruisverhouding. De roosters ontworpen in dit hoofdstuk werden inmiddels geproduceerd en geïnstaleerd in het FleXCT-systeem.

Hoofdstuk 6 tenslotte behandelt hoe men multicontrastsimulatieresultaten van GATE kan benchmarken. Dit kan worden gedaan door de methode van de virtuele roosters te gebruiken om de referentiewaarden te bepalen die nodig zijn voor het benchmarken. Door het registreren en opslaan van de individuele fotontrajecten is het mogelijk om referentiewaarden te bepalen voor transmissie, refractie en lokale bundelverbreding via eenvoudige berekeningen, zonder dat hiervoor extra Monte Carlo-simulaties nodig zijn. De interpretatie van deze referentiewaarden wordt uitgebreid besproken en het benchmarken van GATE simulaties wordt aan de hand van voorbeelden geïllustreerd.

Aan het einde van de thesis worden de resultaten uit dit werk samengevat, gevolgd door een bespreking van potentiële verdere ontwikkelingen in navolging van deze resultaten.

Publications

Journal articles

- **Sanctorum, J.**, De Beenhouwer, J., and Sijbers, J. (2020). X-ray phase contrast simulation for grating-based interferometry using GATE. *Optics Express*, 28(22), 33390–33412. https://doi.org/10.1364/OE.392337
- De Samber, B., Renders, J., Elberfeld, T., Maris, Y., **Sanctorum, J.**, Six, N., Liang, Z., De Beenhouwer, J., and Sijbers, J. (2021). FleXCT: a flexible X-ray CT scanner with 10 degrees of freedom. *Optics Express*, 29(3), 3438–3457. https://doi.org/10.1364/OE.409982
- **Sanctorum, J.**, Sijbers, J., and De Beenhouwer, J. (2022). Virtual grating approach for Monte Carlo simulations of edge illumination-based x-ray phase contrast imaging. *Optics Express*, 30(21), 38695–38708. https://doi.org/10.1364/OE.472145
- Huyge, B., **Sanctorum, J.**, Jeurissen, B., De Beenhouwer, J., and Sijbers, J. (2023). Fiber Orientation Estimation from X-ray Dark Field Images of Fiber Reinforced Polymers Using Constrained Spherical Deconvolution. *Polymers*, 15(13), 2887. https://doi.org/10.3390/polym15132887
- Vanthienen, P.-J., **Sanctorum, J.**, Huyge, B., Six, N., Sijbers, J., and De Beenhouwer, J. (2023). Grating designs for cone beam edge illumination X-ray phase contrast imaging: a simulation study. *Optics Express*, 31(17), 28051–28064. https://doi.org/10.1364/OE.495789
- Francken, N., **Sanctorum, J.**, Paramonov, P., Sijbers, J., and De Beenhouwer, J. (2024). Edge illumination x-ray phase contrast simulations using the CAD-ASTRA toolbox. *Optics Express*, 32(6), 10005–10021. https://doi.org/10.1364/OE.516138
- Francken, N., **Sanctorum, J.**, Sanctorum, J. G., Vanthienen, P.-J., Sijbers, J., and De Beenhouwer, J. (2024). Inline edge illumination X-ray phase contrast imaging through mask misalignment. *Optics Express*, 32(18), 32048–32061. https://doi.org/10.1364/OE.525730

- Francken, N., **Sanctorum, J.**, Huyge, B., Sijbers, J., and De Beenhouwer, J. (2025). Efficient X-ray dark field contrast simulations using a condensed history approach. *Optics Express*, 33(2), 3562–3576. https://doi.org/10.1364/OE.544864

- **Sanctorum, J.**, Sijbers, J., and De Beenhouwer, J. (2025). Multi-contrast benchmarking of edge illumination Monte Carlo simulations using virtual gratings. *Journal of Applied Physics*, 137(10), 104904. https://doi.org/10.1063/5.0244152

- Vanthienen, P.-J., Francken, N., **Sanctorum, J.**, Sijbers, J., and De Beenhouwer, J. (2025). Gratings for multi-resolution edge illumination X-ray phase contrast imaging: concept and simulation. *Optics Express*, 33(8), 17886–17902. https://doi.org/10.1364/OE.550252

- Huyge, B., Francken, N., Sanctorum, J. G., **Sanctorum, J.**, De Beenhouwer, J., and Sijbers, J. (2025). Edge illumination X-ray phase contrast imaging with continuous mask motion. *Optics Express*, 33(19), 41271–41286. https://doi.org/10.1364/OE.568153

Conference proceedings

- **Sanctorum, J.**, De Beenhouwer, J., and Sijbers, J. (2018). X-ray Phase-contrast Simulations of Fibrous Phantoms using GATE. In *2018 IEEE Nuclear Science Symposium and Medical Imaging Conference Proceedings (NSS/MIC)*, pages 1–5. https://doi.org/10.1109/NSSMIC.2018.8824641

- **Sanctorum, J.**, De Beenhouwer, J., Weissenböck, J., Heinzl, C., Kastner, J., and Sijbers, J. (2019). Simulated grating-based x-ray phase contrast images of CFRP-like objects. 9th Conference on Industrial Computed Tomography (iCT) 2019, 13-15 Feb, Padova, Italy. *E-Journal of Nondestructive Testing*, 24(3), 1–8. https://doi.org/10.58286/23679

- Fröhler, B., Da Cunha Melo, L., Weissenböck, J., Kastner, J., Möller, T., Hege, H., Gröller, E., **Sanctorum, J.**, De Beenhouwer, J., Sijbers, J., and Heinzl, C. (2019). Tools for the Analysis of Datasets from X-Ray Computed Tomography based on Talbot-Lau Grating Interferometry. 9th Conference on Industrial Computed Tomography (iCT) 2019, 13-15 Feb, Padova, Italy. *e-Journal of Nondestructive Testing*, 24(3). https://doi.org/10.58286/23685

- Weissenböck, J., Fröhler, B., Gröller, E., **Sanctorum, J.**, De Beenhouwer, J., Sijbers, J., Ayalur Karunakaran, S., Hoeller, H., Kastner, J., and Heinzl, C. (2019). An Interactive Visual Comparison Tool for 3D Volume Datasets represented by Non-linearly Scaled 1D Line Plots through Space-filling Curves. 9th Conference on Industrial Computed Tomography (iCT) 2019, 13-15 Feb, Padova, Italy. *e-Journal of Nondestructive Testing*, 24(3). https://doi.org/10.58286/23675

- **Sanctorum, J.**, Sijbers, J., and De Beenhouwer, J. (2021). Dark Field Sensitivity In Single Mask Edge Illumination Lung Imaging. In *2021 IEEE 18th International Symposium on Biomedical Imaging (ISBI)*, p. 775–778. IEEE https://doi.org/10.1109/ISBI48211.2021.9434024
- Huyge, B., **Sanctorum, J.**, Six, N., De Beenhouwer, J., and Sijbers, J. (2021). Analysis Of Flat Fields In Edge Illumination Phase Contrast Imaging. In *2021 IEEE 18th International Symposium on Biomedical Imaging (ISBI)*, p. 1310–1313. IEEE https://doi.org/10.1109/ISBI48211.2021.9433849
- **Sanctorum, J.**, Six, N., Sijbers, J., and De Beenhouwer, J. (2022). Augmenting a conventional x-ray scanner with edge illumination-based phase contrast imaging: how to design the gratings. In B. Müller & G. Wang (Eds.), *Proc. SPIE 12242, Developments in X-Ray Tomography XIV* (p. 1224218). SPIE https://doi.org/10.1117/12.2633455
- Vanthienen, P.-J., **Sanctorum, J.**, Huyge, B., Six, N., Sijbers, J., and De Beenhouwer, J. (2022). Alternative grating designs for cone-beam edge illumination x-ray phase contrast imaging. In B. Müller & G. Wang (Eds.), *Proc. SPIE 12242, Developments in X-Ray Tomography XIV* (p. 122420Z). SPIE https://doi.org/10.1117/12.2632301
- Francken, N., **Sanctorum, J.**, Renders, J., Paramonov, P., Sijbers, J., and De Beenhouwer, J. (2023). A Condensed History Approach to X-Ray Dark Field Effects in Edge Illumination Phase Contrast Simulations. In *45th Annual International Conference of the IEEE Engineering in Medicine & Biology Society (EMBC)*, pages 1–4. https://doi.org/10.1109/EMBC40787.2023.10340826
- Francken, N., **Sanctorum, J.**, Huyge, B., Sijbers, J., and De Beenhouwer, J. (2025). Correcting for focal spot drift in edge illumination X-ray phase contrast imaging. 14th Conference on Industrial Computed Tomography (iCT), 4-7 February 2025, Antwerp, Belgium. *e-Journal of Nondestructive Testing*, 30(2). https://doi.org/10.58286/30746

Conference abstracts

- **Sanctorum, J.**, Janssens, E., den Dekker, A.-J., Senck, S., Heinzl, C., De Beenhouwer, J., and Sijbers, J. (2017). A workflow to reconstruct grating-based X-ray phase contrast CT images: application to CFRP samples. In *4th Conference on X-ray and Neutron Phase Imaging with Gratings, Zurich, Switzerland*
- Janssens, E., De Beenhouwer, J., **Sanctorum, J.**, Senck, S., Heinzl, C., and Sijbers, J. (2017). Dual axis Dark Field Contrast Tomography for visualisation of scattering directions in a CFRP sample. In *4th Conference on X-ray and Neutron Phase Imaging with Gratings, Zurich, Switzerland*

Contents

Chapter 1

Introduction to X-ray imaging

This chapter provides a broad overview of the fundamentals of conventional X-ray imaging and Monte Carlo simulations. A much larger treasure trove of information can be found in Kak and Slaney (1988), Ljungberg et al. (1998), Buzug (2008), Als-Nielsen and McMorrow (2011), Bielajew (2020), and the user guides of Geant4 and GATE.

1.1 On a not so new kind of rays

Visible light is, without doubt, the most well known type of electromagnetic radiation. With wavelengths in the range of 400 to 750 nanometers, its name simply results from the fact that it is the only radiation that the human eye can see. Everything we have ever seen, or ever will see, is light originating from this range of wavelengths. However, being unable to see other wavelengths does not prevent us from using them. Take, for example, microwaves. Having wavelengths a million times longer than those of visible light, microwaves are effectively invisible to the human eye. They are, however, still perfectly capable of heating your food for you, and even if microwave meals are excluded from your culinary preferences, you are most likely still using microwaves on a daily basis through various wireless applications. Next up: infrared radiation. Equally invisible to the eye, but not unnoticed: infrared is the warmth we feel on our skin from the sunlight. Infrared wavelengths are just slightly longer than visible light wavelengths.

Then, once upon a time, there was the X-ray. Having much shorter wavelengths compared to visible light (sub-nanometer), the properties of X-rays are as wonderful as they are useful. X-rays have very high energies and can penetrate through many materials that block visisble light, such as biological soft tissue. Their penetrating power is an interesting feature, which was noticed by Wilhelm Röntgen at the time of the discovery of the

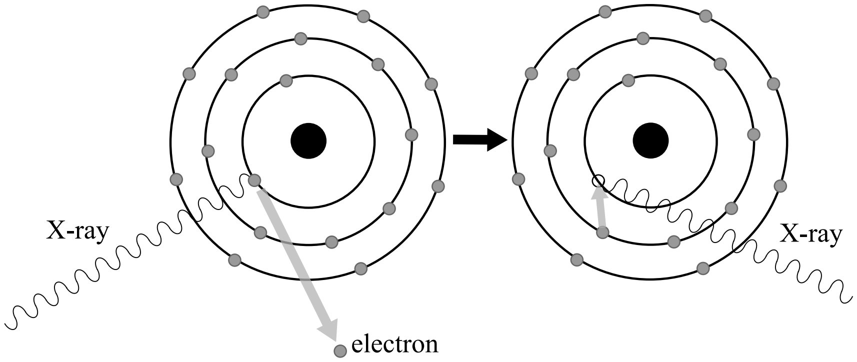

Figure 1.1: Illustration of the photoelectric effect, where an inner shell electron is ejected from the atom by absorbing the energy of an incoming X-ray. The energy lost by the outer shell electron occupying the vacancy is emitted as a characteristic X-ray photon or an Auger electron (not shown). Modified from Janssens (2018).

X-ray (Röntgen, 1898). However, X-rays can still be blocked by relatively thin layers of heavier materials such as lead or gold. This implies that X-rays, despite their high penetrating power, still interact with matter they travel through. Without the existence of these interactions, X-rays would be significantly less useful, and you would most likely be reading the last page of this dissertation.

In the following sections, the fundamentals of X-ray imaging will be briefly addressed. It will be shown that the interactions of X-rays in matter lead to attenuation of X-ray beams, which forms the basis for radiographic and tomographic imaging with X-rays.

1.2 X-ray interactions in matter

The four most common interactions contributing to the attenuation of X-rays are 1) the photoelectric effect, 2) Compton (or incoherent) scattering, 3) Rayleigh (or coherent) scattering, and 4) electron-positron pair production. The probability for each of these interactions to occur is material- and energy dependent, and is described by its respective cross section σ_i. The total cross section σ_{tot} is given by the sum of the photoelectric (σ_{pe}), Compton (σ_{Compton}), Rayleigh (σ_{Rayleigh}), and pair production (σ_{pp}) cross sections:

$$\sigma_{\text{tot}} = \sigma_{\text{pe}} + \sigma_{\text{Compton}} + \sigma_{\text{Rayleigh}} + \sigma_{\text{pp}}. \tag{1.1}$$

1.2.1 The photoelectric effect

Photoelectric absorption, illustrated in Fig. 1.1, occurs if an incoming X-ray photon has an energy larger than the binding energy of an inner shell electron. In that case, the

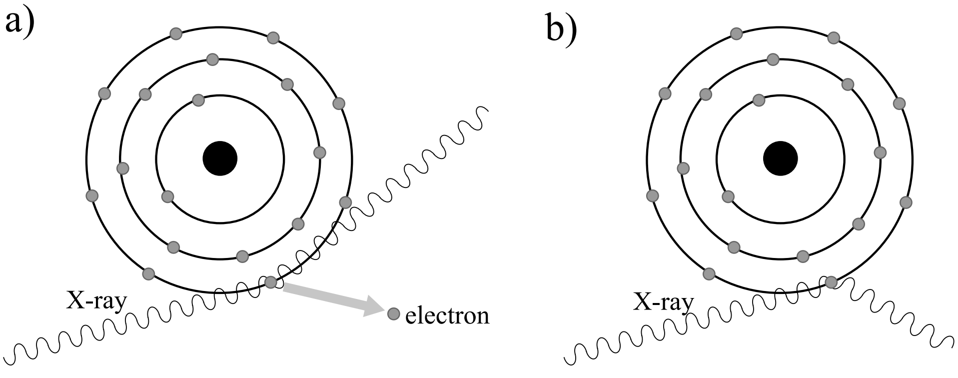

Figure 1.2: Illustration of a) inelastic Compton scattering, where an X-ray photon transfers energy to a weakly bound electron, and b) elastic Rayleigh scattering, where the X-ray is deflected by the electron without energy loss. Modified from Janssens (2018).

photon can be absorbed to eject the electron from the atom. The resulting vacancy in the inner electron shell will be occupied by an electron from an outer shell, emitting its excess energy as a characteristic X-ray photon or Auger electron. The photoelectric effect is a major contribution to the total attenuation cross section for diagnostic X-rays (50 keV – 140 keV) and the dominant effect for lower energies. Given its dependency on the X-ray energy and material atomic number Z, it is often the main source of X-ray image contrast formation, whereas scattering interactions are responsible for contrast degradation (e.g., blurring) and contribute to the total dose received by the patient in clinical imaging.

1.2.2 Compton scattering

Incoherent Compton scattering is an inelastic scattering event in which an X-ray photon only partially transfers its energy to eject a weakly bound electron, without being absorbed in the process. As a result, the photon loses energy and its traveling direction is changed. The wavelength shift corresponding to the energy loss can be written as

$$\Delta\lambda = \frac{h}{m_e c}\left(1 - \cos\theta\right), \tag{1.2}$$

where h denotes Planck's constant, c the vacuum speed of light, m_e the electron mass, and θ the scattering angle. This implies that no photon energy is transferred for forward scattering, whereas the energy transfer is maximal for backward scattering. Fig. 1.2 illustrates the Compton scatter process. The Compton effect becomes dominant in water and soft tissue for X-ray energies above 30 keV, but depends on the electron density rather than on Z. Since there is little difference in electron density between distinct tissues, Compton scattering provides low-contrast information.

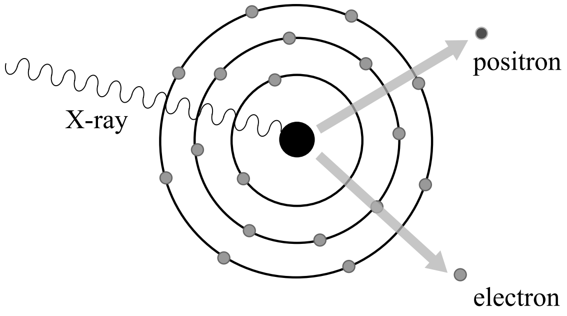

Figure 1.3: Illustration of the pair production process, where an electron-positron pair is created within the Coulomb field of the nucleus. Pair production can occur in the electron field as well (not shown). Modified from Janssens (2018).

1.2.3 Rayleigh scattering

Coherent Rayleigh scattering, illustrated in Fig. 1.2, is an elastic scattering event between the incoming X-ray photon and the electrons of an atom in the material. As a result, no photon energy is lost during the interaction. The photon is deflected by the electron cloud, hereby undergoing a change in direction. If the elastic scattering occurs at the nucleus, this interaction is known as Thomson scattering. Coherent scattering is mainly important at the lowest X-ray energies.

1.2.4 Pair production

At very high energies, X-rays have a finite probability for electron-positron pair creation within the Coulomb field of the nucleus (Fig. 1.3). The energy threshold for electron-positron pair production is 1.022 MeV, since this is the energy equivalent to the mass of the two particles. Pair production in the electron field requires 2.044 MeV. In matter, a positron will only travel a short distance before encountering an electron, causing an annihilation process producing two photons traveling in opposite directions. This annihilation process forms the foundation of positron emission tomography (PET). Although the contribution of pair production to the total attenuation will be negligible in the range of energies relevant for most X-ray imaging applications (rarely above 240 keV (du Plessis et al., 2017)), it becomes relevant for high energy (MeV) X-ray imaging systems (Katsuyama et al., 2007), and is even dominant above 10 MeV for lead and above 30 MeV for water.

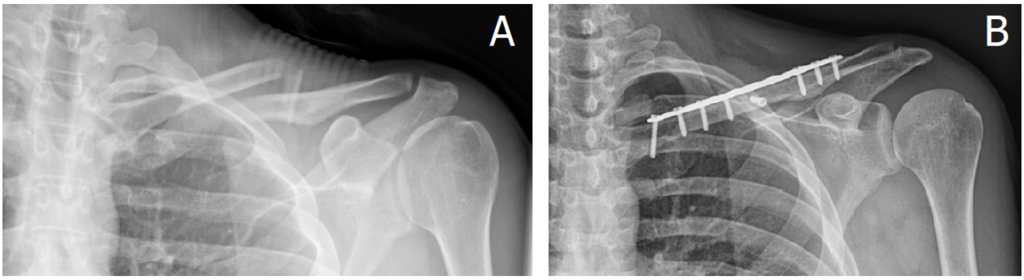

Figure 1.4: a) Medical X-ray image of a clavicle fracture showing a clear bayonet apposition. b) X-ray image of the same shoulder after surgery, where the bone has been repositioned and fixed with a titanium plate and screws.

1.3 X-ray imaging

Medical X-ray images are arguably the most well known application of X-ray physics. An example of a medical X-ray image is shown in Fig. 1.4. Imaging, however, requires a clear contrast mechanism. Without sufficient contrast, X-ray images would not be very useful. Given that the X-ray interaction cross sections in Eq. (1.1) depend on the material the X-ray is traveling through, different materials will lead to different amounts of interactions. The higher the density and atomic number of the material, the higher the number of X-rays lost in interactions. Furthermore, X-rays traveling longer distances through a certain material will have a higher interaction probability. As such, three parameters capable of providing contrast can be identified: atomic number, mass density, and distance traveled through the material. Using the law of Lambert-Beer, this contrast mechanism can be formulated in a concise way.

1.3.1 The Lambert-Beer law

Assume that a monochromatic X-ray beam with intensity I_0 illuminates a homogeneous object with thickness Δz. The intensity of the transmitted beam I is determined by how much of the X-ray intensity is lost as a result of the interactions described in Section 1.2. As mentioned earlier, this depends on the distance Δz traveled through the material, as well as on the atomic number Z and the mass density ρ.

In practice, the effect of Z and ρ on the X-ray beam attenuation is expressed through the material- and energy dependent linear attenuation coefficient μ. Given that a linear attenuation coefficient can be associated with every interaction type, and since μ_i is proportional to σ_i, Eq. (1.1) implies that:

$$\mu_{\text{tot}} = \mu_{\text{pe}} + \mu_{\text{Compton}} + \mu_{\text{Rayleigh}} + \mu_{\text{pp}}. \tag{1.3}$$

The transmitted X-ray intensity through a homogeneous object with thickness Δz is then given by the Lambert-Beer law (Beer, 1852; Pfeiffer and Liebhafsky, 1951; Mayerhöfer et al., 2020):

$$I = I_0 \mathrm{e}^{-\mu_{\mathrm{tot}} \Delta z}. \tag{1.4}$$

As is clear from Eq. (1.4), the transmitted intensity drops exponentially as a function of the distance travelled through the material. In reality, most objects are not homogeneous, and Eq. (1.4) has to be generalized to an integration over a spatially varying $\mu(z)$:

$$I = I_0 \mathrm{e}^{-\int \mu(z) \mathrm{d}z}, \tag{1.5}$$

where the subscript in μ_{tot} has been omitted for the sake of simplicity. If the shape and composition of an object is known, Eq. (1.5) can be used to predict the X-ray intensity measured in a plane behind the object, providing a mathematical basis for X-ray imaging. It should be noted that Eq. (1.5) is valid for a monochromatic (i.e. a single photon energy) X-ray beam. For polychromatic beams, the energy dependence of $\mu(z)$ has to be taken into account, and the right-hand side of Eq. (1.5) has to be integrated over the energy spectrum (Six et al., 2019). In practice however, this is often omitted in computed tomography using polychromatic sources (Section 1.4), leading to beam hardening artifacts (Van de Casteele et al., 2002).

1.3.2 Generation of X-rays

Although natural X-ray sources do exist (e.g., cosmic radiation or radioactive isotopes), X-rays intended for imaging purposes in a lab or clinical environment are generated in a controlled way using X-ray tubes. A typical X-ray tube consists of a cathode and an anode, as illustrated by Fig. 1.5. The cathode is heated to a temperature of approximately 2400 K, resulting in the thermionic emission of electrons. Due to the acceleration voltage applied between cathode and anode, the electrons freed from the cathode are accelerated towards the anode target. Upon arrival at the anode, the electrons are subject to a strong deceleration due to interaction with the anode material, often tungsten. Energy lost by the electrons in the deceleration process is emitted in the form of X-ray radiation, known as bremsstrahlung. The energy of the emitted bremsstrahlung X-rays depends on the amount of energy lost by the decelerating electrons, resulting in a broad, continuous X-ray energy spectrum. The acceleration voltage of the X-ray tube determines the upper energy limit of the spectrum.

In addition to the bremsstrahlung, an electron hitting the anode can free an inner shell electron from an anode atom. As described in Section 1.2.1, the electron occupying the vacancy will emit a characteristic X-ray photon. The energy of characteristic X-rays is determined by the difference in energy between the electron shells involved in the process. As a result, only a limited and discrete set of characteristic X-ray energies is possible for a given material (hence the name characteristic X-rays). In the X-ray emission spectrum, these characteristic energies will appear as distinct peaks on top of the bremsstrahlung profile. An example of a typical X-ray spectrum is shown in Fig. 1.5.

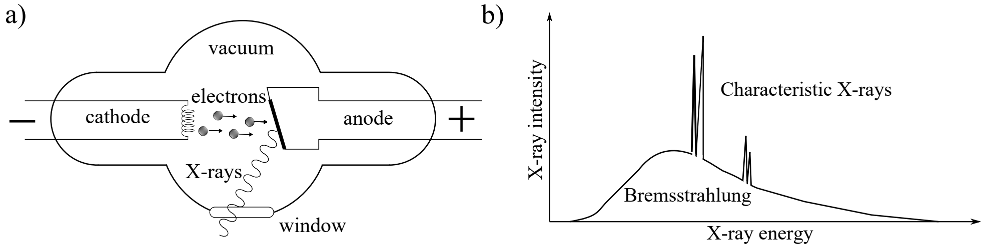

Figure 1.5: a) Schematic overview of an X-ray tube: X-rays are produced by accelerating electrons generated at the cathode towards the anode. b) Typical X-ray spectrum showing a combination of bremmstrahlung and characteristic X-rays. Modified from Janssens (2018).

X-rays will only be emitted from the area on the anode targeted by the accelerated electrons. The size of this area, also known as the focal spot size, finally affects the image quality. In general, larger spots will result in more image blurring. The energy dissipated by the electrons heat the anode, which is mitigated by rotating the anode, allowing the material to cool down. However, the brightness of small (microfocus) focal spots is still limited by the risk of melting the anode material, since the same material is being heated repeatedly. Liquid metal jet anodes (Hemberg et al., 2003) make use of a stream of liquid metal that replaces the rotating anode, ensuring a continuous replacement of the anode material. This effectively removes the risk of melting the anode (it is already molten), allowing for increased brightness using smaller focal spots. However, liquid metal jet anodes can be prone to evaporation of the anode material due to the high electron flux.

A more dramatic way of generating X-rays, is by means of large-scale synchrotron facilities (Bilderback et al., 2005). Synchrotrons are large electron rings, in which the electrons are accelerated by sequences of magnets to speeds close to the speed of light. The X-rays produced by the curved trajectory of the relativistic electrons are millions of times brighter than radiation produced from conventional X-ray tubes. As such, synchrotron facilities are a unique class of X-ray sources, with applications ranging from high-resolution imaging to crystallography.

1.3.3 Projection radiography

A standard X-ray imaging setup requires an X-ray source to generate the X-ray beam and a detector to capture the radiation after interaction with the object of interest. Historically, fluorescent screens and photographic film were used to acquire X-ray projection images, known as radiographs, but the development of detector technology has led to a shift towards digital radiography. Here, the X-rays absorbed in the detector generate an electric current, which is converted to an image. The most common detector type is probably the energy integrating flat panel detector, where a scintillator layer converts X-ray photons into visible light, which is in turn captured by a photodiode. This type of detector captures the total intensity accumulated in each pixel during a set integration time. More recently, however, photon counting detectors have gained increased interest (Taguchi and Iwanczyk, 2013; Greffier et al., 2025). These detectors are capable of measuring single photon interactions and provide additional spectral information, as well as showing improved spatial resolution and possible dose reduction. In addition, unlike energy-integrating detectors, the recorded total number of counts in photon counting detectors is unaffected by electronic noise, lowering the noise in the images to its theoretical limit (Swank, 1973).

In general, an increased number of X-rays arriving at a detector pixel will result in a higher intensity recorded by that pixel. It is, however, common practice to reverse the contrast in X-ray images. This means that bright pixels correspond to strong X-ray attenuation rather than high X-ray transmission. To convert the transmission contrast to attenuation contrast (AC), the measured intensity is divided by the intensity without object (flat field correction) and the negative logarithm is taken (log-correction). The resulting projection image is then, following Eq. (1.5), given by

$$-\ln\left(\frac{I}{I_0}\right) = \int \mu(z)\mathrm{d}z. \tag{1.6}$$

Eq. (1.6) forms the standard forward model for CT, the imaging method discussed in Section 1.4, which extends two-dimensional (2D) to three-dimensional (3D) imaging.

1.4 X-ray computed tomography

Although projection radiography is a useful imaging method with many applications, Fig. 1.4 also demonstrates its main disadvantage: 2D X-ray images lack depth information. If the screws were translated slightly along the optical axis, this would result in the same projected image. Hence, extracting reliable information with respect to the 3D distribution of materials inside objects is impossible from a single radiograph. Multiple projections from different viewing angles are required to retrieve the 3D spatial information. In X-ray computed tomography (XCT), multiple radiographs are acquired (Section 1.4.1) and combined to reconstruct a 3D representation of the imaged object (Section 1.4.2).

1.4.1 Acquiring X-ray projections

CT requires the acquisition of multiple radiographs, each taken from a different viewing angle. Changing the viewing angle can be done by rotating the source and detector gantry around the object, or by using a rotation stage for the object while keeping the source and

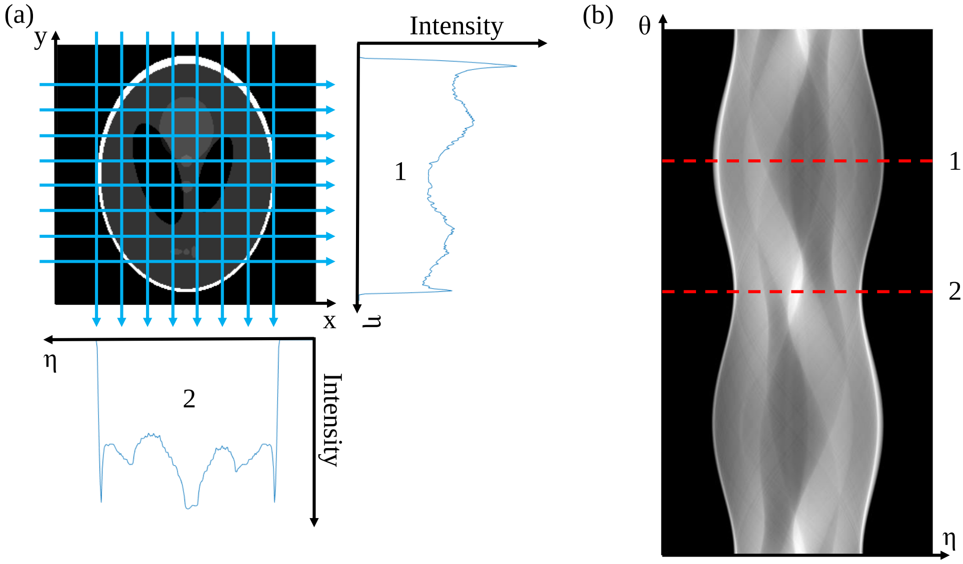

Figure 1.6: (a) Example of two orthogonal 1D projections of a 2D Shepp-Logan phantom, showing the projected intensity. (b) Sinogram of the same phantom resulting from 720 equally spaced projections over a full angular range of 360°. The dashed lines indicate the angles corresponding to the intensity profiles shown in (a).

detector at fixed positions. These are the standard approaches for medical CT and micro-CT, respectively.

A simplified example of a 2D Shepp-Logan phantom (Shepp and Logan, 1974) projected onto 1D line profiles is shown in Fig. 1.6. Depending on the projection angle θ, a different intensity profile $I(\eta)$ will be acquired. The full set of projections can be represented in a single sinogram, having one spatial and one angular coordinate (rather than two spatial coordinates in the original image). As indicated by the arrows in Fig. 1.6, a parallel beam geometry was assumed for the creation of this sinogram, which means that all projecting rays follow parallel trajectories. Extending the parallel beam geometry to 3D results in 2D projections that can be represented by a stack of sinograms. Modern CT systems, however, usually exhibit a cone beam geometry, where all rays connecting source to detector lie in a cone originating from the focal spot. Considering only the central slice in a 3D cone beam geometry leads to a 2D fan beam geometry.

1.4.2 Tomographic reconstruction

The objective of CT is to reconstruct the (3D) volume from its projection images. The reconstructed volume can be used to extract cross-sectional slices or to compute a rendered image. Fig. 1.7 shows the CT reconstruction of the treated clavicula fracture shown in

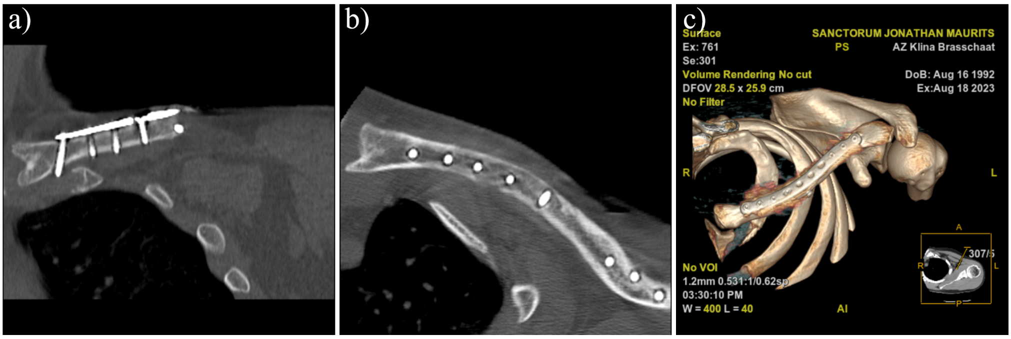

Figure 1.7: Coronal (a) and axial (b) slices through the reconstructed CT volume of the treated clavicula fracture shown in Fig. 1.4, providing 3D information about the positions of the screws. c) 3D rendering of the reconstructed CT volume, clearly showing the position of the titanium plate with respect to the bone.

Fig. 1.4. In contrast to Fig. 1.4, Fig. 1.7 provides reliable 3D information on the position of the titanium plate and screws in the body. Reconstructing a volume from its projections requires dedicated mathematical algorithms, which aim at inversion of the forward model from Eq. (1.6). Through the projection data, the left-hand side of this equation is known. From these known values, the reconstruction algorithm estimates the spatially dependent attenuation coefficient μ.

Assuming a 2D parallel beam geometry for simplicity, each line L that crosses a 2D object is defined by its distance to the origin (η) and its rotation angle with respect to the y-axis (θ),

$$L(\eta,\theta) = \{(x,y) \in \mathbb{R}^2 : \eta = x\cos\theta + y\sin\theta\}. \tag{1.7}$$

The projection of a 2D object onto 1D projections is then given by the Radon transform. The Radon transform of μ maps each possible line through the object to the line integral of $\mu(s)$ along that line, with s denoting the position on the line L:

$$\begin{aligned} p(\eta,\theta) &= \int_{L(\eta,\theta)} \mu(s)\mathrm{d}s \\ &= \int_{-\infty}^{+\infty}\int_{-\infty}^{+\infty} \mu(x,y)\delta_D(x\cos\theta + y\sin\theta - \eta)\mathrm{d}x\mathrm{d}y. \end{aligned} \tag{1.8}$$

Here, δ_D denotes the Dirac delta function. Associating each line with a point in a projection image, it is clear from (1.6) that the Radon transform of μ yields the collection of all possible flat field and log-corrected X-ray projections of μ. This mathematical foundation for CT has existed since the early 20th century (Radon, 1917), but the development of XCT as an imaging technique was initiated only many decades later (Cormack, 1963, 1964; Hounsfield, 1973; Ambrose, 1973). It should be noted that tomography as a method is used with various types of radiation, such as radio waves (Bracewell, 1956), terahertz radiation (Hu and Nuss, 1995; Mittleman et al., 1997; Ferguson et al., 2002; Lumbeeck et al., 2023), neutrons (Matsumoto and Krata, 1983), and electrons (De Rosier and Klug, 1968; Crowther et al., 1970).

1.4.2.1 Analytical reconstruction

The most intuitive approach to reconstructing an object from its projections is to redistribute all projected values back along the projection directions, which is known as back projection. In practice, however, this leads to poor quality reconstructions. Instead, an improved version of the back projection method is commonly used: the filtered back projection (FBP). As its name implies, the back projection is in this case preceded by a filtering step. As understood from the Fourier slice theorem, lower frequencies are sampled much more densely relative to higher frequencies in the Fourier transform of the object function. The underlying reason is that the 1D Fourier transform of a parallel projection of an object is equal to a slice of the 2D Fourier transform of the object. The dominant low-frequency sampling leads to significant blurring in the reconstructed image domain. By applying a ramp filter $|\omega_s|$ in the Fourier domain, the lower frequencies are suppressed, improving the level of detail in the reconstruction.

$$\mu(x,y) = \int_0^{\pi} \int_{-\infty}^{+\infty} \tilde{p}(\omega_s,\theta)|\omega_s|e^{2\pi i\omega_s(x\cos\theta+y\sin\theta)}\mathrm{d}\omega_s\mathrm{d}\theta. \tag{1.9}$$

Here, $\tilde{p}(\omega_s,\theta)$ is the Fourier transform of $p(\eta,\theta)$. Eq. (1.9) provides the inverse of the Radon transform (Eq. (1.8)). The derivation of the FBP algorithm can be found in detail in (Kak and Slaney, 1988), as well as considerations regarding the practical implementation of the reconstruction method for parallel and fan beam geometries. The pixel-dependent weight factor in the backprojector associated with the fan beam reconstruction (Gullberg, 1979) can be omitted by rebinning the fan beam data to parallel projections (Besson, 1999). By setting the Fourier components of the highest frequencies to zero, the noise level of the reconstruction is reduced. For the 3D cone beam geometry, the approximate Feldkamp-Davis-Kress (FDK) algorithm (Feldkamp et al., 1984) is the most widely used analytical reconstruction method. Eq. (1.9) yields an exact reconstruction of the original object under the assumption that an infinite number of projection angles is available. In practice, however, the number of projections will always be limited. If a lot of high quality projection data is available, FBP yields fast and high-quality reconstructions. Reducing the number of projections leads to degraded reconstructions suffering from artifacts.

1.4.2.2 Algebraic reconstruction

In practice, both imaging and reconstruction are discrete processes in CT. A finite number of projections is acquired using a finite number of detector pixels, and the object is reconstructed on a discrete pixel grid (although in some cases parametric or mesh reconstruction is possible (Elberfeld et al., 2023; Renders et al., 2024)). As a result, the

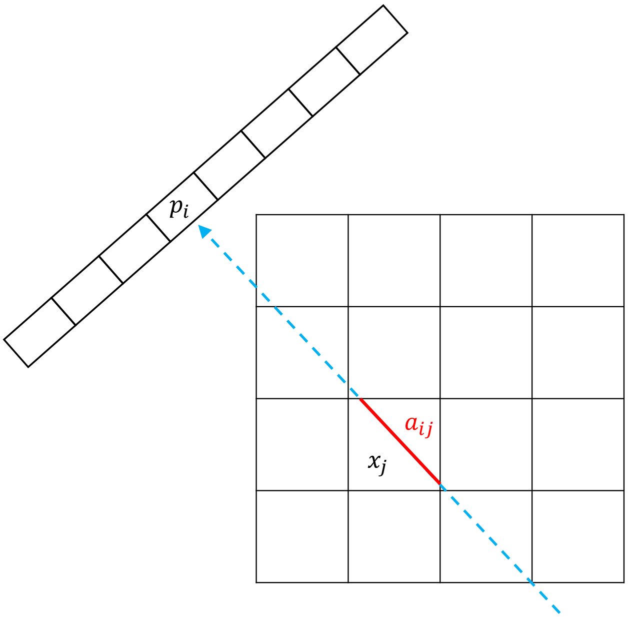

Figure 1.8: Graphical representation of a forward projection as modeled by Eq. (1.10), showing the intersection length (in red) corresponding to the weight a_{ij} for detector pixel p_i and voxel x_j.

continuous analytical formulas from the previous section are discretized for real world CT reconstructions. Alternatively, the discrete nature can be incorporated in the reconstruction model itself. In that case, the projection model from Eq. (1.8) is replaced by the following linear system of equations:

$$\boldsymbol{p} = \boldsymbol{A}\boldsymbol{x}. \tag{1.10}$$

Here, $\boldsymbol{x}$ is the vectorized object, where each element x_j corresponds to the local linear attenuation coefficient $\mu(s)$ of the respective voxel. The flat field corrected and log-corrected projection data (Section 1.3.3) is stored in vector $\boldsymbol{p}$. The (forward) projection data p_i are modeled as a weighted sum of the linear attenuation coefficients in $\boldsymbol{x}$ by the projection matrix $\boldsymbol{A}$, representing a discretized form of the Radon transform. Conversely, the transposed projection matrix $\boldsymbol{A}^{\mathrm{T}}$ is a discretized version of the back projection. The matrix elements a_{ij} represent the intersection lengths of the rays arriving at p_i with voxel x_j. This is illustrated in Fig. 1.8.

Solving Eq. (1.10) directly by performing $\boldsymbol{A}^{-1}\boldsymbol{p} = \boldsymbol{x}$ is in general not possible as the inverse of $\boldsymbol{A}$ cannot be determined. As such, the best possible solution $\boldsymbol{x}^*$ is expressed as a minimization problem:

$$\boldsymbol{x}^* = \arg\min_{\boldsymbol{x}} \|\boldsymbol{A}\boldsymbol{x} - \boldsymbol{p}\|, \tag{1.11}$$

where $\|\cdot\|$ denotes some vector norm, usually the squared 2-norm $\|\cdot\|_2^2$. Algebraic reconstruction methods aim to approximate the solution x^* using iterative schemes. Well-known algorithms for solving the inverse problem for CT are the Algebraic Reconstruction Technique (ART) (Gordon et al., 1970), the Simultaneous Iterative Reconstruction Technique (SIRT) (Gilbert, 1972; Gregor and Benson, 2008), and the Simultaneous Algebraic Reconstruction Technique (SART) (Andersen and Kak, 1984). Taking the widely used SIRT algorithm as an example, consider an initial guess $\boldsymbol{x}^{(0)}$ for the reconstructed volume, for example the 0-vector. SIRT then iteratively computes consecutive corrections to the initial guess according to the update scheme

$$\boldsymbol{x}^{(k+1)} = \boldsymbol{x}^{(k)} + \boldsymbol{C}\boldsymbol{A}^{\mathrm{T}}\boldsymbol{R}\left(\boldsymbol{p} - \boldsymbol{A}\boldsymbol{x}^{(k)}\right). \tag{1.12}$$

Here, $\boldsymbol{p} - \boldsymbol{A}\boldsymbol{x}^{(k)}$ is called the projection difference, and $\boldsymbol{C}$ and $\boldsymbol{R}$ denote the inverse column and row sums, respectively:

$$c_{jj} = \left(\sum_i a_{ij}\right)^{-1}, \tag{1.13}$$

$$r_{ii} = \left(\sum_j a_{ij}\right)^{-1}. \tag{1.14}$$

As a side note, we mention that SIRT can be interpreted as a Landweber algorithm where the relaxation parameter follows from Eq. (1.13) and Eq. (1.14) (Landweber, 1951; Gregor and Benson, 2008). Iterative reconstruction methods tend to be flexible with respect to unconventional geometries (Nguyen et al., 2021) and more advanced acquisition protocols such as dynamic (4D) imaging (Van Eyndhoven et al., 2015) and extended field-of-view (FOV) imaging (Sanctorum et al., 2021b), or when prior knowledge is available (Batenburg and Sijbers, 2011). It should be noted that iterative tomographic reconstruction is not limited to Landweber-type algorithms and that other, more general solvers such as gradient descent or quasi-Newton methods can be used as well (Six et al., 2021).

1.5 Monte Carlo simulations for X-ray imaging

The Lambert-Beer law (Eq. (1.5)) provides a method to compute projection images from an object with a known spatial distribution of linear attenuation coefficients. Indeed, by integrating $\mu(s)$ along straight lines connecting the source and detector, an artificial X-ray image (forward projection) can be simulated. This is the fundamental principle underlying deterministic ray-tracing tools for X-ray imaging simulations. Although this is often sufficient, for example for modeling tomographic reconstruction (van Aarle et al., 2016; Paramonov et al., 2024), other applications (e.g., the design of imaging setups or dose calculations) require a more detailed physics-based approach.

Monte Carlo (MC) modeling is a popular method for all applications where measurements are not feasible or where the complexity of the problem prevents the use of analytic models (Metropolis and Ulam, 1949; Raeside, 1976). Attempting to model physics through probabilistic estimates, it provides a numerical solution that models the interaction of objects, such as photons, with other objects or their environment. A stochastic solution is determined by random sampling of relationships based on particle physics theory and experimental data until convergence is reached. The history of every simulated particle can be analyzed, and MC simulations find several applications in (nuclear) medical imaging, such as detector and system design, quantification, and correction methods for image degradation. In this dissertation, all simulations are performed using the Geant4-based GATE MC framework (Santin et al., 2003; Jan et al., 2011). In the following sections, two key aspects of MC simulations will be introduced: the generation of random numbers and sampling techniques. Random numbers are essential to mimic the stochastic nature of particle interactions, whereas sampling the relevant probability density function (PDF) is required to obtain correct values for the stochastic variable of interest.

1.5.1 Random number generation

Generating arbitrary samples from a given PDF relies on randomness. As such, full-scale MC simulations require large sequences of random numbers. The order of these sequences should be unpredictable and free from any patterns. In the early days of MC calculations, random number tables (e.g., RAND) were used for this purpose, but today these tables have become obsolete. In its most elementary form, a random number is understood as a particular value of a continuous random variable distributed on the unit interval.

A seemingly natural way to produce random numbers is by monitoring the output of a physical process (e.g., electronic noise or quantum effects). This concept is gaining momentum in more recent literature (Ma et al., 2016; Cirauqui et al., 2024), but is still rarely used in practice for MC simulations. The main reason for this is repeatability: retracing the exact steps of a particular MC experiment requires knowledge of the correct sequence of random numbers that was used. Hence, the most popular approach to generate random numbers is to deterministically calculate series of (pseudo-)random numbers from a random starting seed. As paradoxical as the previous sentence may seem, this approach is in fact very effective for MC simulations. There is a practical reason for this: if a mathematically calculated sequence of pseudo-random numbers and a sequence of true random numbers pass a set of reasonable randomness tests (see e.g., L'Ecuyer (1988)) equally well, there is no real ground to favor one over the other. However, it is possible that the pseudo-random number sequence begins to repeat itself once a certain number of values has been generated. This number is called the period of the sequence. If the period is very large, this behavior is of little importance. However, it is clear that the period should always at least be large enough for its intended purpose.

An academic example of an algorithm to produce pseudo-random numbers, is the 'mid-square' method (Raeside, 1976). It consists of taking an n-digit number N_1 as the seed of the sequence, squaring it to form a 2n-digit number, and extracting the middle n digits to form the second number in the sequence N_2. If less than 2n digits are obtained, zeros are placed in the left-most positions to obtain a 2n-digit number. The third pseudo-random number N_3 is obtained by squaring N_2 and extracting its middle n digits. This procedure is subsequently repeated until the sequence is considered long enough. In practice, other methods are being applied to ensure high-quality pseudo-random number sequences with long periods (James, 1990; James and Moneta, 2020).

1.5.1.1 Multiplicative linear congruential generators

One of the earliest and most well-known random number generators is the multiplicative linear congruential generator (MLCG). Here, every successive integer is obtained by multiplication of the previous one with a carefully chosen multiplier *a* (L'Ecuyer, 1988) and adding a constant *b*:

$$s_{i+1} = (as_i + b) \mod m. \tag{1.15}$$

This method is implemented in Geant4 for a 32-bit and a 64-bit word length *m*. The higher order bits are lost at multiplication, leaving pseudorandom lower-order bits. When b is chosen as an odd number, a period of 2^{32} can be obtained for a 32-bit word length. However, MC simulations may exhaust the MLCG period, and this type of random number generator can lead to biased results. In addition, the generation of independent series is not straightforward.

1.5.1.2 Lagged Fibonacci generators

In a standard Fibonacci series, each element is the sum of the two preceding elements. A generalization of this concept can be used to construct a Fibonacci random number generator. Here, each number is computed by performing some operation $\odot$ on the two preceding numbers, most commonly addition, subtraction, multiplication, and the exclusive-or operation. In practice, lagged versions of Fibonacci sequences are always used, where each number results from two numbers that have occurred somewhere earlier in the sequence, but not necessarily the last two:

$$s_i = (s_{i-j} \odot s_{i-k}) \mod m, \quad j > k. \tag{1.16}$$

If $m = 2^u$, it is possible to obtain a period close to 2^{j+u-1}.

1.5.1.3 Advanced long period generators

In so-called universal generators, two different approaches are combined to obtain a very long period and excellent randomness behavior (Marsaglia et al., 1990). The RANMAR generator, which is the default generator in Geant4, employs this technique by combining a lagged Fibonacci generator with an arithmetic sequence (James, 1990). RANMAR reaches a period of about 2^{144}, exhibits excellent statistical behavior, and allows the generation of independent streams, required for parallelization. Starting from the same random seed yields exactly the same results. Due to these properties, RANMAR became widely used for long MC simulations.

In GATE, the user has three random number generators at their disposal: JamesRandom (Marsaglia et al., 1990), Ranlux64 (Marsaglia and Zaman, 1991; Lüscher, 1994), and Mersenne Twister (Matsumoto and Nishimura, 1998). JamesRandom is a C++ implementation of the RANMAR universal generator, whereas RANLUX64 is based on the subtract-with-borrow RCARRY generator with period 2^{570} (James, 1990; James and Moneta, 2020). The Mersenne Twister algorithm is known as a reliable, fast generator with a very long period ($2^{19937}-1$). A comparative study found no systematic differences between GATE simulation results obtained with the three available generators, suggesting that it is recommended to use the faster Mersenne Twister (Sepehri et al., 2020).

1.5.2 Sampling methods

A Monte Carlo procedure aims to draw independent random samples from some probability law via the use of independent (pseudo-)random numbers. A typical example is the estimation of π by taking the ratio of the area of the circle S_c to the area of the square S_s as shown in Fig. 1.9. The ratio R equals

$$R = \frac{S_c}{S_s} = \frac{\pi\left(\frac{d}{2}\right)^2}{d^2} = \frac{\pi}{4} \Rightarrow \pi = 4\frac{S_c}{S_s}. \tag{1.17}$$

This implies an estimate of π can be computed by randomly sampling N points within the square and counting the number of points inside the circle N_c. The estimate of π is then given by $\hat{\pi} = 4\frac{N_c}{N}$. The factor 4 can be incorporated in the counting process by assigning a score of 4 to points within the circle and a score of 0 to points outside of the circle.

The generation of (pseudo-)random numbers has already been explored in Section 1.5.1, and the following sections will discuss methods for converting random numbers into random samples (Raeside, 1976).

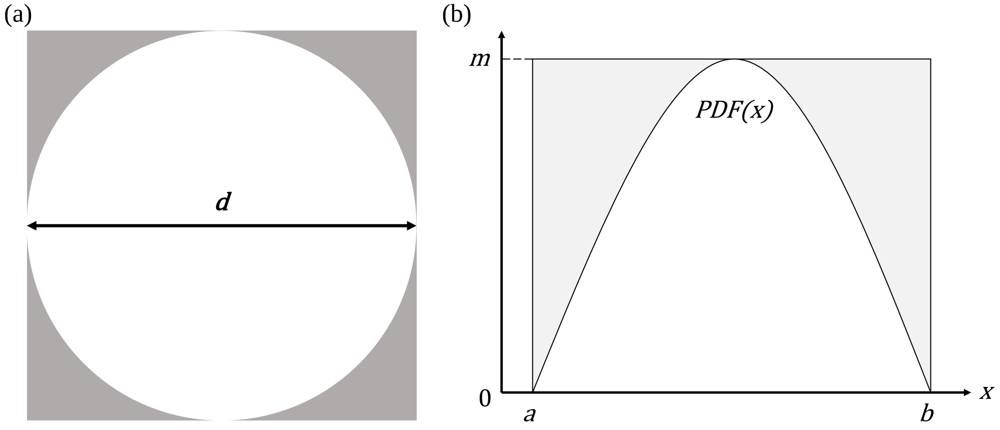

Figure 1.9: a) Circle embedded inside a square. The side of the square equals the circle diameter d. b) Example of a probability density function $PDF(x)$.

1.5.2.1 The direct method

Consider a cumulative distribution function (CFD) $F(x) = P(X \leq x)$ corresponding to the integral of the probability density function $PDF(x)$ over the interval $[x_1, x]$:

$$F(x) = \int_{x_1}^{x} PDF(x')dx'. \tag{1.18}$$

In the direct method, a random sample is created by replacing $F(x)$ by a uniformly distributed random number from the interval $[0,1]$ and subsequently solving Eq. (1.18) for x. This method can be used if it is straightforward to determine the inverse function of $F(x)$.

As an example, consider a simplified case of a photon traveling a random distance between interactions (see also Section 1.3.1). This process is governed by the exponential probability law, with $\mu e^{-\mu z}dz$ the probability that an interaction will occur in the distance interval $[z, z+dz]$. The corresponding CFD is:

$$F(z) = \int_{0}^{z} \mu e^{-\mu z'} dz' = 1 - e^{-\mu z}. \tag{1.19}$$

Replacing $F(z)$ by the uniformly distributed random number $0 < s_r < 1$ and solving for z yields a random sample for the distance traveled by the photon:

$$s_r = 1 - e^{-\mu z} \Rightarrow z = -\frac{\ln(1 - s_r)}{\mu}. \tag{1.20}$$

1.5.2.2 Rejection sampling

In practice, an application of the direct method is not always feasible. Alternatively, the rejection sampling method can be used. As the name suggests, some of the generated random samples are in this case rejected on the basis of some criterion. Consider a simple PDF as depicted in Fig. 1.9, with upper bound m and $PDF(x) = 0$ for $x < a$ and $x > b$. Subsequently, independent pseudo-random samples can be generated from two uniform distributions $p_x(u) = 1/(b-a)$ and $p_y(v) = 1/m$ to produce points $(a+u_i, v_i)$, where u_i and v_i are the samples obtained from $p_x(u)$ and $p_y(v)$, respectively. All these points are enclosed by the rectangle shown in Fig. 1.9, with some of the points falling above the curve $PDF(x)$ and some falling below it. Following the rejection method, all points falling above the curve are rejected and only the points falling on or below the curve are used to compute the desired samples x_i through the scheme $x_i = a + u_i$. This procedure is equivalent to random sampling from the probability density $PDF(x)$ (Raeside, 1976).

1.5.2.3 Mixed methods

When the previous two methods are not applicable independently, a mixture is commonly used. Here, the PDF is written as the product of two probability distribution functions $PDF(x) = p_1(x) \cdot p_2(x)$. An x value is determined using the direct method on $p_1(x)$ and the rejection method is applied to $p_2(x)$ with that x. A detailed example concerning the simulation of Compton scattering using a combination of the direct and rejection method can be found in Raeside (1976).

1.5.3 Monte Carlo simulation software

A wide variety of MC simulation platforms suitable for X-ray imaging has been developed during the last few decades. Examples are EGSnrc (Kawrakow, 2000), McXtrace (Bergbäck Knudsen et al., 2013), GATE (Santin et al., 2003; Jan et al., 2011), and GAMOS (Arce et al., 2011). GAMOS and GATE are both built on top of Geant4 (Agostinelli et al., 2003; Allison et al., 2006, 2016)). Using general purpose nuclear physics codes such as Geant4 ensures high flexibility in simulation design. The main advantages are that they are extensively tested and widely used. They benefit from long-term existence and support, and are continuously evolving following new hardware and software developments. Compared to dedicated code, they show fewer simplifying assumptions and fewer limitations on their possible applications.

Since GATE has been designed as an upper layer for the Geant4 nuclear physics code, it takes advantage of all Geant4 features. This includes a great variety of physics models and basic event timing information, as well as geometry modeling and visualization tools. Its object-oriented design ensures high modularity. In addition, GATE has been using a scripting (macro) language for many years, allowing the user to easily design simulations. GATE has been developed as an international collaboration effort (the OpenGATE collaboration), and was publicly released in 2004. It is now shared by a large research community, while long-term support and maintenance is still ensured by the OpenGATE collaboration (Sarrut et al., 2022). Since 2024, two decades after its initial release, GATE version 10 provides a simple-to-use yet flexible Python-based interface through which users can set up Geant4 simulations, replacing the macro interface. Given that almost all of the simulation and implementation work in this dissertation is based on GATE (version 8), the following sections are used to summarize some core aspects of Geant4 and GATE.

1.6 Geant4

Geant4 is a widely used general purpose nuclear physics code with a great variety of physics models. In general, certain a priori information about the physics processes that occur, expressed in the form of probability density functions (PDFs), is required for performing MC simulations. Partial and total cross-section data provide this information when simulating photon interactions. These cross-sections are based on the material composition, and the data is subsequently used to calculate the path length and the type of interaction. During a simulation, the PDFs are sampled using randomly generated numbers. The energy of a photon is either dissipated along its path, or the photon can penetrate the scattering and attenuating media to reach the detector. At the detector, another PDF decides whether it should be accounted for, or discarded. The following sections will address photon interactions and particle transportation in Geant4.

1.6.1 Photon interactions in Geant4

The Geant4 physics package includes electrons, positrons, γ-rays, X-rays, optical photons, muons, hadrons, and ions. When using the low-energy extension for electromagnetic interactions, the modeling of photons and electrons is extended and verified down to 250 eV, covering atomic numbers between 1 and 99. It furthermore includes Rayleigh scattering. The low-energy processes make direct use of shell cross-section data instead of parameterizations, since the atomic shell structure is often more important at low energies compared to higher energies. In general, photon transport and interaction mechanisms are governed by four processes: pair production, Compton scatter, Rayleigh scatter, and the photoelectric effect (see Section 1.2). Each process involves two distinct steps: calculating and using the total cross sections and generating the final state. The total cross section's energy dependence for each process is extracted from data libraries (Amako et al., 2005), which provide cross sections for a discrete set of photon energies. For an intermediate energy E, the total cross section is thus obtained by logarithmic

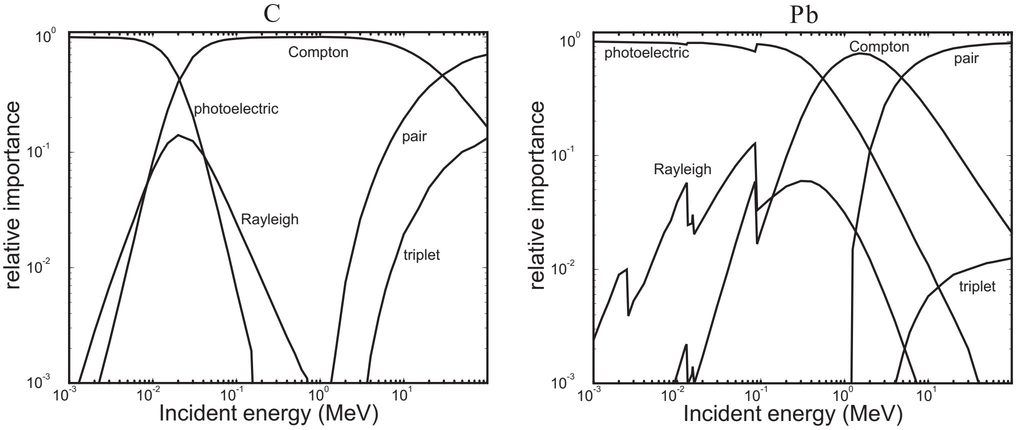

(a) (b)

Figure 1.10: Relative importance (i.e. fraction of the total cross section) of different photon interaction mechanisms in (a) carbon and (b) lead. Modified from Bielajew (2020).

interpolation:

$$\log\left(\sigma(E)\right) = \frac{\log(\sigma_1)\log(E_2/E) + \log(\sigma_2)\log(E/E_1)}{\log(E_2/E_1)}, \tag{1.21}$$

with E_1 and E_2 the nearest lower and higher energy for which σ_1 and σ_2 are tabulated, respectively. The mean free path for a certain process is then given by

$$\Delta l = \frac{1}{\sum_i \sigma_i(E) n_i}, \tag{1.22}$$

for a particle with energy E. Here, $\sigma_i(E)$ is the microscopic integrated cross section of the process at energy E, and n_i is the atomic density of the ith element in the material. $\sum_i$ is the sum over all the elements composing the material. The relative contributions of the different photon cross section are shown in Fig. 1.10 for carbon (low-Z material) and lead (high-Z material). The photoelectric effect is dominant for carbon below 20 keV, while Compton scatter is the dominant process for higher energies up to 30 MeV. Compton scatter is dominant in a much smaller energy range in the case of lead, ranging from 700 keV to 4 MeV. This implies that for most X-ray imaging applications, the image contrast is dominated by either the photoelectric effect or Compton scatter (see Section 1.2).

1.6.2 Particle transportation in Geant4

In Geant4, the simulation setup defines a world geometry consisting of analytical or parameterized volumes that have been assigned certain material properties. The number of particles initially generated at the source (events) depends on the source definition. During a single event, every (secondary) particle generated is represented by a track, labeled with a trackID. Each track holds all the temporary information concerning a specific particle during its transport from one point to another. A particle is transported one step at a time, from interaction point to interaction point, until it either ceases to exist or reaches the boundary of the world. It is assumed that the chosen step size is small enough to ensure that the particle cross sections remain approximately constant during each step. In principle, a very small step size should be used for an accurate simulation, but the computational cost increases with decreasing step size. The particle tracking algorithm used by Geant4 consists of two essential parts: the sampling of the number of interaction lengths and the evaluation of the distance to the next interaction point. The number of mean free paths (interaction lengths) that a particle travels can be written as (Agostinelli et al., 2003):

$$N_{\Delta l} = \int \frac{dx}{\Delta l(x)}. \tag{1.23}$$

Furthermore, given that the CFD of a random variable N_R denoting the number of mean free paths between a given point and the point of interaction is given by (cfr. Eq. (1.19))

$$P(N_R \leq N_{\Delta l}) = 1 - e^{-N_{\Delta l}}, \tag{1.24}$$

the number of interaction lengths can be sampled using the direct method (see Section 1.5.2.1) as $N_{\Delta l} = -\ln(s_N)$, with $0 < s_N < 1$ a uniformly distributed random number. The distance that the particle has to travel before a given process occurs in the current medium is given by $N_{\Delta l}\Delta l(x)$, i.e. the number of interaction lengths multiplied by the inverse of the macroscopic cross section for that process in the current material. As such, a travel distance is obtained for each process. The shortest among these distances yields the effective step over which the particle will be transported and determines which process is triggered, provided that the step is not limited by geometric boundaries or thresholds such as energy cuts and maximum step limits. $N_{\Delta l}$ is updated after each step Δx according to

$$N'_{\Delta l} = N_{\Delta l} - \frac{\Delta x}{\Delta l(x)}. \tag{1.25}$$

This includes the case of boundary crossing into a new medium, where tracking is continued in the new medium until an interaction point is reached.

1.7 GATE

GATE is written in C++ and has a modular structure built on three fundamental layers (Staelens and Buvat, 2009): (1) the core layer, (2) the application layer, and (3) the user layer. The core layer defines the basic mechanisms available in GATE for geometry definition, time management, source definition, digitization, and data output, whereas the application layer consists of derived classes to model-specific objects or processes. The functionality provided by each class is available via script commands in the user layer (replaced by a Python interface in GATE version 10). As a result, the end-user of GATE does not have to manipulate any C++ code, and a complete experiment can be defined using the GATE script language (or Python interface). This includes object geometry, source definition, camera geometry, detector electronics, physics processes, time passing, kinetic parameters, and output format.

1.7.1 Building the simulation geometry

The spatial distribution of a source in GATE can be specified using five two-dimensional shapes (circle, annulus, ellipse, square, and rectangle), and four three-dimensional shapes (sphere, ellipsoid, cylinder, and parallelepiped). In addition, the angular distribution of the departing particles can be defined using azimuthal and polar angles, allowing for different angular spans (e.g., fan beam or cone beam). Sources can also be described using images, which results in a voxelized description. Modeling a scanner system or digital phantom in GATE is based on basic elements known as logical volumes. A logical volume is defined by its name, shape, size, and material composition. It becomes a physical volume once it is placed at a specific position. To replicate and place logical volumes at multiple positions and orientations, repeaters can be used. Repeaters are elementary geometrical transformations such as rotations and translations, applied in succession. Combining various types of repeaters (e.g., ring, linear, and cubic array) to create more complex structures is also possible. During a simulation, time is explicitly kept track of by a virtual clock that synchronizes all time-dependent processes. The user provides the start and stop times of the acquisition and the sampling interval. In each time slice, the geometry is kept at rest (whereas the particle transport proceeds), and an update is performed at the transition to the next time slice.

1.7.2 Detection and digitization

Certain parts of the scanner geometry act as sensitive detectors where particle interactions are recorded. Interactions that occur inside the detector parts of the scanner create hits. The information stored in these hits includes the energy that has been deposited, the interaction positions, the origin of the particle, the type of interaction, the volume name in which the interaction took place, and the time information.

Subsequently, a chain of processing modules takes a list of hits from the sensitive detectors and transforms them into pulses, referred to as singles. This so-called digitizer can be controlled using the GATE scripting language. A chain starts with the adder, summing the deposited energy of all hits to yield a pulse. The energy-weighted centroid of the hit positions yields the position of the pulse, and the time of the pulse is set to that of the first hit within the volume. Secondly, the readout procedure of the scanner is triggered. The energy response instruction applies a blurring to the energy of the pulse, and an energy discrimination is performed to set an acceptance window (thresholder electronics).

Detector modeling is facilitated by predefined global systems, where the geometric hierarchy is automatically accounted for by the corresponding data output formats (ASCII and ROOT (Brun and Rademakers, 1997)).

1.7.3 Computational efficiency of GATE

Monte Carlo simulations are known for their notoriously long computation times. Realistic acquisitions in GATE may for example, in some cases, take several days or longer to complete on a single CPU. An important reason why GATE simulations are computationally expensive is that neither Geant4 nor GATE were initially built with efficiency as a primary objective. Geant4 comes with great flexibility and generality, inherited by GATE, including the photon transport model, navigation algorithms and PDFs. The general particle tracking algorithms of Geant4 are accurate and detailed, but this results in slow navigation through voxelized and parameterized geometries. This has a direct impact on the computational cost of GATE simulations. As a result, several strategies have been implemented to improve the computational efficiency of GATE simulations, including fast navigation algorithms (De Beenhouwer et al., 2008), parallelization (De Beenhouwer et al., 2007), dedicated variance reduction techniques (Staelens et al., 2006) and efficient data analysis (De Beenhouwer et al., 2009).

Chapter 2

Introduction to X-ray phase contrast imaging

This chapter provides a broad overview of the fundamentals of X-ray phase contrast imaging and wave optics simulation. Information beyond the contents of this chapter can be found in Goodman (1996), Born and Wolf (1999), Bartels (2013), Endrizzi (2018), Momose et al. (2020), Olivo (2021), and Paganin and Pelliccia (2021).

2.1 Introducing the second introduction

Some might be surprised to find a second introductory chapter in this dissertation, possibly assuming that all important X-ray matters have been covered in the previous chapter. Regardless of the delight or despair this might evoke, there is still plenty of important X-ray physics left to uncover. Chapter 1 has already introduced us to the essentials of X-ray imaging, building up from the fundamental nature of X-rays and their interactions with matter. As relevant and important as all of that may be, we are currently still looking at an incomplete picture. Indeed, in all the previous sections, X-rays have been approached from a particle perspective, with X-rays being described as photons or rays. Although this suffices for a description of attenuation-based X-ray imaging, a proper understanding of the principles of X-ray phase contrast imaging requires a wave optics description of X-ray physics. The current chapter aims at removing this missing wedge of information by addressing the (equally beautiful) wavelike nature of X-rays. First, some rather general theoretical considerations will be made, providing a useful context for the introduction of two new contrast types. Furthermore, the practical realization of X-ray phase contrast imaging will be discussed, as well as an alternative approach to the simulation of X-ray imaging. The final section of this chapter will be a bridge to the next chapters, where the original results obtained during this PhD are presented.

Figure 2.1: (a) A ray of visible right refracting at the air-material boundaries of a transparent piece of plastic. (b) Distorted view of a pen partially submerged in water due to refraction of light.

2.2 On waves and X-ray refraction

2.2.1 Refracting Röntgen's rays

Refraction, of which the basic principle is demonstrated in Fig. 2.1, is perhaps the most well-known optical phase effect. Most people encounter it on a regular basis in daily life, as illustrated in Fig. 2.1, where a distorted view of a pen partially submerged in water is shown. The distortion visible in the submerged part of the pen results from the refraction of light at the water surface, which forms a boundary between two media: water and air. Refraction effects are typically described by one of the most well-known formulas from high school optics: Snell's law. Imagine a ray of light entering a medium (water, glass), with index of refraction n_1, from vacuum (or air), with index of refraction n_0, having an angle of incidence θ_0. In absence of imagination, simply look at Fig. 2.2. After entering the medium, the light ray will have changed direction, expressed by the angle of refraction θ_1. This angle can be calculated using Snell's law:

$$n_0 \sin(\theta_0) = n_1 \sin(\theta_1). \tag{2.1}$$

The index of refraction of vacuum is 1. Hence, visible light rays entering a material from vacuum (or air) will refract toward the surface normal, i.e. $\theta_1 < \theta_0$, since $n > 1$ for any material other than vacuum. Visible light entering vacuum will for the same reason typically refract away from the normal. This principle is more generally applicable for arbitrary media, in the sense that visible light rays will refract toward the normal if $n_1 > n_0$ and away from the normal if $n_1 < n_0$.

All of the above will probably sound familiar to anyone that has ever taken high-school level physics courses. However, X-rays prefer to live by a slightly different set of optics rules. First, let us rewrite (2.1) by substituting $1 - \delta$ for n:

$$(1 - \delta_0) \sin(\theta_0) = (1 - \delta_1) \sin(\theta_1). \tag{2.2}$$

Why, one might ask. Luckily, there is a good reason for this modification: in contrast to visible light, the index of refraction for X-rays is smaller than 1. But it is only slightly

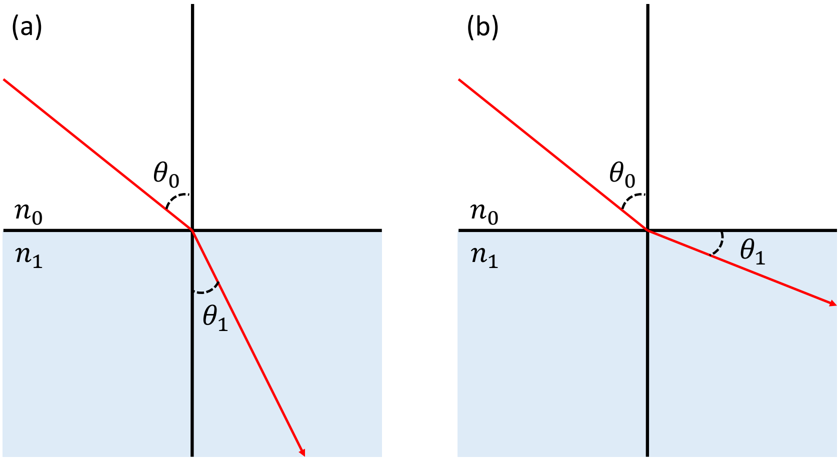

Figure 2.2: (a) Schematic depiction of the refraction of a ray of visible light entering a medium from vacuum. The refraction is oriented toward the surface normal. (b) Schematic depiction of the refraction of an X-ray entering a medium from vacuum. The X-ray is refracted away from the surface normal. The drawing is not to scale.

smaller, with δ typically in the order of 10^{-7} or even less. Hence, in the case of X-rays, this 'decrement of the index of refraction' (δ) becomes the relevant material parameter, which is why it makes sense to write Snell's law as in Eq. (2.2). The fact that $1-\delta<1$ has some seemingly counterintuitive consequences. In contrast to visible light rays, X-rays refract away from the surface normal when entering a material from vacuum, as illustrated in Fig. 2.2. At a secondary level, this implies that X-rays do not show the effect of total internal reflection, as visible light does (e.g. observation of Snell's window when swimming underwater). In contrast, X-rays show total **external** reflection for large enough angles of incidence, or equivalently, sufficiently small grazing angles ($\alpha_c \approx 0.0256^\circ$ for $\delta \approx 10^{-7}$). Total external reflection is an important underlying principle for reflective X-ray optics (Wolter, 1952a,b).

At this point, some questions might have formed in the reader's mind, such as how all of this is related to X-ray phase contrast imaging, and why we are still considering rays instead of waves. Some might also wonder what the winning numbers of the lottery will be next week, but that is beyond the scope of this work. The other questions are addressed in the remainder of this chapter, where the following (sub)sections will loosely follow the much more detailed derivations found in Paganin and Pelliccia (2021) and the references therein.

2.2.2 A different point of view: the wave nature of X-rays

To get a more fundamental understanding of phase effects, we will have to take a step back and introduce the wave-optical description of light. Let us start with briefly touching upon the historical perspective, by considering the free space d'Alembert wave equations resulting from the Maxwell equations for the electric and magnetic fields, **E** and **B**, respectively:

$$\left(\frac{1}{c^2}\frac{\partial^2}{\partial t^2} - \nabla^2\right)\mathbf{E}(x,y,z,t) = \mathbf{0}, \tag{2.3}$$

$$\left(\frac{1}{c^2}\frac{\partial^2}{\partial t^2} - \nabla^2\right)\mathbf{B}(x,y,z,t) = \mathbf{0}. \tag{2.4}$$

In Eq. (2.3) and Eq. (2.4), x, y, and z are Cartesian spatial coordinates, t denotes the time, ∇^2 is the Laplacian in three spatial dimensions, and c is a speed given by the Maxwell relation:

$$c = \frac{1}{\sqrt{\mu_0 \varepsilon_0}}. \tag{2.5}$$

In Eq. (2.5), $\varepsilon_0 \approx 8.854187 \cdot 10^{-12}$ F/m and $\mu_0 \approx 4\pi \cdot 10^{-7}$ H/m are the electrical permittivity and the magnetic permeability of free space, respectively. The d'Alembert equations imply two interesting facts. First, **E** and **B** are described by wave equations, indicating electromagnetic disturbances propagate as waves in vacuum. Furthermore, the speed c of these electromagnetic waves, given by (Eq. (2.5)), corresponds extremely well to the speed of light in vacuum ($c_0 \approx 299792458$ m/s), suggesting that light is an electromagnetic wave. This was a radical observation in the late 19th centure, and unified three seemingly separate fields in physics: electricity, magnetism and (visible-light) optics.

The main take-away message is that all electromagnetic radiation, and therefore X-rays, exhibit typical wavelike behavior, which was (deliberately) overlooked in Chapter 1. However, this does not imply that the particle-oriented approach from Chapter 1 is wrong: electromagnetic radiation has very clear particle-like properties as well (Einstein, 1905; Compton, 1923; Lewis, 1926). In short, X-rays can be waves or particles, depending on how you decide to look at it (Sakurai and Napolitano, 2017).

We conclude this section by noting that the pair of vector equations in Eq. (2.3) and Eq. (2.4) is constructed from six scalar vacuum field equations, all having the following form:

$$\left(\frac{1}{c^2}\frac{\partial^2}{\partial t^2} - \nabla^2\right)\Psi(x,y,z,t) = 0, \tag{2.6}$$

where $\Psi(x,y,z,t)$ should be interpreted as a complex function known as the wave function, used to describe the X-ray field. Although polarization is implicitly neglected by using a scalar-wave description, this assumption is reasonable in many paraxial imaging and diffraction contexts (Paganin and Pelliccia, 2021).

2.2.3 The projection approximation for X-ray wavefronts

Taking a closer look at the wave function introduced in Section 2.2.2, we recall that $\Psi(x,y,z,t)$ is a complex number at each point in space (x,y,z) and at each point in time t. This means it can be associated with a magnitude and phase as follows:

$$\Psi(x,y,z,t) = \sqrt{I(x,y,z,t)}e^{i\phi(x,y,z,t)}. \tag{2.7}$$

In Eq. (2.7), the magnitude of $\Psi(x,y,z,t)$ is written as the square root of the field intensity $I(x,y,z,t)$, such that

$$I(x,y,z,t) = |\Psi(x,y,z,t)|^2, \tag{2.8}$$

and $\phi(x,y,z,t)$ denotes the phase of the wave function. At each point in time, surfaces of constant phase represent wave fronts of the X-ray field. The wave fronts typically move in a direction that is away from the source generating the waves.

Assuming monochromatic, and therefore perfectly coherent, waves, the time development at a given point in space is described by a fixed angular frequency $\omega = 2\pi f = ck$, where f denotes the frequency and k is the wavenumber corresponding to the vacuum wavelength λ via $k = 2\pi/\lambda$. As such, the variables can be separated:

$$\Psi(x,y,z,t) = \psi_\omega(x,y,z)e^{-i\omega t}. \tag{2.9}$$

Substituting Eq. (2.9) in Eq. (2.6) yields the Helmholtz equation in vacuum:

$$\left(\nabla^2 + k^2\right)\psi_\omega(x,y,z) = 0. \tag{2.10}$$

It should be noted that, while monochromatic plane waves are an idealization, any polychromatic electromagnetic field in a given volume of free space described by a scalar function $\Psi_p(x,y,z,t)$ can be spectrally decomposed as a superposition of monochromatic fields:

$$\Psi_p(x,y,z,t) = \frac{1}{2\pi}\int_0^\infty \psi_\omega(x,y,z)e^{-i\omega t}d\omega. \tag{2.11}$$

Hence, even for a polychromatic wave function $\Psi_p(x,y,z,t)$, we can always interpret $\psi_\omega(x,y,z)e^{-i\omega t}$ as a monochromatic component of the spectral decomposition.

The vacuum wave equation for coherent scalar electromagnetic waves may be generalized to account for the presence of material media. Such media are here assumed to be static, non-magnetic, and sufficiently slowly spatially varying, so that they may be described by the position-dependent refractive index $n_\omega(x,y,z)$. This refractive index is the same physical quantity as the index of refraction previously associated with X-ray refraction in Section 2.2.1. The presence of a medium alters the vacuum wavelength and wavenumber as follows:

$$\lambda \rightarrow \lambda_{n_\omega} = \frac{\lambda}{n_\omega(x,y,z)}, \tag{2.12}$$

$$k \rightarrow k_{n_\omega} = kn_\omega(x,y,z), \tag{2.13}$$

resulting in the following equation:

$$\left(\nabla^2 + k^2 n_\omega^2(x,y,z)\right) \psi_\omega(x,y,z) = 0. \tag{2.14}$$

Interestingly, Eq. (2.14) is mathematically equivalent to the time-independent Schrödinger equation for non relativistic electrons in the presence of a scalar scattering potential, and the time-independent form of the Klein–Gordon equation, explaining the similarities that exist between the fields of X-ray optics, electron optics (Knoll and Ruska, 1932) and neutron optics (Kallmann, 1948).

Under the assumption that our monochromatic complex scalar X-ray wave field is paraxial, $\psi_\omega(x,y,z)$ can be written as

$$\psi_\omega(x,y,z) = \tilde{\psi}_\omega(x,y,z) e^{ikz}, \tag{2.15}$$

expressing that all wavefronts may be obtained by slightly deforming planar surfaces perpendicular to the optical axis (z) via multiplication of the plane wave e^{ikz} by an envelope $\tilde{\psi}_\omega(x,y,z)$. Note that $|\tilde{\psi}_\omega(x,y,z)|^2 = |\psi_\omega(x,y,z)|^2 = I_\omega(x,y,z)$.

Inserting Eq. (2.15) into Eq. (2.14) yields the inhomogeneous paraxial equation:

$$\left(2ik\frac{\partial}{\partial z} + \nabla_\perp^2 + k^2\left(n_\omega^2(x,y,z) - 1\right)\right) \tilde{\psi}_\omega(x,y,z) = 0, \tag{2.16}$$

where the term containing the second derivative of the envelope with respect to z is omitted since it is small compared to the other terms (paraxial assumption), and $\nabla_\perp^2$ denotes the transverse Laplacian in the (x,y) plane. If it is furthermore assumed that the object is sufficiently slowly varying in space so that the spread of the X-ray waves in the transverse plane can be neglected, then the transverse Laplacian can be discarded as well, yielding:

$$\frac{\partial}{\partial z}\tilde{\psi}_\omega(x,y,z) \approx \frac{k}{2i}\left(1 - n_\omega^2(x,y,z)\right) \tilde{\psi}_\omega(x,y,z). \tag{2.17}$$

By neglecting the transverse spread of the field, it is effectively assumed that the influence of the sample upon the X-rays that traverse it is well approximated by the projection of that sample onto a single plane. This assumption, also known as the projection approximation, is valid in many cases for high-energy radiation like X-rays, but is less suitable for short propagation distances (Morgan et al., 2010a,b). A more in-depth discussion on the validity of these approximations is found in Paganin and Pelliccia (2021).

2.2.4 The index of refraction revisited

The approximations introduced in Section 2.2.3 have brought the wave description closer to the ray description used in Section 2.2.1. It is worthwhile to travel a little further on this path. Fig. 2.3 shows a monochromatic X-ray wavefront traveling parallel to the positive z-axis, hereby illuminating a simple object from the left. The object is totally contained

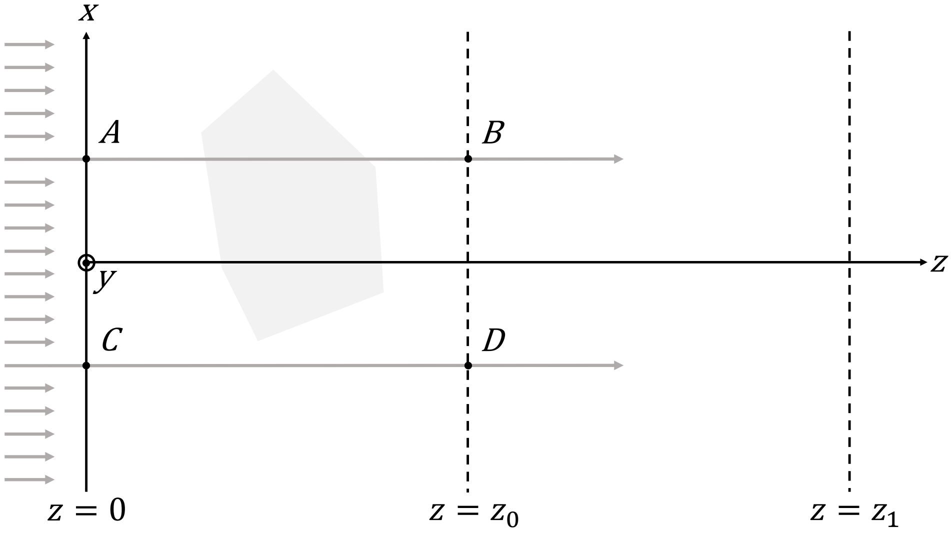

Figure 2.3: Schematic overview of an X-ray wavefront propagating in the positive z-direction, through an object under the projection approximation.

within the slab of space between $z = 0$ and $z = z_0 \geq 0$, and is described by its refractive index distribution $n_\omega(x,y,z)$. The latter will only differ from unity (the refractive index of vacuum, see Section 2.2.1) within the volume occupied by the object. The goal is to determine the complex wave function in the plane $z = z_0$ (the exit surface of the object), as a function of the complex wave function at the entrance surface $z = 0$ and the refractive index distribution of the object. Eq. (2.17) is, for each fixed point (x,y), a linear first-order ordinary differential equation. This equation can be immediately integrated with respect to z, which can be interpreted as the projection taking place:

$$\tilde{\psi}_\omega(x,y,z=z_0) \approx \exp\left(\frac{k}{2i}\int_0^{z_0}\left(1-n_\omega^2(x,y,z)\right)dz\right)\tilde{\psi}_\omega(x,y,z=0). \tag{2.18}$$

It gets even more interesting when a complex form is introduced for the index of refraction. The real part of this complex index of refraction corresponds to the refractive index in the conventional sense (Section 2.2.1). However, the imaginary part of the complex refractive index is a measure of the absorptive properties of a sample (Section 1.3 in Chapter 1). The complex index of refraction can thus be written as:

$$n_\omega = 1 - \delta_\omega + i\beta_\omega, \tag{2.19}$$

where $|\delta_\omega|, |\beta_\omega| \ll 1$. Substituting Eq. (2.19) in Eq. (2.18) yields the following result for the projection approximation:

$$\tilde{\psi}_\omega(x,y,z_0) \approx \exp\left(\frac{k}{i}\int_0^{z_0}\left(\delta_\omega(x,y,z) - i\beta_\omega(x,y,z)\right)dz\right)\tilde{\psi}_\omega(x,y,0), \tag{2.20}$$

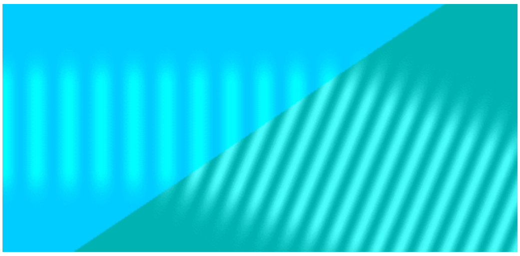

Figure 2.4: Illustration of the wave-interpretation of refraction at the boundary of two different materials (indicated by different background colors in the image), where refraction results from deformations in the wavefront.

where the terms with δ_ω^2, β_ω^2, and $\delta_\omega \beta_\omega$ have been discarded since they are small compared to the other terms. This shows that the exit wave may be obtained from the entrance wave via multiplication by a complex-valued and position-dependent transmission function $T(x,y)$:

$$T(x,y) = \exp\left(-ik \int_0^{z_0} \left(\delta_\omega(x,y,z) - i\beta_\omega(x,y,z)\right) dz\right). \tag{2.21}$$

Omitting the explicit notation of the integration limits, we can write the position dependent phase shift due to the object as:

$$\Delta\phi_\omega(x,y) = -k \int \delta_\omega(x,y,z) dz. \tag{2.22}$$

Eq. (2.22) quantifies the deformation of the X-ray wavefronts due to passage through the object. For each fixed transverse coordinate (x,y), phase shifts (and the associated wavefront deformations) are continuously accumulated along rays such as AB in Fig. 2.3. The phase shifts associated with passage of an X-ray wave through an object quantify the refractive properties of that object. In the more general wave picture (compared to the less general ray picture), refraction is associated with wavefront deformation rather than ray deflection. As will be seen later, Eq. (2.22) is key in the development of X-ray phase contrast CT.

Let us now consider the second term in the integrand of Eq. (2.21), which contains the imaginary part of the refractive index. This term describes the attenuation of the X-ray wave by the object and leads to a fairly familiar expression by taking the squared modulus of Eq. (2.20):

$$|\tilde{\psi}_\omega(x,y,z=z_0)|^2 = I(x,y,z=z_0) = e^{-2k\int \beta_\omega(x,y,z)dz} I(x,y,z=0). \tag{2.23}$$

Indeed, for $\mu_\omega(x,y,z) = 2k\beta_\omega(x,y,z)$ this expression yields the Lambert-Beer law previously discussed in Section 1.3.1. By taking the negative logarithm, we rediscover the standard forward model for attenuation-based X-ray imaging (Eq. (1.6)):

$$-\ln\left(\frac{I(x,y,z=z_0)}{I(x,y,z=0)}\right) = \int \mu_\omega(x,y,z)dz \tag{2.24}$$

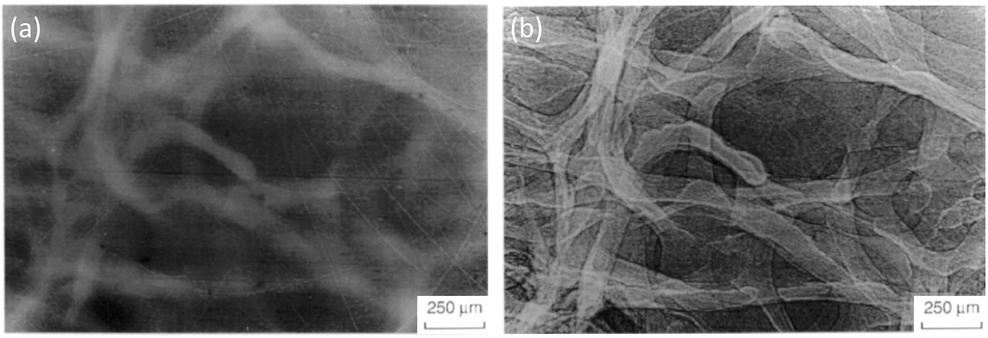

Figure 2.5: Early propagation-based phase contrast image of a 7 mm thick sample of human vertebra, acquired at a synchrotron facility (ESRF). (a) Contact image showing pure attenuation contrast. (b) Phase-modulated image at a propagation distance of 100 cm. Adapted from Cloetens et al. (1996).

In particular, if a two-dimensional position sensitive detector is placed in the plane $z = z_0$ in Fig. 2.3, and the illuminating radiation has an intensity $I_\omega(x, y, z = 0)$ that is approximately constant with respect to x and y, then all contrast in the resulting contact image will be due to local absorption of rays such as AB in Fig. 2.3. However, the contact image contains no contrast that is due to the phase shifts expressed by Eq. (2.22). The lack of phase contrast in conventional contact X-ray imaging results in poor image contrast for soft tissue and low-Z materials, being almost non-absorbing for hard X-rays. Fortunately, the following sections will discuss how the power of phase shifts can be harnessed for X-ray imaging.

2.3 X-ray phase contrast imaging

2.3.1 On the origin of phase contrast

Consider X-ray waves propagating in free space (vacuum), under the assumption that all waves in this space are both paraxial with respect to the optical axis and monochromatic. In vacuum, the complex index of refraction $n_\omega(x, y, z)$ equals 1, which simplifies Eq. (2.16) to:

$$\left(2ik\frac{\partial}{\partial z} + \nabla_\perp^2\right) \tilde{\psi}_\omega(x, y, z) = 0, \tag{2.25}$$

which is known as the free-space paraxial equation. The so-called diffraction problem is now to determine the wave field over the plane $z_1 > z_0$, given the disturbance over the plane $z = z_0$. Based on the above free-space paraxial equation, the solution to the diffraction problem may be written as:

$$\tilde{\psi}_\omega(x, y, z_1 > z_0) = \mathscr{D}_{\Delta z} \tilde{\psi}_\omega(x, y, z_0), \tag{2.26}$$

with $\mathscr{D}_{\Delta z}$ the Fresnel diffraction operator, which propagates the forward traveling field a distance Δz from $z = z_0$ to $z = z_1$. The Fresnel diffraction operator $\mathscr{D}_{\Delta z}$ is given by (Paganin and Pelliccia, 2021):

$$\mathscr{D}_{\Delta z}\tilde{\psi}_\omega(x,y,z_0) = e^{ik\Delta z}\mathscr{F}^{-1}\left[e^{-\frac{i}{2k}(k_x^2+k_y^2)\Delta z}\mathscr{F}\left[\tilde{\psi}_\omega(x,y,z_0)\right]\right], \tag{2.27}$$

where $\mathscr{F}$ denotes the Fourier transform operator. In contrast to Eq. (2.23), the squared modulus of Eq. (2.26) (i.e. the intensity of the propagated field) now depends on both the intensity and phase of the unpropagated field (Bartels, 2013). The latter is of key importance for phase contrast imaging, since it implies that the Fresnel diffraction pattern, namely the propagated intensity over the plane $z_1 > z_0$, provides the phase contrast that was missing from the contact image described by Eq. (2.24). As illustrated by Fig. 2.5, this effect forms the basis for propagation-based phase contrast imaging (Snigirev et al., 1995; Cloetens et al., 1996). It immediately becomes clear that the phase-modulated image shows much stronger contrast compared to the contact image. The origin of the phase modulation is that the thin object, due to density variations, acts as a locally divergent or convergent X-ray lens. As a result, the local ray density on the detector will decrease or increase compared to the situation without the sample, and the corresponding detector pixels will detect a lower or higher intensity. The object to detector distance through which the wave propagates before reaching the detector plays a crucial role, explaining why the contact image is free of phase contrast (Fig. 2.5). Another characteristic feature of propagation-based phase contrast is the edge contrast, visible around edges as dark and white bands, where the intensity is deflected outward from the geometrical projection of the edge of the sample.

2.3.2 Phase contrast from X-ray refraction

It is worthwhile to take a step back in order to see how X-ray phase contrast is related to X-ray refraction. To this end, consider a plane wave traveling in the z-direction with amplitude ψ_0 that has undergone an x-dependent phase distortion $\phi(x)$ due to the interaction with a phase object (Davis et al., 1995):

$$\psi_\omega(x,y,z) = \psi_0 e^{ikz+i\phi(x)}. \tag{2.28}$$

As illustrated by Fig. 2.4, the resulting wave will have locally changed its direction from $\mathbf{k} = k\mathbf{e_z}$ to $\mathbf{k}' = k'_x\mathbf{e_x} + k'_y\mathbf{e_y} + k'_z\mathbf{e_z}$, with $\mathbf{e_x}$, $\mathbf{e_y}$, and $\mathbf{e_z}$ denoting Cartesian unit vectors. We may thus also write:

$$\psi_\omega(x,y,z) = \psi_0 e^{i\mathbf{k}'\cdot\mathbf{r}}, \tag{2.29}$$

with $\mathbf{r} = x\mathbf{e_x} + y\mathbf{e_y} + z\mathbf{e_z}$. Following Eq. (2.28), the gradient of the outgoing wave field is given by:

$$\nabla\psi_\omega(x,y,z) = i\psi_\omega(x,y,z)\left(\frac{\partial\phi(x)}{\partial x}\mathbf{e_x} + k\mathbf{e_z}\right). \tag{2.30}$$

Likewise, following Eq. (2.29), we can write:

$$\nabla \psi_\omega(x,y,z) = i\psi_\omega(x,y,z)\mathbf{k}'. \tag{2.31}$$

From Eq. (2.30) and Eq. (2.31), it is clear that the new direction of the wave is given by:

$$\mathbf{k}' = \frac{\nabla \psi_\omega(x,y,z)}{i\psi_\omega(x,y,z)} = \frac{\partial \phi(x)}{\partial x}\mathbf{e_x} + k\mathbf{e_z}. \tag{2.32}$$

The local angular change in direction α (i.e. the refraction) can be calculated from the magnitude of the cross product, $|\mathbf{k}\times\mathbf{k}'| = |\mathbf{k}||\mathbf{k}'|\sin\alpha$, yielding:

$$\sin(\alpha(x)) = \frac{1}{k}\frac{\partial \phi(x)}{\partial x}\frac{1}{\sqrt{1+\left(\frac{1}{k}\frac{\partial\phi(x)}{\partial x}\right)^2}}. \tag{2.33}$$

For small phase variations, i.e. $\left(\frac{1}{k}\frac{\partial\phi(x)}{\partial x}\right)^2 \ll 1$, the angle between the initial and final propagation direction can be approximated as:

$$\alpha(x) \approx \frac{\lambda}{2\pi}\frac{\partial \phi(x)}{\partial x}, \tag{2.34}$$

providing a quantitative relationship between the gradient of the phase shift induced by an object and the resulting refraction of the X-ray beam. This can be generalized to the (x,y)-plane using the transverse gradient $\nabla_\perp$ (Paganin and Pelliccia, 2021):

$$(\alpha_x(x,y), \alpha_y(x,y)) = \frac{1}{k}\nabla_\perp \phi(x,y). \tag{2.35}$$

In practice, many commonly used phase contrast methods measure phase derivatives, with the following methods providing image contrast dependent upon the first derivative of the phase in the transverse plane (as in Eq. (2.35)): speckle-based imaging (SBI), analyser-based imaging (ABI), grating-based interferometry (GBI), and edge illumination (EI). This type of phase contrast is also known as differential phase contrast (DPC). However, propagation-based imaging (PBI) is sensitive to the second derivative of the phase, and crystal interferometry is capable of direct phase shift measurements. The phase contrast imaging techniques mentioned here will be briefly addressed further in the text, with an emphasis on GBI and EI, as those two methods are the focus of the results presented in the next chapters of this dissertation.

All phase gradient methods have in common that measuring the transverse phase gradient requires a certain propagation distance as well as the creation of a transverse intensity gradient. This intensity gradient can occur within a single image (SBI) or between consecutive images (GBI, ABI), which implies multiple images are required for phase retrieval. In EI, the shaping of the beam behind the sample induces the intensity gradient. In general, single-image methods are faster, whereas multi-image methods can achieve a higher spatial resolution (Paganin and Pelliccia, 2021).

2.3.3 The effect of unresolved phase variations

Let us consider a situation where the phase effects induced by an object cannot be resolved by the imaging system. In that case, assume we can split the phase into two components, $\phi_1(x)$ and $\phi_2(x)$, representing the slowly-varying and rapidly-varying components of the phase, respectively, with the latter being small in amplitude (Nesterets, 2008; Nesterets and Gureyev, 2016; Paganin and Pelliccia, 2021):

$$\phi(x) = \phi_1(x) + \phi_2(x). \tag{2.36}$$

This difference in oscillation speed between the two components $\phi_1(x)$ and $\phi_2(x)$ is a construction that depends on the spatial resolution of the imaging system. Hence, the slowly-varying component is that which can be spatially resolved by the imaging system. However, although the rapidly-varying components cannot be spatially resolved by the system, they do induce a third type of contrast, known as dark field contrast. This can be seen by explicitly writing down the contributions to the intensity in the output plane (Paganin and Pelliccia, 2021):

$$\begin{aligned}\frac{I_{out}(x)}{I_{in}(x)} &= 1 + 2\mathrm{Re}[\upsilon]\frac{\partial\phi(x)}{\partial x} + \mathrm{Im}[\upsilon]\frac{\partial}{\partial x}\ln\left(I_{in}(x)\right) \\ &+ |\upsilon|^2\left(\frac{\partial\phi(x)}{\partial x}\right)^2 + \frac{|\upsilon|^2}{4}\left(\frac{\partial}{\partial x}\ln\left(I_{in}(x)\right)\right)^2,\end{aligned} \tag{2.37}$$

where υ is a complex parameter with units of length. The terms containing the derivative of the phase, i.e. the second and fourth, are those of interest for this discussion, as the other terms are related to attenuation effects. Eq. (2.37) describes the ideal case where the spatial resolution of the imaging system is arbitrarily good. In practice, the resolution is finite. As obvious as this may sound, it implies an important difference in the measurable signal. Indeed, phase variations smaller than the system resolution give a qualitatively different type of contrast, despite being generated by the same underlying physical process. In a realistic acquisition process, the incident intensity is averaged over the extent of the point spread function (PSF) of the detector system. This yields the following spatial average (Paganin and Pelliccia, 2021):

$$\left\langle\frac{\partial\phi(x)}{\partial x}\right\rangle = \left\langle\frac{\partial(\phi_1(x)+\phi_2(x))}{\partial x}\right\rangle \approx \left\langle\frac{\partial\phi_1(x)}{\partial x}\right\rangle. \tag{2.38}$$

The rapidly-varying component of the phase is canceled by the average over the PSF, leaving the slowly-varying component only. This corresponds to conventional differential phase contrast imaging, now under the realistic assumption of finite spatial resolution. In the fourth term of Eq. (2.37), we find the quadratic phase term, which behaves differently when averaged by the PSF (Paganin and Pelliccia, 2021):

$$\begin{aligned}\left\langle\left(\frac{\partial\phi(x)}{\partial x}\right)^2\right\rangle &= \left\langle\left(\frac{\partial\phi_1(x)}{\partial x}\right)^2\right\rangle + \left\langle\left(\frac{\partial\phi_2(x)}{\partial x}\right)^2\right\rangle \\ &+ 2\left\langle\frac{\partial\phi_1(x)}{\partial x}\frac{\partial\phi_2(x)}{\partial x}\right\rangle \approx \left\langle\left(\frac{\partial\phi_2(x)}{\partial x}\right)^2\right\rangle.\end{aligned} \tag{2.39}$$

In this case, the ϕ_2 term does not disappear. On the contrary: the first term can now be neglected, as the slow-varying component of the phase has, by definition, a small transverse derivative. In addition, the cross term is a covariance that averages to zero as, in this case, it is a rapidly changing component that becomes negligible once averaged over the PSF. The remaining term may be identified with the local variance of the rapidly-varying signal $\partial\phi_2(x)/\partial x$. If we recall from Eq. (2.34) that:

$$\alpha_2(x) \approx \frac{1}{k}\frac{\partial\phi_2(x)}{\partial x}, \tag{2.40}$$

with α_2 the deflection angle due to $\phi_2(x)$, it is clear that $\langle(\partial\phi_2(x)/\partial x)^2\rangle$ is proportional to the variance of the deflection angle induced by the spatially unresolved rapid phase fluctuations (Paganin and Pelliccia, 2021):

$$\left\langle\left(\frac{\partial\phi_2(x)}{\partial x}\right)^2\right\rangle = k^2\left\langle(\alpha_2(x))^2\right\rangle = \mathrm{Var}\left(\alpha_2(x)\right). \tag{2.41}$$

In summary, the rapidly varying component $\phi_2(x)$ yields a detectable position-dependent signal, even though the rapid fluctuations in $\phi_2(x)$ are unresolved. This signal can contain important information regarding a sample, distinct from the other attributes of position-dependent attenuation and position-dependent phase shifts.

2.3.4 On the origin of dark field contrast

The origin of the rapid phase fluctuations responsible for the dark field contrast (DFC) is a popular topic within the rapidly evolving X-ray phase contrast literature, with the earliest works dating back almost a century (Slack, 1926; von Nardroff, 1926). While the physical interpretation of the dark field signal in those early works is that of unresolved multiple refraction, the interpretation given in more recent literature is often that of (ultra) small-angle X-ray scattering or (U)SAXS (Khelashvili et al., 2006; Pfeiffer et al., 2008; Yashiro et al., 2010; Endrizzi et al., 2014). In practice, several authors have also used the two interpretations interchangeably (Willer et al., 2018; Gassert et al., 2021; How and Morgan, 2022).

Regardless of the interpretation, the dark field signal is measured as a local angular broadening of the X-ray beam (Eq. (2.41)), commonly modeled by a Gaussian angular distribution with scattering width $\sigma^2 = \mathrm{Var}(\alpha_2)$ (Bech et al., 2010a):

$$A(\alpha_2) = \frac{1}{\sqrt{2\pi}\sigma}\exp\left(-\frac{\alpha_2^2}{2\sigma^2}\right). \tag{2.42}$$

For example, if a sample contains numerous microstructures that are smaller than the system resolution, the unresolved multiple refraction at the interfaces of the microstructures cause the beam to spread into a cone with a very small angular opening. Assuming that the unresolved structures are particles that can be modeled as spheres of radius R, the scattering width (i.e. the local angular broadening) can be estimated by (von Nardroff, 1926):

$$\sigma^2 = \left(\frac{\Delta\delta}{\ln 2}\right)^2 \left(\ln\left(\frac{2}{\Delta\delta}\right) + 1\right) N_0, \tag{2.43}$$

where N_0 is the average number of particles encountered and $\Delta\delta$ is the difference in refractive index decrement between the particles and the surrounding material. N_0 is given by:

$$N_0 = \rho_N \pi R^2 d, \tag{2.44}$$

where ρ_N is the particle number density and d the distance covered in the sample. SAXS, on the other hand, is related to the acceleration of electrons by the oscillating electric field of the incoming X-ray beam, which results in the emission of secondary waves with the same frequency (Gommes et al., 2021). Due to nanometric differences in electron density within the sample, the secondary waves will interfere along the propagation direction, hereby generating the SAXS signal. Guided by the SAXS interpretation of DFC, many models to quantify the DFC signal are based on SAXS (Lynch et al., 2011; Strobl, 2014). It should be noted that (U)SAXS exists as a standalone material analysis technique, which is, however, not optimized for fast 2D imaging purposes (Ilavsky et al., 2013; Magnin et al., 2023).

In practice, the physical interpretation of the dark field depends on the length scale of the electron density variations: unresolved multiple refraction is caused by variations at the microscale, whereas pure SAXS-induced DFC results from variations at the nanoscale. Recently, it has been experimentally shown that both multiple refraction and SAXS independently generate a dark field signal (Magnin et al., 2025). This implies that, in samples with structural features in the nanometer to micrometer range, the effects of multiple refraction cannot be entirely isolated from other scattering phenomena that may contribute to DFC generation. A full quantitative description of the DFC thus would require incorporation of both physical interpretations in the model.

2.3.5 Spatial and temporal coherence

Coherence is a key aspect in many X-ray phase contrast imaging methods. In short, two wave fields are considered to be coherent if there is a fixed phase difference between two points in space or in time. Therefore, if two waves are perfectly coherent, the phase of the first wave can always be determined from the phase of the second wave, and vice versa. As mentioned in Section 2.2.3, perfect coherence requires monochromatic waves, which means that in practice there will almost always be a certain degree of decoherence. This is known as partial coherence, the degree of which is a measure for the potential of two waves to interfere with each other. As the concept of partial coherence is closely tied to the ability of two separate optical disturbances to form interference fringes when combined, this can be expressed mathematically by the complex degree of coherence (Bartels, 2013):

$$\gamma(\mathbf{r_1},\mathbf{r_2},\Delta t) = \frac{\Gamma(\mathbf{r_1},\mathbf{r_2},\Delta t)}{\sqrt{\Gamma(\mathbf{r_1},\mathbf{r_1},0)\Gamma(\mathbf{r_2},\mathbf{r_2},0)}}, \tag{2.45}$$

where $\Gamma(\mathbf{r_1},\mathbf{r_2},\Delta t)$ denotes the mutual coherence function, given by:

$$\Gamma(\mathbf{r_1},\mathbf{r_2},\Delta t) = \langle \psi_\omega(\mathbf{r_1},t+\Delta t)\psi^*_\omega(\mathbf{r_2},t)\rangle. \tag{2.46}$$

In Eq. (2.46), $\langle\cdot\rangle$ denotes the time average and the superscript $*$ denotes complex conjugation. From Eq. (2.46), it is clear that $\Gamma(\mathbf{r_1},\mathbf{r_1},0)$ and $\Gamma(\mathbf{r_2},\mathbf{r_2},0)$ are equal to the respective mean intensities $I(\mathbf{r_1})$ and $I(\mathbf{r_2})$. The degree of coherence is essentially about the capacity of wave fields to form interference fringes: the higher the degree of visibility of such interference fringes, the higher the degree of coherence (Zernike, 1938; Paganin and Pelliccia, 2021). For monochromatic wave fields, the complex degree of coherence has a unit modulus. For quasi-monochromatic wave fields, expressed as a superposition of non-zero monochromatic components within a narrow spectral range, the modulus of the complex degree of coherence satisfies $|\gamma(\mathbf{r_1},\mathbf{r_2},\Delta t)| \leq 1$.

In Eq. (2.45), coherence of a wave field is expressed as correlations between points separated in both space and time. However, it is interesting to consider spatial and temporal correlations separately as well. For $\Delta t = 0$, Eq. (2.46) yields the mutual intensity:

$$\Gamma(\mathbf{r_1},\mathbf{r_2}) = \langle \psi_\omega(\mathbf{r_1},t)\psi^*_\omega(\mathbf{r_2},t)\rangle, \tag{2.47}$$

describing the spatial (transversal) coherence properties. An important aspect of spatial coherence is that spatial correlations of a wave field can be induced by free-space propagation: a larger spatial coherence length can be generated by choosing an X-ray source with a smaller intensity distribution or by increasing the distance to the source (Zernike, 1938; Bartels, 2013).

The influence of the spectral bandwidth of a quasi-monochromatic wave field can be addressed by considering the special case of the mutual coherence function for $\mathbf{r_1} = \mathbf{r_2}$, yielding the temporal coherence function:

$$\Gamma(\mathbf{r_1},\Delta t) = \langle \psi_\omega(\mathbf{r_1},t+\Delta t)\psi^*_\omega(\mathbf{r_1},t)\rangle. \tag{2.48}$$

The modulus of the complex degree of temporal coherence, which is given by $\gamma(\mathbf{r_1},\Delta t) = \Gamma(\mathbf{r_1},\Delta t)/\Gamma(\mathbf{r_1},0)$, is a measure for the correlation of the wave field at a given point in space $\mathbf{r_1}$ for two points in time separated by a time difference Δt. For a spectral density with Lorentzian shape with bandwidth $\Delta\omega$, the modulus of the temporal coherence function can be written as (Bartels, 2013):

$$|\gamma(\Delta t)| = e^{-\Delta t/\tau_c}, \tag{2.49}$$

where τ_c denotes the coherence time, i.e. the time after which the coherence is considered to be lost. The coherence time corresponds to a longitudinal coherence length $l_l = c\tau_c$, and a low longitudinal coherence can limit the resolution of propagation-based X-ray imaging experiments (Bartels, 2013). The specific coherence requirements depend on the applied imaging method and the desired resolution.

2.3.6 Propagation-based imaging

As mentioned earlier in the text, free-space propagation techniques require arguably the simplest setup, since the introduction of an appropriate propagation distance between the sample and the detector can be sufficient to measure phase effects. PBI requires a certain degree of spatial coherence (see Section 2.3.5). The spatial coherence length, given by (Endrizzi, 2018):

$$l_s = \frac{\lambda d_{SOD}}{2\sqrt{2\ln 2}\sigma_s}, \tag{2.50}$$

has to be comparable to or larger than the inverse spatial frequency of the feature of interest in order to obtain significant phase contrast. In Eq. (2.50), σ_s is the standard deviation of the spatial source intensity distribution, and d_{SOD} is the distance between the source and the object. In practice, this means that the source has to be relatively small or that the object must be placed at a sufficiently large distance from it. In addition, the spatial resolution of the imaging system must be high enough to avoid washing out the interference fringes. This is expressed by the standard deviation of the total point spread function (PSF) of the system σ_{sys} (Endrizzi, 2018):

$$\sigma_{sys}^2 \approx \left(1 - \frac{1}{M}\right)^2 \sigma_s^2 + \frac{1}{M^2}\sigma_d^2 + \frac{1}{2}\sqrt{\frac{1}{2}\lambda d_{ODD}}, \tag{2.51}$$

where d_{ODD} is the object to detector distance, M is the geometrical magnification, and σ_d is the detector PSF.

The contrast retrieval in propagation-based X-ray phase contrast imaging is usually performed by means of the so-called transport of intensity equation or TIE (Langer et al., 2008; Gureyev et al., 2009):

$$-\nabla_\perp \cdot (I(x,y,z)\nabla_\perp \phi(x,y,z)) = k\frac{\partial I(x,y,z)}{\partial z}, \tag{2.52}$$

which is a continuity equation expressing the local conservation of optical energy. Although the TIE will not be discussed here in detail, it is worth mentioning that the TIE can be generalized to incorporate dark field effects (Leatham et al., 2023). Extracting both attenuation and phase requires the acquisition of more than a single image, for example by changing the propagation distance or by changing the energy, unless some constraints can be imposed. Consider, for example, a single-material object with projected thickness $d_{obj}(x,y)$ that is being illuminated by monochromatic plane waves of uniform intensity I_0. In addition, assume that the refractive index decrement δ_ω and linear attenuation coefficient μ_ω are known. The projection approximation then enables both the phase and the amplitude at the exit surface of the object to be obtained from $d_{obj}(x,y)$, as Eq. (2.22) and Eq. (2.23) simplify to:

$$\Delta\phi(x,y) = -k\delta_\omega d_{obj}(x,y) \tag{2.53}$$

and

$$I_\omega(x,y,z=z_0) = I_0 e^{-\mu_\omega d_{obj}(x,y)}, \tag{2.54}$$

respectively. The projected thickness of a single-material sample may be obtained from a single propagation-based phase contrast image, for a sufficiently small propagation distance, by solving the TIE exactly under the given assumptions (Paganin et al., 2002; Paganin and Pelliccia, 2021):

$$d_{obj}(x,y) = -\frac{1}{\mu_\omega} \ln\left(\mathscr{F}^{-1}\left[\frac{\mathscr{F}\left[I(x,y,z_1)\right]}{I_0\left(1+\frac{\delta_\omega \Delta z}{\mu_\omega}\left(k_x^2+k_y^2\right)\right)} \right] \right). \tag{2.55}$$

Eq. (2.55) has been widely used due to its practical advantages, such as simplicity, speed, noise robustness, and the ability to process time-dependent objects frame-by-frame. However, these advantages come at the cost of the previously stated assumptions. Remarkably, dark field contrast retrieval was unlocked only relatively recently in propagation-based X-ray phase contrast imaging (Gureyev et al., 2020).

2.3.7 Other phase contrast imaging methods

Although the PBI configuration is arguably the most straightforward X-ray phase contrast imaging setup, it is not the only (nor the oldest) X-ray phase contrast imaging method. In addition to PBI, several other X-ray phase contrast imaging methods exist. A relatively recent overview can be found in Endrizzi (2018), from which some key points will be addressed here concerning crystal interferometry, analyzer-based imaging, and speckle-based or single-grid methods.

2.3.7.1 Bonse-Hart crystal interferometry

The earliest example of an X-ray phase contrast imaging system, is the crystal interferometer of Bonse and Hart (Bonse and Hart, 1965), built from a single monolithic crystal cut in three silicon beam splitters in Laue geometry that split, redirect and recombine the X-ray beam (Fig. 2.6). Coherent beams are formed by dividing the incoming X-ray beam at the beam splitter S and successively at the transmission element T. They meet again at the analyzer A, where they interfere. In an ideal scenario, with a perfect plane wave and a perfect crystal, the field is perfectly uniform until a sample is introduced in one of the arms of the interferometer. If a sample is placed in one beam path, the phase shift induced by the sample will produce an interference pattern from which the phase shift can be extracted. The method shows very high phase sensitivity and the beam quality requirements are not very strict. However, the silicon crystals act as monochromator selecting a narrow spectral width. This means a very intense beam is required to avoid excessively long exposure times. In practice, local phase shifts, arising for example from strain and defects in the crystal, will generate interference patterns that will be superimposed to the modulations imposed by the sample. Due to the high sensitivity and limitations to sample size, the crystal interferometer is best suited for high resolution imaging at synchrotron

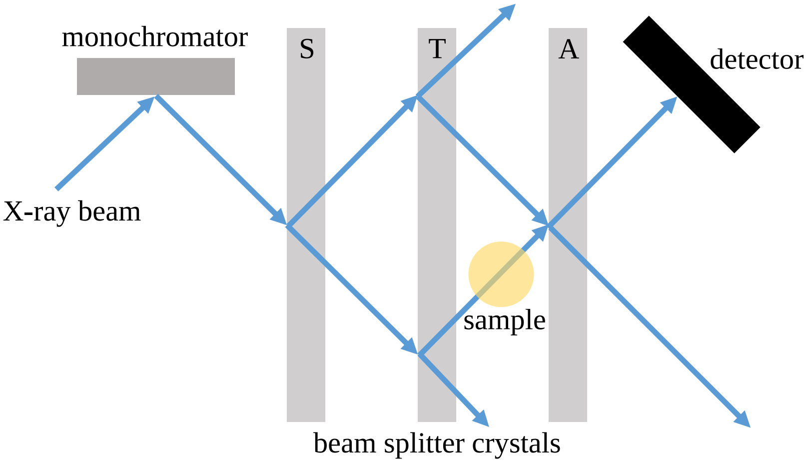

Figure 2.6: Schematic picture of a Bonse-Hart crystal interferometer based on three beam splitter crystals: the beam splitter S, the transmission element T, and the analyser A. Image not to scale.

sources where the requirement of high beam intensity is met (Momose and Fukuda, 1995; Yoneyama, 2022).

2.3.7.2 Analyzer-based imaging

Analyzer-based imaging, also known as diffraction enhanced imaging (DEI), emerged at synchrotron facilities more or less simultaneously with propagation-based imaging (Davis et al., 1995; Chapman et al., 1996, 1997), although there are some examples of preliminary versions of the technique (Goetz et al., 1979). Analyzer-based methods make use of crystals both for beam preparation and analysis (see Fig. 2.7). The crystal arrangement preceding the sample acts as a collimator and monochromator for the incoming X-ray beam, while the crystal preceding the detector serves as a fine angular filter (analyzer). In this configuration, the collimated beam penetrates the sample and is subsequently analyzed by the analyzer crystal, which deflects the beam onto the detector. The goal of the method is to measure the first derivative of the phase by detecting refraction angles (see Eq. (2.34)). The incidence angle of the analyzer crystal can be tuned such that the refracted part of the beam is reflected onto the detector. When the angular tuning is varied (rocking the analyzer), different refraction angles are analyzed, which results in the recording of a so-called rocking curve. While rocking the analyzer, the deflection angle results in a modulation of intensity, since the reflectivity and transmissivity of the crystal is a function of the incident beam angle. A full data set therefore contains images from several positions on the rocking curve.

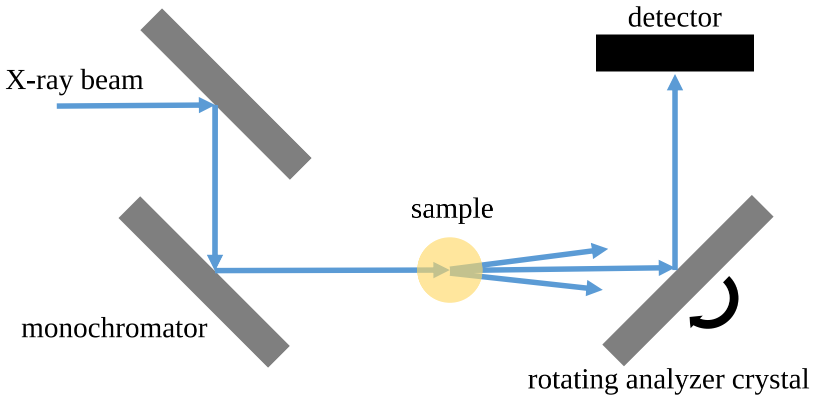

Figure 2.7: Schematic overview of an analyzer-based X-ray phase contrast imaging setup with a rotating analyzer crystal. Image not to scale.

2.3.7.3 Single grid and speckle-based methods

Single grid and speckle-based methods form a wide class of related X-ray phase contrast imaging techniques. They make use of single absorption grids with one-dimensional (Wen et al., 2008; Liu et al., 2023) or two-dimensional (Morgan et al., 2011) periodicity, phase gratings with different shapes (Kagias et al., 2016; Liu et al., 2023), or even random patterns such as sandpaper (Zanette et al., 2014). Such techniques attempt to recover sample information from sample-induced deformations in the detected intensity pattern, generated by the mask, hereby making use of Fourier or real space analysis methods. The common factor in all of these methods is that a known structure is applied to the wave field, of which the modifications are directly tracked. An overall reduction of the structured beam intensity is related to absorption of the radiation within the sample, while the spatial distortions of the known intensity patterns are used to determine the phase shifts imposed to the wavefront by the sample. Although there has been a gradual shift from synchrotron radiation towards lab-based X-ray sources, detecting the changes in the intensity pattern often requires a (very) high resolution detector.

2.4 Grating-based interferometry

A popular alternative for crystal X-ray interferometers is found in grating-based X-ray interferometers (Momose, 2003). Grating-based interferometry (GBI) is related to crystal interferometry in the sense that it consists of a beam splitter and a beam analyzer as well. GBI is also related to ABI by its ability to measure the first derivative of the phase. Like ABI and crystal interferometry, GBI emerged as an X-ray phase contrast imaging technique at synchrotron facilities (David et al., 2002; Momose et al., 2003), but has found its way to lab sources (Pfeiffer et al., 2006). Early on, grating interferometers were used for coherence measurements (Cloetens et al., 1997, 1999; Pfeiffer et al., 2005). The working principle of grating-based imaging is based on the creation of intensity modulations through the Talbot self-imaging effect (Berry and Klein, 1996; Wen et al., 2013). This phase contrast imaging method has become increasingly popular over the past two decades, with the advent of Talbot (Momose et al., 2003) and Talbot-Lau (Pfeiffer et al., 2006) interferometers, and is still in active development (Bech, 2022; Momose et al., 2022). It should be noted that non-interferometric grating-based setups exist as well (Huang et al., 2009; Wu et al., 2021), where two absorption gratings are used to create a resolvable moiré pattern under weakly coherent conditions.

2.4.1 The Talbot effect

The Talbot self-imaging effect is an optical diffraction effect, reported for the first time in the early nineteenth century using visible light (Talbot, 1836; Strutt Rayleigh, 1881). It was then observed that light passing through a grating has the ability to replicate an image of that grating at fixed propagation distances, now known as Talbot distances. Early demonstrations of the Talbot effect in 1D and 2D using hard synchrotron X-rays followed shortly after the demonstration of propagation-based X-ray phase contrast imaging (Cloetens et al., 1997, 1999). Talbot effects are generated by both amplitude gratings and phase gratings, when coherent X-rays illuminate a grating whose period is smaller than the transverse coherence length. Amplitude gratings are regular structures in which the gratings bars absorb the incoming X-ray beam, whereas the grating bars of phase gratings induce a local phase shift with negligible attenuation of the X-ray beam. An amplitude grating with period (or pitch) g, illuminated by a coherent plane wave with wavelength λ, produces self-images at regular Talbot distances behind the grating, given by (Suleski, 1997):

$$d_n = 2n\frac{g^2}{\lambda}, \tag{2.56}$$

with $n \in \mathbb{N}$. In addition, self-images laterally shifted by half the grating pitch $(g/2)$ are generated at intermediate Talbot distances (Momose et al., 2003):

$$d_n = (2n+1)\frac{g^2}{\lambda}. \tag{2.57}$$

When phase gratings are used, the self-images are not generated at the integer Talbot distances, but instead appear at fractional Talbot distances (Cloetens et al., 1997; Momose et al., 2003), also known as Lohmann distances (Suleski, 1997):

$$d_n = \left(n+\frac{1}{2}\right)\frac{g^2}{\lambda} \tag{2.58}$$

where the intensity modulation of the self-images depends on the phase shift induced by the phase grating (Momose et al., 2003). Considering three common types of gratings (amplitude gratings, π-shifting phase gratings, and $\pi/2$-shifting phase gratings), the

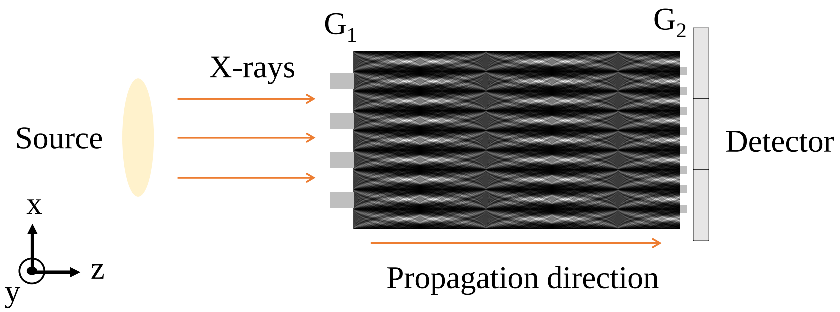

Figure 2.8: Schematic overview of a grating-based interferometer with a π-shifting phase grating (not to scale). Since the period of the intensity modulation for a π-shifting phase grating is half the grating period of G_1, g_2 must equal $g_1/2$.

integer and fractional Talbot distances can be summarized as (Weitkamp et al., 2006):

$$d_n = n\frac{1}{\eta^2}\frac{g^2}{2\lambda}. \tag{2.59}$$

Here, $\eta = 1$ for amplitude gratings and $\pi/2$-shifting phase gratings, and $\eta = 2$ for π-shifting phase gratings. Eq. (2.59) yields the positions along the optical axis at which the intensity fringe contrast takes a maximum or minimum. Amplitude gratings will exhibit maximum fringe contrast at even Talbot orders n, while phase gratings do so at odd Talbot orders. For π-shifting phase gratings, the period of the intensity modulation in the self-images is half that of the grating itself. If the grating is not illuminated by a plane wave, but by a spherical wave, the Talbot distances are shifted and the fringe spacing is stretched due to the geometrical magnification (Weitkamp et al., 2006).

2.4.2 Talbot interferometry

A Talbot interferometer relies on a coherent X-ray source that emits X-rays towards a detector. On their path to the detector, the X-rays encounter two gratings: G_1 and G_2 (Weitkamp et al., 2005), as shown in Fig. 2.8. The first grating (G_1) in Fig. 2.8 generates an interference pattern at regular propagation distances, with the same period (or half for a π-shifting grating) as that of grating G_1 (self-images). The distances d_n at which it occurs are given by Eq. (2.59), where $g = g_1$, the pitch of the first grating G_1. Placing an object in the beam will distort the wavefront, causing the interference pattern to change. As the fringes of the interference pattern are not resolvable by the detector, these changes cannot be measured directly. Therefore, an absorbing analyzer grating (G_2) is placed directly in front of the detector, which has a pitch that matches the periodicity of the undistorted interference pattern at that position. By shifting this grating along x (Fig. 2.8), the portion of the interference pattern intensity that is being transmitted varies. This generates, for every detector pixel, an intensity curve that oscillates as a function of the x-translation

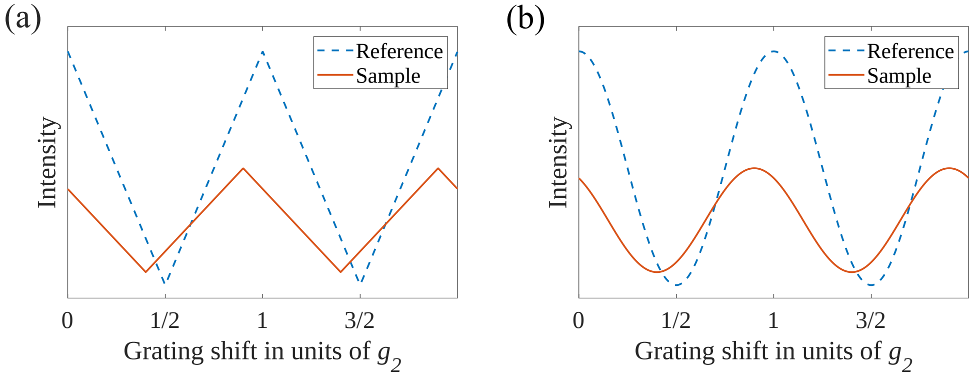

Figure 2.9: (a): Ideal case triangular phase stepping curves. (b): Cosine shaped phase stepping curves.

of G_2, hereby effectively translating the undetectable phase modulation into a detectable intensity modulation. The parameters defining these curves can be retrieved from a set of images taken at different G_2 positions x_g, a procedure known as phase stepping, using a phase retrieval algorithm (Creath, 1988; Weitkamp et al., 2005).

In the ideal case, the modulation of the intensity in the phase stepping curve of a pixel can be modeled by a triangle wave (Weber et al., 2011). The triangular wave function f_{TW} is given by:

$$f_{\text{TW}}(x) = \frac{2}{\pi}\arcsin(\sin x), \tag{2.60}$$

and the ideal case model is written as

$$I(x_g) = a_0 + a_1 f_{\text{TW}}\left(2\pi\frac{x_g}{g_2} + \Phi_1 + \pi\right), \tag{2.61}$$

were g_2 denotes the pitch of the analyzer grating G_2. The phase factor $+\pi$ is introduced to match the interpretation of Φ_1 in Eq. (2.61) to the interpretation in Eq. (2.62), as the latter is more common in literature.

Due to system imperfections such as variations in the widths and periodicity of the gratings, detector imperfections, polychromaticity, and limited coherence, the intensity will be blurred in most experiments (Weber et al., 2011) (Fig. 2.9). Therefore, the phase stepping curve corresponding to the detector pixel is typically described by a cosine function (Momose et al., 2006; Pfeiffer et al., 2008; Bech et al., 2010b):

$$I(x_g) = a_0 + a_1\cos\left(2\pi\frac{x_g}{g_2} + \Phi_1\right). \tag{2.62}$$

By estimating the model parameters a_0, a_1, and Φ_1 from the intensity modulation curve with object in the beam ($I_s(x_g)$), as well as from the intensity modulation curve without object in the beam ($I_r(x_g)$), the AC (or equivalently the transmission T), DPC ($\nabla_x \phi$) and DFC (V) images can be calculated in every pixel (Bech et al., 2010b):

$$T = \frac{a_{0,s}}{a_{0,r}}, \tag{2.63}$$

$$\nabla_x \phi = \frac{g_2}{\lambda d_{1,2}} \left[\Phi_{1,s} - \Phi_{1,r} \right], \tag{2.64}$$

$$V = \frac{a_{1,s}/a_{0,s}}{a_{1,r}/a_{0,r}}, \tag{2.65}$$

with $d_{1,2}$ the distance between G_1 and G_2. The AC signal is hence the constant offset of the phase stepping curve, while the first derivative of the phase of the wavefront is related to the phase shift of the intensity modulation curve compared to the reference curve. Eq. (2.64) results from Eq. (2.34), by considering that the shift in the interference pattern is approximately given by $\Delta x_s \approx \alpha d_{1,2}$ and $\Delta x_s / g_2 = \Delta \Phi_1 / 2\pi$ (Engelhardt et al., 2008). The DFC signal is determined by the relative amplitude of the curve, which can be understood as a measure of how visible the interference pattern is. Increased scattering will result in increased blurring of the interference pattern, thereby reducing the amplitude of the stepping curve, which is why the DFC signal is often referred to as the (normalized) visibility $V = V_s / V_r$. The visibility of a phase stepping curve is given by:

$$V_r = \frac{I_{max,r} - I_{min,r}}{I_{max,r} + I_{min,r}} = \frac{\left(I_{max,r} - I_{min,r}\right)/2}{\left(I_{max,r} + I_{min,r}\right)/2} = \frac{a_{1,r}}{a_{0,r}}. \tag{2.66}$$

The phase retrieval, i.e. the estimation of the function parameters from the phase stepping measurements, can be performed through different procedures. In real measurements, the parameters can be estimated from a least squares fit of a sine (or cosine) to the measured points (Weber et al., 2011). It is also possible to treat Eq. (2.62) as the first order approximation of a Fourier series (Pfeiffer et al., 2008; Bech et al., 2010b). As an alternative to the phase stepping approach explained above, G_2 can be slightly tilted around the z-axis to generate moiré fringes, of which the changes induced by the presence of an object in the X-ray beam can also be recovered (Momose et al., 2003, 2004).

The visibility of the fringes is an important figure of merit for the efficiency of the interferometer. Concerning the longitudinal coherence (monochromaticity), it has been shown how a deviation of the X-ray wavelength from its design value λ_0 affects fringe contrast (Weitkamp et al., 2005). As such, an approximate expression for the monochromaticity (expressed by the width $\Delta\lambda$ of the wavelength distribution around λ_0) required to maintain good contrast for a given Talbot order n is (Weitkamp et al., 2006):

$$\frac{\lambda_0}{\Delta\lambda} \gtrsim n. \tag{2.67}$$

This implies that a grating interferometer can be operated with fairly polychromatic radiation. In addition, it can be shown that that the transverse spatial coherence length required to obtain a given visibility V_r is (Weitkamp et al., 2006):

$$l_s \geq 0.94 n g_2 \left(\ln V_r \right)^{-1/2}, \tag{2.68}$$

which can be related to the source size through Eq. (2.50). Although synchrotron facilities can easily meet the coherence requirements, lab sources in general do not. However, this can be overcome by introducing a third grating (G_0, not shown) between the first one (G_1) and the source, as will be discussed in the next section.

2.4.3 Talbot-Lau interferometry

It can be shown that by inserting an additional absorption grating (G_0) in front of the X-ray source, a sufficiently strong intensity modulation pattern can be generated at G_2, even if incoherent sources are used for imaging (Clauser and Reinsch, 1992; Pfeiffer et al., 2006). Such a three-grating interferometer is known as a Talbot-Lau interferometer and is the standard configuration for lab systems. The slits of the source grating will act as an array of mutually incoherent sources, which, due to their reduced individual widths, are each in itself small enough to be sufficiently spatially coherent. By carefully scaling the distances between the three gratings, the interference patterns caused by the individual slits will coincide at a specific Talbot distance. Hence, the coinciding patterns all incoherently contribute to a single detectable pattern. To achieve this, the fringe patterns of neighboring virtual sources should be displaced by exactly one fringe period (or multiples thereof) with respect to each other. This condition is fulfilled if the pitch of G_0 is (Pfeiffer et al., 2006; Weitkamp et al., 2006):

$$g_0 = \frac{d_{0,1}}{d_{1,2}} g_2, \tag{2.69}$$

where $d_{0,1}$ denotes the propagation distance between G_0 and G_1. Thus, in a Talbot–Lau interferometer, the effective coherence length determining the visibility of the fringes is given by the size of the individual virtual sources, rather than the total size of the source. In this way, the Talbot–Lau interferometer allows an efficient implementation of phase contrast imaging with low brilliance lab sources. The spatial resolution of the images, however, is determined by the total source size and the distances between source and sample and between sample and detector in exactly the same way as for a non-interferometric imaging system. The Talbot–Lau interferometer does not increase spatial resolution in any way, but it allows for phase sensitivity where it would otherwise not be accessible (Weitkamp et al., 2006).

2.5 Edge illumination

Edge illumination emerged in the early 21st century, as a product of synchrotron experiments inspired by analyzer-based methods (Olivo et al., 2001), and was later transferred to lab systems with extended focal spots (Olivo and Speller, 2007a). As we shall see shortly, the EI setup shows, at first sight, a striking physical resemblance with the standard GBI setup. In contrast to GBI, however, EI is a non-interferometric phase contrast

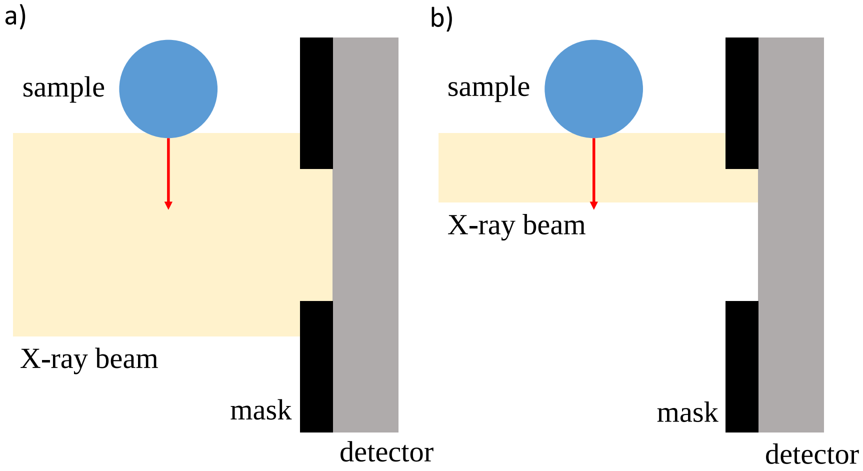

Figure 2.10: (a) Experimental setup for X-ray imaging with a smaller effective pixel size. The red arrow indicates the scanning direction of the sample. (b) Original edge illumination configuration, where a narrow beam impinges the edge of the effective pixel. The narrower the beam, the stronger the detected phase contrast.

imaging method (Munro et al., 2010a). The EI gratings (or masks) are not designed to produce interference patterns, but rather to subdivide the incoming X-ray beam, making EI suitable for incoherent imaging conditions. Like GBI and ABI, EI is sensitive to the first derivative of the phase, and the so-called illumination curves collected with a conventional EI setup are similar in appearance to the rocking curves acquired with ABI. Single mask configurations derived from EI, commonly known as beam tracking methods, have also been proposed (Vittoria et al., 2014). The experimental configuration of beam tracking resembles that of the methods discussed in Section 2.3.7.3, but its contrast retrieval mechanism is more closely related to EI and ABI. In contrast, the retrieval procedure for single grid methods is more closely related to GBI.

2.5.1 Principles of edge illumination

The original edge illumination setup resulted from an attempt to improve the phase contrast acquired with fairly large pixels using synchrotron radiation (Olivo et al., 2001). It was shown that the contrast can be improved by masking the outer parts of the detector pixel, retaining only the central region for illumination (Fig. 2.10). However, it was also observed that the major contributions to the detected phase contrast arose from the narrow regions around the mask edges (the effective pixel edges), whereas the portion of the beam illuminating the central pixel region merely contributed to the background signal. As such, it suffices to retain a narrow beam, aiming at the effective pixel edge, to achieve a good phase contrast signal (Fig. 2.10). Indeed, if a sample is transported through the X-ray beam to acquire an image, it will locally deflect the X-ray beam due to refraction.

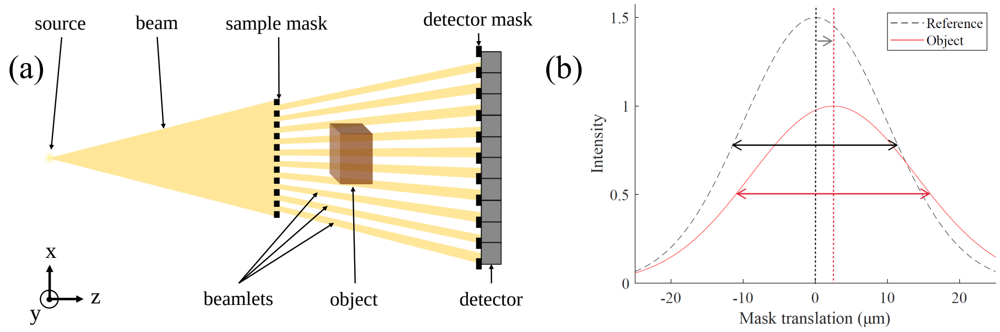

Figure 2.11: (a) schematic overview of an EI system (not to scale). (b) illustration of an IC with and without sample. The arrows indicate the IC shift and broadening, which are linked to refraction and dark field, respectively. The transmission is given by how much the area under the IC is reduced.

This deflection will be directed towards the pixel center when the sample is entering the narrow beam, hereby increasing the measured intensity. Conversely, when the sample is leaving the beam, the X-rays will be refracted away from the pixel center, lowering the measured intensity. Recalling that refraction is related to the first derivative of the phase (Eq. (2.34)), this provides an effective way to acquire phase contrast images with larger pixels. The original EI configuration shown in Fig. 2.10, where a narrow beam illuminates the effective pixel edge, explains the origin of the name of the method.

2.5.2 The conventional edge illumination setup

The standard EI setup for X-ray phase contrast imaging under lab conditions is depicted in Fig. 2.11. The main components of an EI setup are the two absorbing gratings: one in front of the sample and one in front of the detector. In contrast to the scanning setup described in the previous section, the double-mask configuration enables image acquisition in a single shot with an area detector (Olivo and Speller, 2007a). The first grating is known as the sample mask and serves as a beam splitter, subdividing the incoming X-ray beam in several smaller beamlets. In a standard EI configuration, each beamlet corresponds to exactly one pixel column on the detector. The amount of illumination received by each pixel depends on the relative position between the sample mask and the second grating, known as the detector mask. By shifting the sample mask along the x-direction in Fig. 2.11, the projected positions of the beamlets on the detector mask will shift accordingly. If the projected beamlet falls perfectly within the aperture of the detector mask, the measured intensity is maximal. Shifting away from this position to either side will gradually decrease the received illumination until the beamlet is fully blocked by the grating bar, resulting in minimal illumination.

The detector pixel illumination as a function of the sample mask translation is referred to as the illumination curve (IC) (Endrizzi et al., 2014). The IC, depicted in Fig. 2.11, can be used to retrieve the three different contrasts. First, part of the incoming X-rays will be absorbed by the object, reducing the total intensity in the beamlet and the area under the IC (AC). Secondly, refraction in the object will deflect the beamlet from its original path, shifting the IC (DPC). Finally, angular broadening due to unresolvable microstructures increases the IC width (DFC). In practice, an EI experiment involves sampling the IC with a finite number of grating shifts, known as mask stepping. At least three IC positions are required to retrieve all three contrasts. Contrast retrieval is usually performed by fitting the sampled IC with a Gaussian function in the sample mask plane:

$$\mathrm{IC}(x_s) = \frac{a}{c\sqrt{2\pi}} \exp\left(-\frac{(x_s - b)^2}{2c^2}\right), \tag{2.70}$$

with a the area under the IC, b the position of the mean, and c^2 the variance. As such, transmission, beamlet shift, and beamlet broadening in the sample mask coordinate system are given by

$$T = \frac{a_s}{a_r}, \tag{2.71}$$

$$\Delta b = b_s - b_r, \tag{2.72}$$

$$\Delta c^2 = c_s^2 - c_r^2, \tag{2.73}$$

respectively, where the projection with sample and corresponding reference flat field are denoted by indices s and r, respectively. The AC can be computed from T as $-\ln T$, although this additional conversion step is strictly speaking only required for CT. The local X-ray refraction angle α (DPC) can be calculated from Δb by accounting for the distance between sample and detector d_{OD} and the magnification M (Diemoz et al., 2013):

$$\alpha = \frac{M}{d_{\mathrm{OD}}} \Delta b. \tag{2.74}$$

Here, it is assumed that the small angle approximation holds. Similarly, the angular broadening σ^2 (DFC) can be calculated from Δc^2 (Astolfo et al., 2016; Doherty et al., 2023):

$$\sigma^2 = \left(\frac{M}{\mathrm{d_{OD}}}\right)^2 \Delta c^2. \tag{2.75}$$

Under certain circumstances, such as residual transmission through the grating bars, an offset might be present in the measured IC. This can be modeled by adding an offset parameter to the model in Eq. (2.70) (Endrizzi and Olivo, 2014; Vittoria et al., 2015; Astolfo et al., 2016). Similarly, overlap of neighboring beamlets can hamper the detection of weaker dark field signals, which can be compensated for by simultaneous fitting of neighboring curves (Maughan Jones et al., 2018; den Dekker et al., 2013).

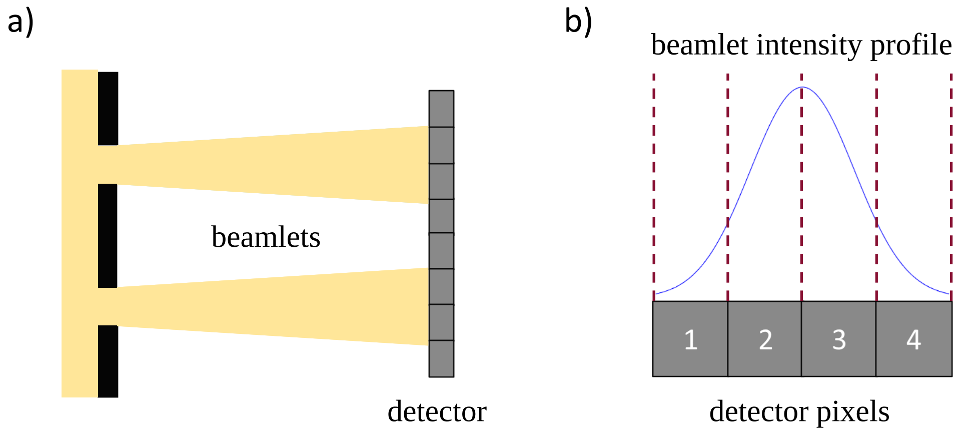

Figure 2.12: a) Schematic depiction of a single mask beam tracking configuration. b) Example of how the beamlet intensity is distributed over several adjacent detector pixels in a beam tracking approach, allowing for direct sampling of the beamlet profile.

2.5.3 Comparison with the grating-based interferometer setup

Although the standard setups for GBI and EI look very similar, there is a crucial difference in the design of the gratings for the respective techniques. GBI gratings typically have smaller apertures, in the order of a few microns, as their purpose is to generate and analyze interference patterns (Pfeiffer et al., 2006; Bech et al., 2010b). EI apertures can be up to an order of magnitude larger, as their purpose is to generate and analyze spatially separated beamlets (Olivo and Speller, 2007a; Endrizzi and Olivo, 2014). Similarly, GBI grating periods are typically much smaller compared to EI grating periods, as each detector pixel column in a GBI setup covers multiple interference fringes, whereas a detector pixel column in EI matches a single beamlet. As a result, EI gratings typically show lower duty cycles compared to gratings for GBI. Interestingly, these considerations also imply that the spatial resolution in GBI is limited by the detector pixel size (Weitkamp et al., 2006), while in EI the spatial resolution is limited by the sample mask aperture size if a sub-pixel sample stepping procedure, known as dithering, is applied (Hagen et al., 2014b).

Whereas in conventional EI each beamlet illuminates one pixel column, a modified EI setup was proposed where a single beamlet illuminates multiple adjacent pixel columns (Vittoria et al., 2014, 2015). Such a single mask configuration allows for direct sampling of the beamlet intensity profile using the detector pixels, provided that the pixels are small enough (Vittoria et al., 2014) or that the geometrical magnification is large enough (Vittoria et al., 2015). This approach, which is shown schematically in Fig. 2.12, is known as beam tracking. Assuming a Gaussian beamlet intensity profile, the beam tracking contrast retrieval procedure is essentially the same as the IC-based contrast retrieval procedure for conventional EI (Vittoria et al., 2018).

2.6 X-ray phase and dark field contrast CT

The advancements in both GBI and EI resulted in the development of quantitative X-ray phase contrast tomography using synchrotron radiation and lab sources (Momose et al., 2004; Pfeiffer et al., 2007; Hagen et al., 2014a,b), soon followed by dark field contrast tomography (Wang et al., 2009b; Bech et al., 2010a; Endrizzi et al., 2017; Doherty et al., 2023). In addition, tomographic imaging has been applied to many other phase contrast imaging methods as well (Wernick et al., 2003; Alloo et al., 2022; Xiao et al., 2022; Yoneyama, 2022). Most of the concepts introduced in Section 1.4 for attenuation contrast CT are almost directly applicable to DPC and DFC, although there a some important differences, which will be highlighted in this section. It should be noted that joint reconstruction methods, capable of reconstructing two, or even all three contrasts simultaneously from the stepping data have been proposed as well (von Teuffenbach et al., 2017; Chen et al., 2017; Six et al., 2024).

2.6.1 X-ray phase contrast computed tomography

Both GBI and EI measure differential X-ray phase contrast, i.e. the first derivative of the phase. Hence, the DPC images have to be integrated in order to apply standard tomographic reconstruction methods (Weitkamp et al., 2005). Indeed, from Eq. (2.22) and Eq. (2.34) it follows that:

$$\alpha(x,y) = -\frac{\partial}{\partial x}\int \delta(x,y,z)dz. \tag{2.76}$$

Alternatively, the derivative can be incorporated in the FBP reconstruction algorithm (Eq. (1.9)) by replacing the ramp filter $|\omega_s|$ by the Hilbert filter (Pfeiffer et al., 2007; Faris and Byer, 1988):

$$\tilde{h} = \frac{|\omega_s|}{2\pi i\omega_s}. \tag{2.77}$$

For algebraic reconstruction methods, the derivative is taken into account by incorporating a discrete differential operator $\boldsymbol{D}$ (e.g. the forward differences operator) in the forward model. Eq. (1.10) then reads:

$$\boldsymbol{p} = \boldsymbol{DAx}, \tag{2.78}$$

which can be solved using iterative reconstruction schemes (Hahn et al., 2015; Six et al., 2024).

2.6.2 X-ray dark field contrast computed tomography

The angular broadening associated with DFC can be modeled by introducing a material dependent linear diffusion coefficient $\varepsilon(x,y,z)$ (Khelashvili et al., 2006; Bech et al., 2010a; Wang et al., 2009b; Doherty et al., 2023):

$$\sigma^2(x,y) = \int \varepsilon(x,y,z)dz. \tag{2.79}$$

This expression is mathematically equivalent to the forward model for conventional attenuation contrast CT (Eq. (1.6)), implying that the same reconstruction algorithms can be applied. For GBI, the angular broadening is related to the normalized visibility by (Bech et al., 2010a):

$$\sigma^2(x,y) = -\frac{g_2^2}{2\pi^2 d_{1,2}^2} \ln V(x,y). \tag{2.80}$$

The dark field signal can have a very strong directional dependence when (strongly) ordered microstructures are present in the sample (Jensen et al., 2010a,b; Revol et al., 2012; Malecki et al., 2013). Although X-ray phase contrast imaging with multi-directional sensitivity is relatively common (Gustschin et al., 2021; Tao et al., 2023), there is an intrinsic difference with directional dark field imaging in the sense that the refractive index decrement δ is a scalar value, except for some crystalline materials (Bricogne et al., 2005), whereas the generalized linear diffusion coefficient (the scattering strength) is best described by a tensor (Bayer et al., 2014; Malecki et al., 2014). Tomographic reconstruction of this tensor provides information about the orientation of unresolved microstructures, and the forward model in this case is given by (Vogel et al., 2015):

$$\sigma^2(x,y) = \sum_j v_j \int \zeta_j^2(x,y,z)dz, \tag{2.81}$$

where $\zeta_j(x,y,z)$ denotes the effective scattering coefficient for the sampled scattering direction j, and v_j is a weighting factor depending on the orientation of the beam, the scattering direction and the sensitivity direction of the imaging system. After reconstruction, an ellipsoid can be fitted to the reconstructed effective scattering coefficients, which is in turn related to a scattering tensor (Wong, 1994). A generalized model relying on spherical harmonics instead of scattering tensors was later introduced as well (Wieczorek et al., 2016). The microstructure orientations are extracted from the reconstructed scattering distribution by means of the Funk-Radon transform (Wieczorek et al., 2018; Funk, 1913) or constrained spherical deconvolution (Huyge et al., 2023a; Tournier et al., 2007).

2.7 Wave optics simulations for X-ray imaging

The classical Monte Carlo approach to simulating X-ray images, which was introduced in Section 1.5, can be very effective in predicting X-ray images with absorption contrast, but cannot compute X-ray phase contrast images without additional modifications. Traditionally, the simulation of X-ray phase contrast images employs wave optics, building on the concepts introduced in Section 2.2. In general, three main aspects have to be considered in wave optics: (i) the interaction of the X-ray wave with the simulated phantom object, (ii) the interaction of the X-ray wave with the optical components (if present), and (iii) the free-space propagation between optical components and objects. For the sake of simplicity, the notation $\tilde{\psi}(x,y,z)$ will be adopted to denote complex wavefront amplitudes, replacing the energy-explicit notation $\tilde{\psi}_\omega(x,y,z)$. Detailed examples of efficient wave optics implementations for grating-based interferometry and edge illumination can be found in Spindler et al. (2025) and Vittoria et al. (2013), respectively.

2.7.1 X-ray interactions in objects and gratings

In contrast to the extensive modeling of X-ray interactions in Monte Carlo simulations, X-ray wave optics simulations usually employ a much more concise description of the interaction physics, summarized by the complex index of refraction (Eq. (2.19)). The complex wavefront amplitude of the outgoing wave field $\tilde{\psi}_{out}(x,y,z_0)$ is then computed from the complex wavefront amplitude of the incoming wave field $\tilde{\psi}_{in}(x,y,0)$ by multiplication with the complex transmission function of the object $T(x,y,z_0)$ (Eq. (2.21)), which is a direct application of the projection approximation (Eq. (2.20)) (Weitkamp, 2004):

$$\tilde{\psi}_{out}(x,y,z_0) = T(x,y,z_0)\,\tilde{\psi}_{in}(x,y,0). \tag{2.82}$$

The assumption that the effect of the object on the passing wavefront can be described by Eq. (2.82) is virtually always justified for thin optical components such as gratings and masks, where in the most straightforward implementations $T(x,y,z_0)$ equals 1 for perfectly transmitting apertures and $T(x,y,z_0)$ equals 0 for perfectly absorbing grating bars (Vittoria et al., 2013). Partial transmission and absorption can then be modeled by choosing values between 0 and 1. Likewise, $T(x,y,z_0)$ can be used to assign a phase shift to the grating bars, required for modeling the phase grating (G_1) in GBI (Malecki et al., 2012).

Determining the complex transmission function of specific optical components and other objects, characterized by their material properties and thickness, requires knowledge of their respective complex index of refraction. Energy-dependent values for β and δ can be extracted from databases[1] or calculated from theoretical models (Als-Nielsen and McMorrow, 2011), based on:

$$\beta = \frac{\mu\lambda}{4\pi}, \tag{2.83}$$

and

$$\delta = \frac{r_e\lambda^2}{2\pi}\rho_e, \tag{2.84}$$

respectively. In Eq. (2.83), μ is the linear attenuation coefficient introduced earlier in Eq. (1.3). In Eq. (2.84), r_e denotes the classical electron radius and ρ_e the material electron density. For energies sufficiently far away from absorption edges, such that the real

---

[1] `https://henke.lbl.gov/optical_constants/`

part of the forward atomic scattering factor $f(0) = f_1(0) + if_2(0)$ is approximately equal to the atomic number Z, we may write (Henke et al., 1993; Peter et al., 2014):

$$\rho_e \approx f_1(0)\rho_a \approx Z\rho_a = Z\frac{\rho}{m_a}, \tag{2.85}$$

with ρ_a the atomic number density, m_a the atomic mass, and ρ the mass density. The linear attenuation coefficient μ can be expressed in terms of the total cross-section σ_{tot} (Eq. (1.1)) as (Malecki et al., 2012; Peter et al., 2014):

$$\mu = \frac{\rho N_A}{A}\sigma_{tot}, \tag{2.86}$$

where N_A denotes Avogadro's number and A is the atomic mass number. In case of a compound material consisting of more than one type of atom, Eq. (2.83) and Eq. (2.84) can be modified to weighted sums over all atom types that are present (James, 1962):

$$\beta = \frac{\lambda}{4\pi}\sum_{j=1}^{N_t} \rho_{a,j}\mu_{a,j}, \tag{2.87}$$

$$\delta = \frac{r_e\lambda^2}{2\pi}\sum_{j=1}^{N_t} \rho_a f_{1,j}(0), \tag{2.88}$$

with N_t the total number of different atom types. Near absorption edges, a more general expression for the electron density of a material (with known stoichiometric composition) that includes dispersion corrections should be used (Daillant and Gibaud, 2009):

$$\rho_e = \rho N_A \frac{\sum_{j=1}^{N_t} n_j \frac{Z_j + f_j' + if_j''}{M_j}}{\sum_{j=1}^{N_t} n_j}, \tag{2.89}$$

where the real (f_j') and imaginary (f_j'') part of the anomalous atomic form factor are referred to as the dispersion corrections, M_j is the molar mass, and n_j is the number of atoms of type j present in the stoichiometric formula. In the previous expression, $f' = f_1 + f_{rel} - Z$, with f_{rel} the relativistic correction factor, and $f'' = f_2$ (Chantler, 1995). Eq. (2.89) yields the following generalized expressions for the calculation of β and δ for a compound material (Daillant and Gibaud, 2009):

$$\beta = \frac{r_e\lambda^2}{2\pi}\rho N_A \frac{\sum_{j=1}^{N_t} n_j \frac{f_j''}{M_j}}{\sum_{j=1}^{N_t} n_j}, \tag{2.90}$$

and

$$\delta = \frac{r_e\lambda^2}{2\pi}\rho N_A \frac{\sum_{j=1}^{N_t} n_j \frac{Z_j + f_j'}{M_j}}{\sum_{j=1}^{N_t} n_j}. \tag{2.91}$$

The atomic form factors and other physical variables required for the computation of the complex index of refraction can be requested from online databases such as NIST FFAST

(Chantler, 1995, 2000; Chantler et al., 2005) and NIST XCOM (Berger et al., 2010). It is common to express the extracted attenuation data as mass-attenuation coefficients (μ/ρ) rather than linear attenuation coefficients μ.

In cases where the effect of the object on the X-ray wave cannot be represented by a single slice, one can use a multi-slice approach (Cowley and Moodie, 1957). In the multi-slice method, the sample is represented by a series of consecutive thin slices, such that Eq. (2.82) can be applied consecutively to each individual slice. The transmitted wave function for a given slice is then propagated to the next slice (see Section 2.7.2) and becomes the incident wave function for that slice. This process is repeated until the wave function is obtained in the exit plane. The multi-slice method is expected to be valid as long as a sufficient number of closely spaced slices are taken, such that the spread of the wave function caused by Fresnel diffraction within the slice does not exceed the spatial resolution required for the calculation. This can be expressed as (Włodarczyk and Pietrzak, 2015):

$$(\delta x)^2 + (\delta y)^2 \ll \delta z \lambda, \tag{2.92}$$

where the small lateral spread of the wavefunction is expressed by δx and δy, and δz is a small propagation distance equal to the slice thickness. More rigorous wave-optical approaches should be applied in circumstances where the paraxial and projection approximations are challenged by thicker objects and diverging X-ray beams (Sung et al., 2013).

2.7.2 Free-space propagation

Since in most cases finding an analytical solution is not possible, calculating the free-space propagation of a wave field following Eq. (2.26) requires the numerical implementation of the Fresnel diffraction operator $\mathscr{D}_{\Delta z}$ (Eq. (2.27)). To this end, a discrete representation of $\tilde{\psi}(x,y,z)$ is introduced, with sampling interval lengths Δx and Δy for the x and y coordinates, respectively:

$$\tilde{\psi}(x,y,z) \to \tilde{\psi}(n_x\Delta x, n_y\Delta y, z). \tag{2.93}$$

Here, n_x and n_y are the grid indices of the $N_x \times N_y$ grid on which the wavefront is discretized, i.e. $n_{x,y} \in [0, N_{x,y} - 1]$ for $N_{x,y} \in \mathbb{N}_0$. The discrete representation of free-space propagation then becomes (Bartels, 2013):

$$\tilde{\psi}(x,y,z_1) = e^{ik\Delta z}\mathrm{DFT}^{-1}\left(e^{-\frac{i\Delta z}{2k}\left(k_x^2+k_y^2\right)}\mathrm{DFT}\left(\tilde{\psi}(x,y,z_0)\right)\right), \tag{2.94}$$

where DFT denotes the discrete Fourier transform, which can be performed efficiently by means of the fast Fourier transform (FFT) algorithm (Cooley and Tukey, 1965), and $k_x = n_x\Delta k_x$ and $k_y = n_y\Delta k_y$ should be interpreted as discrete sampling points on a grid with grid spacings defined as:

$$\Delta k_x = \frac{2\pi}{N_x\Delta x} \tag{2.95}$$

and

$$\Delta k_y = \frac{2\pi}{N_y \Delta y}. \tag{2.96}$$

By introducing the discrete Fresnel numbers:

$$F_x = \frac{(\Delta x)^2}{\lambda \Delta z} \tag{2.97}$$

and

$$F_y = \frac{(\Delta y)^2}{\lambda \Delta z}, \tag{2.98}$$

the complex exponential inside the inverse discrete Fourier transform in Eq. (2.94) can be expressed as (Bartels, 2013):

$$e^{-\frac{i\Delta z}{2k}\left(k_x^2+k_y^2\right)} = \exp\left(-\frac{i\pi n_x^2}{N_x^2 F_x}\right)\exp\left(-\frac{i\pi n_y^2}{N_y^2 F_y}\right). \tag{2.99}$$

This indicates that Fresnel propagation of a given wave field with a discrete $N_x \times N_y$ pixel representation only depends on the combination of wavelength, propagation distance and pixel size (Eq. (2.97) and Eq. (2.98)). To ensure proper sampling of the complex exponential in Eq. (2.99) at smaller Fresnel numbers, the incident wave field can be embedded in a larger array using symmetric padding (mirror reflections at the borders or replication of the border values). Proper sampling implies that the sampling interval is sufficiently small for the Nyquist frequency $f_N = 1/(2\Delta x)$ to exceed the high-frequency components of the phase. Adhering to this criterion will avoid aliasing artifacts in the simulation. A detailed investigation of the sampling requirements for the complex exponential in Eq. (2.99) can be found in Voelz and Roggemann (2009), and some key points will be addressed below. First, it should be noted that performing the propagation in Eq. (2.26) by multiplication in Fourier space with the transfer function $H(k_x,k_y)$, which is given by:

$$H(k_x,k_y) \equiv e^{ik\Delta z} e^{-\frac{i\Delta z}{2k}\left(k_x^2+k_y^2\right)}, \tag{2.100}$$

is analytically equivalent to performing the propagation in real space by means of a convolution ($*$) with the impulse response $h(x,y)$:

$$\tilde{\psi}(x,y,z_1) = \mathscr{F}^{-1}\left[H(k_x,k_y)\mathscr{F}\left[\tilde{\psi}(x,y,z_0)\right]\right] = \tilde{\psi}(x,y,z_0) * h(x,y). \tag{2.101}$$

Here, $h(x,y)$ forms a Fourier pair with $H(k_x,k_y)$. In their discretized form, however, the two different approaches are only fully interchangeable if (Voelz and Roggemann, 2009):

$$\Delta x = \frac{\lambda \Delta z}{L_x} \Leftrightarrow \frac{\lambda \Delta z}{L_x \Delta x} = 1, \tag{2.102}$$

which is known as the ideal sampling condition. Here, L_x denotes the size of the sampling array along the x-axis. The same applies to the y-axis. In Eq. (2.102), $\lambda\Delta z/L_x\Delta x$ can be interpreted as a sampling regime factor, where a value less than 1 indicates an undersampled $h(x,y)$ and oversampled $H(k_x,k_y)$, a value equal to 1 indicates ideal sampling, and a value greater than 1 indicates an oversampled $h(x,y)$ and undersampled $H(k_x,k_y)$. However, maintaining the ideal sampling condition can be inconvenient. Considering again the x-axis, the ideal sampling criterion can be expressed in terms of the number of samples N_x:

$$N_x = \frac{\lambda \Delta z}{(\Delta x)^2} = \frac{L_x^2}{\lambda \Delta z}. \tag{2.103}$$

For a given simulation, this condition may dictate either too many samples for a practical FFT calculation or too few for adequate sampling of the source or observation planes. Note that this expression for N_x is the inverse of the discrete Fresnel number defined earlier (Eq. (2.97)).

As mentioned earlier, the total size of the sampling array should be larger than the region-of-interest (ROI) for the calculation of the wavefront propagation to avoid nonphysical edge effects. In other words, if we denote the support length (the ROI) of the source field ($z = z_0$) by l_0 and the support length of the observation field ($z = z_1$) by l_1, then $\{l_0, l_1\} < L_x$. However, if the transfer function method is used when $h(x,y)$ is undersampled and $H(k_x,k_y)$ is oversampled, the width l_1 of the field in the observation plane that can be modeled accurately is limited to (Voelz and Roggemann, 2009):

$$l_1 \leq l_0 + \frac{\lambda \Delta z}{\Delta x}, \tag{2.104}$$

which is typically less than L_x. The transfer function method tends to produce a field in the observation plane that diminishes outside of the range given by Eq. (2.104). The two orthogonal variables x and y can be evaluated separately, so the same considerations apply to the y-axis.

2.7.3 Divergent X-ray beams

The projection and paraxial approximations together imply that the measured intensity over the planar detector at $z = z_1$, illuminated by a spherical wave $(I_{sw}(x,y,z = z_1))$, is equal to the intensity that would be measured if the same thin object were illuminated by z-directed plane waves with the detector moved to a distance of z_1/M downstream of the object $(I_{pw}(x,y,z = z_1/M))$. Here, M denotes the geometric magnification. This equality holds up to a transverse magnification and a multiplicative scaling M^2 (Paganin and Pelliccia, 2021):

$$M^2 I_{sw}(x,y,z = z_1) = I_{pw}\left(\frac{x}{M}, \frac{y}{M}, z = \frac{z_1}{M}\right). \tag{2.105}$$

Eq. (2.105) is know as the Fresnel scaling theorem. The scaling of x and y by a factor $1/M$ on the right-hand side of Eq. (2.105) stretches the plane wave illumination image $I_{pw}(x,y,z = z_1/M)$ to be the same size as the spherical wave illumination image. The factor of M^2 accounts for energy conservation, since geometric magnification by a factor of M will increase the area of an image by a factor of M^2, thereby reducing the intensity by a factor of $1/M^2$. For numerical computation of magnified or de-magnified images, proper numerical sampling of the phase on a grid that is parallel to the optical axis becomes problematic. The requirement for adequate sampling may necessitate an impracticably large number of pixels. The Fresnel scaling theorem sidesteps this issue, by reducing the computation of a Fresnel diffraction pattern of an expanding or contracting wave to an equivalent calculation for a parallel wave.

If the paraxial approximation starts to break down for increasingly divergent X-ray fields, the non-paraxial angular spectrum method gives a more suitable description of the wave field propagation (Novotny and Hecht, 2012; Bartels, 2013). In the angular spectrum method, spherical waves are expanded as a series of plane waves with variable amplitudes and propagation directions. Recently, a method was presented for numerically efficient and accurate simulations of divergent beams propagating through diffracting structures using the multi-slice method, by applying a coordinate system transformation that transforms the divergent spherical wave into a plane wave (Munro, 2019).

2.8 Design of X-ray phase contrast imaging systems

Over the past two decades, the transition of X-ray phase contrast imaging (XPCI) from synchrotron facilities to lab systems has been successfully established (Endrizzi, 2018). This transition has been achieved in particular for GBI (Pfeiffer et al., 2006) and EI (Olivo and Speller, 2007a; Olivo, 2021). A natural consequence of this evolution is that the research field is becoming increasingly oriented towards the development of real-world applications, such as non-destructive testing (Glinz et al., 2021; Shoukroun et al., 2022b), security screening (Olivo et al., 2009; Miller et al., 2013) and (bio)medical imaging (Pfeiffer et al., 2013; Birnbacher et al., 2021; Massimi et al., 2022). Among these examples, medical XPCI is arguably the most acclaimed application, even more so since the recent demonstration of medical X-ray dark field imaging of human lungs with GBI (Urban et al., 2022). Although GBI is currently a more widespread method, EI is particularly promising due to its low coherence requirements and relatively strong mechanical robustness (Endrizzi, 2018). As the number of XPCI applications steadily grows, so does the need for reliable simulation tools to support the design of novel imaging systems and the development of advanced analysis methods. However, the employment of simulation tools for these purposes poses multiple challenges.

First, wave optics simulators have proven to be a very valuable tool for the simulation of diffraction effects, but efficient implementations often have to rely on the projection approximation when modeling X-ray interactions in samples. MC simulators such as GATE, on the other hand, showcase extremely detailed interaction models and built-in tools for designing complex phantoms, but typically lack the default incorporation of any phase effects. As such, in Chapter 3, this issue is addressed by upgrading GATE with the necessary tools for XPCI simulations.

In addition, MC simulations are known for their notoriously long computation times, which hamper the often large parameter studies that are required for designing optimized XPCI systems. In Chapter 4, it is demonstrated how this problem can be mitigated by introducing the concept of virtual gratings. Subsequently, this method is applied to the design of a pair of gratings for the FleXCT micro-CT system in Chapter 5.

Finally, Chapter 6 addresses the question of how to properly benchmark multi-contrast simulation results, which is achieved through simultaneous extraction of detailed information about photon trajectories from the MC simulations by relying on the flexibility of the virtual grating approach.

Chapter 3

X-ray phase contrast simulations using GATE

This chapter is published as:

- Sanctorum, J., De Beenhouwer, J., and Sijbers, J. (2020). X-ray phase contrast simulation for grating-based interferometry using GATE. *Optics Express*, 28(22):33390–33412

3.1 Introduction

A number of different approaches has been proposed for X-ray phase contrast imaging (XPCI) simulations, typically based on numerical wavefront propagation (Weitkamp, 2004; Malecki et al., 2012), MC simulations (Wang et al., 2009a; Prodi et al., 2011; Cipiccia et al., 2014), or a combination of both (Bartl et al., 2009; Peter et al., 2014). More recently, the combination of analytical and empirical input data has been explored to reduce simulation times (Vignero et al., 2018). The latter approach, however, does not include dark field imaging. In this chapter, we propose to apply the approach suggested by Peter et al. (2014) to GATE and use Monte Carlo simulations in combination with subsequent numerical wavefront propagation. GATE is used for modeling the X-ray interactions in the sample, whereas the wave optics part is used to incorporate coherent effects. To this end, we extend the existing GATE framework with additional tools for the purpose of XPCI simulations, by adding X-ray refraction to the physics library and by associating each photon with a complex wavefront amplitude. We discuss the key aspects of the simulation framework, and show and discuss the simulation results. The methodology presented in this chapter will be demonstrated for GBI, but is applicable to PBI and EI as well.

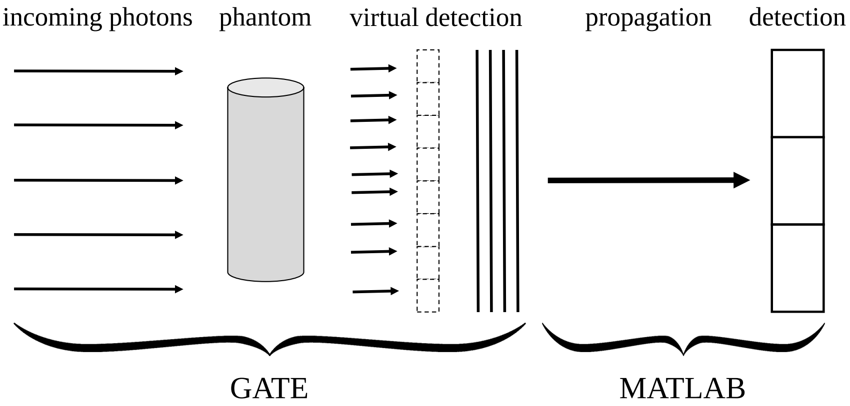

Figure 3.1: Schematic overview of the implemented simulation framework.

3.2 Methods

In this section, we will first briefly address the simulation approach and the corresponding additions to GATE. The concept of using a consecutive combination of MC simulation and wavefront propagation for XPCI was originally introduced by Peter et al. (2014), where egs++ was chosen as MC framework. In this chapter, we will pave the way for the simulation of advanced contrast modalities using GATE's versatile macro interface. Moreover, we will address aspects that were unexplored in the work of Peter et al. (2014), such as 2D radiography including detailed phantom design (Section 3.3). Different approaches to the wavefront construction will be presented, as well as considerations with respect to the implementation of phase stepping and phase retrieval.

3.2.1 Extensions to the GATE source code

GATE forms the first part of the simulation pipeline, where the X-ray interactions in the phantom are simulated (Section 3.2.1.1). Despite regular advances in the list of GATE functionalities, for example with respect to CT (Jan et al., 2011), XPCI has not been taken into account apart from our preliminary work (Sanctorum et al., 2018, 2019). In our modified version of GATE 8.0, the X-rays are collected in a discretized wavefront at a virtual plane, placed behind the phantom (Section 3.2.1.3). In the second part of the simulation, the constructed wavefront interacts with the gratings and is propagated towards the detector (Section 3.2.2.1). At the detector, phase stepping is performed. A schematic overview of the simulation flow is shown in Fig. 3.1. In order to assess the simulation results free from detector effects, the simulations in this chapter are performed without the incorporation of extensive detector modeling. Hence, we will proceed under idealized imaging conditions, and Eq. (2.61) will be used for fitting whenever phase retrieval is performed. Section 3.2.2.4 describes the phase retrieval procedure using Eq. (2.61).

3.2.1.1 Introducing phase effects in GATE

The physics related to the absorption effects is already present in GATE by default. However, as described in Peter et al. (2014), taking phase effects into account requires the photons to have an additional property (a phase or optical path length) and the inclusion of refraction as an additional physics process. In order to define these, each material in the simulation is associated with the decrement δ of the real part of its complex index of refraction, $n = 1 - \delta + i\beta$. This is implemented in such a way that the user can easily add this property to the GATE material database on request by specifying a set of δ values in the macro (a GATE script configuring a simulation) for a custom energy range:

```
/gate/refractiveindex/setRefractionIndex ‘name’ ‘E1’ ‘d1’
/gate/refractiveindex/setRefractionIndex ‘name’ ‘E2’ ‘d2’
...
```

Here, the material name is denoted by `‘name’`. Next, the energy and δ values are specified. These values can be extracted from data tables (Henke et al., 1993), see Section 2.7.1. Having defined the material properties, a phase ϕ is associated with each photon p. When traveling through a certain material, the phase added to the initial photon phase is given by Eq. (2.22), where k is the photon wave number in vacuum and the integral is calculated over the path followed by the photon. Tracking of the optical path length was done using the processGate library (De Beenhouwer et al., 2009).

In addition, the physics library of GATE was extended with the X-ray refraction process. At the boundary between one material (with refractive index decrement δ_1) and another (with refractive index decrement δ_2), the photon undergoes a deterministic refraction process (see Eq. (2.2)), governed by Snell's law (Wang et al., 2009a):

$$(1-\delta_1)\sin\theta_1 = (1-\delta_2)\sin\theta_2. \tag{3.1}$$

with θ_1 the angle between the direction of the incoming photon in the first material and the surface normal, and θ_2 the angle between the direction of refracted photon in the second material and the surface normal. The refraction process (named `XrayRefraction`) is implemented in the GATE source code and is activated in the macro by:

```
gate/physics/addProcess XrayRefraction
```

which is similar to the activation of the other physics processes.

3.2.1.2 Introducing surface roughness

Now that refraction is included in our GATE simulations, the roughness of the surface at which it occurs can be taken into account. To this end, we propose to use a simplified but effective model. For the refraction process, the key aspect of surface roughness is the local orientation of the surface normal. Hence, the roughness modeling can be simplified by introducing local variations in the surface normal with respect to the mean surface, using a stochastic model. The local surface normal undergoes a slight deflection from its original position every time a photon hits, and the rotation axis for the deflection is drawn uniformly from all possible directions. The magnitude follows a Gaussian distribution, expressing the expectation that smaller deviations are more likely than larger ones. Other probability distributions could be of interest depending on e.g. the designed phantom, but such a discussion exceeds the scope of our work. This surface roughness model was applied to the simulations described in Section 3.3.2 and Section 3.3.3. Note that the presented approach to model the surface roughness is similar to the treatment of optical photons in GATE for e.g. explicit modeling of scintillator effects.

3.2.1.3 Wavefront construction in GATE

After interacting with the phantom, the photons arrive at a virtual detector plane, positioned directly behind the phantom. To construct the X-ray wavefront in that plane, the photons are coherently added based on their position, energy, and phase. This plane is not the actual detector in the simulation, but only serves as an intermediate step to switch from a particle representation to a wave representation. For each photon, the position where it first hits the virtual detector plane is determined, and this position is used to assign the photon to a certain wavefront pixel. In this way, the wavefront is generated in GATE, one photon at a time. Rather than adding intensities, as one would do for standard absorption imaging, complex amplitudes are added. In this way, interference effects are accounted for in the final part of the simulation, where the wave propagation and the interaction with the gratings are implemented as described in Section 2.7.

In GATE, the wavefront construction is done by discretizing the two-dimensional virtual plane into $N_x \times N_y$ pixels of size $\Delta x \times \Delta y$. To coherently add the photons arriving at the same pixel, the photons are assigned complex wave amplitudes Ψ. Given that every photon p is represented by a position in the plane $\mathbf{r}$, an energy E, and a phase ϕ, we write $p \dashrightarrow p\{\mathbf{r}, E, \phi\}$. Using this notation, we transform the particle representation into a wave representation at position $\mathbf{r}$:

$$p\{\mathbf{r}, E, \phi\} \iff p\{\mathbf{r}, \Psi(E, \phi)\}, \tag{3.2}$$

where

$$\Psi(E, \phi) = \sqrt{E} \exp(-i\phi). \tag{3.3}$$

The position $\mathbf{r}$ determines to which pixel of the wavefront a certain photon contributes. If we write $\mathbf{r} = (r_x, r_y)$ and define the continuous coordinates of the central point of pixel

(x,y) as (x_c, y_c), the condition for arriving at a certain pixel is given by

$$\begin{aligned} & p\{\mathbf{r}, \Psi(E,\phi)\} \in P(x,y) \\ & \quad \Longleftrightarrow \left(r_x \in [x_c - \Delta x/2, x_c + \Delta x/2[\right) \wedge \left(r_y \in [y_c - \Delta y/2, y_c + \Delta y/2[\right), \end{aligned} \tag{3.4}$$

where $P(x,y)$ is the set of photons arriving at wavefront pixel (x,y).

Assuming $N(x,y)$ photons arrive in pixel (x,y) and using the photon wave representations, the coherent addition of the complex amplitudes Ψ_n is written as:

$$\tilde{\psi}(x,y) = \sum_{n=1}^{N(x,y)} \Psi_n = \sum_{n=1}^{N(x,y)} \sqrt{E_n} \exp\left(-i\phi_n\right). \tag{3.5}$$

In Eq. (3.5), $\tilde{\psi}(x,y)$ denotes the complex wavefront amplitude resulting from the contributions of the $N(x,y)$ photons arriving at pixel (x,y). By adding complex wave amplitudes, both the gained phase and the energy of each photon are taken into account when determining the total complex wavefront amplitude. The employed complex amplitude summation allows one to simulate the interference effects needed to construct the correct initial state of the wavefront. The sum can also be formulated as:

$$\tilde{\psi}(x,y) = \sum_{n=1}^{N(x,y)} \sqrt{E_n} \cos\phi_n - i \sum_{n=1}^{N(x,y)} \sqrt{E_n} \sin\phi_n. \tag{3.6}$$

In our implementation, the real and imaginary part of the wavefront is stored in two data vectors, replacing the energy and phase. However, both representations are completely equivalent.

The user defines the number of pixels in the gridded plane with the following macro commands:

```
/gate/processGate/setGridX ‘number of pixels’
/gate/processGate/setGridY ‘number of pixels’
```

The corresponding physical dimensions are defined using

```
/gate/processGate/setPhysicalGridX ‘size’
/gate/processGate/setPhysicalGridY ‘size’
```

However, deciding on the grid spacing requires careful thought, as explained in Section 2.7.2, since the pixel size of the wavefront must allow proper sampling of the smallest structures in the simulation (Malecki et al., 2012).

In total, three such grids are generated as output: the real part, the imaginary part, and the number of photons arriving in every wavefront pixel:

```
/gate/processGate/setOutputNameReal ‘filename’
/gate/processGate/setOutputNameImag ‘filename’
/gate/processGate/setOutputNameCounts ‘filename’
```

The wavefront construction is initialized in the macro using

```
/gate/processGate/enableGrid
```

As was the case for the `XrayRefraction` process, the wavefront construction relies on the processGate library for the collection of photons at the virtual plane. A complete example of a GATE macro can be found in Appendix A.

3.2.2 Processing GATE output

In the second part of the simulation, the resulting wavefront from GATE interacts with grating G_1 and is further propagated towards G_2 (Section 3.2.2.1). After interacting with G_2, the detection takes place and the phase stepping is performed.

3.2.2.1 Wave optics computations

The GBI system is modeled within the paraxial and projection approximations as a sequence of three events. The first event is the interaction of the wavefront with the first grating G_1, which is defined as a phase grating. This interaction introduces a phase modulation in the wavefront. Subsequently, the resulting wavefront propagates through free space (second event) towards the absorption grating G_2 and the detector, which form the final part of the imaging system (third event). In our work, this three-step imaging protocol was implemented in MATLAB, since MATLAB allows a straightforward implementation and supports the ASTRA toolbox for tomographic reconstruction (van Aarle et al., 2016). Hence, the binary files containing the real and imaginary vectors of the wavefront are first loaded into MATLAB and reshaped to the original size of the wavefront.

An ideal G_1 phase grating is constructed by using a superposition of two identical rectangular Dirac combs, of which one is shifted along the x-direction by the grating bar width and multiplied by an exponential phase factor $\exp(i\phi)$ (O'Shea et al., 2003). This yields a grating that has 100% transmission over its full range, but introduces a phase shift of ϕ in a regular pattern. For Talbot interferometry, this phase shift is typically π or $\pi/2$. Mathematically, a phase grating with bar width b and pitch g_1 is expressed as

$$\begin{aligned} G_1(x) = \operatorname{comb}\left(\frac{x}{g_1}\right) * \Bigg(&\left[\operatorname{rect}\left(\frac{x}{b}\right) * \delta_D(x)\right] \\ &+ \left[\operatorname{rect}\left(\frac{x}{b}\right) * \delta_D(x-b)\right] \exp(i\phi)\Bigg), \end{aligned} \tag{3.7}$$

where $*$ denotes the convolution operator, the comb function can be written as

$$\operatorname{comb}\left(\frac{x}{g_1}\right) = \sum_{n=-\infty}^{+\infty} \delta_D(x - ng_1), \tag{3.8}$$

and

$$\operatorname{rect}\left(\frac{x}{b}\right) = \begin{cases} 1, & x \in \left[-\frac{b}{2}, \frac{b}{2}\right[\\ 0, & \text{otherwise} \end{cases}. \tag{3.9}$$

The effect of G_1 on the wavefront is subsequently simulated by means of a point-wise multiplication of the wavefront with the 2D extension of the $G_1(x)$ function. Straightforward implementation is achieved through the built-in MATLAB function *pulstran*. Propagation of the wavefront is subsequently performed as described in Section 2.7.2. For our numerical simulation, the effect of G_2, with bar width b_2 and pitch g_2, is simulated similarly to the effect of G_1. However, since G_2 is an absorption grating, only one Dirac comb is needed:

$$G_2(x) = \operatorname{comb}\left(\frac{x}{g_2}\right) * \operatorname{rect}\left(\frac{x}{b_2}\right). \tag{3.10}$$

The effect of this grating on the wavefront is subsequently applied through point-wise multiplication of the propagated wavefront intensity with the 2D extension of $G_2(x)$. In this way, we obtain the final intensity at the detector, required for generating the phase stepping images.

3.2.2.2 Phase stepping and detection

Finally, for simulating the detector intensity, a detector pixel size p_d is defined and the wavefront intensity $|\tilde{\psi}(x,y)|^2$ is integrated over every detector pixel. Since $p_d \geq \{\Delta x, \Delta y\}$, a detector pixel will overlap with many wavefront pixels, meaning the integration corresponds to a summation over those wavefront pixels that overlap with a certain detector pixel. As a result, phase stepping images are generated by repeatedly shifting the G_2 array (with periodic boundary conditions) over a number of wavefront pixels, corresponding to the desired displacements of the grating. For every shifted position of G_2, the intensity arriving at the detector is recalculated and a phase stepping image is generated.

3.2.2.3 Subpixel phase stepping

The discrete nature of the phase stepping procedure in 3.2.2.2 imposes certain limitations on the accuracy with which phase stepping can be performed. Indeed, if the grating and the wavefront are defined on the same discrete grid, required for the point-wise multiplications, the smallest meaningful shift is determined by the pixel size of the grid. The same is true for the definition of the pitch of G_2. However, in some occasions, it might

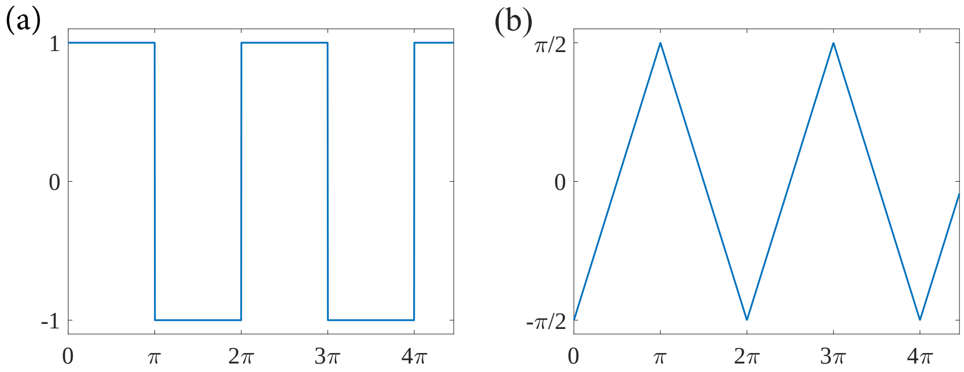

Figure 3.2: (a) Square wave with period 2π, mean 0 and amplitude 1. (b) The primitive function of the square wave, up to a constant.

not be possible to express the desired shift by an integer number of grid pixels. Therefore, we propose to use a subpixel phase stepping approach to omit these restrictions. In order to do this in practice, a fractional transmission between 0 and 1 is assigned to every wavefront pixel, rather than exactly 0 or 1 as was done in the pixel-based procedure described above.

To determine the correct transmission factor F_{trans} in a certain pixel (x,y) of the wavefront, we propose to calculate the difference $F_{\text{trans}} = P_{G_2}(x_1) - P_{G_2}(x_0)$, where $P_{G_2}(x)$ is given by

$$P_{G_2}(x) = \frac{1}{2\Delta x}\left[x + \frac{g_2}{4} f_{\text{TW}}\left(\frac{2\pi}{g_2}x\right)\right]. \tag{3.11}$$

Here, it is assumed that x_0 and x_1 are the real world coordinates of the wavefront pixel boundaries along the stepping direction. For convenience, assume $x_0 = 0$ for pixels $(x,y) = (1,y)$. The rationale for this procedure is understood by considering $G_2(x)$ as a modified square wave. First, assume $f_{\text{SW}}(x)$ denotes a regular square wave as shown in Fig. 3.2 and given by

$$f_{\text{SW}}(x) = \text{sgn}(\sin x). \tag{3.12}$$

The primitive function of $f_{\text{SW}}(x)$ is given by $(\pi/2) f_{\text{TW}}(x)$, up to a constant term, and is also shown in Fig. 3.2. Subsequently, we transform $f_{\text{SW}}(x)$ to $G_2(x)$ by adding an offset of 1 and dividing the result by 2. In this way, the square wave has a minimum value of 0 and a maximum value of 1, expressing the transmission of the grating. The desired periodicity is attained by the transformation $x \to 2\pi x/g_2$. Therefore, we write

$$G_2(x) = \frac{1}{2}\left[1 + f_{\text{SW}}\left(\frac{2\pi}{g_2}x\right)\right]. \tag{3.13}$$

Next, this result must be transformed into a version for which the integral over a wavefront pixel expresses the transmitted fraction in that pixel. Assume, for example, that $\Delta x = g_2/2$ and that a certain pixel is perfectly aligned with a transmitting grating line.

The surface under the $G_2(x)$ curve in the pixel is then simply the width Δx times 1, yielding a value of Δx. However, as $G_2(x)$ in this pixel is fully transmitting, we introduce a scaled version $\tilde{G}_2(x)$ such that this calculation yields 1. In order to achieve this, we scale $G_2(x)$ with a factor $1/\Delta x$:

$$\tilde{G}_2(x) = \frac{1}{2\Delta x}\left[1 + f_{\mathrm{SW}}\left(\frac{2\pi}{g_2}x\right)\right]. \tag{3.14}$$

Integration yields:

$$\int \tilde{G}_2(x)\mathrm{d}x = \frac{1}{2\Delta x}\int \mathrm{d}x + \frac{1}{2\Delta x}\int f_{\mathrm{SW}}\left(\frac{2\pi}{g_2}x\right)\mathrm{d}x. \tag{3.15}$$

Since the last term corresponds to the primitive of the square wave, we get

$$\int \tilde{G}_2(x)\mathrm{d}x = \frac{1}{2\Delta x}\left[x + \frac{g_2}{4}f_{\mathrm{TW}}\left(\frac{2\pi}{g_2}x\right)\right] + \mathrm{const.} \tag{3.16}$$

This result equals, up to a constant, $P_{G_2}(x)$ as defined in Eq. (3.11). The transmitted fraction in a pixel is thus determined by calculating the area under $\tilde{G}_2(x)$ over the range of the pixel, or in other words, by computing the definite integral of $\tilde{G}_2(x)$. By definition, we have:

$$F_{\mathrm{trans}} = \int_{x_0}^{x_1} \tilde{G}_2(x)\mathrm{d}x \tag{3.17}$$

$$= \frac{1}{2\Delta x}\left[x_1 + \frac{g_2}{4}f_{\mathrm{TW}}\left(\frac{2\pi}{g_2}x_1\right)\right] - \frac{1}{2\Delta x}\left[x_0 + \frac{g_2}{4}f_{\mathrm{TW}}\left(\frac{2\pi}{g_2}x_0\right)\right] \tag{3.18}$$

$$= P_{G_2}(x_1) - P_{G_2}(x_0). \tag{3.19}$$

The integration constants cancel out in the definite integral, and we obtain a straightforward way to precalculate the transmitted fraction in every pixel. Indeed, given that the pixel size Δx is fixed, $F_{\mathrm{trans}}(m,n)$ is simply computed as $F_{\mathrm{trans}}(m,n) = P_{G_2}(m\Delta x) - P_{G_2}([m-1]\Delta x)$. This is evaluated directly for every pixel in the wavefront. The effect of phase stepping is incorporated by shifting $P_{G_2}(x)$ accordingly.

3.2.2.4 Triangle wave phase retrieval

Under idealized imaging conditions, the phase stepping curve is described by a triangular model. Hence, a triangular wave form (Eq. (2.61)) is fitted to the measured phase stepping points following a least squares optimization procedure. For simplicity, we consider only a single pixel and therefore omit the explicit notation of pixel indices (i, j). Since proper initialization of the parameters a_0, a_1 and ϕ_1 generally improves the optimization performance, we will first describe an automated procedure for finding such starting values.

Suppose that only four measurements (four steps) are available, sampled over a single period of the phase stepping curve, for initial estimation of the three parameters of a triangle wave. First, as a single period of a triangle wave shows either two or three consecutive slopes, at least two of these four measurements are situated on the same slope. This means that one of the slopes can be easily estimated and, as a result, all other slopes are also known. It is not immediately known which points lie on the same slope, but this is deduced by calculating the slopes between adjacent measurements. Indeed, the points lying on the same slope are found by extracting the steepest slope from the set of calculated slopes, as the slope connecting points lying on a different side of the triangle will always be less steep.

Having assigned the same slope to these two points residing on the same side of the triangle, the slope for the neighboring points can be computed. If we connect a neighboring point to the last know point, and the slope corresponds to the one found for the known point, the neighboring point is assumed to lie on the same side and is assigned the same slope. If no correspondence can be found, the neighboring point must lie on the other side of the triangle and therefore is assigned the opposite slope. Using periodic boundary conditions, the first and last point in the series can also be considered to be neighbors. Generally speaking, due to the periodicity, every point can be shifted by $\pm 2\pi$, allowing to move it to an equivalent position that is closer to its neighbor than π. This means that, in case the adjacent measurements are more than π apart, we find the equivalent position at the same side of the triangle as the neighboring point. In this way, we are able to assign a slope to every point.

Subsequently, the points and slopes are used to find an estimate of the height and position of the extrema of the phase stepping curve. These estimates are the crucial element for finding the starting values, as the position of the peak leads to an estimate of the phase shift ϕ_1, whereas the mean of the extrema yields an estimate of a_0, which in turn leads to an estimate of the amplitude a_1. This searching procedure is fully automated and leads to appropriate starting values for the fitting procedure.

3.2.3 Alternative wavefront construction using ROOT

When building the wavefront in GATE, the wavefront resolution and number of contributing photons are fixed as soon as the MC simulation is initialized. Changing these parameters thus requires a new simulation. Alternatively, all photon tracking data generated with GATE, including position, energy, and phase of each photon, can be saved as a tree structure in ROOT-format (Brun and Rademakers, 1997). A ROOT-program written in C++ is applied to extract the photon information from the tree structure, in order to coherently add the photon contributions.

An advantage of separating the MC simulation and the wavefront construction, is that the sampling parameters of the wavefront are, in that case, independent of the MC simulation. Changing the wavefront grid size therefore does not require a new MC experiment. Following this approach, however, the output size of the GATE simulations depends on the number of photons, increasing rapidly as more photons are generated. Thus, the gained flexibility comes at the cost of large amounts of intermediate ROOT-data and the inclusion of an additional step in the procedure (three instead of two), where a loop over all photons saved in the ROOT-file is required to build the wavefront. Which of the two aforementioned approaches is the most suitable one therefore highly depends on whether the user requires flexibility or computational efficiency.

3.3 Experiments

3.3.1 Validation tests

To validate the performance of our proposed X-ray phase contrast simulator, three distinct tests were run. First, the simulated intensity profile resulting from refracting a 20 keV parallel beam at a spherical phantom in GATE was compared to the theoretically expected profile, following Wang et al. (2009a). The simulated sphere with radius 100 μm was homogeneous, consisted of water and was assigned $\delta = 2.0 \cdot 10^{-6}$ to ensure a visible refraction effect. In total, $20 \cdot 10^6$ photons were considered in GATE for the generation of the profile.

Subsequently, the phase gained by the photons was compared with the expected theoretical result. For this, a GATE simulation was performed with 10^5 parallel beam photons at 25 keV. A homogeneous 4 mm × 4 mm epoxy layer with a thickness of d_{epoxy} = 1 mm was placed between source and detector. The detector size was 5 mm × 5 mm and the expected number of photons entering the epoxy layer was therefore $\approx 62 \cdot 10^3$.

Finally, the propagation method was tested by propagating a plane wave, starting from the phase grating, assuming 25 keV X-rays and an induced phase shift of π. The n-th fractional Talbot distance d_n is then given by (Weitkamp et al., 2006):

$$d_n = n\frac{g_1^2}{8\lambda}, \tag{3.20}$$

where g_1 is the grating pitch, which was assumed to be 4 μm. The pattern was simulated up until the 7th fractional Talbot distance.

3.3.2 Radiography

In this section, the simulation of a 2D radiograph is demonstrated using the described workflow. Prior to discussing the simulation, the GATE phantom used in this simulation is briefly described.

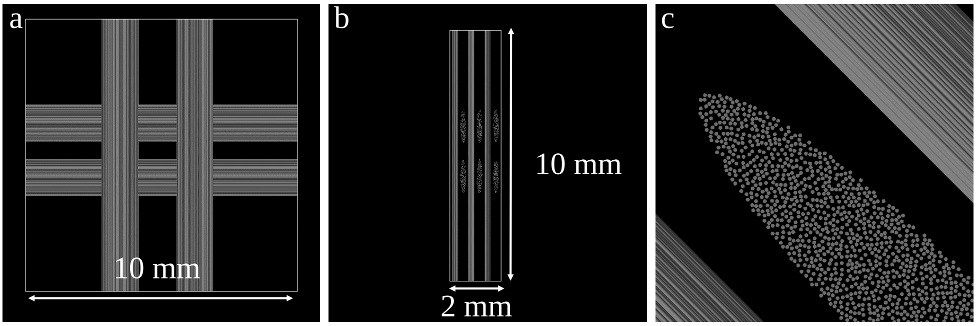

Figure 3.3: CFRP phantom as seen in GATE, showing a front view (a), side view (b) and a zoomed in image (c). A central FOV of 5 mm × 5 mm of the front view is used for the simulation. The gray cylinders show the positions of the carbon fibers, surrounded by an epoxy matrix visualized by a transparent box.

3.3.2.1 Phantom design

The phantom was a simplified model of a carbon fiber reinforced polymer (CFRP), which is an advanced composite material used in many industrial applications. A CFRP consists of a number of bundles of carbon fibers, embedded in a resin, often epoxy. The combination of low-density materials and strongly ordered microstructures makes CFRPs interesting objects for XPCI imaging (including DFC). For our experiments, a phantom was constructed containing 12 fiber bundles, arranged in layers in pairs of two. Bundles in the same layer were mutually parallel, and the orientation within a layer alternates between horizontal and vertical. The cross section of the bundles was elliptical in shape with short and long axis lengths of 112.5 μm and 675 μm, respectively, and the resin material was epoxy. The phantom as represented in GATE is shown in Fig. 3.3.

For practical reasons, the size was limited in terms of thickness (2 mm) and field of view (5 mm × 5 mm). In order to induce unresolved multiple refraction, the microstructure was modeled down to the scale of individual carbon fibers. The number of fibers in a bundle was determined through the number density ρ_N (Sanctorum et al., 2019):

$$\rho_N = \left(\frac{1}{\pi r_f^2}\right)\left(1+\frac{\rho_f}{\rho_r}\left(\frac{1}{c_f}-1\right)\right)^{-1}. \tag{3.21}$$

Here, r_f is the radius of a single fiber, ρ_f the mass density of the fiber material, ρ_r the resin mass density, and c_f the carbon fiber weight fraction. The positioning of the fibers in the bundle was done in a randomized way, allowing the generation of 12 unique bundles for the phantom. Assuming a weight fraction of 0.60 and a fiber radius of 3.5 μm, this resulted in approximately 2570 fibers per bundle, of which the positions were determined by Poisson disc sampling (Sanctorum et al., 2019). The phantom as a whole contained over 30,000 individual fibers. Given that the dark field signal is orientation dependent (Jensen et al., 2010a), we expect to observe differences between horizontal and vertical fiber bundles in the simulation results.

If the fibers are modeled as perfectly smooth cylinders in GATE, the refraction at each individual fiber will generate an intensity profile similar to the one shown in Fig. 3.5. The superposition of many of these perfect refraction events can, due to the low overall absorption of the phantom materials, result in artifacts, as the positive peaks at the edges will dominate the contrast. This is resolved by introducing a surface roughness for the fibers as discussed in Section 3.2.1.2. Surface roughness is a useful addition to the simulation model, given that it is often a highly relevant property of CFRP materials (Yao and Chen, 2013; Wu et al., 2019). Although the implemented model is a simplification, it is considered to be sufficient for our goals, since the most important effect of the surface roughness is taken into account. The scale at which we expect local surface normal variations to occur is submicrometer (Zaitsev et al., 2008), and the potential differences between using the stochastic model and using a well-defined map of local variations are therefore not expected to have a strong effect on the global result. Furthermore, it should be noted that the error propagation in this case does not differ from that of conventional Geant4. The surface roughness model essentially just adds a randomization to a computational step that would occur anyway, namely the calculation of the surface normal vectors at the intersection points.

3.3.2.2 Simulation

The simulation was performed in GATE with $250 \cdot 10^9$ parallel beam photons at an energy of 25 keV. For the wave propagation, a π-shifting phase grating with a pitch of 4 μm was chosen. The matching absorption grating at the first fractional Talbot distance therefore had a pitch of 2 μm (Weitkamp et al., 2006). The wavefront pixel size was set to 0.1 μm × 0.1 μm to keep the sampling well below the fiber size, resulting in a 50,000 × 50,000 grid. For the GATE simulation, we used the Hopper HPC cluster installed at the University of Antwerp [1] The wave propagation part was performed on a local server with 16 (dual) cores. While performing the phase stepping, images were collected from the 50,000 × 50,000 grid on a 250 × 250 detector. These phase stepping images were subsequently inserted in the phase retrieval algorithm (see Section 2.4) to finally yield the transmission image, visibility map (DFC) and DPC image.

In addition, a second radiography simulation was performed. The experimental conditions were identical to those in the simulation described above, but with a slightly tilted

---

[1] Hopper was in operation from late 2014 until the summer of 2020. It was a HPE system consisting of 168 nodes with two 10-core Intel E5-2680v2 Ivy Bridge generation CPUs connected through a FDR10 InfiniBand network. This cluster was moved out in the summer of 2020 to make space for the installation of Vaughan, but 24 nodes with 256 GB were recovered for further use. Hopper was finally decommissioned in the summer of 2023.

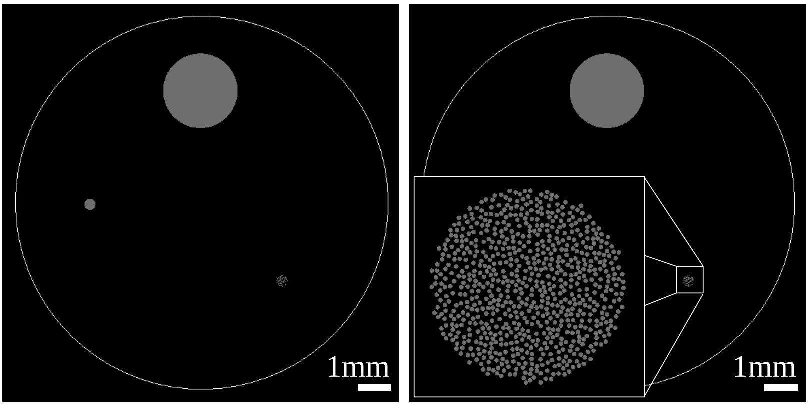

Figure 3.4: GATE phantom used for the CT simulation. The gray cylinders show the positions of the carbon fibers and cylinders, surrounded by the epoxy matrix visualized by a transparent cylinder.

phantom (rotation around the optical axis). As was already mentioned, the dark field contrast is orientation dependent, meaning the simulation results with a rotated phantom are expected to differ from those of the previously described experiment, even though the experimental conditions and phantom were identical.

3.3.3 Computed tomography

In the following, the simulation of sinograms for CT is demonstrated, using the described workflow. We limited the study to 2D sinograms to keep the computation times reasonable. As was done in Section 3.3.2, a brief description of the phantom used in the simulation is given prior to demonstrating our results. For the tomographic reconstruction of the simulated sinograms, a SIRT implementation of the open source ASTRA-toolbox version 1.8.3 (Palenstijn et al., 2011; van Aarle et al., 2015, 2016) was used with 100 iterations on the GPU (NVIDIA GeForce GTX 1080) for the AC reconstruction, and FBP was used for reconstructing DFC (Ram-Lak filter) and DPC (Hilbert filter).

3.3.3.1 Phantom design

The phantom used for the CT simulation, which is also based on CFRP properties, is shown in Fig. 3.4. This phantom contained three cylinders consisting of carbon. Two cylinders, one with a radius of 1 mm and one with a radius of 150 μm, were solid, whereas the third cylinder, also having a 150 μm radius, was filled with 700 fibers with radius 3.5 μm to simulate microstructure. These fibers were identical to those in Section 3.3.2.1 and were positioned following the same position sampling procedure. The three

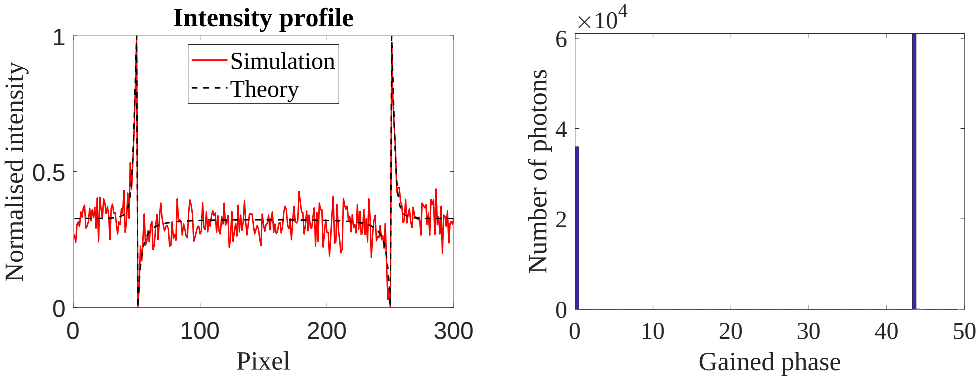

Figure 3.5: (a) Simulated and theoretical normalised intensity profiles resulting from refraction at a spherical phantom with $\delta = 2.0 \cdot 10^{-6}$. (b) Phase gained by 10^5 parallel beam photons at 25 keV, of which a subset of 62% crossed a 1 mm thick epoxy layer with $\delta_{\text{epoxy}} = 3.43593 \cdot 10^{-7}$.

cylinders were embedded in an epoxy cylinder (radius 5 mm). Since the solid cylinders were homogeneous, the DFC signal is expected to be zero. In contrast, the fiber bundle is expected to induce a strong DFC signal. DFC reconstructions have proven to be a valuable tool for the determination of fiber orientations and defects in reinforced polymer samples (Revol et al., 2013; Prade et al., 2017; Senck et al., 2018).

3.3.3.2 Simulation

In the simulation experiments, $30 \cdot 10^9$ photons were simulated in a parallel beam in GATE at an energy of 25 keV. For the wave optics part, we assumed a π-shifting phase grating (G_1) with a pitch of 4 μm. The matching absorption grating (G_2) at the first fractional Talbot distance therefore had a pitch of 2 μm. To investigate the effect of surface roughness on the AC image, sinograms were simulated both with and without surface roughness. For each of the two simulations, 200 equiangular projections were simulated, spanning an angular range of 180°. Five phase steps were simulated for every orientation.

3.4 Results

3.4.1 Validation tests

The theoretical intensity profile as demonstrated by Wang et al. (Wang et al., 2009a) and the simulated intensity profile are shown in Fig. 3.5, where the 300 pixels are each 1 μm

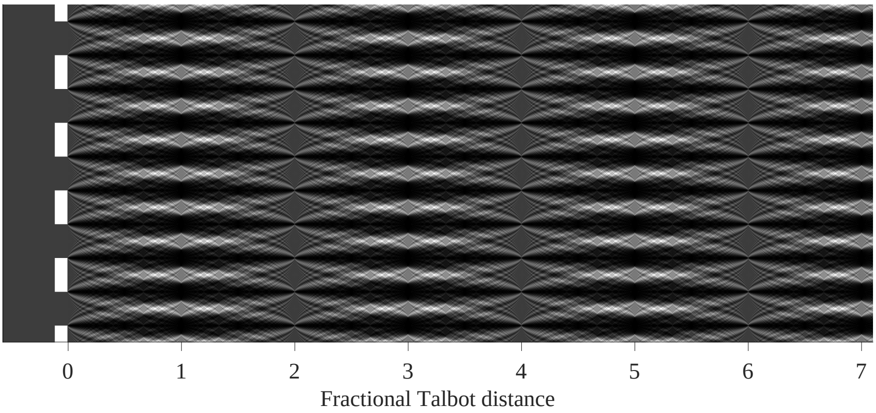

Figure 3.6: Simulated wavefront intensity up to the 7th fractional Talbot distance for a 25 keV plane wave after interaction with a 4 μm pitch π-shifting grating. A higher gray value indicates a higher intensity (arbitrary units).

wide. The simulated results are in good agreement with the theoretical expectations, with a relative difference of -1.79% in average intensity. Due to the photon statistics from the MC simulation, some fluctuations are visible in the simulated profile. The simulation was performed with a 300×300 pixels detector. This means that on average, we would expect each background pixel to collect about 200 photons. Increasing this number by simulating more photons at the source would lower the noise in the intensity profile, at the cost of a longer simulation time. The results of the simulation with the epoxy layer are shown in Fig. 3.5. From the model and the fact that $\delta_{\text{epoxy}} = 3.43593 \cdot 10^{-7}$ at 25 keV, the gained phase was expected to be $\Delta\phi = k_p \delta_{\text{epoxy}} d_{\text{epoxy}} = 43.5$. It can be seen that the simulation results in a correct fraction of photons with the expected phase gain of 43.5. The other photons have not intersected the phantom and thus did not undergo a phase shift, expressed by the peak at a phase gain of zero. This demonstrates that the phase gained during the simulation corresponds to the theoretically predicted phase.

Finally, the wave propagation was evaluated. As expected, a Talbot carpet is observed when visualizing the wavefront intensity as a function of the distance from the grating. The resulting pattern is shown up to the 7th fractional Talbot distance in Fig. 3.6, covering a field of view of approximately 20 μm × 200 mm. The pattern matches the Talbot distances calculated from Eq. (3.20), indicated on the horizontal axis.

3.4.2 Radiography

The images after phase retrieval of the CFRP phantom with horizontal and vertical bundles are shown in Fig. 3.7. Note that the horizontal fiber bundles are not visible in the DFC and DPC images. This is because the fiber bundles are oriented perpendicular to

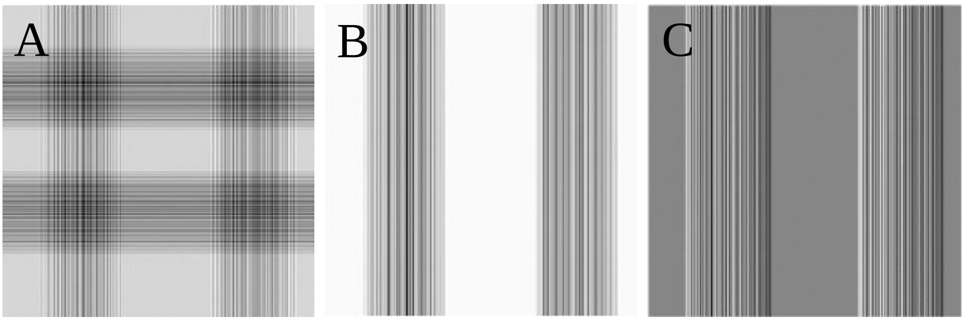

Figure 3.7: Simulated images for the CFRP phantom shown in Fig. 3.3. (a) Transmission image, (b) DFC image, and (c) DPC image. The horizontally oriented fiber bundle is not visible in the DFC and DPC images. Color scale bars are omitted due to the qualitative nature of the discussion in the main text.

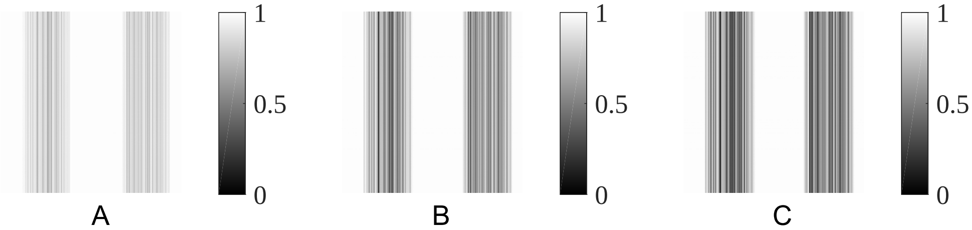

Figure 3.8: Simulated visibility for the phantom shown in Fig. 3.3, acquired at (a) the first fractional Talbot distance, (b) the third fractional Talbot distance, and (c) the fifth fractional Talbot distance. Note that the scaling of the grey values in these images differs from the scaling in Fig. 3.7.

the grating bars, and the interferometer is only sensitive to phase variations perpendicular to the bar orientation. In contrast to the horizontal bundles, the vertical fiber bundles are clearly visible in both DPC and DFC. The presence of the internal structure of the fiber bundles is apparent in all contrasts. The DFC signal (visibility) is clearly lowered because of scattering in the vertical bundle. Note that the visibility reduction caused by the fibers affects the retrieved DPC image as well (Bech et al., 2010b).

Furthermore, the dark field signal or visibility is known to depend on the so-called autocorrelation length of the GBI setup (Strobl, 2014). The autocorrelation length is defined by the geometry of the interferometer as (Lynch et al., 2011):

$$\xi = \frac{\lambda d_{ODD}}{g_2}. \tag{3.22}$$

In short, ξ is an indication of the size of the microstructures that will give rise to a dark field signal, given the geometrical parameters describing the GBI setup. The exact depen-

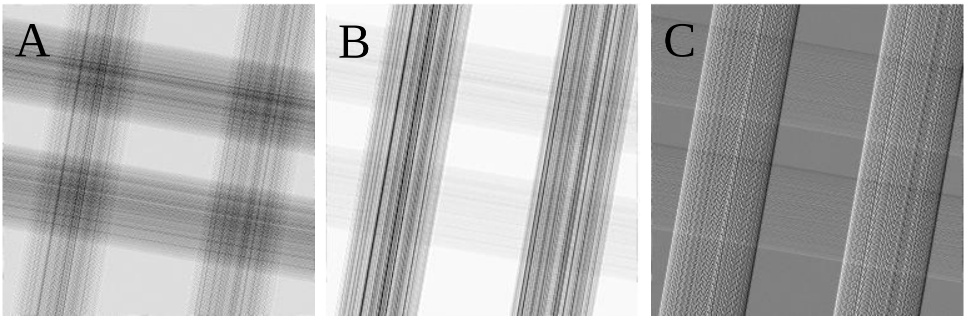

Figure 3.9: Simulated images for the CFRP phantom shown in Fig. 3.3, but with a slightly tilted phantom. (a) Transmission image, (b) DFC image, and (c) DPC image. The horizontally oriented fiber bundle is now visible in the DFC and DPC images. Color scale bars are omitted due to the qualitative nature of the discussion in the main text.

dency of V on ξ is related to the properties of the scattering structures in the object and is not always trivial, although microspheres are a well-studied case (Lynch et al., 2011; Strobl, 2014). For a qualitative demonstration of this dependency, the simulated radiograph from the phantom shown in Fig. 3.3 was acquired for three different propagation distances at the first, third and fifth fractional Talbot distance. In Fig. 3.8, we demonstrate the evolution of the visibility while increasing the propagation distance, hereby effectively changing the autocorrelation length of the simulated setup (Strobl, 2014). The notable decrease in visibility with increasing propagation distance clearly indicates that the dark field signal in GBI indeed depends on the autocorrelation length. However, it should be noted that this dependency only applies to GBI and other related dark field imaging methods where the dark field contrast retrieval is based on the visibility reduction of an intensity modulation that depends on the fringe period. Indeed, the magnitude of the visibility reduction depends on the scattering angle, which in turn depends on the size of the diffracting particles (Paganin and Pelliccia, 2021). For EI and related methods on the other hand, the grating period does not affect the dark field signal as the retrieval is based on a direct measurement of local beam broadening.

In the second simulation, the fiber bundles were slightly rotated, tilting them away from their perfectly horizontal and vertical orientations. The corresponding images are shown in Fig. 3.9. As can be observed, the horizontal bundles now show up in both the DPC and the DFC images. However, a more faint appearance is observed in comparison to the vertical bundles, as the latter still resulted in a stronger phase variation and scatter component along the sensitivity direction of the simulated interferometer. As can be seen in the images, the discretization of the tilted bundles on the 250 $\times$ 250 grid leads to some visual degradation effects in the images. See Section 3.5 for further considerations.

Figure 3.10: Simulated sinograms for (a) absorption contrast; (b) differential phase contrast; and (c) dark field contrast. Color scale bars are omitted due to the qualitative nature of the discussion in the main text.

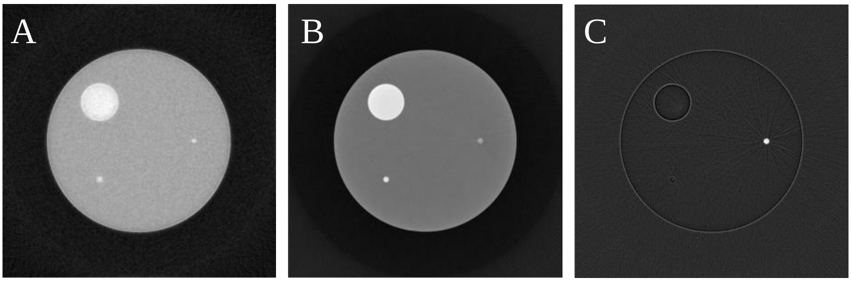

Figure 3.11: CT reconstructions of the sinograms shown in Fig. 3.10. Color scale bars are omitted due to the qualitative nature of the discussion in the main text.

3.4.3 Computed tomography

The simulated projection data (sinograms) with surface roughness, resulting from the phase retrieval, are shown in Fig. 3.10. Looking at the DFC sinogram, it is immediately clear that the cylinder with microstructures yields a strong dark field signal due to the unresolved multiple refraction of the X-rays. As the cylinder edges deflect X-rays, they show up in the dark field sinogram for the larger cylinders. In the DPC sinogram, the edge enhancement effect is also visible. The tomographic images, shown in Fig. 3.11, were reconstructed from the sinograms using the ASTRA toolbox. As expected from the sinogram, the fiber bundle gives a strong dark field signal in the CT reconstruction. The star streak artifact surrounding the fiber bundle is a typical effect of using the Ram-Lak filter in the FBP reconstruction algorithm in the presence of a locally strong signal, similar to high density streaks in conventional absorption CT. This effect can be mitigated by using filters that suppress the highest frequencies (Lyra and Ploussi, 2011). In addition, the edges of the cylinders are enhanced in the DFC image. Slight differences are visible between the smaller solid cylinder and the fiber bundle in both the absorption and the phase contrast reconstruction. As the reconstructed phase contrast image is no longer proportional to the derivative of the phase shift, the edge enhancement disappears after reconstruction. The typical high frequency noise present in the AC and DFC reconstruc-

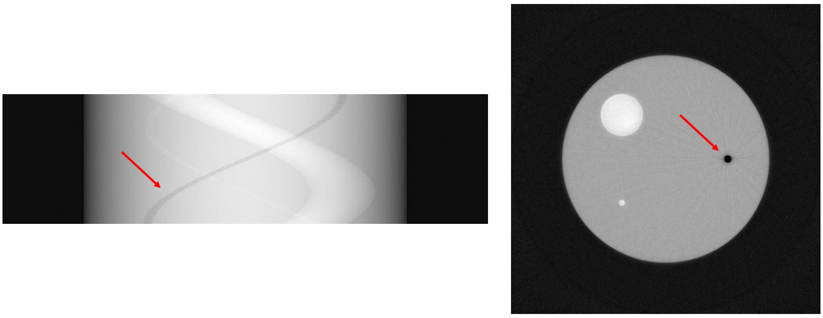

Figure 3.12: Simulated AC sinogram and corresponding tomographic reconstruction for the phantom described in Section 3.3.3.1, without surface roughness of the fibers. The red arrow indicates the affected fiber bundle in both the sinogram and the reconstruction. Color scale bars are omitted due to the qualitative nature of the discussion in the main text.

tions is missing from the phase contrast reconstruction. This is due to the integration of the differential phase during reconstruction by means of the Hilbert filter, resulting in the amplification of lower frequencies, which in turn changes the noise properties of the image (Köhler et al., 2011). The AC sinogram and reconstruction from the simulation without surface roughness are shown in Fig. 3.12 (see Discussion).

To illustrate how the computation time scales with the complexity of the phantom, the plot in Fig. 3.13 shows the computation time for a simulation with 10^6 photons for a total amount of fibers ranging from 100 to 30 000. The latter being the approximate number of fibers in the phantom used for the radiographs. The following data points were collected: 100, 500, 1000, 2000, 5000, 10 000, 15 000, 20 000, 25 000, and 30 000 fibers. From the plot, a linear increase in computation time can be observed. For clarity, only the MC computation time was considered, as the time required for the wavefront propagation is independent of the number of fibers in the phantom.

3.5 Discussion

The validation tests demonstrate the correct behavior of the key simulation elements with respect to the theoretical expectations of photon refraction (Fig. 3.5), phase shifts (Fig. 3.5), and wavefront propagation (Fig. 3.6). It should be noted that an alternative validation approach could be to evaluate the simulations using experimental results. At the time of the development of the simulation tool, the authors did not have a phase contrast imaging system available at their lab. Hence, it was decided to instead rely on established theory to test the simulator. However, later work has indirectly shown agreement between GATE simulation results and experimental data (Huyge et al., 2025). In

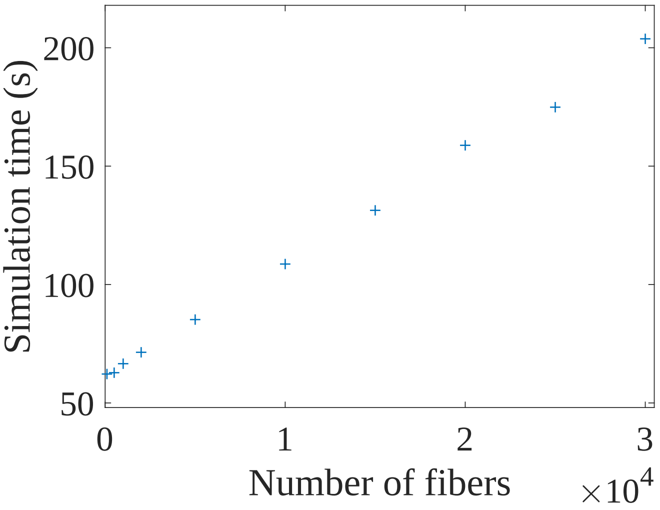

Figure 3.13: Computation time for the MC simulation for a constant number of 10^6 photons, but a varying amount of fibers in the phantom.

addition, the simulation framework was used to validate another ray tracing simulator (Francken et al., 2024a), which was in turn found to yield results that were in agreement with experimental data (Francken et al., 2024b, 2025). A recent comparison between experimental and simulated EI data, performed after publication of the original manuscript, is presented in Appendix B. In Fig. 3.5, the refraction introduces a positive and a negative peak at the phantom edge, since photons are deflected outwards. The magnitude of the positive peak in Fig. 3.5 is significantly larger than its negative counterpart. Given the parallel beam configuration, the two main contributions to the magnitude of the observed peaks in the intensity profile are, most likely, monochromaticity and surface smoothness. A reduction in either of those can be expected to smear out the peaks, as in both cases the spread in photon deflection directions increases. Simulation experiments (not shown here) revealed that the effect of polychromaticity is negligible, which is an indication that the smoothness of the surfaces is the main factor. Indeed, introducing surface roughness into the simulations effectively mitigated the effects. Surface roughness was taken into account through a stochastic model, which does not use a detailed map of the surface of individual fibers but allows one to simulate the global effect the roughness has on the projection data in a more efficient way.

The simulated radiographs in Fig. 3.7 and Fig. 3.9, show that our GATE-based XPCI simulation framework is able to generate the different types of contrast: the transmission image shows the higher absorption in the fiber bundles, whereas the invisible horizontal bundles in the DPC and DFC images reflect the absence of phase gradients along the x-direction in those bundles. The fiber bundles in the phantom appear non-smooth in the images, which can be explained by the fact that, for our parallel beam geometry, projecting the 5 mm × 5 mm FOV on a 250 × 250 detector results in each pixel representing 20

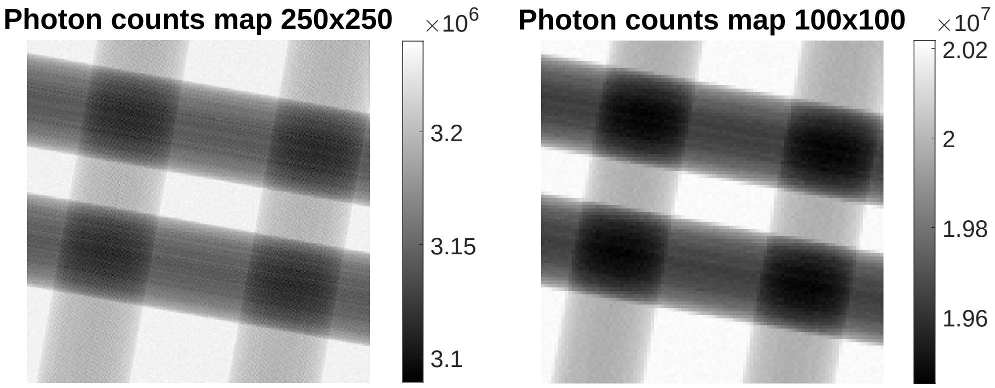

Figure 3.14: a) Photon counts map of the CFRP phantom acquired with a 20 μm pixel size, resulting in a 250×250 image size. b) Photon counts map of the CFRP phantom acquired with a 50 μm pixel size, resulting in a 100×100 image size. In comparison to the 250×250 image, the discretization artifacts inside the fiber bundles are strongly reduced in the 100×100 image. However, the larger pixel size results in a coarser representation of the tilted edges.

μm × 20 μm of the FOV. As the fibers are 7 μm in diameter, this leads to a moiré-like effect (darker and lighter vertical and horizontal bands) in combination with the structure of the superposed fiber bundles. In addition, as the fibers are perfectly parallel, the discretization on the detector pixel grid is expected to introduce linear partial volume or aliasing effects. Similar but more severe image degradation effects resulting from the discretization are apparent in the tilted fiber bundles in Fig. 3.9. To show that these artifacts are indeed related to the discretization and not to the wavefront propagation or contrast retrieval, the corresponding simulated contact image is shown in Fig. 3.14 for two different detector resolutions (20 μm and 50 μm pixel size). These contact images are simply maps of the accumulated photon counts in every pixel of a detector placed directly behind the object, without any gratings or wavefront propagation. It is clear that, for the same pixel size as in Fig. 3.9 (20 μm), similar discretization effects are visible in the contact image. This indicates that the presence of these artifacts is indeed unrelated to the wavefront propagation or the contrast retrieval. In addition, the introduction of a larger pixel size (50 μm) clearly reduces the degradation effects inside the fiber bundles, at the cost of a coarser representation of the tilted edges in the image. In real experiments, these degradation effects would most likely not be visible due to the blurring of the image by the source and detector point spread functions.

In Fig. 3.10, the sinogram data show the expected absorption effects. In the DPC and DFC images, the expected edge enhancement is present and the DFC signal of the fiber bundle is clearly visible. The CT reconstructions in Fig. 3.11 show streaking and edge effects in the DFC image similar to those reported by Peter et al. (2014). The difference between epoxy (matrix) and carbon (cylinders and fibers) is visible in both the AC and

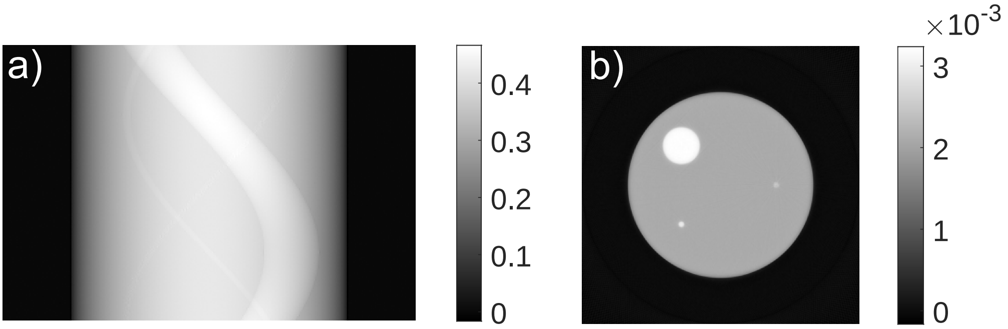

Figure 3.15: a) Log-corrected sinogram of the photons counts in the contact image of the phantom shown in Fig. 3.4, without surface roughness (arbitrary units). b) CT reconstruction of the log-corrected photon counts sinogram (arbitrary units). The negative density artifact visible in Fig. 3.12 is in this case not present.

DPC images. For the CT simulation, the detector pixel size was 50 μm, which is significantly larger than the fiber diameter, resulting in smoother projection data compared to the radiographs of Section 3.4.2. Although the CFRP phantom designed for this demonstration case was only a simplified representation of an actual fiber-reinforced polymer sample, which typically shows woven structures of curved fibers and crossing fibers instead of parallel fiber bundles, the main features required to demonstrate X-ray phase and dark field contrast imaging simulations were present. However, it is possible to extend the modeling to crossing fibers (Elberfeld et al., 2018) or even curved fibers (Elberfeld et al., 2023) by making use of STL files in GATE, but this advanced level of detailed modeling is out of scope for this work.

In Fig. 3.12, the AC sinogram and its tomographic reconstruction are shown for a simulation using the phantom from Section 3.3.3.1 without surface roughness. In other words, the individual fibers all exhibit perfectly smooth surfaces. As can be seen from Fig. 3.12, the absorption contrast in the fiber bundle is severely impacted. This effect can be understood from the intensity profile shown in Fig. 3.5. Towards the edges of the sphere, the intensity drops at the inner side of the edge, while a positive peak appears just outside of the sphere. These peaks are present because photons are deflected outward (Hentschel et al., 1987; Wang et al., 2009a) and can cause negative density effects (Lange et al., 2012). In addition, curved surfaces have been shown to cause caustics when illuminated by parallel beam synchrotron radiation, and it was suggested that surface roughness acts as a mitigating factor for this effect (Evsevleev et al., 2019). The same effects occur in the individual fibers in the fiber bundle, leading to the non-physical effects shown in Fig. 3.12. Indeed, since the phantom contains over 700 fibers, a superposition of many of these intensity peaks is created and amplified by the wavefront propagation. Due to this effect, the intensity originating from the fiber bundle can appear to be higher compared to the same amount of material but concentrated in a single cylinder. For strongly absorbing phantoms, this effect might go unnoticed, but the phantom used for the CT simulation solely consists of low-absorbing materials. This allows the effect to dominate the contrast, contributing to negative density effects. To illustrate that the negative density effect in the AC sinogram and reconstruction in Fig. 3.12 results from the amplification of the peaks by the propagation of the wavefront, the log-corrected sinogram of the contact images (photon counts maps) is shown in Fig. 3.15 for the case without surface roughness. It is clear that the negative density artifact is absent in both the contact image sinogram and its reconstruction.

Recently, an advanced digital phantom was presented to demonstrate the phase contrast simulation of a human thorax based on a full wave simulation approach (Sung et al., 2015). To this end, the authors assumed that the refractive index of the phantom changes gradually within the imaged object and at the boundaries, allowing the use of an approximated solution to the wave equation known as the first Rytov approximation (Sung et al., 2013; Sung and Barbastathis, 2013). Their work is primarily oriented towards free-space propagation phase contrast imaging, but a procedure for combining the calculated attenuation and phase maps to generate a differential phase contrast image was also proposed. In contrast to the method presented in our work, Sung et al. (2015) did not include explicit modeling of the interferometer. An advantage of incorporating the interferometer explicitly in the simulation is that this allows analysis of the phase stepping images, which are of interest when exploring phase retrieval methods. In Sung et al. (2013), the possibility of using the full wave approach as a forward model for tomography is briefly discussed. Given the computational requirements inherent to the MC part of our work, it is practically unfeasible to use our framework for this same purpose. However, the MC part allows for detailed modeling of photon-matter interactions such as Compton scatter and photoelectric absorption, relying on their respective physical cross sections. Furthermore, tracking the individual refraction events of photons at microstructures is an important feature of the MC part for accurate modeling of the unresolved multiple refraction underlying the dark field image formation process. By passing the output of the MC part to the wave optics part, both particle and wave properties are present in the simulations. Dark field contrast images were not simulated in Sung et al. (2015), and details smaller than approximately 125 μm were not (yet) included in their phantom, whereas microstructures well below 10 μm were taken into account in our work. It should be noted that, while the work presented in Sung et al. (2015) focuses on the phase contrast modality, our work intends to explore the dark field contrast modality as well, which could explain the difference in methodology. Indeed, an as accurate as possible phase contrast image at a human scale clearly benefits from exploiting the wave properties to a maximum, whereas a Monte Carlo approach is well-suited for the detailed modeling of the multiple refraction underlying the dark field contrast. The latter is also gaining increasing interest with respect to medical applications such as lung imaging (Willer et al., 2018).

Several improvements to our simulation framework can be considered. Firstly, we did not focus on incoherent radiation and the need for grating G_0 for lab-based cone beam sources. Adequate modeling of G_0 as part of the MC simulation significantly increases the complexity of the MC part and was out of scope of this study. Secondly, polychromaticity was not included in the simulation experiments. Although not shown, it can be taken into account in the propagation part of the framework by integrating over the energy spectrum (Weitkamp, 2004). Lastly, MC simulations are notoriously known to be computationally expensive, and our simulation framework is no exception. Adding additional refraction interactions to every photon trajectory certainly prolongs the simulation time. Despite our efforts to at least reduce the data output storage requirements (Section 3.2.2) and the use of a computer cluster, this is still a mayor limitation. Improving the computational efficiency is, therefore, important future work. An efficient GPU implementation of the simulation code could therefore substantially decrease the computation time. Notwithstanding the shortcomings mentioned above, the results shown in this study demonstrate the ability of our simulation framework to generate X-ray phase contrast CT projection data of phantoms with realistic properties, paving the way for simulation studies on phase contrast system design, acquisition strategies, phase retrieval and reconstruction.

3.6 Conclusion

In this chapter, we extended GATE, a framework for Monte Carlo-based medical imaging simulations, with novel tools to simulate X-ray phase contrast imaging. The GATE output was post-processed for wavefront propagation to allow the simulation of grating-based imaging. The implementation was validated by comparing the simulation results to the expected theoretical results, which were found to be matching. Furthermore, 2D radiography simulations were presented as well as sinogram simulations for CT reconstruction. Realistic CFRP phantoms were designed and it was shown that the resulting simulations produce the most important effects expected from an actual CFRP sample, demonstrating that the framework can generate the most relevant effects in phase and dark field imaging. To our best knowledge, this is the first time a 2D dark field image for a CFRP-like phantom was simulated with such detailed fiber modeling at the presented scale (5 mm × 5 mm FOV).

Acknowledgments

The computational resources and services used in this work were provided by the HPC core facility CalcUA of the Universiteit Antwerpen, and VSC (Flemish Supercomputer Center), funded by the Research Foundation - Flanders (FWO) and the Flemish Government. Financial support was provided by Research Foundation - Flanders (FWO) (G090020N, G094320N) and EU Interreg (0386).

Chapter 4

Virtual grating approach for edge illumination simulations

This chapter is published as:

- Sanctorum, J., Sijbers, J., and De Beenhouwer, J. (2022a). Virtual grating approach for Monte Carlo simulations of edge illumination-based x-ray phase contrast imaging. *Optics Express*, 30(21):38695–38708

4.1 Introduction

In the previous chapters, we have seen that X-ray phase contrast imaging (XPCI) simulators are typically based on either wave optics calculations (Weitkamp, 2004; Malecki et al., 2012; Vittoria et al., 2013; Sung et al., 2015), Monte Carlo (MC) code (Wang et al., 2009a; Millard et al., 2014; Cipiccia et al., 2014; Tessarini et al., 2022; Brombal et al., 2022a,b), or a combination thereof (Bartl et al., 2009; Peter et al., 2014; Ritter et al., 2014; Sanctorum et al., 2018, 2020; Langer et al., 2020). In addition, ray tracing-based (Bliznakova et al., 2015; Włodarczyk and Pietrzak, 2017; Wilde and Hesselink, 2020; Bliznakova et al., 2022) and empirical methods (Vignero et al., 2018) have been reported. Some of these studies have explicitly included simulations for EI (Vittoria et al., 2013; Millard et al., 2014; Cipiccia et al., 2014; Włodarczyk and Pietrzak, 2017; Brombal et al., 2022a,b). In Chapter 3, we have demonstrated the hybrid (MC and wave optics) simulation of XPCI for GBI using an extended version of GATE. Within this framework, the MC code is used to generate a wavefront, which is subsequently propagated through the gratings towards the detector using wave optics. The additional wave optics calculations allow to account for coherent effects, which are essential to GBI (Weitkamp et al., 2006). EI, on the other hand, is designed as a non-interferometric XPCI method. Hence, geometrical optics can typically be used to describe image formation, and phase shifts are modeled as refraction effects (Munro et al., 2010a; Diemoz and Olivo, 2014). As the calculation of interference patterns is not required for EI, the simulation can be performed entirely in GATE, as demonstrated in earlier work (Sanctorum et al., 2021a; Huyge et al., 2021). MC simulations, however, are notoriously known to be computationally demanding, leading to long simulation times. To reduce simulation times, dedicated implementations with simplified grating interaction models have been presented, where the interactions in the grating are governed by the well-known Lambert-Beer law, instead of distinct interaction cross sections (Buchanan et al., 2020). However, system design parameter studies, where possibly hundreds or more variations of the grating geometry are tested, easily require hundreds of MC simulations. Even simply stepping the EI illumination curve (IC) already requires multiple simulations (Brombal et al., 2022b). Hence, there is a need for computationally efficient MC simulation strategies in order to perform these studies in an effective way.

In this chapter, we introduce the concept of virtual gratings to drastically reduce the total simulation time for situations where many grating parameter variations are needed. The proposed concept is based on replacing the explicitly defined gratings (with fixed parameters) by continuous volumes that register the photon trajectory at the grating position. As such, the grating parameters can be defined after the MC simulation, regardless of the presence of other objects in the beam path. One MC simulation therefore serves as a basis for a virtually infinite number of possible experimental configurations. To our best knowledge, the work presented in this chapter provides the first demonstration of an effective approach to capture the full phase space of grating parameters with a single MC simulation.

4.2 Methods

4.2.1 Simulation models for gratings

Modeling the effect of the gratings is a crucial aspect of the simulation. Different approaches exist, which can be roughly divided in three categories: (1) modeling the grating as a plane under the projection approximation (2D) (Millard et al., 2014; Sanctorum et al., 2018, 2020; Fu et al., 2019; Bartl et al., 2009; Malecki et al., 2012; Vittoria et al., 2013; Ritter et al., 2014; Peter et al., 2014; Bliznakova et al., 2022; Tessarini et al., 2022), (2) modeling the grating as a volume with bars extending along the direction of the optical axis (3D) (Brombal et al., 2022a,b; Sanctorum et al., 2021a; Huyge et al., 2021), or (3) simulation frameworks where the effect of the grating is accounted for implicitly, without introducing the gratings as components in the simulation (Sung et al., 2015; Vignero et al., 2018; Wilde and Hesselink, 2020).

Two-dimensional (flat) grating models are common in, but not restricted to, wave-optics simulations and involve either an idealized binary representation of the grating (Millard et al., 2014; Sanctorum et al., 2018, 2020; Fu et al., 2019) or application of a complex transmission function (projection approximation) (Bartl et al., 2009; Malecki et al., 2012; Vittoria et al., 2013; Ritter et al., 2014; Peter et al., 2014; Bliznakova et al., 2022; Tessarini et al., 2022). However, assuming the gratings are infinitesimally thin is not always a valid approximation. X-rays can, for example, intersect the grating bars under an angle, impacting the effective distance traveled through the material. To incorporate these effects, grating bars are modeled as full 3D objects (Brombal et al., 2022a,b; Sanctorum et al., 2021a; Huyge et al., 2021). Three-dimensional MC models of membranes have been used for simulating speckle-based imaging as well (Quénot et al., 2021). However, as long as the gratings are a fixed part of the simulation model, any change in grating geometry requires a new MC simulation.

4.2.2 Virtual gratings in GATE

If the EI XPCI simulation is performed entirely in GATE without virtual gratings, the two gratings (sample mask and detector mask) are explicitly modeled as physical objects in the simulation. The photons will therefore interact with the grating bars the same way as with any object in the beam path. To make a clear distinction with the virtual gratings that we will define soon, gratings that are directly modeled in GATE will be called explicit gratings in the remainder of the text. As mentioned in Section 4.1, an explicit grating model requires a new MC simulation whenever a grating parameter, such as pitch or aperture size, is changed. To drastically decrease the computation time when many parameter variations are required, we propose to use an alternative simulation approach, which we will call the virtual grating approach. This concept essentially encompasses the decoupling of the grating parameters from the MC simulation, in such a way that these can be defined after completion of the MC simulation. As such, the photon interactions within the phantom and detector are preserved, regardless of the choice of grating parameters. In other words, a single MC simulation can serve as a basis for a virtually unlimited number of grating parameter variations.

To achieve this high degree of flexibility, the concept of virtual volumes is introduced in GATE, using the ProcessGATE library (De Beenhouwer et al., 2009). The virtual volumes replace the explicit gratings in GATE, as shown in Fig. 4.1. These volumes are defined as (box) volumes in a GATE macro, and are named as follows:

```
/gate/world/daughters/name virtualvolume1
/gate/world/daughters/name virtualvolume2
```

for source and detector mask, respectively. To activate the virtual grating code in GATE, the following macro command is added:

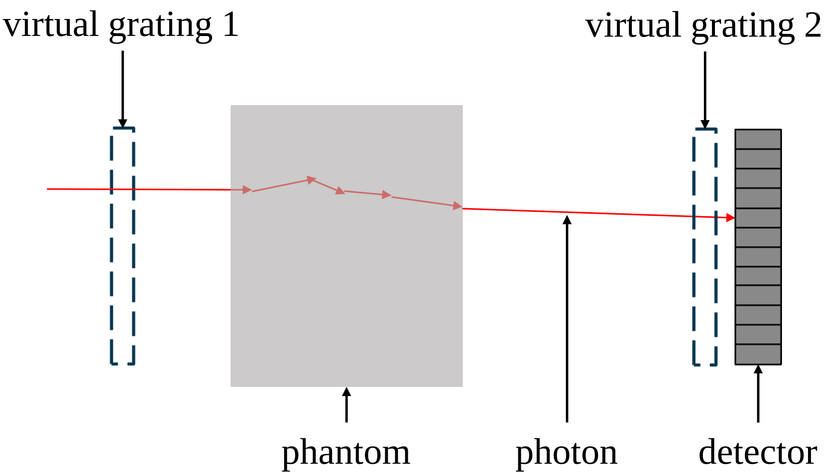

Figure 4.1: Positioning of the virtual grating volumes in GATE (not to scale). The source (not shown) is positioned to the left of virtual grating 1.

```
/gate/processGate/enableVirtualVolume
```

When activated, the standard ROOT output of GATE will be extended with additional parameters. In short, the ROOT output of a simulation is a structured list of information on the interactions and trajectories of all detected photons (Brun and Rademakers, 1997). It stores, for example, the 3D coordinates of the position where the photon deposited its energy in the detector, as well as the position where it was generated in the source. For virtual grating simulations, twelve new parameters are added to this list, storing the coordinates of the intersection points with the front and back planes of the two virtual gratings. With these additional parameters at hand, it is possible to reconstruct the photon trajectories within the virtual gratings after the simulation. As will be shown in Section 4.2.3, knowing these trajectories allows for the definition of grating parameters after the MC simulation. More specifically, we can decide post-simulation which photons are blocked by grating bars and which photons are transmitted, by defining grating bars within the virtual grating volume. As the photon interactions in phantom and detector are taken into account by default, this approach provides an efficient way to set up parameter variation studies without the need for additional MC simulations. Important parameters that can be varied post-simulation with the virtual grating approach are the pitch, aperture size, grating thickness, shift, and rotation. As a result, misalignment effects can be analyzed as well. We note that the proposed approach is not limited to rectangular gratings and allows for the insertion of more exotic grating designs such as asymmetric (Endrizzi et al., 2016; Fu et al., 2019) or even bent (Wu et al., 2021) and circular (Dreier et al., 2020) masks.

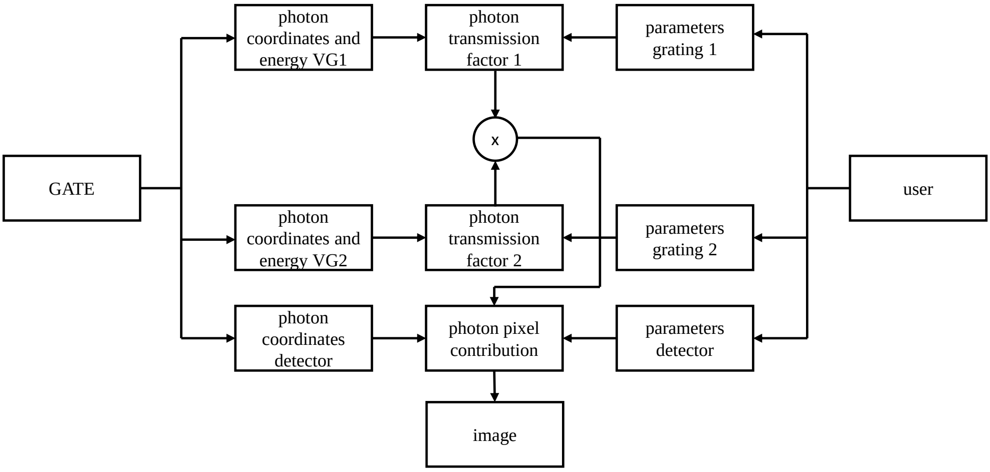

Figure 4.2: Schematic depiction of the processing of virtual grating (VG) simulation results.

4.2.3 Processing virtual grating simulation results

In this section, the processing of the virtual grating simulation output will be discussed. Fig. 4.2 shows a schematic overview of the image formation based on virtual gratings output. Through its ROOT output, GATE provides information on each photon's energy and position coordinates in the virtual grating volumes and the detector. The user provides information on the position of apertures and grating bars, through the definition of the grating parameters. The combined knowledge of grating bar locations and photon trajectories allows us to determine whether or not a photon intersects a grating bar. If a grating bar is encountered, the distance traveled through the bar is calculated. The user defines the material of the grating bar and the corresponding energy-dependent attenuation coefficient. Subsequently, the Lambert-Beer law is used to determine the transmission factor of each photon. This yields a value between 0 and 1, acting as a weight for the final contribution of the photon to the summed intensity at the detector. As each grating yields a transmission factor, the total weight of the photon's contribution is given by the multiplication of the two weight factors.

Since the simulation output holds the location where the photon is absorbed within the detector volume, the detector pixel boundaries are user-defined as well. This allows for example for post-simulation variations in detector pixel size. Finally, the image is formed by adding all transmission factor-weighted photons for each pixel. A detailed example of analytical transmission factor calculation can be found in Section 4.2.4 for the most commonly used EI configuration, consisting of two rectangular gratings (Endrizzi, 2018). An extensive overview of all possible mask geometries is beyond the scope of this dissertation, but we note that similar reasoning leads to equivalent expressions for other grating configurations.

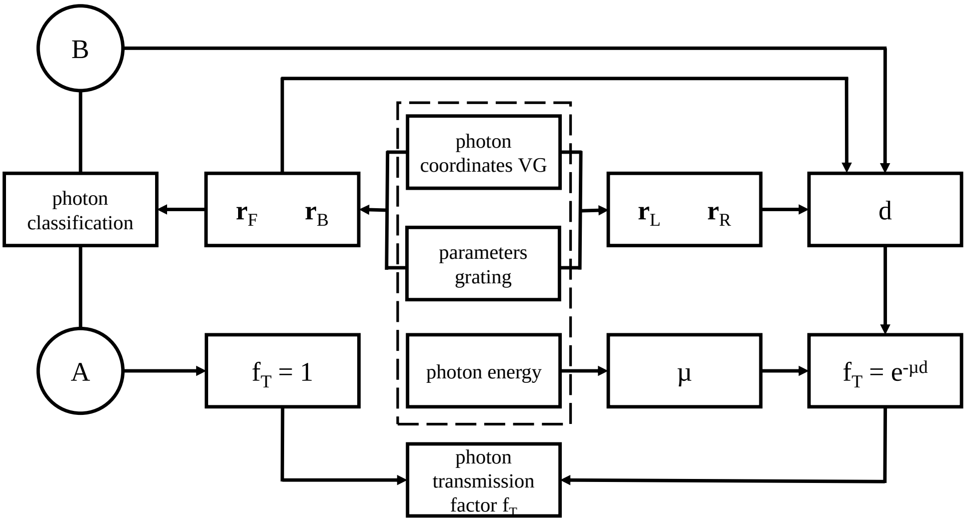

Figure 4.3: Schematic overview of the determination of photon transmission factors. The calculation is based on the information enclosed by the dashed contour.

4.2.4 Analytical calculation of photon transmission factors

The calculation of photon transmission factors is based on the user-defined grating parameters, the photon energies from GATE, and the intersection coordinates with the initial virtual grating volumes. A schematic overview is shown in Fig. 4.3. From the intersection coordinates with the front and back planes of the virtual grating volume, the intersections with the effective, user defined, front and back planes of the grating are computed ($\mathbf{r_F}$ and $\mathbf{r_B}$, respectively). These planes do not necessarily coincide with the virtual grating boundaries as defined in GATE, depending on the user-defined material thickness and shift (Fig. 4.4).

The possible intersection types are depicted in Fig. 4.4. If both $\mathbf{r_F}$ and $\mathbf{r_B}$ lie within the same aperture, the photon does not intersect the grating bars and is classified as an A-type photon. A-type photons are immediately assigned a transmission factor $f_T = 1$, indicating full transmission. If this is not the case, the photon intersects a grating bar and is classified as a B-type photon. In Fig. 4.5, it is demonstrated that, for the case of oblique incidence, all grating bar planes (extended to infinity) are intersected. However, the intersection points of interest are in any case the middle two points with respect to the z-coordinate. The intersection coordinates within the side planes are given by $\mathbf{r_L}$ and $\mathbf{r_R}$ for left and right, respectively.

Although rather exceptional, the simulated geometry might lead to a certain number of photons with nearly perpendicular incidence on the central grating bars. If this is the case, B-type photons can be further split in two subclasses: B_1 for perpendicular incidence photons and B_2 for oblique incidence. B_1-type photons are easier to handle, as it can be

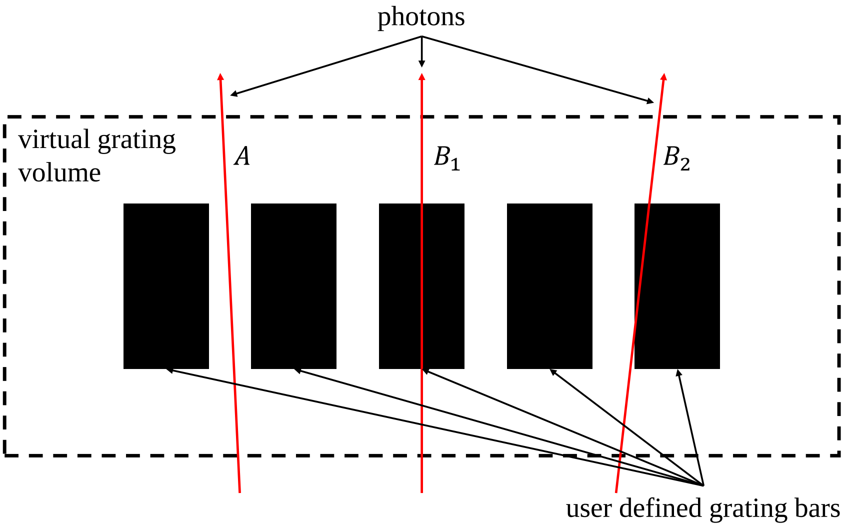

Figure 4.4: Photon classification based on intersection type.

safely assumed that they will intersect only the front and back planes of the grating bars.

The four intersection points can often be determined analytically through application of solid-geometry concepts. Each photon trajectory is described by a line, using the intersection points with the front and back planes of the virtual grating volume, $\mathbf{r}_{\text{in}} = (x_{\text{in}}, y_{\text{in}}, z_{\text{in}})$ and $\mathbf{r}_{\text{out}} = (x_{\text{out}}, y_{\text{out}}, z_{\text{out}})$, and a parameter κ_0:

$$\mathbf{r_{line}} = \mathbf{r}_{\text{in}} + \kappa_0 \left(\mathbf{r}_{\text{out}} - \mathbf{r}_{\text{in}}\right), \tag{4.1}$$

with $\mathbf{r_{line}} = (x, y, z)$ the coordinates of a point on the line, defined by the value of the free parameter κ_0. The x- and y-dimensions of the virtual grating volume are assumed to be large enough such that no other virtual volume boundaries are crossed.

Rectangular grating bars, defined by the user, can be described by four intersecting planes (assuming the grating is large enough, such that the top and bottom planes are never intersected). Planes in three-dimensional space are defined using two free parameters κ_1 and κ_2. In general, points on a plane are given by

$$\mathbf{r_{plane}} = \mathbf{r_0} + \kappa_1 \mathbf{r_1} + \kappa_2 \mathbf{r_2}, \tag{4.2}$$

which is defined by three points: $\mathbf{r_0}$, $\mathbf{r_1}$, and $\mathbf{r_2}$. For the case of rectangular gratings parallel to the detector plane, a natural choice for these points is

$$\begin{cases} \mathbf{r_0} = (0, 0, z_g) \\ \mathbf{r_1} = (1, 0, 0) \\ \mathbf{r_2} = (0, 1, 0) \end{cases} \tag{4.3}$$

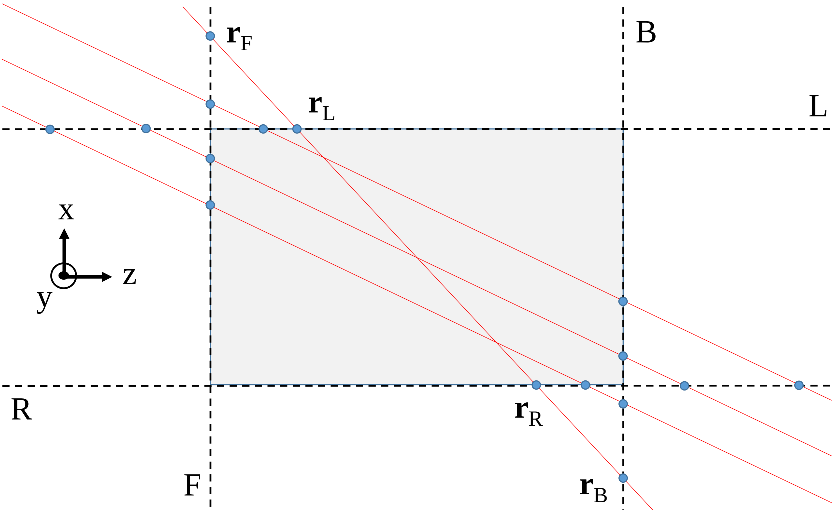

Figure 4.5: Possible oblique intersection scenarios of a photon trajectory and a grating bar.

for the front and back planes, and

$$\begin{cases} \mathbf{r_0} = (x_g, 0, 0) \\ \mathbf{r_1} = (0, 0, 1) \\ \mathbf{r_2} = (0, 1, 0) \end{cases} \tag{4.4}$$

for the side planes. Here z_g and x_g indicate the position of the front or back plane along the z-axis and the position of the side plane along the x-axis, respectively. Both z_g and x_g follow from the user-defined grating geometry. Assuming the grating bar center along the z-axis coincides with the center of the virtual volume, z_g can be written as

$$z_g = \frac{z_{\text{in}} + z_{\text{out}}}{2} \pm \frac{1}{2} d_g, \tag{4.5}$$

where the sign of the second term depends on the plane (front or back). Here, d_g is the grating thickness. Likewise, x_g can be written as

$$x_g = x_c \pm \frac{1}{2}(1 - d_c) g, \tag{4.6}$$

where again the sign depends on the side plane (left or right). In this equation, x_c is the center of the grating bar along the x-axis, g the grating pitch and d_c the duty cycle.

The intersection point of the photon trajectory with one of the four planes is subsequently found by simply stating $\mathbf{r_{line}} = \mathbf{r_{plane}}$, and solving for κ_0, κ_1, and κ_2. Finally, Eq. (4.1) (or Eq. (4.2)) then yields

$$\begin{cases} x = \frac{1}{2}\left(x_{\text{out}} - x_{\text{in}} \pm d_g \frac{x_{\text{out}} - x_{\text{in}}}{z_{\text{out}} - z_{\text{in}}}\right) \\ y = \frac{1}{2}\left(y_{\text{out}} - y_{\text{in}} \pm d_g \frac{y_{\text{out}} - y_{\text{in}}}{z_{\text{out}} - z_{\text{in}}}\right) \\ z = \frac{1}{2}\left(z_{\text{out}} + z_{\text{in}} \pm d_g\right) \end{cases} \tag{4.7}$$

for the front and back plane, and

$$\begin{cases} x = x_c \pm \frac{1}{2}(1 - d_c)g \\ y = y_{\text{in}} + \frac{y_{\text{out}} - y_{\text{in}}}{x_{\text{out}} - x_{\text{in}}}\left(x_c - x_{\text{in}} \pm \frac{1}{2}(1 - d_c)g\right) \\ z = z_{\text{in}} + \frac{z_{\text{out}} - z_{\text{in}}}{x_{\text{out}} - x_{\text{in}}}\left(x_c - x_{\text{in}} \pm \frac{1}{2}(1 - d_c)g\right) \end{cases} \tag{4.8}$$

for the side planes. As such, the intersection points with the grating bar can be calculated directly from Eq. (4.7) and Eq. (4.8), based on the six virtual grating output parameters (x_{out}, x_{in}, y_{out}, y_{in}, z_{out}, z_{in}) and four user-defined values (d_c, g, x_c, d_g).

As soon as the intersection points are determined, the distance d traveled by the photon in the bar can be calculated. This distance is combined with the material- and energy-dependent attenuation coefficient μ. Subsequently, a transmission factor is calculated through application of the Lambert-Beer law.

As a side note, we mention that the transmission factor calculation depicted in Fig. 4.3 can be generalized to gratings where the apertures are not gaps but consist of a different material than the grating bars. Instead of assigning 1 to the class-A photons, the Lambert-Beer law can be applied with the corresponding attenuation coefficient. In the same way, the presence of a grating substrate can be taken into account.

4.3 Experiments

To verify and demonstrate the proposed simulation approach, a series of test simulations is performed. In Section 4.3.1, validation tests are presented that allow a comparison of simulation results obtained from equivalent explicit and virtual grating simulations in GATE. In addition, in Section 4.3.2, a simulation is defined that demonstrates the formation of a 2D-image using virtual gratings. Finally, in Section 4.3.3, a simulation to demonstrate the effect of sample mask misalignment is presented. Simulations are performed in GATE assuming a Gaussian, polychromatic 40 kV source with 50 μm focal spot size (full width at half maximum). For all simulations, the source to detector distance (SDD) is fixed at 1800 mm, with a sample mask magnification of 3/2. The object, if present, is placed directly behind the sample mask. All simulations were performed in air (world material) and unless stated otherwise, the following physics processes were included in the simulation: `PhotoElectric`, `Compton`, `RayleighScattering`, `XrayRefraction`, `ElectronIonisation`, `Bremsstrahlung`, `eMultiple-Scattering`.

4.3.1 Validation tests

To validate the results produced with the virtual grating approach, equivalent simulations with explicit gratings are performed. Equivalent means that the exact same geometry is constructed, with the only difference being the definition of the gratings as either explicit or virtual gratings. As the goal is to demonstrate that the virtual grating approach provides a good approximation to the explicit grating approach, the explicit grating results act as the ground truth. The implications of the virtual grating approximation will be discussed in more detail in Section 4.5.

Two test cases are presented. First, a comparison between a virtual and explicit sample mask is made at the level of the beamlet profiles. Thus, only a single grating is present in the simulated geometry. To make the comparison, the beamlet profiles are sampled at the detector with 1 μm pixels. A fan beam geometry is used to generate 1D detector profiles with 14 beamlets, spanning 2100 pixels, for which 10^7 photons are simulated. The gratings are defined as 220 μm thick gold gratings with a projected pitch of 150 μm. Given the magnification of 3/2, this results in a sample mask pitch of 100 μm, whereas the aperture size is 20 μm. In addition, a test is performed with both sample and detector mask in place. Here, sample mask parameters are identical to the first test case. The goal of this test is to perform a comparison at the level of the ICs, being the actual measurements in EI experiments. To ensure a good sampling of the IC, stepping is performed with the sample mask in 15 steps of 3 μm. For the explicit grating approach, this means 15 MC simulations are performed with 10^7 photons each, again considering 14 beamlets. As the comparison is now performed at the IC level, the pixel size is increased to 150 μm, such that each beamlet corresponds to one pixel. The detector mask has a pitch of 149.75 μm, since it is placed right in front of the detector, and an aperture size of 32 μm. It should be noted that there is no need for a new virtual grating simulation for this test, as the flexibility of the approach includes neglecting the presence of one of the two, er even both, gratings. Changing the pixel size can, as mentioned earlier, also be done post-simulation.

4.3.2 2D image simulation with virtual gratings

To demonstrate XPCI simulations with a virtual grating approach, AC, DPC, and DFC images of a beryllium sphere are simulated. The sphere has a diameter of 7 mm, and the contrasts are extracted from the sampled ICs by means of a Gaussian fit (Eq. (2.70)). In the MC simulation, the 101×101 pixels detector is illuminated by 10^8 photons. The pixel size is set to 150 μm, whereas the grating parameters are identical to those in Section 4.3.1. A flat field simulation without sphere is performed with the same simulation parameters. Stepping of the sample mask to generate the IC is done post-simulation, using the virtual grating output.

4.3.3 Simulation of sample mask misalignment

An important aspect of designing and building an EI setup is the matching and alignment of the two gratings (Doherty et al., 2020; Shoukroun et al., 2022a). Using the same virtual grating simulation output as in Section 4.3.2, we demonstrate the effect of a misalignment between sample mask and detector mask. To this end, the z-shift of the sample mask is varied in the flat field simulation results. The variation is performed in the range of ± 5 mm shift with respect to the optimal position.

4.4 Results

4.4.1 Validation tests

In Fig. 4.6, the beamlet profiles resulting from the virtual and explicit grating simulations are plotted together. As is clear from the plots, there is a very strong agreement between the profiles generated with either method in the valleys between adjacent beamlets, where the impact of the grating bars on the profiles is mostly present. As refraction by grating bars is not taken into account in the case of virtual gratings, an explicit grating simulation without refraction in the grating bars (labeled NR in the plot) is included for further comparison. We refer to Section 4.5 for a more elaborate discussion.

Fig. 4.7 shows a comparison of ICs resulting from virtual and explicit grating simulations. To avoid cluttering and redundancy, plots are shown for just two different pixels, which we will denote pixel 1 and pixel 8. Pixel 1 corresponds to the first beamlet in Fig. 4.6, starting from the left. Accordingly, pixel 8 corresponds to the eighth beamlet and is therefore located closest to the center of the profile. From these plots, it is clear that also for the case of two gratings the virtual grating results are consistent with the explicit grating results. Both the sampled points and the fitted Gaussians show a good agreement. Altogether, the plots from Fig. 4.6 and Fig. 4.7 indicate that the virtual grating approach provides a valid approximation for the explicit grating approach. Further considerations are provided in Section 4.5.

By using virtual gratings, the total computation time can be reduced significantly while yielding highly similar results. The advantage grows fast when the size of the parameter study increases, leading to time reductions of easily one or two orders of magnitude. This is illustrated in the right panel of Fig. 4.7, where the total computation time is plotted for an increasing number of parameter variations (grating translations). The GATE simulations are much more expensive (750 s each) compared to the post-simulation parameter iterations (1.3 s each). Hence, the total time needed for the post-simulation virtual grating iterations increases slowly, appearing almost constant in the plot.

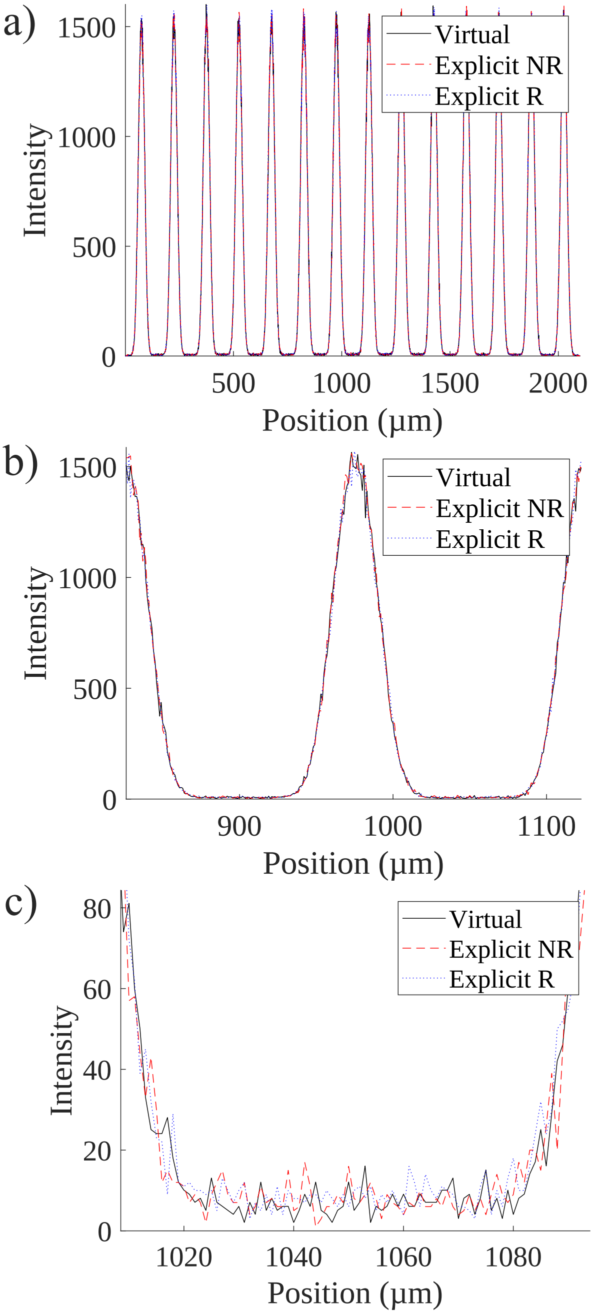

Figure 4.6: Comparison of simulated virtual and explicit grating beamlet profiles. a) Plot showing all 14 beamlets. b) Zoom on a single beamlet. c) Zoom on the valley between adjacent beamlets.

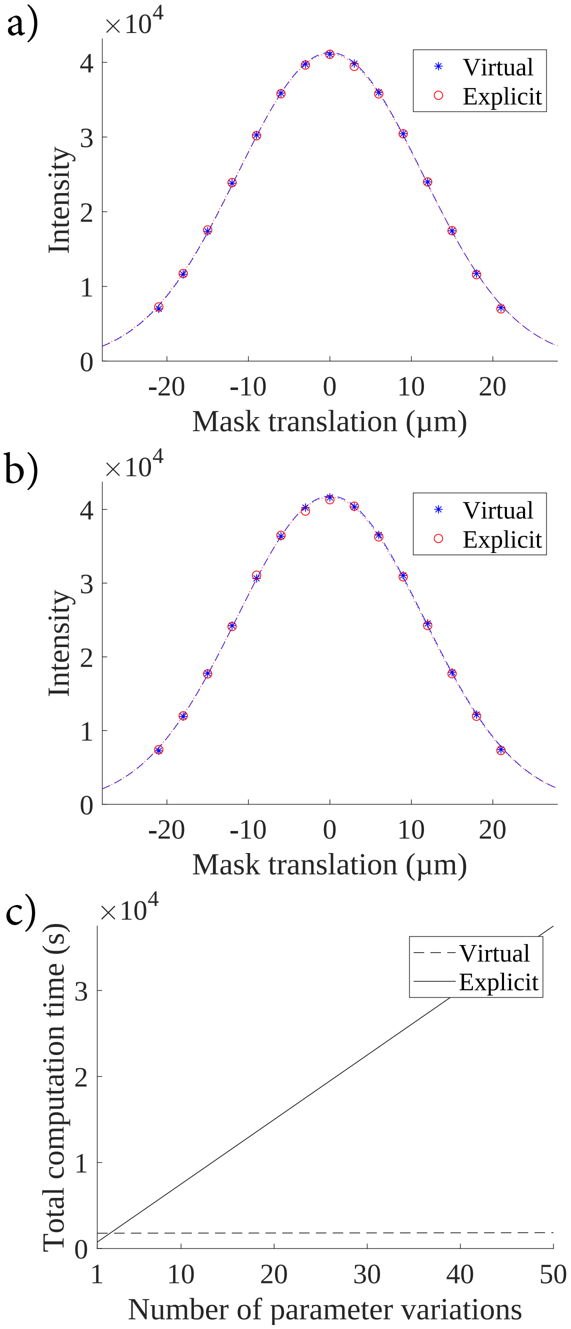

Figure 4.7: Comparison of simulated virtual and explicit grating ICs, including Gaussian fit. a) ICs for pixel 1. b) ICs for pixel 8. c) Total computation time for an increasing number of parameter (grating translation) variations.

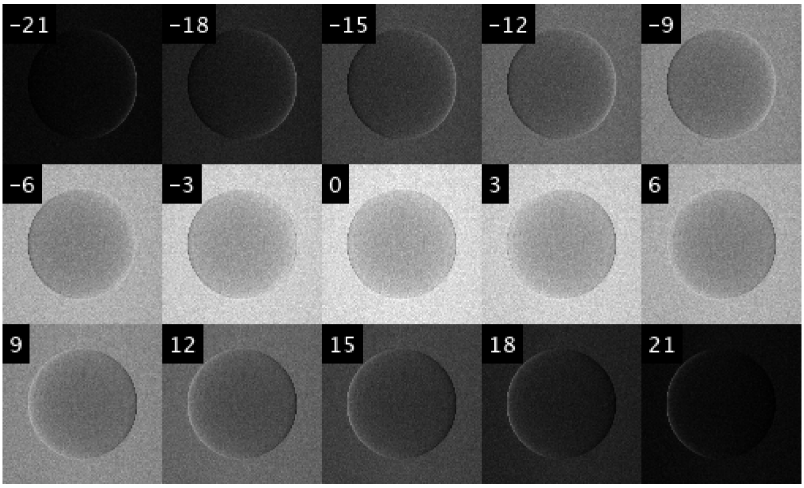

Figure 4.8: Images generated by virtual stepping of the sample mask. The values in the image corners are grating shifts expressed in μm. Color scale bars are omitted due to the qualitative nature of the discussion in the main text.

4.4.2 2D image simulation with virtual gratings

The 15 images generated by virtual stepping of the sample mask, with the beryllium sphere in place, are shown in Fig. 4.8. As expected, the overall intensity decreases with increasing misalignment between the two gratings. From these images, an IC can be constructed for every image pixel, on which a Gaussian fit is performed. Applying Eq. (2.71), Eq. (2.72), and Eq. (2.73) results in the separation of transmission, DPC and DFC. The result, after calculating AC from the transmission, is shown in Fig. 4.9. All three contrasts adhere to the expectations, with clear AC and DPC signals, and DFC only showing up at the object edges.

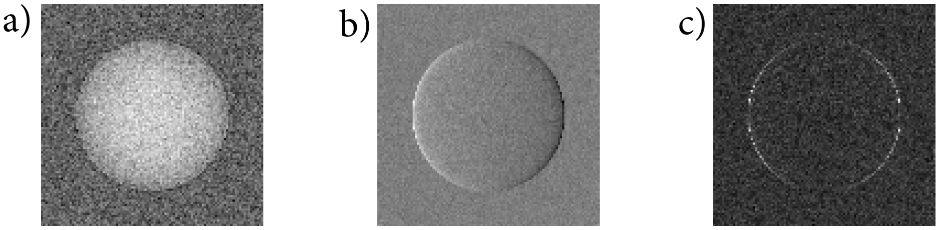

Figure 4.9: a) AC, b) DPC, and c) DFC images extracted from the mask stepping images shown in Fig. 4.8. Color scale bars are omitted due to the qualitative nature of the discussion in the main text.

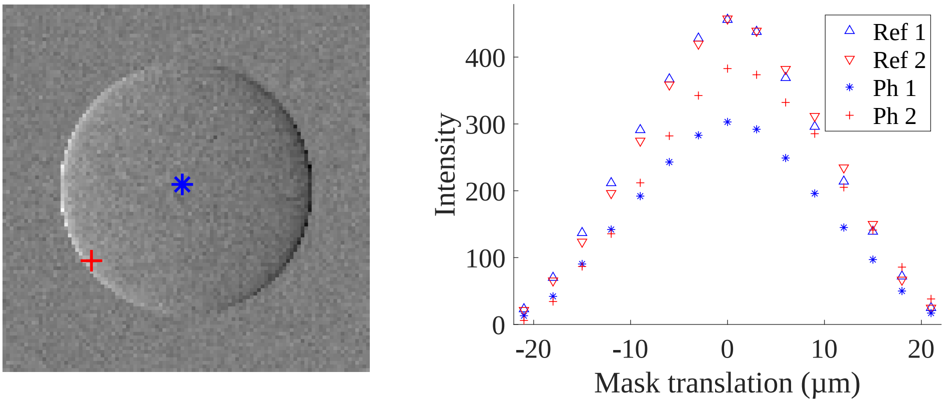

Figure 4.10: ICs extracted from the images shown in Fig. 4.8 (markers Ph 1 and Ph 2), with the location of the respective pixels indicated on the DPC image in the left panel, using the same markers. The ICs of the corresponding flat field pixels are indicated with markers Ref 1 and Ref 2.

In Fig. 4.10, two ICs are plotted, corresponding to different locations within the projected object. The IC corresponding to the pixel closer to the edge has clearly shifted due to refraction, whereas the IC in the center of the object has lowered more due to stronger attenuation.

4.4.3 Simulation of sample mask misalignment

In Fig. 4.11, the flat field intensity distribution resulting from a varying amount of sample mask misalignment is shown for 21 cases, with a z-shift ranging between -5 mm and +5 mm relative to the optimal position. The position of the sample mask along the x-axis corresponds to the maximum of the IC. An increasing reduction in intensity towards the image edges is visible, as the detector mask partially blocks the incoming beamlets departing from the non-matching sample mask (Shoukroun et al., 2022a). This effect is even more apparent in Fig. 4.12, where horizontal line profiles through the images in Fig. 4.11 are plotted.

4.5 Discussion

The results in Section 4.4.1 indicate that the virtual grating approach is a valid approximation for the explicit grating approach. Almost identical results (see Fig. 4.6 and Fig. 4.7) are obtained with a strongly reduced total computation time. A single MC simulation was sufficient to generate the virtual grating beamlet profiles and ICs, as all grating parameters were defined post-simulation. With respect to the simulation time, it should be

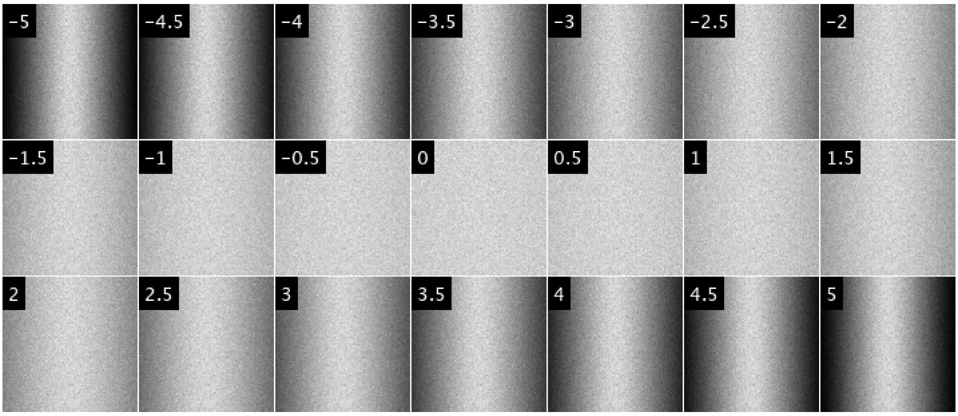

Figure 4.11: Overview of the effect of increasing misalignment between the sample and detector masks. The values in the image corners are sample mask z-shifts relative to the optimal position, expressed in mm. Color scale bars are omitted due to the qualitative nature of the discussion in the main text.

noted that a further speed-up can be achieved in GATE by splitting the simulation over multiple CPUs. This has not been discussed here, as the speed-up would be the same for explicit and virtual grating simulations, leading to the same conclusion regarding the relative simulation time reduction. Alternatively, variance reduction techniques are sometimes implemented to achieve a reduced simulation time (Tessarini et al., 2022).

In Fig. 4.8 it is demonstrated how the proposed approach adequately captures the effect of the two gratings on the final image, resulting in the successful retrieval of the different contrast types, shown in Fig. 4.9. The fact that these contrast types result from local changes in the IC is illustrated by Fig. 4.10. A comparison between the contrast images retrieved from the virtual gratings and the contrast images retrieved from the corresponding explicit gratings simulation is provided in Appendix C. In addition, the effect of poor grating alignment was demonstrated using the same virtual grating MC output, introducing variations in the position of the sample mask along the z-axis. Fig. 4.11 and Fig. 4.12 clearly show how the beamlets generated by the sample mask drift further away from the detector mask apertures if the misalignment increases. This illustrates the relevance of accurate grating alignment for EI. The advantage of a well-aligned system is that the more homogeneous background signal allows for phase retrieval with a minimal number of IC points. In contrast, a system with more misalignment can still be used for phase contrast imaging, but requires more mask steps to ensure proper sampling of the IC everywhere in the FOV.

The virtual grating approach provides a high level of flexibility with respect to post-simulation grating design. Obviously, other setup parameter variations cannot be taken into account with virtual gratings. Changing the SDD of the setup in GATE, for example,

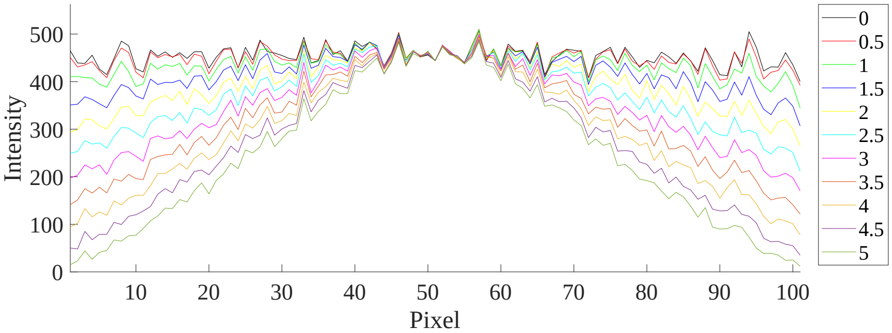

Figure 4.12: Line profiles taken from the images shown in Fig. 4.11, showing the increasing intensity reduction towards the edges of the images due to the misaligned sample mask position. The values in the legend are z-shifts relative to the optimal position, expressed in mm.

will always require a new simulation, as the photon trajectories are different. Likewise, for a dithering procedure, the photon trajectories inside the phantom change. In general, the virtual grating approach models variations in grating parameters, but not in phantom, source and detector properties.

In the proposed approach, the grating bars are essentially modeled as purely absorbing 3D objects, where the absorption is calculated from attenuation coefficients through the Lambert-Beer law. Whereas this is obviously an approximation compared to a full MC grating bar model that includes explicit scattering events and refraction (Sanctorum et al., 2021a; Huyge et al., 2021), it provides a more accurate grating representation than the often-used projection approximation (i.e. infinitely thin gratings). This is illustrated in Fig. 4.13, where a comparison is made between detector profiles simulated with virtual gratings, explicit gratings and the projection approximation. The simulated setup corresponds to the two-mask setup presented in Section 4.3.1, but with a larger detector. Shadowing effects that increase towards the detector edges are visible when 3D grating models are used (Huyge et al., 2021). This shadowing effect is also known as angular filtration, and is taken into account in our model but not in the projection approximation.

As scaling up the technology is an important goal for future EI applications (Olivo, 2021), simulation requirements are expected to shift more towards cone beam systems with a larger field of view. As such, angular filtration becomes an increasingly important effect, implying the thickness of the gratings must be taken into account. Therefore, infinitely thin grating models will most likely become insufficient for future grating design studies, since these will require 3D grating models. The increased relevance of 3D grating models in future MC simulations for EI illustrates the potential of the virtual grating approach.

To demonstrate that the residual difference between virtual and explicit grating models is primarily due to refraction effects, an additional profile is plotted that results from purely

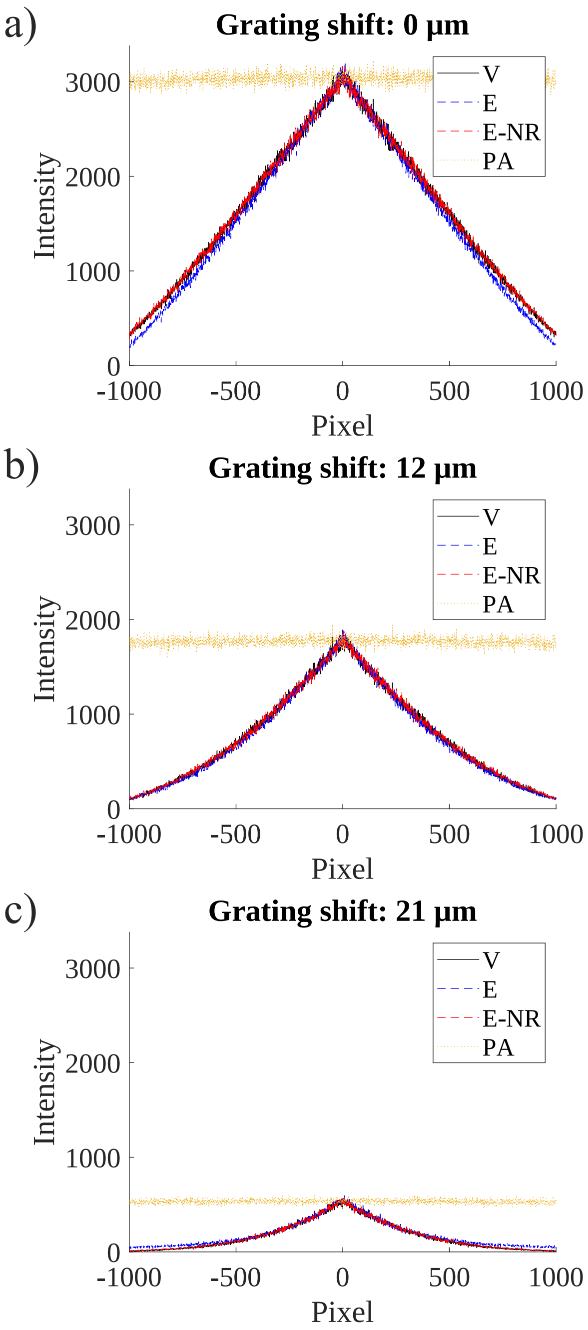

Figure 4.13: Comparison of simulated detector profiles for different mask stepping positions. A shift of 0 μm corresponds to perfectly aligned gratings. V: virtual gratings. E: explicit gratings. E-NR: explicit gratings without bar refraction. PA: projection approximation.

absorbing explicit gratings, which neither refract nor reflect the X-ray photons. This profile is practically identical to the virtual grating profile, indicating that the differences are indeed due to refraction in the grating bars. The goal of the proposed approach is thus not to give an as detailed as possible modeling of all possible photon interactions in the grating bars, but to provide a balanced trade-off between simulation detail and total simulation time. This is achieved by including the predominant grating bar effect, being attenuation of the polychromatic photon beam. This ensures that effects such as beam hardening due to residual grating bar transmission are taken into account (Endrizzi and Olivo, 2014).

As indicated by the increased number of output variables in the ROOT output, the increased flexibility of the virtual grating approach comes at the cost of increased output file sizes. The twelve additional variables are stored with double precision, implying that for every 10^6 detected photons the file size increases with 96 MB. To keep the file size reasonable for very large simulations with very high numbers of simulated photons, several modifications to the current implementation can be considered. The most obvious modification would arguably be storing variables with single precision, hereby lowering the additional file size by 50%. In addition, if the virtual volume is defined as a box with planes parallel to the detector plane, all photons will enter and leave the virtual volume at the same z-coordinates. Here, it is assumed that the box is large enough such that it is unlikely for photons to enter or leave through planes other than the front and back planes. If this is the case, all photons share their z-coordinates, meaning those need to be stored only once. This would reduce the additional file size by another 33%. However, if the virtual volumes defined by the user are not box-shaped, this is not always possible. Finally, it can be considered to reduce the number of output variables in the ROOT output itself, as there may be output variables that the user does not need for their application. The reduction in file size would then depend on the number of variables which is removed from the output.

It should be noted that, since the same MC simulation is used for the generation of various images with different grating parameters, all the images generated from this MC simulation will exhibit highly similar photon statistics. Therefore, if a sufficient amount of photons is generated in the virtual grating simulation, this will immediately keep the noise low for all parameter variations. The similarity in noise properties is apparent from Fig. 4.12. Finally, although not explicitly demonstrated in this work, we stress that the virtual grating approach is applicable beyond rectangular grating designs. It can be applied to less conventional, non-rectangular grating configurations as well, as long as intersection points between photon trajectories and grating components can be calculated in either an analytical or numerical way.

4.6 Conclusion

An alternative simulation approach was proposed to reduce the computation time in full MC XPCI simulations with varying grating parameters. To this end, the concept of virtual grating volumes was introduced. By allowing the definition of grating parameters post-simulation, the amount of required MC simulations for a parameter study, and therefore the total computation time, can be reduced significantly. The results presented in this chapter show the feasibility of adopting the proposed virtual grating approach to reduce the total simulation time, especially when many variations of grating parameters (pitch, aperture, thickness) and position are required. It should be noted that, whilst using GATE for our MC simulations, the presented concepts are generic and therefore applicable in any MC environment for XPCI simulations. We believe that this simulation approach has the potential to facilitate the design of future EI systems, hereby supporting the propagation of XPCI as a standard imaging method.

Acknowledgments

The research presented in this chapter was financially supported by the Research Foundation - Flanders (FWO) through grant numbers S003421N (FoodPhase), G094320N, and G090020N as well as the EU Interreg Flanders - Netherlands Smart*Light (0386) project.

Chapter 5

Grating design for augmenting a conventional X-ray scanner with EI

This chapter is published as:

- Sanctorum, J., Six, N., Sijbers, J., and De Beenhouwer, J. (2022b). Augmenting a conventional x-ray scanner with edge illumination-based phase contrast imaging: how to design the gratings. In Müller, B. and Wang, G., editors, *Proc. SPIE 12242, Developments in X-Ray Tomography XIV*, page 1224218. SPIE

5.1 Introduction

Edge illumination has been successfully transferred from synchrotron facilities to lab-based X-ray systems (Zamir et al., 2017; Olivo, 2021) and is a valuable tool for non-destructive testing (Shoukroun et al., 2022b), security (Olivo et al., 2009) and biomedical imaging (Massimi et al., 2022). Existing EI imaging systems are typically custom-made setups, with components carefully selected to achieve optimal imaging conditions. However, if a conventional X-ray micro-CT scanner is already available, it is worthwhile considering augmenting it with phase contrast imaging functionalities, instead of complementing it with a separate EI imaging system. Therefore, rather than installing a dedicated EI XPCI system, our goal is to enable XPCI in an existing, custom-built, TESCAN UniTOM XL system at the University of Antwerp, FleXCT, which is a novel and highly flexible scanning system consisting of ten motorized axes, allowing a wide range of non-standard scans such as tiled and off-center scans, conveyor belt, laminography, dynamic zooming, and helical tomography (De Samber et al., 2021). To enable EI-based X-ray phase contrast imaging, two gratings have to be incorporated in the existing FleXCT system. Although many system properties have been shown to influence the EI image quality (Olivo et al., 2009), these are not necessarily free parameters in our case. Indeed, the fact that the EI components are to be installed in an already existing setup, limits the range of modifications to the CT-scanner that can still be considered reasonable (e.g. source and detector are already installed and the system size is fixed). As such, the two EI gratings are the most essential pieces of experimental equipment that have to be designed. The design parameters of these gratings, mainly the pitch, duty cycle and material thickness, impact the achievable image quality. Thus, a dedicated parameter study is carried out to determine optimal parameters for the new gratings, relying on MC XPCI simulations (Sanctorum et al., 2020). In this Chapter, we report on the methodology and results of the parameter study. The effective experimental realization of the augmented FleXCT-scanner using the gratings designed in this Chapter will be reported elsewhere (Huyge et al., 2023b). The presented procedure is transferable to other attenuation-based CT-systems and its use is therefore not limited to the FleXCT system. To our best knowledge, this is the first demonstration of grating design for augmentation of an existing X-ray scanner with EI-based XPCI.

5.2 Methods

During the simulation phase, experimental parameters such as the system geometry and focal spot are taken into account. The tube voltage and geometrical magnification are set based on the envisaged applications, which is mainly the imaging of fruits for quality control, including apples, pears, and tomatoes. Therefore, the goal is to achieve a phase sensitive field of view within the FleXCT system of approximately 10-by-10 cm^2 in the object plane, with a system magnification of 1.5 and a 80 kV tube voltage to ensure sufficient X-ray transmission through the typically 5 to 10 cm thick pieces of fruit that mainly consist of water. The optimization of the design parameters is based on maximizing peak-to-peak contrast in the phase contrast signal and finding a trade-off between grating bar transmission and shadowing effects (angular filtration). The peak-to-peak contrast is given by the difference between the positive and negative peak values in the DPC signal. By dividing this by the standard deviation of the background DPC signal, the peak-to-peak contrast-to-noise ratio (p2p-CNR) is defined as:

$$\mathrm{CNR} = \frac{\alpha_{max} - \alpha_{min}}{\sigma_\alpha}. \tag{5.1}$$

Shadowing effects arise when a cone beam illuminates a pair of rectangular gratings and are more severe towards the detector edges (Huyge et al., 2021). In the following sections, design values for the pitch, aperture, and thickness parameters which are considered optimal for the FleXCT system will be determined for both gratings.

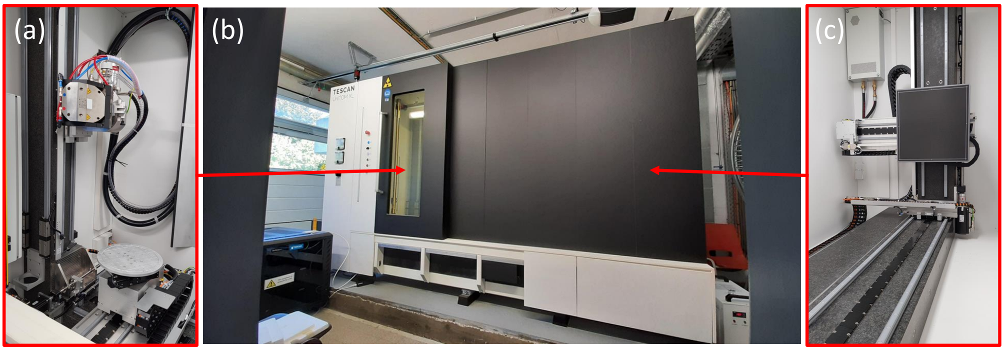

Figure 5.1: The FleXCT micro-CT scanner installed at imec-Vision Lab at the University of Antwerp (b). The side panels show (a) the X-ray source and sample rotation stage, and (c) the flat panel detector. Image courtesy by Joaquim Sanctorum.

5.2.1 Monte Carlo simulations

Simulations were performed in order to determine the optimal parameters of the gratings required for EI-based XPCI. More specifically, the parameter study is based on MC simulations, for which our in-house modified version of GATE (Jan et al., 2011; Sanctorum et al., 2020) is used. Although originally intended for combination with wave optics to enable XPCI simulations of grating-based interferometry, the full MC simulation of EI experiments using our GATE-based tool is possible as well (Huyge et al., 2021; Sanctorum et al., 2021a). In the MC framework, the standard approach is to model grating bars as 3D objects in the simulation, with energy-dependent attenuation properties following from the material. In this Chapter, the virtual grating approach (Sanctorum et al., 2022b) is used to impose grating parameter variations post-simulation, which reduces the total simulation time.

5.2.2 The FleXCT system

The designed EI gratings are to be incorporated in the FleXCT micro-CT scanner (De Samber et al., 2021), a customized UniTOM XL model from TESCAN (see Fig. 5.1 and Fig. 5.2). This highly flexible system allows a wide range of non-standard XCT scans such as tiled and off-center scans, laminography, helical tomography, conveyor belt, and dynamic zooming. Its ten motorized axes enable movement of sample, source, and detector. Additionally, the ‘FlexRayTools’ software (De Samber et al., 2021) was written to enable the reconstruction of the non-standard XCT projection data using the ASTRA Toolbox, a highly efficient and open source set of tools for tomographic projection and reconstruction (Palenstijn et al., 2011; van Aarle et al., 2015, 2016). After successful installation of the gratings (illustrated in Fig. 5.3), the FleXCT system will also facilitate XPCI imaging, including dark field contrast.

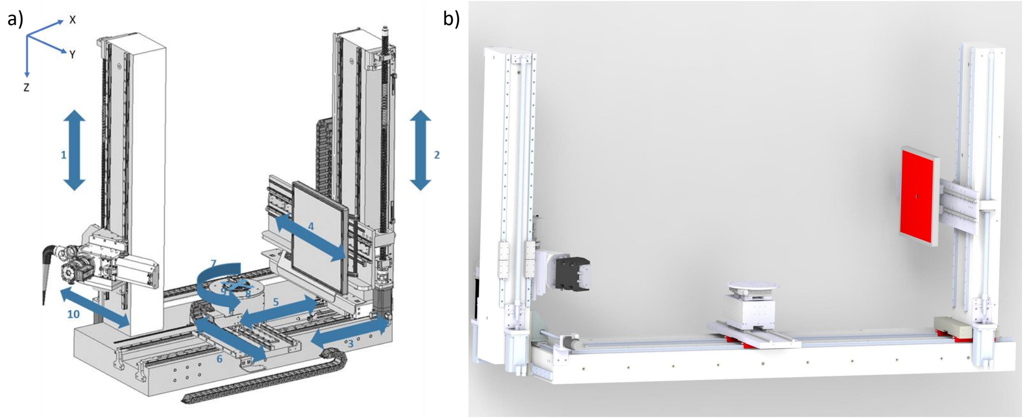

Figure 5.2: a) Schematic overview of the FleXCT micro-CT scanner, showing the ten degrees of freedom. b) Digital twin of the FleXCT system. Image courtesy by Joaquim Sanctorum and Pieter-Jan Vanthienen, respectively.

5.3 Experiments

5.3.1 System geometry

Although the FleXCT system has a variable source-to-detector distance (SDD) and geometrical magnification, a choice has to be made prior to the optimization of the grating parameters, as the gratings are designed for a specific magnification. Therefore, the SDD remains fixed at 1800 mm in the simulations, with a sample mask magnification of 3/2. Our goal is to achieve a phase sensitive area in the sample mask plane of approximately 100 mm by 100 mm. The focal spot of the simulated 80 kV polychromatic X-ray source (Nazemi et al., 2021) is varied in size and four different spot sizes are considered: 5 μm, 20 μm, 50 μm, and 85 μm. These values correspond to the full width at half maximum (FWHM) of a Gaussian focal spot. Due to the fact that an EI system is only phase sensitive in the direction perpendicular to the grating bars, the simulations are performed using a 1D line detector for the sake of simulation efficiency. This 1D detector consists of 101 pixels with a pixel size of 150 μm. The detector itself is constructed in GATE from 208 μm thick Gadox, preceded by a 750 μm thick carbon layer and a 250 μm thick plastic layer. In addition, 200 μm amorphous silicon is introduced behind the Gadox layer. The detector electronics were not modeled in GATE to avoid erroneous assumptions with respect to their effects on the image.

5.3.2 Simulation

A beryllium cylinder with a diameter of 6.9 mm is used as a phantom in the simulations. Sample mask apertures in the range of 5 to 50 μm are considered, whereas for

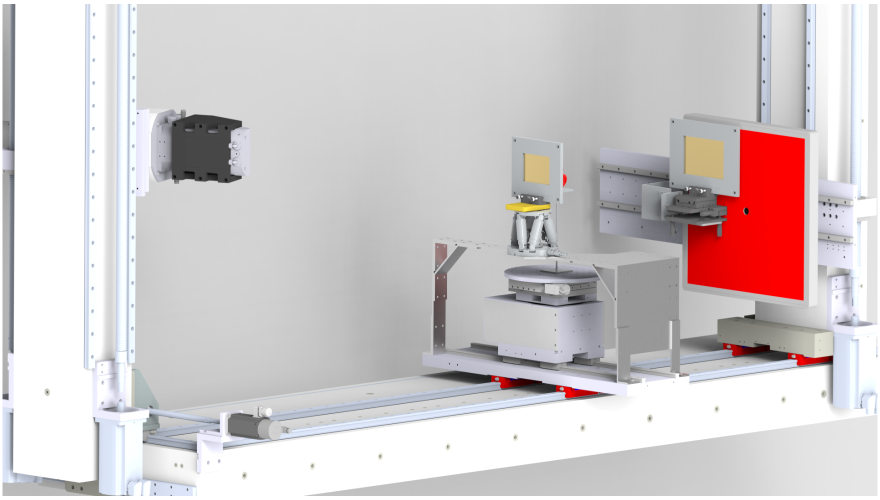

Figure 5.3: Illustration of the augmented FleXCT system after installation of the gratings for EI XPCI. Image courtesy by Pieter-Jan Vanthienen.

each sample mask aperture three distinct detector mask aperture sizes are simulated, corresponding to 1.5, 1.6, or 1.7 times the sample mask aperture. Seven phase steps are performed to sample the IC, in combination with three dithering steps. In total, this results in 15456 generated profiles, including 3864 flat field profiles. The thickness of the gold grating bars is determined through a trade-off between grating bar transmission and grating bar shadowing (angular filtration), for which a separate set of MC simulations is performed. In these simulations, the bar thickness is varied between 150 μm and 350 μm, and different levels of Al filtration are considered.

5.4 Results and discussion

5.4.1 Shadowing and grating bar transmission

Fig. 5.4 shows the transmission through the grating bar material for an increasing gold layer thickness and different effective spectra, resulting from filtration by 0.5 mm, 1.0 mm and 2.0 mm of aluminum. Ideally, the transmission should be below 1%, although 5% is an acceptable level of transmission for EI systems (Olivo et al., 2009). The plot indicates that, for the envisaged tube voltage of 80 kV, a gold bar thickness greater than 200 μm is required to satisfy this condition. By increasing the thickness further to 350 μm, the ideal 1% transmission level comes within reach. Such a large grating thickness, however, introduces a significant amount of shadowing towards the detector edges, as is clear from the line profiles in Fig. 5.4. In this figure, detector line profiles are shown for increasing grating bar thicknesses. As a reference, an additional line profile (P) is plotted, resulting from idealized gratings under the projection approximation, which are

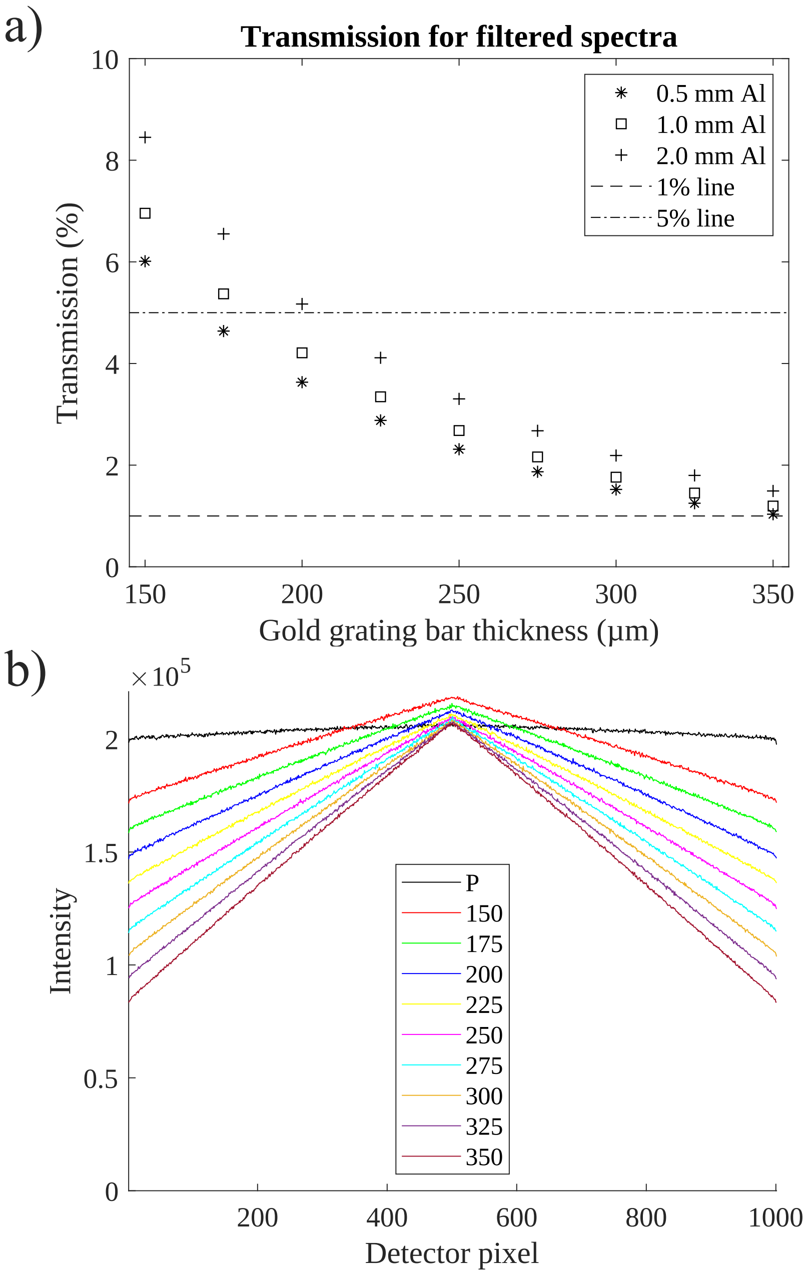

Figure 5.4: a) Grating bar transmission levels. b) Line profiles for different grating bar thicknesses, legend expressed in μm. The profile resulting from a perfectly absorbing and perfectly flat grating is indicated by P.

infinitesimally thin and perfectly absorbing. From comparison to this reference profile, it is clear that thinner gratings, although resulting in less shadowing, allow more transmission through the grating bars. Hence, there is a trade-off between transmission and shadowing effects. To quantify the amount of shadowing introduced by the grating bars, the ratio between the intensity at the profile edge and the intensity in the center (no shadowing) is determined and plotted in Fig. 5.5. In order to limit shadowing as much as possible while keeping transmission well below the critical 5% level, the optimal thickness of the gold bars is estimated to be 225 μm. This corresponds to an intensity ratio of 65.7%.

5.4.2 Grating aperture size and CNR analysis

As the grating pitches are defined by the SDD and geometrical magnification, the only parameters left to determine are the duty cycles, i.e. the aperture sizes. Given the SDD of 1800 mm, pixel size of 150 μm, and magnification of 1.5, the sample mask pitch must be 100 μm. As the detector mask cannot be put at the exact same position as the detector panel, the pitch should be slightly less than the pixel size and was set to 148 μm. To perform the aperture size optimization, the differential phase in each pixel is retrieved through Gaussian fitting of the sampled IC points. Subsequently, the peak-to-peak contrast is extracted from the resulting profiles and compared to the background fluctuations to yield the contrast-to-noise ratio (p2p-CNR). The results of this operation are shown in Fig. 5.5 for sample mask aperture values in the range of 5 to 50 μm and a detector mask to sample mask aperture ratio of 1.5. It should be noted that the same amount of photons was simulated for every focal spot. In an actual experiment, however, the focal spot size would determine the flux: larger focal spots tend to yield a higher flux. By simulating the same amount of photons, we effectively remove this effect from the plot in Fig. 5.5.

The optimal p2p-CNR value is reached at different aperture sizes, depending on the focal spot. However, in practice, some focal spot sizes are more relevant than others. The 5 μm focal spot is close to the smallest focal spot size achievable with the FleXCT system. In EI, however, the majority of the X-rays will be blocked by the gratings. Therefore, the flux generated at the source has to be sufficiently large in order to keep acquisition times reasonable. As such, it is unlikely that the 5 μm spot will be used often in practice. In contrast, a spot size around 50 μm is expected to be much more suitable. When the flux has to be maximized, this can be increased to 85 μm, or reduced to 20 μm if less focal spot blur is desirable, though it has been shown that the point spread function (PSF) of the DPC signal depends mainly on the aperture size, as long as that size is smaller than the focal spot blur (Diemoz et al., 2015). In line with these practical considerations, the optimal sample mask aperture is deduced from the 50 μm focal spot curve in Fig. 5.5, where the maximal p2p-CNR is reached around 20 μm. As this value is also close to optimal for the 20 μm spot and still yields 80% of the maximum p2p-CNR for the 85 μm focal spot, a 20 μm aperture is considered to be the best candidate for the optimal sample

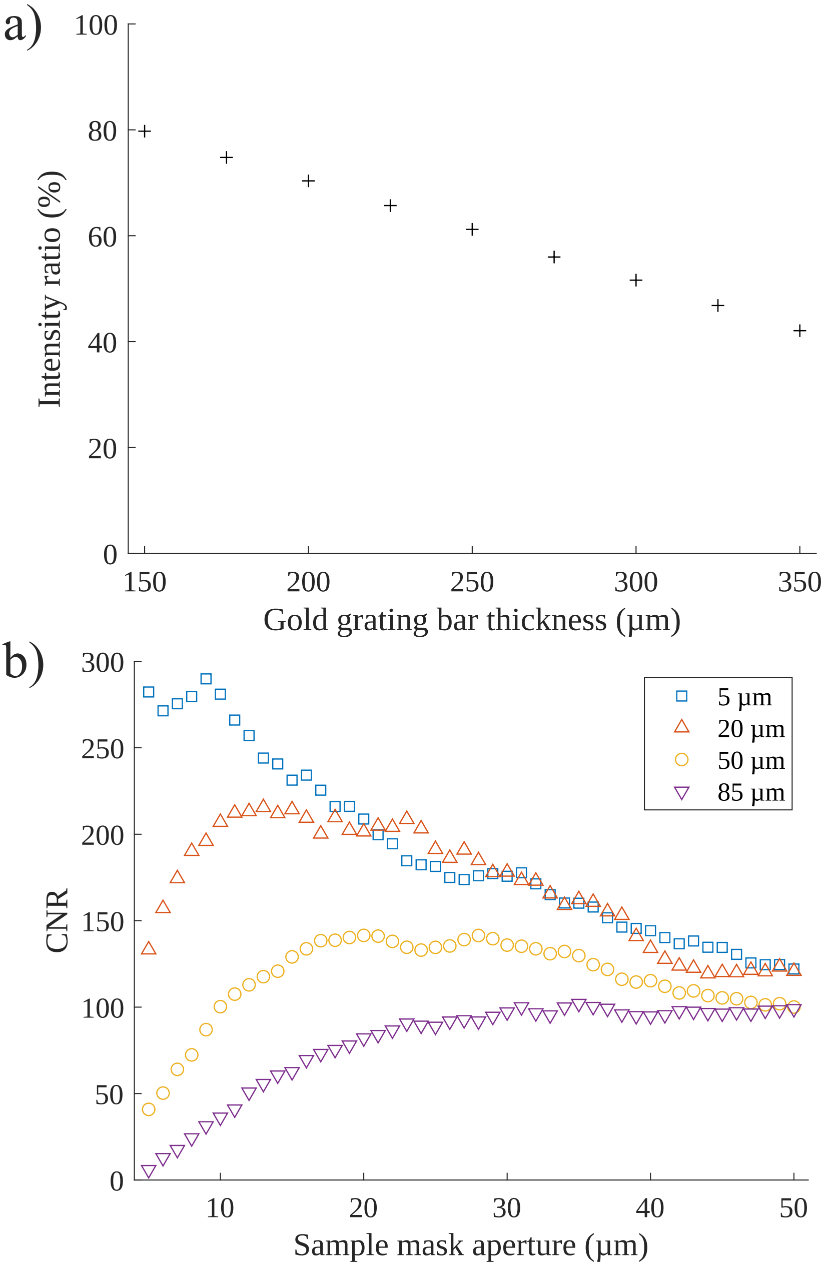

Figure 5.5: a) Intensity ratio between edge and center pixels. b) peak-to-peak CNR extracted from the retrieved DPC for different focal spot sizes.

mask design. Although not shown, no significant p2p-CNR gain could be perceived by increasing the aperture size ratio to 1.6 and 1.7. This ratio was ultimately kept at 1.5, corresponding to a 30 μm aperture size for the detector mask. In this work, the p2p-CNR was chosen as the metric for optimizing the aperture size, due to the characteristic refraction peaks present in cylinder profiles. Other possible metrics include the angular sensitivity (Diemoz et al., 2015) and the accuracy (Astolfo et al., 2016) (Chapter 6). It should be noted that it is implicitly assumed that the geometrical optics approximation is valid for the MC simulations performed in this Chapter. However, given that the spatial resolution in EI is determined by the aperture size for fully dithered images, some caution is required when interpreting results for the smallest focal spot (5 μm) and smaller apertures (below approximately 10 μm), considering the weighted mean energy of the 80 kV spectrum (38.4 keV), as diffraction effects will become increasingly important at higher spatial resolution (see also Section 6.2.2).

5.5 Conclusion

In this Chapter, we have presented the design of EI gratings for the augmentation of the FleXCT system to a phase sensitive X-ray scanner. Through peak-to-peak contrast analysis of simulated profiles, optimal aperture sizes for sample and detector mask were deduced. In the final grating design, the sample mask has a pitch of 100 μm and aperture of 20 μm, whereas the detector mask has a pitch and aperture size of 148 μm and 30 μm, respectively. Additionally, the material thickness was determined based on a trade-off between shadowing effects and grating bar transmission. Based on this analysis, the gold bar thickness was set to 225 μm. The next important step is the integration and alignment of the newly designed components into the FleXCT system, on which we intend to report in future work. The steps undertaken in this work are not specific to the FleXCT system, and are applicable to support the augmentation of any X-ray scanner with EI-based XPCI.

Acknowledgments

The contents presented in this Chapter are the result of a collaboration between J. Sanctorum and N. Six, under supervision of J. Sijbers and J. de Beenhouwer. J. Sanctorum designed and performed the simulations, and N. Six performed the p2p-CNR analysis on the simulated intensity profiles. N. Six received a PhD fellowship from the FWO (11D8319N). This research was also supported by EU Interreg Flanders - Netherlands Smart*Light (0386), Research Foundation - Flanders (FWO) (G090020N, G094320N, S003421N), and Agentschap Innoveren & Ondernemen (Vlaio) (HBC.2020.2159). We wish to express our gratitude towards prof. dr. Alessandro Olivo from University College London (UK) for valuable feedback on the simulation results.

Chapter 6

Multi-contrast benchmarking of edge illumination simulations

This chapter is published as:

- Sanctorum, J., Sijbers, J., and De Beenhouwer, J. (2025). Multi-contrast benchmarking of edge illumination Monte Carlo simulations using virtual gratings. *Journal of Applied Physics*, 137(10):104904

6.1 Introduction

Whereas X-ray phase contrast imaging (XPCI) has become widely recognized for its capability to yield high contrast compared to conventional AC, DFC has been receiving increased interest in recent years due to its unique ability to provide information about unresolved microstructures (Pfeiffer et al., 2008; Endrizzi et al., 2014). The increased accessibility of XPCI using compact laboratory systems has boosted its development (Bravin et al., 2013; Endrizzi, 2018; Momose, 2020; Olivo, 2021; Quenot et al., 2022), resulting in various applications such as spectral imaging and material decomposition (Ji et al., 2020; Braig et al., 2020; Brombal et al., 2024), virtual histology (Massimi et al., 2022), and clinical dark field imaging of lungs (Urban et al., 2022). Both DPC and DFC are related to the X-ray refractive index of the object, but as opposed to DPC, DFC results from refractive index fluctuations that cannot be resolved by the imaging system (Lynch et al., 2011). This results in a local increase in angular spread of the X-ray beam (Bech et al., 2010b; Endrizzi and Olivo, 2014), referred to as angular broadening (see Section 2.3.4). DFC is becoming increasingly important and is for certain applications even more of interest than AC or DPC. The measurement of the DFC signal is traditionally performed with XPCI methods featuring special X-ray optics. Examples are analyzer based imaging (ABI) (Rigon et al., 2007), grating-based interferometry (GBI) (Pfeiffer et al., 2008), edge illumination (EI) (Endrizzi et al., 2014), beam tracking (BT) (Vittoria et al., 2014), single-grid imaging (SGI) (Wen et al., 2010) and speckle-based imaging (SBI) (Zanette et al., 2014). More recently, however, DFC imaging has been demonstrated using propagation-based imaging (PBI) as well (Gureyev et al., 2020; Leatham et al., 2023). Whereas GBI is arguably the most popular experimental configuration for DFC imaging, EI is emerging as well as a suitable DFC imaging method for lab-based setups (Matsunaga et al., 2020; Olivo, 2021). In contrast to recent developments in GBI (Yan et al., 2020; Sauter et al., 2021; Urban et al., 2022; Organista et al., 2023; Spindler et al., 2023), DFC is hardly ever explicitly considered when making design choices for multi-contrast EI systems. Indeed, most studies are predominantly oriented towards DPC, while assessment of DFC is minimal or even absent (Olivo and Speller, 2007b; Olivo et al., 2009, 2013; Diemoz et al., 2015; Havariyoun et al., 2019; Kallon et al., 2020; Sanctorum et al., 2022b; Brombal et al., 2023; Vanthienen et al., 2023). A rare exception is the work of Astolfo et al. (2016, 2017) concerning the design of a large field-of-view (FOV) EI system. It has been shown that, compared to AC and DPC, DFC is significantly more sensitive to grating imperfections and misalignment (Endrizzi et al., 2015) and is affected by polychromatic effects such as beam hardening, resulting from both the imaged object and partially transmitting grating bars (Endrizzi and Olivo, 2014; Vittoria et al., 2015). Furthermore, it has been suggested that the choice of system and grating parameters could influence the linearity of the measured DFC (Astolfo et al., 2022), which is highly relevant for tomography applications (Doherty et al., 2023).

Optimization and design of EI setups often relies on computer simulations (Olivo et al., 2009; Vittoria et al., 2013; Astolfo et al., 2016; Buchanan et al., 2020; Sanctorum et al., 2022b; Vanthienen et al., 2023). Benchmarking the simulated DFC signal originating from an arbitrary object is not trivial and is often omitted. Since the first observations of X-ray beam broadening due to microstructures (Slack, 1926), there have been many efforts in modeling this effect and relating it to unresolved sample properties (von Nardroff, 1926; Khelashvili et al., 2006; Yashiro et al., 2010; Bech et al., 2010a; Lynch et al., 2011; Malecki et al., 2012; Millard et al., 2013; Strobl, 2014; Modregger et al., 2017; Wilde and Hesselink, 2021a,b; Meyer et al., 2021; How et al., 2023; Taphorn et al., 2023; Auenhammer et al., 2024). In practice, simulation models are often simplified to reduce simulation times, for example by condensing the dark field effect in a single (linear) material parameter or by imposing an a priori scattering distribution (Rigon et al., 2007; Bech et al., 2010a; Scattarella et al., 2013; Astolfo et al., 2016; Francken et al., 2023, 2025). Another possible approach is to calibrate the linear model using experimental data (Astolfo et al., 2016), but this quickly becomes unfeasible if there is a directional dependency in the signal, due to the complicated sampling schemes involved in measuring directional DFC (Sharma et al., 2017; Huyge et al., 2023a). Amongst other methods, Monte Carlo (MC) simulators are commonly used for EI-XPCI simulations (Peter et al., 2014; Cipiccia et al., 2014; Astolfo et al., 2016; Sanctorum et al., 2022a). A balanced approach, which avoids a number of limiting assumptions, such as isotropic distributions or linearity, whilst keeping the simulation cost reasonable, is to explicitly model the microstructures in the simulation (Millard et al., 2013; Sanctorum et al., 2020; Huyge et al., 2023a). In such a MC simulation, the angular broadening is generated by the combined effect of many refraction events. The retrieved DFC will depend on the characteristics of the simulated setup and contrast retrieval algorithm (Astolfo et al., 2016, 2017). As such, in order to assess which parameters yield the most accurate result, the retrieved DFC must be benchmarked using a reference value (Scattarella et al., 2013). In general, however, such a reference value is not readily available for comparison.

In this chapter, we demonstrate an approach to simultaneously simulate the retrieved contrasts (AC, DPC and DFC) and corresponding reference values, allowing full multi-contrast benchmarking of MC simulation results. The presented method relies on the virtual grating approach from Chapter 4, which was recently developed to reduce simulation times for large parameter studies (Sanctorum et al., 2022a). We show how this method can be used for multi-contrast benchmarking of simulation results and briefly discuss both its limitations and other potential applications.

6.2 Methods

6.2.1 Finding reference values using virtual gratings

Multi-contrast reference values are required for the complete benchmarking of EI simulations, meaning the reference T, α, and σ^2 are to be determined for each X-ray beamlet. Here, σ^2 is the increase in angular variance of photon directions within a single beamlet. The angular variance is a measure for the spread in photon directions relative to the average direction in the beamlet. This is illustrated in Fig. 6.1.

If a virtual grating volume is placed at the position of the sample mask in the simulation, and a second virtual grating volume is placed at the detector mask position, the direction vectors of the photon trajectories before and after interaction with the phantom can be retrieved. Indeed, if the intersection points with the front and back planes of the virtual grating volume are written as $\mathbf{r}_{\text{in}} = (x_{\text{in}}, y_{\text{in}}, z_{\text{in}})$ and $\mathbf{r}_{\text{out}} = (x_{\text{out}}, y_{\text{out}}, z_{\text{out}})$, then the direction vector for a given photon m is $\mathbf{r}_{\text{d},m} = (x_{\text{d},m}, y_{\text{d},m}, z_{\text{d},m}) = \mathbf{r}_{\text{out},m} - \mathbf{r}_{\text{in},m}$. Due to the orientation of the grating bars (Fig. 2.11), the system will only be sensitive to refraction and broadening along the x-axis. Hence, to make a correct comparison with the contrast retrieval results, the reference σ^2 and α should be estimated from direction vectors projected along the y-axis. Assuming the projected direction vectors are normalized, the average projected direction of N_b photons in a beamlet $\mathbf{r}_{\text{av}} = (x_{\text{av}}, y_{\text{av}}, z_{\text{av}})$ can be written as

$$\mathbf{r}_{\text{av}} = \left(\frac{1}{N_b} \sum_{m=1}^{N_b} x_{\text{d},m}, 0, \frac{1}{N_b} \sum_{m=1}^{N_b} z_{\text{d},m} \right). \tag{6.1}$$

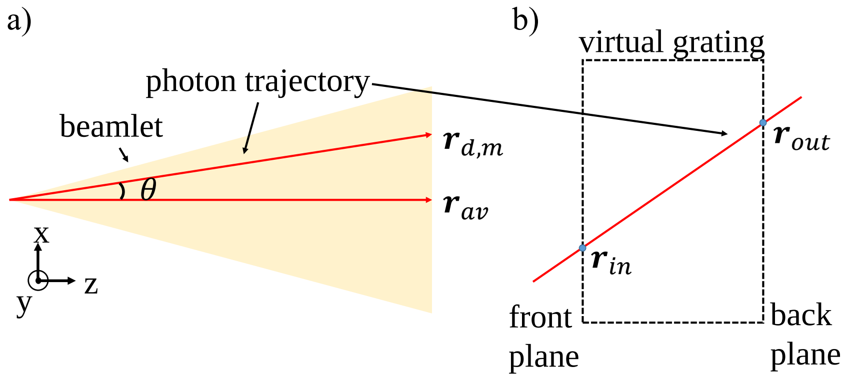

Figure 6.1: a) Close up of a photon trajectory within a beamlet (not to scale). b) Intersection of a photon trajectory with the virtual grating volume.

Subsequently, the individual angular deviations from all projected $\mathbf{r}_{\mathrm{d},m}$ with respect to the average direction $\mathbf{r}_{\mathrm{av}}$ can be found through their respective dot products, yielding the angular variance around the mean direction:

$$\sigma_{\mathrm{av}}^2 = \frac{1}{N_b} \sum_{m=1}^{N_b} \arccos(\mathbf{r}_{\mathrm{d},m} \cdot \mathbf{r}_{\mathrm{av}})^2. \tag{6.2}$$

If $\sigma_{\mathrm{av},0}^2$ denotes the result of Eq. (6.2) for the undistorted beamlet, then the reference for the angular broadening (and thus DFC) is given by:

$$\sigma_{\mathrm{R}}^2 = \sigma_{\mathrm{av}}^2 - \sigma_{\mathrm{av},0}^2. \tag{6.3}$$

The change in average direction of the beamlet can be used to provide a reference for the refraction angle α_{R}:

$$\alpha_{\mathrm{R}} = \arccos(\mathbf{r}_{\mathrm{av}} \cdot \mathbf{r}_{\mathrm{av},\mathbf{0}}), \tag{6.4}$$

yielding a reference value for DPC. In addition, due to the nature of the virtual gratings approach, the transmission reference T_{R} can be generated as well by omitting the gratings in the simulation, resulting in a conventional radiograph. For each measurement point (pixel), the reference values are extracted from the corresponding idealized beamlet, which is defined as the collection of photons passing through the aperture of an infinitesimally thin but perfectly absorbing mask. Hence, undesirable effects such as grating bar transmission and shadowing are eliminated, while still matching the mask stepping. This is a reasonable definition, since it leads to the exact set of photons that would contribute to an idealized EI measurement with perfect gratings. By design, the generated virtual gratings output can be used in parallel to generate simulated detector measurements, meaning that a single MC simulation suffices to simultaneously generate the reference and contrast retrieved values for an arbitrary number of grating geometries (Sanctorum et al., 2022a). Subsequently, these profiles can be converted to T, α and σ^2 through contrast retrieval.

To summarize, the proposed method uses the information stored by the virtual gratings approach to extract a complete set of reference values for all three contrasts, as well as mask stepping measurements. To differentiate between the contrast retrieval results (T, α and σ^2) and the corresponding reference values, we will refer to the latter as T_{R}, α_{R} and σ^2_{R}, respectively.

6.2.2 Geometrical optics model for EI simulations

A full description of X-ray phase effects generally requires wave optics modeling. Using GATE with X-ray refraction but without wavefront propagation, however, implies geometrical optics modeling. Although EI is an imaging method that can, in most cases, be modeled with geometrical optics, it is useful to briefly touch upon the geometrical optics approximation. In general, a distinction is made between three imaging regimes: the Fraunhofer regime, the Fresnel regime, and the geometrical optics regime. Although moving from one regime to another is a gradual change without clear boundaries, differentiation is possible through the Fresnel number N_F (Paganin and Pelliccia, 2021):

$$N_F = \frac{M\left(\Delta x_r\right)^2}{\lambda d_{OD}}, \tag{6.5}$$

where λ denotes the X-ray wavelength and Δx_r is the smallest resolvable transverse characteristic feature size. The typically used condition for using the geometrical optics model is that $N_F \gg 1$, with lower limit $N_F > 10$, demarcating the relevant imaging conditions. Smaller Fresnel numbers lead to the Fresnel ($N_F \approx 1$) and Fraunhofer ($N_F \ll 1$) regimes. An in-depth discussion with respect to aperture size and focal spot can be found in the work of Munro et al. (2010a,b).

6.3 Experiments

A number of virtual gratings simulation experiments was performed in GATE to demonstrate the proposed method. The source-to-detector distance (SDD) of the simulated system was 1800 mm, with a 1.5 magnification factor for the sample mask, placed at distance of 1200 mm from the source. The detector mask was positioned at 5 mm in front of a line-detector, which consisted of 444 pixels with a size of 150 μm. X-rays were generated from a polychromatic 40 kV source (Nazemi et al., 2021) (Fig. 6.2) with a Gaussian focal spot of 50 μm FWHM. Given the system dimensions and the weighted mean X-ray energy of the spectrum (15.3 keV), Eq. (6.5) sets the geometrical optics limit for Δx_r at 18 μm. Since in EI the aperture size determines a lower limit to the smallest resolvable features (Diemoz et al., 2015), this means the aperture size should, in this case, be at least 18 μm. In total, 10^8 photons were generated at the source for every virtual gratings simulation. The phantoms were positioned between the two gratings, 30 mm from the sample

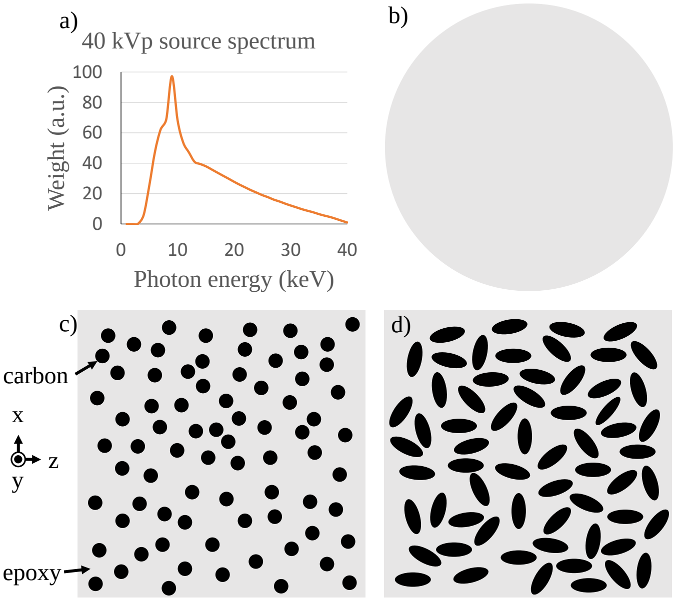

Figure 6.2: a) Spectrum of the simulated 40 kV X-ray source. Schematic view (not to scale) of b) the simulated 10 mm epoxy cylinder, c) the CFRP phantom with 10 μm symmetric fibers, and d) the CFRP phantom with eccentric fibers (semi-axes of 12.5 and 5 μm).

mask. For each phantom, one virtual gratings simulation was performed, providing the required output for generating both the mask stepping results and reference values. To produce the mask stepping profiles, 15 mask steps were taken post-simulation for every grating geometry (Sanctorum et al., 2022a). The sample mask aperture size was varied in steps of 5 μm from 20 μm to 40 μm, whereas the grating thickness for both gratings was varied from 150 μm to 350 μm in steps of 50 μm. The detector mask apertures scaled with the sample mask apertures according to the magnification. This resulted in 25 different parameter combinations and 375 profiles in total for each phantom. For the mask stepping results, gold gratings were considered.

In total, three different phantoms were designed for the simulations. First, a 10 mm thick carbon fiber reinforced polymer (CFRP) phantom was used, consisting of cylindrical carbon fibers embedded in an epoxy matrix. The diameter of the fibers was set to 10 μm. To demonstrate the method on more arbitrarily shaped structures, the fibers were, in a second simulation, elongated to elliptical tubes with a long semi-axis of 12.5 μm and short semi-axis of 5 μm. The y-axis rotation of the eccentric fibers was randomly assigned, in order to avoid global directional dark field effects (Janssens et al., 2017) (Fig. 6.2). A Poisson disc sampling algorithm was used to determine the positions of the symmetric and eccentric fibers in the phantoms, where the longest axis of the eccentric fibers was used to define the minimal separation distance between sampling points. In total, 290755

Table 6.1: Monte Carlo simulation (GATE) and processing (MATLAB) times required to compute the mask stepping profiles for all experiments for each phantom described in Section 6.3. All times are expressed in seconds and the tabulated values are averages of the five parallel simulations.

	GATE	**MATLAB**
Cylinder	5410 ± 20	6940 ± 60
Symmetric fibers	10390 ± 80	4510 ± 30
Eccentric fibers	36500 ± 400	4270 ± 20
Flat field	6480 ± 40	7280 ± 20

sampling points were generated for both phantoms. In addition to the microstructure phantoms, a homogeneous epoxy cylinder with 10 mm diameter was simulated. Finally, a simulation without phantom was performed. The imaging conditions were kept the same for all simulations.

GATE simulations were performed on a server with 16 Intel Xeon E5-2670 @ 2.60GHz CPUs (dual core) and 64GB RAM, using five cores in parallel for each simulation. The subsequent processing and analysis of the virtual grating simulation results was performed in MATLAB R2019a on a local machine with an NVIDIA GeForce GTX 1080 GPU, 6 Intel Core i7-6850K 3.60GHz CPUs (dual core), and 64GB RAM.

6.4 Results

The simulation times in GATE and the subsequent MATLAB processing times required to compute the mask stepping profiles are summarized in Table 6.1. For GATE, the phantom complexity is the main factor determining the simulation time for a given number of photon trajectories (Sanctorum et al., 2020). Since tracking of absorbed photons is stopped after absorption by the phantom, the average simulation time of the cylinder simulation is shorter compared to the average flat field simulation time. The processing times in MATLAB are mostly determined by the number of detected photons, given that the number of virtual gratings parameter variations is kept constant. The higher memory cost associated with an increasing number of photons, i.e. larger arrays, leads to longer computation times.

6.4.1 Interpretation of the reference values

In Fig. 6.3, Fig. 6.4, and Fig. 6.5, α_R and σ_R^2 profiles are plotted jointly with α and σ^2 profiles for the epoxy cylinder and the two fiber phantoms, respectively. In these plots, a distinction is made between type-1 and type-2 reference values.

The type-1 reference values require two simulations: one with and one without object in the beam path. When calculating σ_R^2 using Eq. (6.3), the simulation without object yields $\sigma_{\mathrm{av},0}^2$ and the simulation with object σ_av^2. In the type-2 reference plots, $\sigma_{\mathrm{av},0}^2$ and σ_av^2 both result from the simulation with object. However, $\sigma_{\mathrm{av},0}^2$ is calculated from the photon trajectories registered before interaction with the object and σ_av^2 from the same trajectories after interaction. Since by default only photons reaching the detector plane contribute to $\sigma_{\mathrm{av},0}^2$ and σ_av^2 in GATE, this implies that, for the type-2 case, $\sigma_{\mathrm{av},0}^2$ and σ_av^2 are extracted from the exact same set of simulated photons at different points in time. Hence, type-2 reference values are free from beam hardening effects. Similar considerations apply to type-1 and type-2 versions of α_R with respect to $\mathbf{r}_\mathrm{av}$ and $\mathbf{r}_{\mathrm{av},\mathbf{0}}$ in Eq. (6.4).

Due to the definition of type-2 reference values, the corresponding type-2 plots for the epoxy cylinder in Fig. 6.3 show no fluctuations. Using a type-1 reference with a different set of simulated photons results in statistical fluctuations, visible in the type-1 plots. Furthermore, it can be seen that in the contrast retrieval plots the fluctuations become even more apparent due to the contrast retrieval procedure. The edge effects in the outer cylinder regions can be clearly seen in the reference plots, but are washed out by the contrast retrieval.

It should be noted that all plots in Fig. 6.4 and Fig. 6.5 show fluctuations inside the CFRP phantom region, including the type-2 plots. Outside the object, however, the type-2 profiles are still flat. This indicates that these fluctuations are due to local spatial variations in the object microstructure, which is supported by the absence of these fluctuations in the type-2 profiles of the homogeneous cylinder. Since type-1 reference values are closer to actual EI measurements than type-2 reference values, type-1 will be used in the remainder of the work. Hence, unless stated otherwise, all reference values should be interpreted as type-1 reference values.

6.4.2 Benchmarking contrast retrieval results

In this section, the contrast retrieval results are benchmarked to the corresponding reference values. The assessment is performed in terms of the sum of squared errors (SSE) for α and the accuracy A for T and σ^2, defined as the relative difference between the spatially averaged values (Astolfo et al., 2016):

$$\mathrm{A}_{\sigma^2} = \frac{\langle \sigma^2 \rangle_\mathrm{ROI} - \langle \sigma_\mathrm{R}^2 \rangle_\mathrm{ROI}}{|\langle \sigma_\mathrm{R}^2 \rangle_\mathrm{ROI}|}, \tag{6.6}$$

where $\langle \cdot \rangle_\mathrm{ROI}$ denotes the spatial average in the object region of interest (ROI), which is defined as the image region containing only the object pixels and no background pixels. An equivalent expression is used for A_T. The results of Eq. (6.6) are summarized in heat maps shown in Fig. 6.6 and Fig. 6.7. Each value corresponds to a specific grating geometry, defined by its aperture size and grating thickness. This is indicated on the horizontal and vertical axis, respectively. The color map is chosen such that a green value

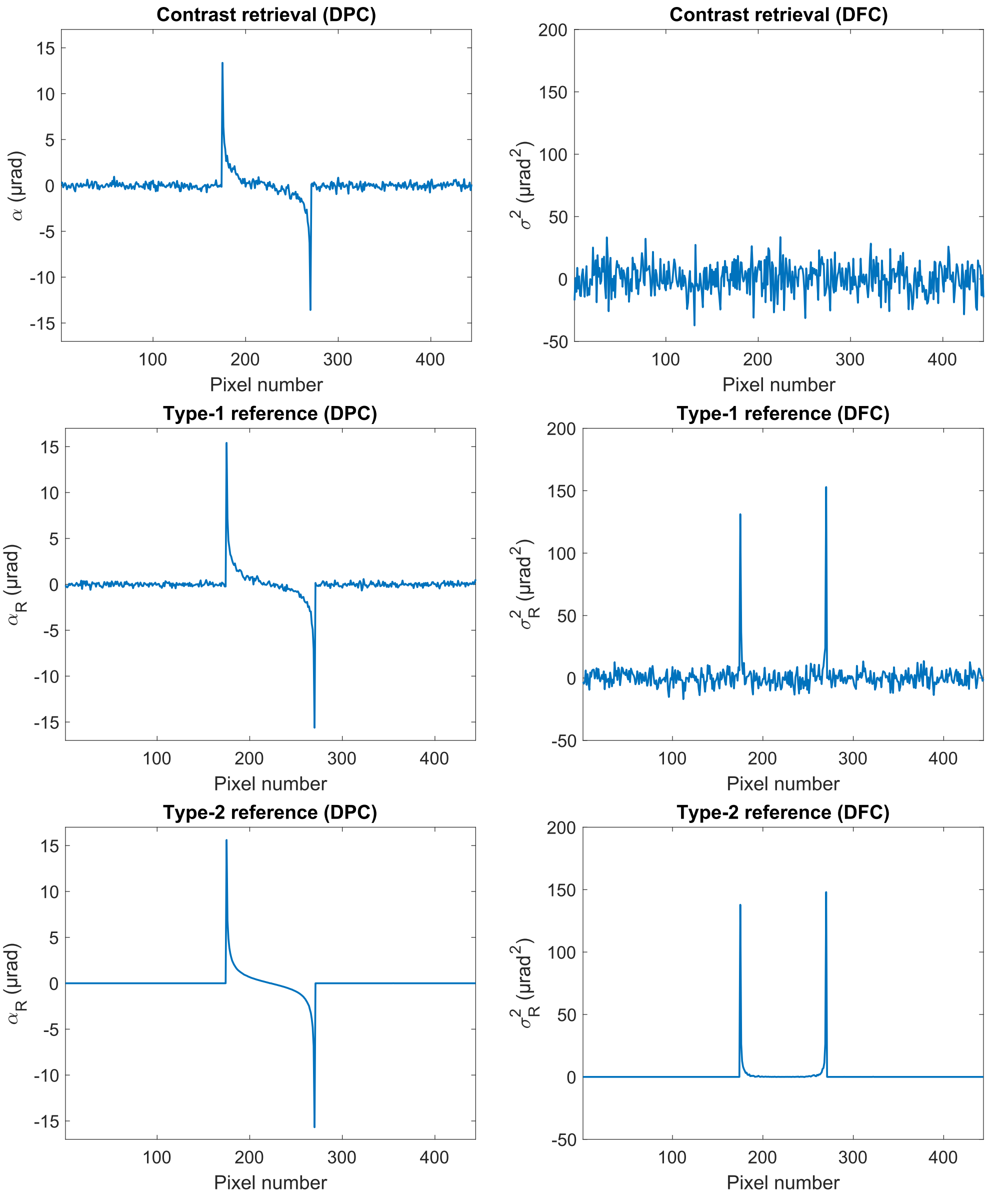

Figure 6.3: α (refraction), α_R (refraction reference), σ^2 (dark field), and σ_R^2 (dark field reference) profiles resulting from the virtual gratings simulation with the single epoxy cylinder. The aperture size was set to 20 μm. For the contrast retrieval results, the grating thickness was set to 200 μm. The cylinder edges are clearly represented in all profiles except for the DFC retrieved from the IC profiles. The contrast retrieval results show the strongest signal fluctuations, whereas the type-2 references are, by definition, completely free of such fluctuations.

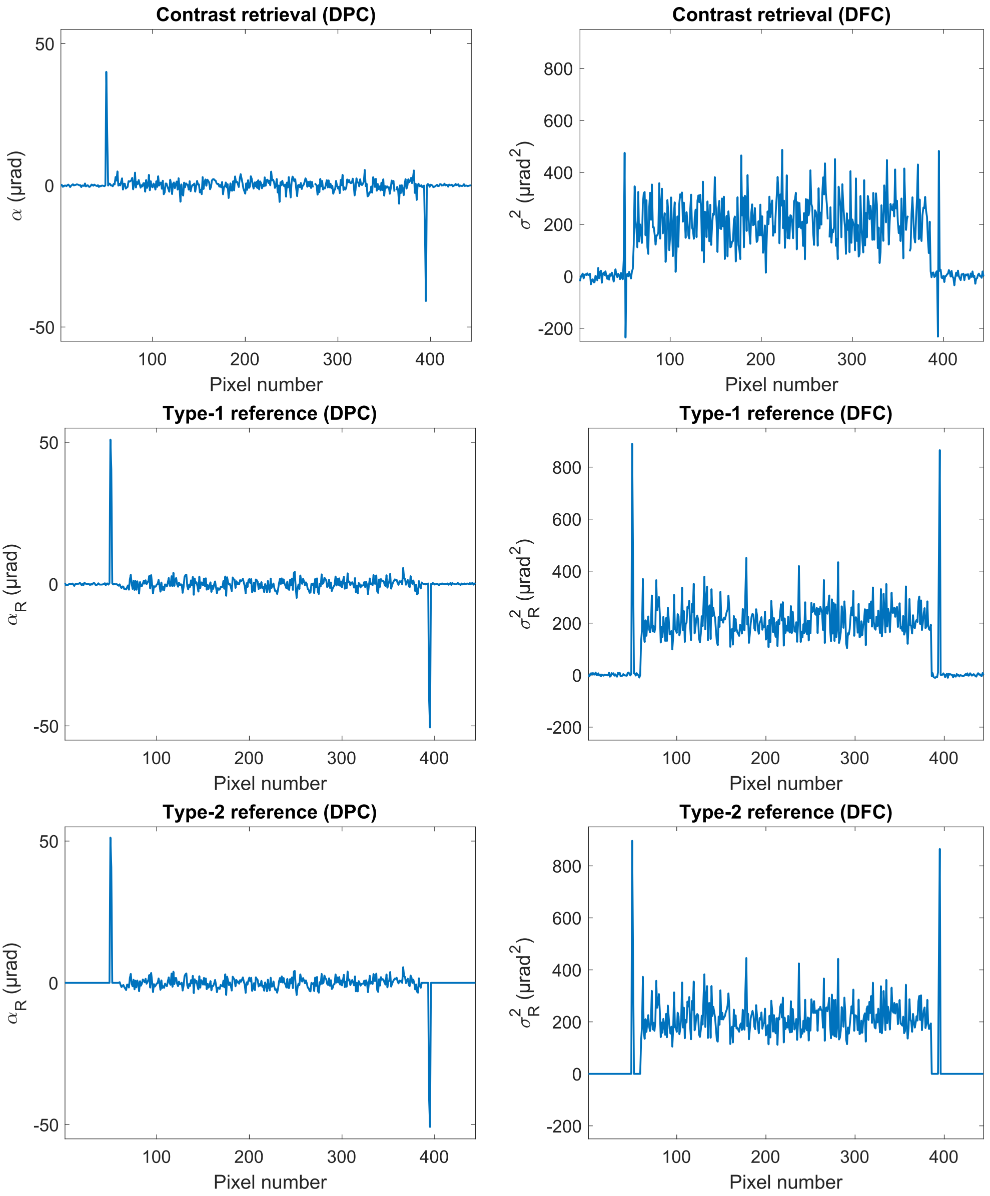

Figure 6.4: α (refraction), α_R (refraction reference), σ^2 (dark field), and σ^2_R (dark field reference) profiles resulting from the virtual gratings simulation with the 10 μm symmetric fiber CFRP phantom. The aperture size was set to 20 μm. For the contrast retrieval results, the grating thickness was set to 200 μm. The CFRP edges are clearly represented in all profiles. Here, the fluctuations only disappear in the background of the type-2 references and not within the CFRP region, indicating that they are in this case related to the presence of microstructures.

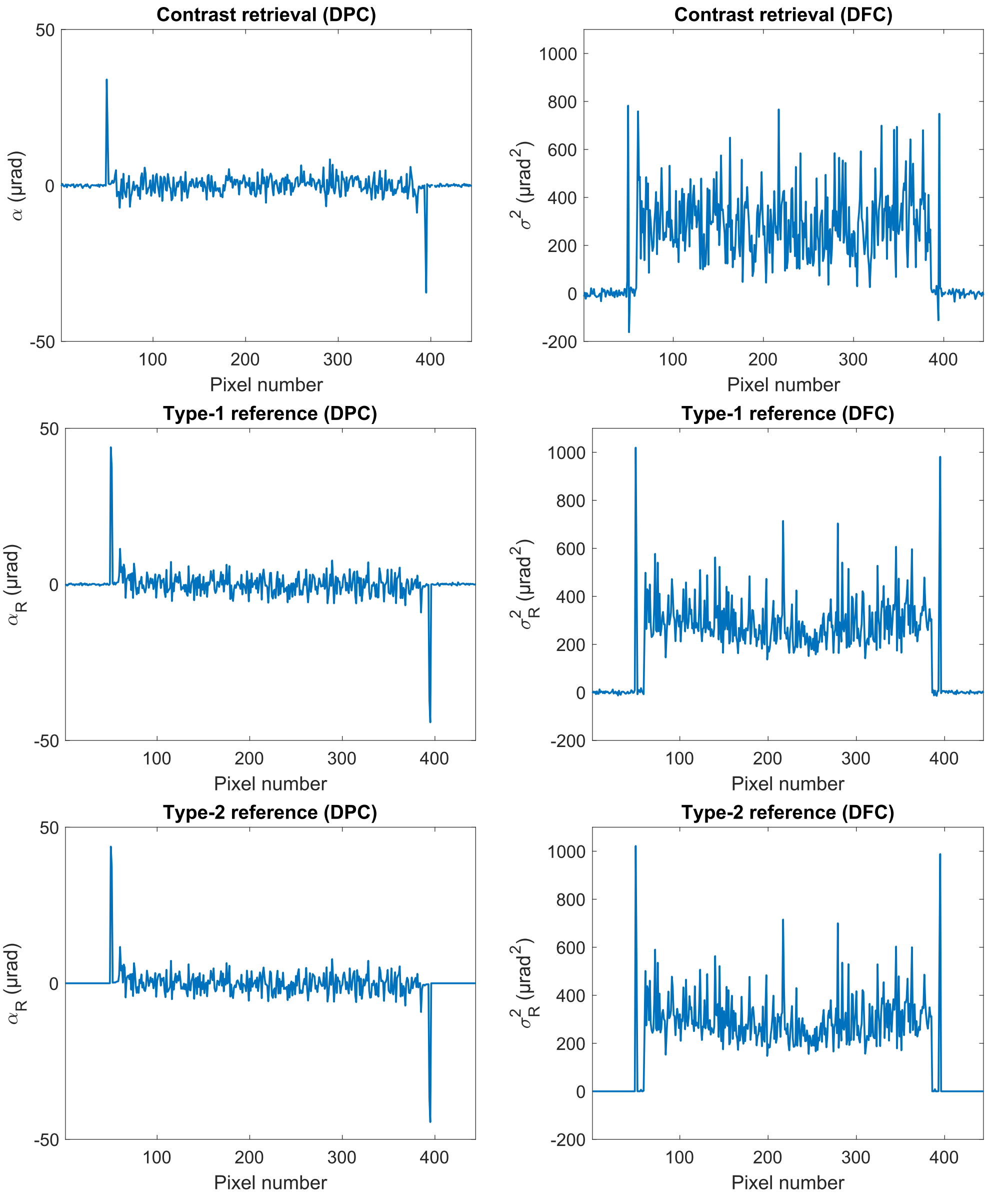

Figure 6.5: α (refraction), α_{R} (refraction reference), σ^2 (dark field), and σ_{R}^2 (dark field reference) profiles resulting from the virtual gratings simulation with the eccentric fiber CFRP phantom. The aperture size was set to 20 μm. For the contrast retrieval results, the grating thickness was set to 200 μm. The average DFC is clearly higher compared to the CFRP with symmetric fibers. In addition, the signal fluctuations within the CFRP are visibly stronger for both DPC and DFC compared to the symmetric fibers, indicating that the magnitude of the fluctuations is related to the microstructure properties.

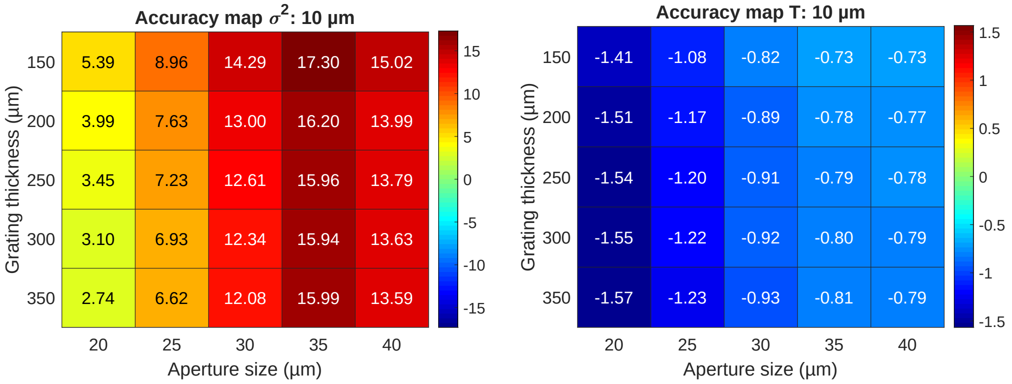

Figure 6.6: Accuracy heat maps of σ^2 (dark field) and T (transmission) for the CFRP phantom with symmetric 10 μm fibers. Tabulated values are expressed in % and represent the accuracy as defined in Eq. (6.6) for different combinations of grating parameters (thickness and aperture size). Values represented by red cells indicate an overestimation of the respective reference values, whereas blue indicates an underestimation. Green cells represent the most optimal grating parameters. Smaller apertures tend to give more accurate σ^2 estimates, whereas larger apertures yield more accurate T values.

corresponds to optimal accuracy, i.e. A close to 0, whereas darker red and blue values indicate stronger deviations. Some degree of saturation in the color scale is tolerated for higher values, to ensure sufficient contrast in the heat map for lower, more optimal values. Tables summarizing the T and σ^2 values used to generate the accuracy heat maps can be found in Appendix D. It can be seen from Fig. 6.6 that smaller apertures tend to give more accurate σ^2 results, which is in line with expectations and the higher DPC sensitivity generally associated with smaller apertures. A similar result is found from the eccentric fibers in Fig. 6.7, where again the 20 μm aperture is more favorable compared to other aperture sizes. In general, the effect of the grating thickness seems to be more subtle than the effect of the aperture size. The heat maps show a gradually decreasing trend for increasing grating thickness, indicating a lowering average σ^2 compared to the σ_{R}^2 (see Appendix D). Differences are, however, small compared to the differences for varying aperture sizes. It should be noted that shadowing is a problem affecting all contrasts for setups with larger cone angles and thicker gratings. Some shadowing is present in the results shown here as well, but only limited for most grating configurations due to the relatively small cone angle in the simulated geometry (2.1°). Judging from the accuracy maps for T, smaller apertures tend to give a more profound underestimation of T. Differences are however small, especially in Fig. 6.7. The slightly decreasing trend observed for A_{σ^2} with increasing grating thickness is present for A_T as well.

The results of the SSE between α and α_{R} are summarized in a heat map shown in Fig. 6.8. The color map, chosen to visualize the SSE, shows darker red for a lower SSE and lighter yellow for a higher SSE. It can be seen that the 40 μm apertures result in the highest SSE,

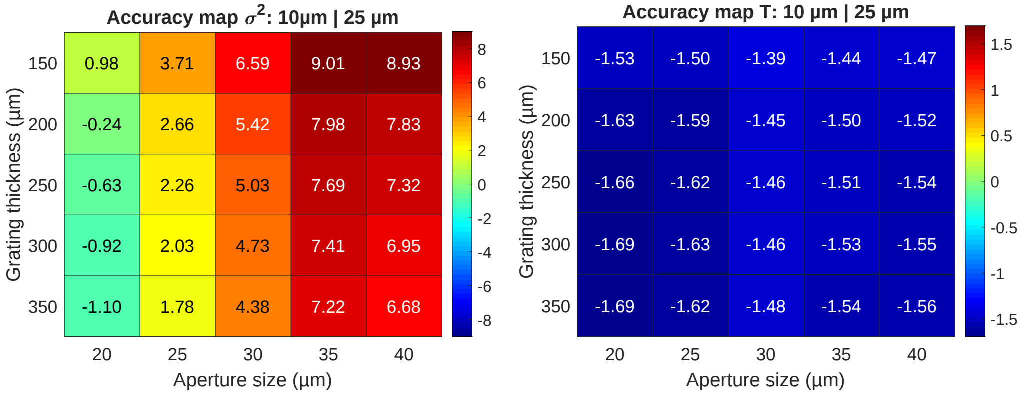

Figure 6.7: Accuracy heat maps of σ^2 (dark field) and T (transmission) for the eccentric fiber phantom (10/25 axis ratio). Tabulated values are expressed in % and represent the accuracy as defined in Eq. (6.6) for different combinations of grating parameters (thickness and aperture size). Values represented by red cells indicate an overestimation of the respective reference values, whereas blue indicates an underestimation. Green cells represent the most optimal grating parameters. The most accurate σ^2 estimate is found for the 20 μm aperture with 200 μm thickness, whereas no clear trend is visible for T values of this phantom.

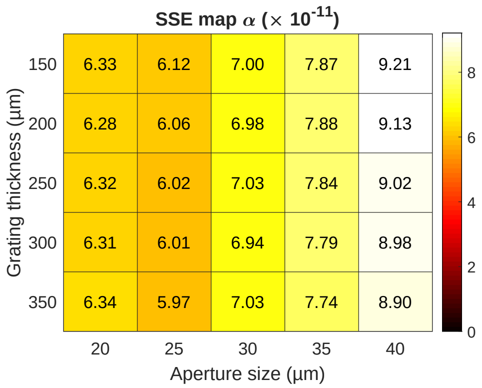

Figure 6.8: SSE (sum of squared errors) heat map of α (refraction) for the single cylinder simulation, showing different combinations of aperture size and grating thickness. Darker red cells indicate lower, more optimal refraction estimates, whereas lighter yellow cells indicate larger deviations from the reference values. Smaller apertures yield more accurate refraction estimates, whereas the grating thickness has only limited influence.

whereas the lowest SSE is found for the 25 μm aperture. The influence of the grating thickness on the SSE appears to be negligible, with a consistently decreasing SSE for thicker gratings only visible with aperture sizes of 25 μm, 35 μm and 40 μm. The negligible SSE variation within columns indicates that the effect of shadowing is small for the considered system geometry. The overall SSE is however clearly higher in the last column.

6.5 Discussion

The results shown in Section 6.4.1 illustrate that the most suitable definition for the reference type is problem-specific. Indeed, although type-1 reference values were chosen here to account for the most relevant physical interactions of X-rays in the phantom, other arguments may lead to different choices. If beam hardening effects are to be removed from the reference, type-2 reference values gain interest. Choosing a type-2 reference does not avoid a change in effective spectrum, but by design absorbed photons do not contribute to the reference. Given that the energy of every photon is stored in the virtual gratings output, a more dedicated approach could be to carefully select a subset of photons from the virtual gratings output, in order to reconstruct the original spectrum. Although this avoids a change in effective spectrum, the significant loss of photons can affect the reference estimates.

Furthermore, the type-2 reference profiles plotted in Fig. 6.4 and Fig. 6.5 reveal that the presence of microstructures leads to fluctuations in α and σ^2 that cannot be attributed to photon statistics or the contrast retrieval procedure. This implies that these fluctuations result from intrinsic phantom properties such as local spatial variations in fiber concentration. It should be noted that such spatial signal fluctuations have received attention in recent experimental work as well (Shoukroun et al., 2023; Esposito et al., 2023), where the standard deviation of α is treated as an alternative contrast type. The method presented in this chapter allows to separate the intrinsic spatial fluctuations from other contributions such as photon statistics and contrast retrieval algorithms. The proposed method therefore seems well-suited to provide additional insight on how these fluctuations are related to specific microstructure properties, especially since this effect is mostly of interest for larger microstructures.

The accuracy and SSE maps shown in Fig. 6.6, Fig. 6.7, and Fig. 6.8, provide a direct comparison of different grating designs for use in EI experiments based on all three contrast types. Fig. 6.6 shows a slow but steady increase in A_T for increasing aperture size. Given that T_R is estimated from fully illuminated pixels, it is indeed to be expected that A_T improves when the effective pixel area illuminated by the beamlet approaches the full pixel size. This trend is less apparent in Fig. 6.7, where the A_T values show a more constant behavior. It is expected that this is due to the stronger beamlet broadening associated with the eccentric fiber phantom. Indeed, gratings with a finite thickness have an increasingly collimating effect with increasing thickness. The larger the angular range of the photons, the more apparent the angular filtration by the gratings and the stronger the underestimation of the transmission. This filtration effect also impacts A_{σ^2}, in combination with the grating bar transmission for thinner gratings, which may in turn contribute to an overestimation of σ^2. Given that the size and shape of the fibers was different in both phantoms for the same total number of fibers, different packing densities are obtained. For the symmetric fibers, the packing density was found to be 7%, whereas for the eccentric fibers this was 17%, i.e. approximately 2.5 times higher. This difference is reflected by the corresponding average and standard deviation of the dark field (σ_R^2), which are consistently higher for the eccentric fiber phantom (see Appendix D). Differences in σ_R^2 between apertures are likely due to a change in number of photons and the effectively illuminated sample area. A possible alternative strategy could be to take the full period into account, although this implies that the set of trajectories used for the reference will no longer spatially match that of the contrast retrieval results. In addition to the examples presented in this chapter, the method is perfectly suited to test contrast retrieval methods, as its primary goal is to assess if information is extracted correctly from the simulation.

In Section 6.3, Eq. (6.5) was used to find a lower limit on Δx_r for the validity of the geometrical optics model. It should be noted that this limit is indeed system dependent. A shorter system ($d_{OD} \downarrow$) would for example result in a smaller Δx_r value. Although, for the 10 μm fiber case, the microstructure size lies below the estimated limit, the associated diffraction effects would not be resolvable with the modeled aperture and pixel sizes. If smaller apertures are of interest, wave optics simulations should be considered. Alternatively, the geometrical optics model could be extended through the geometrical theory of diffraction (Keller, 1962). This would, however, result in a significantly increased computational cost. Hence, the current scope of our work is limited to systems for which the geometrical optics approach is a reasonable approximation. It should be noted that the weighted mean energy of the spectrum was used to determine the Δx_r limit. In practice, however, the majority of X-rays that are not absorbed by the object, and therefore contribute to the measurement, will have higher energies. The associated shorter wavelengths imply a lower effective Δx_r limit for these X-rays.

A practical limit of the presented method is the fact that the virtual gratings approach tends to produce rather large output files for larger simulations (Sanctorum et al., 2022b). If large simulations are required for a specific problem (e.g., 3D CT studies), the size of the output files could reach challenging proportions. A possible way to reduce the required output size would be to develop a dedicated virtual gratings output format storing only the minimal amount of data. Standard ROOT output files store information that is not used in virtual gratings applications. However, in most cases data storage problems are not expected to become a limiting factor.

6.6 Conclusion

A method was presented to simultaneously simulate EI measurement data and corresponding T, α and σ^2 reference values for multi-contrast benchmarking of EI simulations. The example cases presented in this work demonstrate how benchmarking can be performed without the need for additional simulations. Although GATE was used for our simulations, the method can be incorporated in any MC toolbox. Given the increasing interest in multi-contrast imaging, it is expected that the proposed method will prove to be useful for the optimization of future EI systems. In addition, we see a broader potential towards investigating the recently described contrast based on the standard deviation of the refraction signal, attributed to mainly larger microstructures.

Acknowledgments

The research presented in this chapter was financially supported by the Research Foundation - Flanders (FWO) through grant numbers S003421N (FoodPhase), G094320N, and G090020N.

Chapter 7

Conclusion

Monte Carlo simulations have been proven to be an extremely valuable tool for the design and optimization of conventional and phase-sensitive X-ray imaging systems. Application of Monte Carlo simulation methods to X-ray phase contrast imaging does, however, come with a number of challenges. In this dissertation, a number of tools are presented to address these challenges for the simulation of two popular X-ray phase contrast imaging methods, namely grating-based interferometry and edge illumination. Both imaging techniques rely on a set of gratings positioned between the X-ray source and detector, but whereas grating-based interferometry is designed to be an interferometric method, edge illumination is not. This implies that different simulation requirements are to be met, depending on the method.

In Chapter 3, it was shown how the widely-used Monte Carlo simulation framework GATE can be augmented with functionalities that allow for the simulation of grating-based X-ray phase contrast imaging, by implementing X-ray refraction and the construction of X-ray wavefronts from photons that have interacted with a digital phantom. Subsequent propagation of this wavefront by means of wave optics calculations then results in the generation of simulated grating-based phase contrast images. The separation of the Monte Carlo and the wave optics part allows for changes in the grating parameters and propagation distance without having to repeat the time-consuming Monte Carlo calculations.

In contrast to grating-based interferometry, the simulation of edge illumination does not require the fine sampling of interference patterns for image formation. This implies that, in most cases, the memory-intensive wave optics calculations can be safely omitted. However, the Monte Carlo simulations remain very demanding in terms of required CPU computation time, especially when many simulations are required for extensive parameter studies. In Chapter 4, it was demonstrated that the total computation time required for edge illumination grating parameter studies can be vastly reduced by introducing the concept of virtual gratings, which allows for a post-simulation definition of the grating geometry. As such, a single Monte Carlo simulation can serve as a basis for a multitude of different grating designs. The virtual gratings approach was subsequently used to design a pair of gratings for the FleXCT X-ray micro-CT scanner at imec-Vision Lab, in order to augment the already versatile system with edge illumination-based X-ray phase contrast imaging capabilities. The design process of these gratings was presented in detail in Chapter 5. At the time of writing of this thesis, the gratings designed in Chapter 5 have been manufactured and installed in the FleXCT system, which was swiftly followed by the development of innovative concepts for inline and continuous edge illumination-based X-ray phase contrast imaging.

Finally, it is a reasonable question to ask ourselves how to determine whether one simulation result is closer to the desired outcome than the other. Indeed, certainly for the case of X-ray phase contrast imaging, where assessment of the simulation results is rarely based on the directly simulated images, but rather on images derived thereof following a contrast retrieval procedure, this is not a trivial question. Ideally, there is a ground truth with which the simulation results can be compared, a concept also known as benchmarking. In reality, however, such a reference is often not readily available. In Chapter 6, a method is proposed to extract reference values for all three contrasts provided by an edge illumination setup, using the virtual gratings approach. By tracking and storing the trajectories of the individual simulated photons, the transmission, refraction, and local beam broadening can be estimated directly from the photon tracks, without intermediate contrast retrieval steps. In this way, a full set of reference values becomes available for benchmarking the simulation results, without requiring additional Monte Carlo simulations.

Chapter 8

Outlook

Obviously, the development of simulation software for X-ray phase contrast imaging is a never-ending story, which is steadily evolving one improvement at a time. Within the context of the developments in GATE presented in this dissertation, there are several opportunities to extend its functionalities even further. For example, the current implementation of X-ray refraction in GATE is highly deterministic, as this is the most cost-effective way to include phase contrast effects. This might seem counterintuitive given the intrinsic stochastic nature of Monte Carlo simulations, and a few alternative viewpoints have been suggested in the literature accordingly. The most complete description is probably provided by the geometrical theory of diffraction, which associates every diffracted ray by a collection of secondary rays, perpendicular to the diffracted wavefront. The obvious challenge here is the enormous computational burden such an implementation could bring forward. Alternatively, the splitting of photons into multiple secondary photons can be replaced by a stochastic procedure, where the new photon direction is sampled from the possible directions prescribed by the diffraction effect. However, this as well would require a significant number of additional photons that would have to be simulated, to ensure adequate sampling of the probability distribution.

Similarly, the deterministic implementation of the multiple refraction effect underlying the dark field contrast is powerful, but comes with a certain computational cost as well. A possible alternative approach could be to replace the explicitly defined microstructures by a stochastic process governed by a mean free path for unresolved refraction events, similar to the implementation of other physics processes in Geant4. Such a mean free path calculation could account for electron density variations at multiple length scales, allowing the inclusion of dark field effects other than those originating from unresolved multiple refraction. Furthermore, this approach also allows for the incorporation of the directional nature of the dark field signal. Alternatively, a condensed history approach has been proposed for modeling dark field contrast in ray tracing simulations. Such a condensed history approach allows for the combination of many consecutive events into a single event, thereby circumventing the need for explicitly modeled microstructures.

However, the single dark field material parameter currently associated with such an approach does not describe directional dark field effects and relies on a calibration procedure which has to be repeated for every change in material properties. A more complete condensed history approach to modeling the dark field effect should therefore ideally include both directionality and a more straightforward strategy to account for specific material properties.

The previous paragraphs have made clear that the underlying main challenge in performing Monte Carlo simulations for X-ray phase contrast imaging is the high computational cost in combination with long simulation times. A highly-parallelized GPU implementation would therefore mean a step forward in terms of producing the large amounts of simulation data required for e.g., X-ray phase contrast CT studies, but this has so far proven to be a very challenging endeavor for the whole GATE community. In addition, the possible gain is limited by the need to write data to the GPU memory, potentially causing significant overhead.

Finally, the results presented in Chapter 6 show that the proposed method holds promise beyond its initial purpose of serving as a benchmarking tool for edge illumination simulations. Indeed, it was shown that the photon tracking mechanism uncovered fluctuations in the local refraction and broadening reference values that were purely related to the presence of microstructures in the object. It has been proposed in literature that these fluctuations, in the form of the standard deviation of the refraction signal, could be useful as an alternative image contrast type. This is especially interesting for microstructure sizes comparable to or slightly larger than the edge illumination grating aperture size, as this is a largely unexplored twilight zone between fully resolved microstructures yielding pure differential phase contrast and fully unresolved microstructures yielding pure dark field contrast. The reference values produced by the virtual gratings could therefore be used to facilitate a further investigation of this effect, for example by exploring which information concerning the microstructure properties is possibly encoded within the fluctuations.

The currently ongoing developments in the fast-evolving field of X-ray phase contrast imaging bring new simulation challenges for both grating-based interferometry and edge illumination. With the advent of human scale applications such as dark field lung imaging, it becomes clear that the need for efficient and reliable simulations at a larger scale is growing steadily. Hence, the efficient modeling of both gratings and digital phantoms is expected to become even more important in the future. In addition, there is a growing interest in alternative grating designs for both grating-based interferometry (e.g., dual-binary or triangular phase gratings) and edge illumination (e.g., multi-resolution masks). Recent advances in edge illumination towards fast cycloidal and cycloidal-spiral fly scanning (roto-translation) include the application of new grating designs with circular apertures in different arrangements (rectangular or slanted). Fast scanning is an important prerequisite for 4D imaging of dynamic processes, which is currently still extremely challenging for most X-ray phase contrast imaging methods. The simulation methods presented in this thesis are well-suited to support the design and testing of the alternative mask types required for these nascent applications.

In conclusion, I foresee many more future PhD candidates dedicating their best efforts to the exploration of the vast landscape of possibilities that X-ray phase contrast imaging simulations still have to offer, and I can only hope that the contents of this dissertation will prove to be useful on their journey.

Appendices

Appendix A

GATE example macro

This appendix contains a complete example macro containing all required instructions for an X-ray phase contrast simulation in GATE, as introduced in Chapter 3.

```
/control/execute .../verbose.mac #make sure folder is correct

#=====================================================
# GEOMETRY
#=====================================================

/gate/geometry/setMaterialDatabase .../GateMaterials.db

# World
/gate/world/geometry/setXLength 20. mm
/gate/world/geometry/setYLength 20. mm
/gate/world/geometry/setZLength 5. cm
/gate/world/setMaterial Air
/gate/world/vis/forceWireframe
/gate/world/vis/setColor black

# CTscanner system
/gate/world/daughters/name CTscanner
/gate/world/daughters/insert box
/gate/CTscanner/geometry/setXLength  5.0 mm
/gate/CTscanner/geometry/setYLength  0.01 mm
/gate/CTscanner/geometry/setZLength  0.1  mm
/gate/CTscanner/placement/setTranslation 0. 0. 1.5 cm
/gate/CTscanner/setMaterial Air
/gate/CTscanner/vis/forceWireframe
/gate/CTscanner/vis/setColor white

# Module
/gate/CTscanner/daughters/name module
/gate/CTscanner/daughters/insert box
/gate/module/geometry/setXLength  5.0 mm
/gate/module/geometry/setYLength  0.01 mm
/gate/module/geometry/setZLength  0.1 mm
/gate/module/setMaterial Air
```

```
/gate/module/vis/forceWireframe
/gate/module/vis/setColor white

# Cluster
/gate/module/daughters/name cluster
/gate/module/daughters/insert box
/gate/cluster/geometry/setXLength  5.0 mm
/gate/cluster/geometry/setYLength  0.01 mm
/gate/cluster/geometry/setZLength  0.1 mm
/gate/cluster/setMaterial Air
/gate/cluster/vis/forceWireframe
/gate/cluster/vis/setColor white

# Pixel
/gate/cluster/daughters/name pixel
/gate/cluster/daughters/insert box
/gate/pixel/geometry/setXLength 0.1  mm
/gate/pixel/geometry/setYLength 0.010 mm
/gate/pixel/geometry/setZLength 0.1 mm
/gate/pixel/setMaterial Silicon
/gate/pixel/vis/forceSolid
/gate/pixel/vis/setColor red
/gate/pixel/repeaters/insert cubicArray
/gate/pixel/cubicArray/setRepeatNumberX 50
/gate/pixel/cubicArray/setRepeatNumberY 1
/gate/pixel/cubicArray/setRepeatNumberZ   1
/gate/pixel/cubicArray/setRepeatVector 0.1 0.010 0.1 mm

/gate/systems/CTscanner/module/attach module
/gate/systems/CTscanner/cluster_0/attach cluster
/gate/systems/CTscanner/pixel_0/attach pixel

/gate/pixel/attachCrystalSD

# Phantom
/gate/world/daughters/name epoxyBox
/gate/world/daughters/insert box
/gate/epoxyBox/geometry/setXLength 10. mm
/gate/epoxyBox/geometry/setYLength 2.05 mm
/gate/epoxyBox/geometry/setZLength 10. mm
/gate/epoxyBox/setMaterial Epoxy
/gate/epoxyBox/vis/forceWireframe
/gate/epoxyBox/vis/setColor white
/gate/epoxyBox/placement/setTranslation  0. -0.25 0.5 cm
/gate/epoxyBox/placement/setRotationAxis 1 0 0
/gate/epoxyBox/placement/setRotationAngle 90. deg

#/gate/epoxyBox/daughters/name CarbonCylinder
#/gate/epoxyBox/daughters/insert cylinder
#/gate/CarbonCylinder/placement/setTranslation  1.4 0.0 0.0 mm
#/gate/CarbonCylinder/geometry/setRmin 0. mm
#/gate/CarbonCylinder/geometry/setRmax 0.15 mm
#/gate/CarbonCylinder/geometry/setHeight 2.00 mm
#/gate/CarbonCylinder/setMaterial Carbon
#/gate/CarbonCylinder/vis/forceSolid
#/gate/CarbonCylinder/vis/setColor gray

/gate/epoxyBox/daughters/name layer1VerticalFibreCylinder1
/gate/epoxyBox/daughters/insert cylinder
/gate/layer1VerticalFibreCylinder1/placement/setTranslation  1.225 0.8125 0.0 mm
/gate/layer1VerticalFibreCylinder1/geometry/setRmin 0.0 mm
/gate/layer1VerticalFibreCylinder1/geometry/setRmax 0.0035 mm
```

```
/gate/layer1VerticalFibreCylinder1/geometry/setHeight 10.00 mm
/gate/layer1VerticalFibreCylinder1/setMaterial Carbon
/gate/layer1VerticalFibreCylinder1/vis/forceSolid
/gate/layer1VerticalFibreCylinder1/vis/setColor gray


/gate/layer1VerticalFibreCylinder1/repeaters/insert genericRepeater
/gate/layer1VerticalFibreCylinder1/genericRepeater/setPlacementsFilename
    .../placementsGATE2555PoissionDiskFlatBundle_v1.placements
/gate/layer1VerticalFibreCylinder1/genericRepeater/useRelativeTranslation 1

/gate/epoxyBox/daughters/name layer1VerticalFibreCylinder2
/gate/epoxyBox/daughters/insert cylinder
/gate/layer1VerticalFibreCylinder2/placement/setTranslation  -1.525 0.8125 0.0 mm
/gate/layer1VerticalFibreCylinder2/geometry/setRmin 0.0 mm
/gate/layer1VerticalFibreCylinder2/geometry/setRmax 0.0035 mm
/gate/layer1VerticalFibreCylinder2/geometry/setHeight 10.00 mm
/gate/layer1VerticalFibreCylinder2/setMaterial Carbon
/gate/layer1VerticalFibreCylinder2/vis/forceSolid
/gate/layer1VerticalFibreCylinder2/vis/setColor gray


/gate/layer1VerticalFibreCylinder2/repeaters/insert genericRepeater
/gate/layer1VerticalFibreCylinder2/genericRepeater/setPlacementsFilename
    .../placementsGATE2545PoissionDiskFlatBundle_v2.placements
/gate/layer1VerticalFibreCylinder2/genericRepeater/useRelativeTranslation 1

/gate/epoxyBox/daughters/name layer3VerticalFibreCylinder1
/gate/epoxyBox/daughters/insert cylinder
/gate/layer3VerticalFibreCylinder1/placement/setTranslation  1.225 0.1625 0.0 mm
/gate/layer3VerticalFibreCylinder1/geometry/setRmin 0.0 mm
/gate/layer3VerticalFibreCylinder1/geometry/setRmax 0.0035 mm
/gate/layer3VerticalFibreCylinder1/geometry/setHeight 10.00 mm
/gate/layer3VerticalFibreCylinder1/setMaterial Carbon
/gate/layer3VerticalFibreCylinder1/vis/forceSolid
/gate/layer3VerticalFibreCylinder1/vis/setColor gray


/gate/layer3VerticalFibreCylinder1/repeaters/insert genericRepeater
/gate/layer3VerticalFibreCylinder1/genericRepeater/setPlacementsFilename
    .../placementsGATE2593PoissionDiskFlatBundle_v3.placements
/gate/layer3VerticalFibreCylinder1/genericRepeater/useRelativeTranslation 1

/gate/epoxyBox/daughters/name layer3VerticalFibreCylinder2
/gate/epoxyBox/daughters/insert cylinder
/gate/layer3VerticalFibreCylinder2/placement/setTranslation  -1.525 0.1625 0.0 mm
/gate/layer3VerticalFibreCylinder2/geometry/setRmin 0.0 mm
/gate/layer3VerticalFibreCylinder2/geometry/setRmax 0.0035 mm
/gate/layer3VerticalFibreCylinder2/geometry/setHeight 10.00 mm
/gate/layer3VerticalFibreCylinder2/setMaterial Carbon
/gate/layer3VerticalFibreCylinder2/vis/forceSolid
/gate/layer3VerticalFibreCylinder2/vis/setColor gray


/gate/layer3VerticalFibreCylinder2/repeaters/insert genericRepeater
/gate/layer3VerticalFibreCylinder2/genericRepeater/setPlacementsFilename
    .../placementsGATE2564PoissionDiskFlatBundle_v4.placements
/gate/layer3VerticalFibreCylinder2/genericRepeater/useRelativeTranslation 1

/gate/epoxyBox/daughters/name layer5VerticalFibreCylinder1
/gate/epoxyBox/daughters/insert cylinder
/gate/layer5VerticalFibreCylinder1/placement/setTranslation  1.225 -0.4875 0.0 mm
```

```
/gate/layer5VerticalFibreCylinder1/geometry/setRmin 0.0 mm
/gate/layer5VerticalFibreCylinder1/geometry/setRmax 0.0035 mm
/gate/layer5VerticalFibreCylinder1/geometry/setHeight 10.00 mm
/gate/layer5VerticalFibreCylinder1/setMaterial Carbon
/gate/layer5VerticalFibreCylinder1/vis/forceSolid
/gate/layer5VerticalFibreCylinder1/vis/setColor gray


/gate/layer5VerticalFibreCylinder1/repeaters/insert genericRepeater
/gate/layer5VerticalFibreCylinder1/genericRepeater/setPlacementsFilename
    .../placementsGATE2591PoissionDiskFlatBundle_v5.placements
/gate/layer5VerticalFibreCylinder1/genericRepeater/useRelativeTranslation 1

/gate/epoxyBox/daughters/name layer5VerticalFibreCylinder2
/gate/epoxyBox/daughters/insert cylinder
/gate/layer5VerticalFibreCylinder2/placement/setTranslation  -1.525 -0.4875 0.0 mm
/gate/layer5VerticalFibreCylinder2/geometry/setRmin 0.0 mm
/gate/layer5VerticalFibreCylinder2/geometry/setRmax 0.0035 mm
/gate/layer5VerticalFibreCylinder2/geometry/setHeight 10.00 mm
/gate/layer5VerticalFibreCylinder2/setMaterial Carbon
/gate/layer5VerticalFibreCylinder2/vis/forceSolid
/gate/layer5VerticalFibreCylinder2/vis/setColor gray


/gate/layer5VerticalFibreCylinder2/repeaters/insert genericRepeater
/gate/layer5VerticalFibreCylinder2/genericRepeater/setPlacementsFilename
    .../placementsGATE2578PoissionDiskFlatBundle_v6.placements
/gate/layer5VerticalFibreCylinder2/genericRepeater/useRelativeTranslation 1

/gate/epoxyBox/daughters/name layer2HorizontalFibreCylinder1
/gate/epoxyBox/daughters/insert cylinder
/gate/layer2HorizontalFibreCylinder1/placement/setTranslation  0.0 0.4875 0.825 mm
/gate/layer2HorizontalFibreCylinder1/geometry/setRmin 0.0 mm
/gate/layer2HorizontalFibreCylinder1/geometry/setRmax 0.0035 mm
/gate/layer2HorizontalFibreCylinder1/geometry/setHeight 10.00 mm
/gate/layer2HorizontalFibreCylinder1/placement/setRotationAxis 0 1 0
/gate/layer2HorizontalFibreCylinder1/placement/setRotationAngle 90. deg
/gate/layer2HorizontalFibreCylinder1/setMaterial Carbon
/gate/layer2HorizontalFibreCylinder1/vis/forceSolid
/gate/layer2HorizontalFibreCylinder1/vis/setColor gray

/gate/layer2HorizontalFibreCylinder1/repeaters/insert genericRepeater
/gate/layer2HorizontalFibreCylinder1/genericRepeater/setPlacementsFilename
    .../placementsGATE2582PoissionDiskFlatBundle90rot_v1.placements
/gate/layer2HorizontalFibreCylinder1/genericRepeater/useRelativeTranslation 1

/gate/epoxyBox/daughters/name layer2HorizontalFibreCylinder2
/gate/epoxyBox/daughters/insert cylinder
/gate/layer2HorizontalFibreCylinder2/placement/setTranslation  0.0 0.4875 -1.175 mm
/gate/layer2HorizontalFibreCylinder2/geometry/setRmin 0.0 mm
/gate/layer2HorizontalFibreCylinder2/geometry/setRmax 0.0035 mm
/gate/layer2HorizontalFibreCylinder2/geometry/setHeight 10.00 mm
/gate/layer2HorizontalFibreCylinder2/placement/setRotationAxis 0 1 0
/gate/layer2HorizontalFibreCylinder2/placement/setRotationAngle 90. deg
/gate/layer2HorizontalFibreCylinder2/setMaterial Carbon
/gate/layer2HorizontalFibreCylinder2/vis/forceSolid
/gate/layer2HorizontalFibreCylinder2/vis/setColor gray

/gate/layer2HorizontalFibreCylinder2/repeaters/insert genericRepeater
/gate/layer2HorizontalFibreCylinder2/genericRepeater/setPlacementsFilename
    .../placementsGATE2572PoissionDiskFlatBundle90rot_v2.placements
/gate/layer2HorizontalFibreCylinder2/genericRepeater/useRelativeTranslation 1
```

```
/gate/epoxyBox/daughters/name layer4HorizontalFibreCylinder1
/gate/epoxyBox/daughters/insert cylinder
/gate/layer4HorizontalFibreCylinder1/placement/setTranslation  0.0 -0.1625 0.825 mm
/gate/layer4HorizontalFibreCylinder1/geometry/setRmin 0.0 mm
/gate/layer4HorizontalFibreCylinder1/geometry/setRmax 0.0035 mm
/gate/layer4HorizontalFibreCylinder1/geometry/setHeight 10.00 mm
/gate/layer4HorizontalFibreCylinder1/placement/setRotationAxis 0 1 0
/gate/layer4HorizontalFibreCylinder1/placement/setRotationAngle 90. deg
/gate/layer4HorizontalFibreCylinder1/setMaterial Carbon
/gate/layer4HorizontalFibreCylinder1/vis/forceSolid
/gate/layer4HorizontalFibreCylinder1/vis/setColor gray

/gate/layer4HorizontalFibreCylinder1/repeaters/insert genericRepeater
/gate/layer4HorizontalFibreCylinder1/genericRepeater/setPlacementsFilename
    .../placementsGATE2573PoissionDiskFlatBundle90rot_v3.placements
/gate/layer4HorizontalFibreCylinder1/genericRepeater/useRelativeTranslation 1

/gate/epoxyBox/daughters/name layer4HorizontalFibreCylinder2
/gate/epoxyBox/daughters/insert cylinder
/gate/layer4HorizontalFibreCylinder2/placement/setTranslation  0.0 -0.1625 -1.175 mm
/gate/layer4HorizontalFibreCylinder2/geometry/setRmin 0.0 mm
/gate/layer4HorizontalFibreCylinder2/geometry/setRmax 0.0035 mm
/gate/layer4HorizontalFibreCylinder2/geometry/setHeight 10.00 mm
/gate/layer4HorizontalFibreCylinder2/placement/setRotationAxis 0 1 0
/gate/layer4HorizontalFibreCylinder2/placement/setRotationAngle 90. deg
/gate/layer4HorizontalFibreCylinder2/setMaterial Carbon
/gate/layer4HorizontalFibreCylinder2/vis/forceSolid
/gate/layer4HorizontalFibreCylinder2/vis/setColor gray

/gate/layer4HorizontalFibreCylinder2/repeaters/insert genericRepeater
/gate/layer4HorizontalFibreCylinder2/genericRepeater/setPlacementsFilename
    .../placementsGATE2551PoissionDiskFlatBundle90rot_v4.placements
/gate/layer4HorizontalFibreCylinder2/genericRepeater/useRelativeTranslation 1

/gate/epoxyBox/daughters/name layer6HorizontalFibreCylinder1
/gate/epoxyBox/daughters/insert cylinder
/gate/layer6HorizontalFibreCylinder1/placement/setTranslation  0.0 -0.8125 0.825 mm
/gate/layer6HorizontalFibreCylinder1/geometry/setRmin 0.0 mm
/gate/layer6HorizontalFibreCylinder1/geometry/setRmax 0.0035 mm
/gate/layer6HorizontalFibreCylinder1/geometry/setHeight 10.00 mm
/gate/layer6HorizontalFibreCylinder1/placement/setRotationAxis 0 1 0
/gate/layer6HorizontalFibreCylinder1/placement/setRotationAngle 90. deg
/gate/layer6HorizontalFibreCylinder1/setMaterial Carbon
/gate/layer6HorizontalFibreCylinder1/vis/forceSolid
/gate/layer6HorizontalFibreCylinder1/vis/setColor gray

/gate/layer6HorizontalFibreCylinder1/repeaters/insert genericRepeater
/gate/layer6HorizontalFibreCylinder1/genericRepeater/setPlacementsFilename
    .../placementsGATE2573PoissionDiskFlatBundle90rot_v5.placements
/gate/layer6HorizontalFibreCylinder1/genericRepeater/useRelativeTranslation 1

/gate/epoxyBox/daughters/name layer6HorizontalFibreCylinder2
/gate/epoxyBox/daughters/insert cylinder
/gate/layer6HorizontalFibreCylinder2/placement/setTranslation  0.0 -0.8125 -1.175 mm
/gate/layer6HorizontalFibreCylinder2/geometry/setRmin 0.0 mm
/gate/layer6HorizontalFibreCylinder2/geometry/setRmax 0.0035 mm
/gate/layer6HorizontalFibreCylinder2/geometry/setHeight 10.00 mm
/gate/layer6HorizontalFibreCylinder2/placement/setRotationAxis 0 1 0
/gate/layer6HorizontalFibreCylinder2/placement/setRotationAngle 90. deg
/gate/layer6HorizontalFibreCylinder2/setMaterial Carbon
/gate/layer6HorizontalFibreCylinder2/vis/forceSolid
```

```
/gate/layer6HorizontalFibreCylinder2/vis/setColor gray

/gate/layer6HorizontalFibreCylinder2/repeaters/insert genericRepeater
/gate/layer6HorizontalFibreCylinder2/genericRepeater/setPlacementsFilename
    .../placementsGATE2563PoissionDiskFlatBundle90rot_v6.placements
/gate/layer6HorizontalFibreCylinder2/genericRepeater/useRelativeTranslation 1

#/gate/epoxyBox/moves/insert rotation
#/gate/epoxyBox/rotation/setSpeed 0.9 deg/s
#/gate/epoxyBox/rotation/setAxis 0 0 1

/gate/epoxyBox/moves/insert translation
/gate/epoxyBox/translation/setSpeed 0 0.010 0 mm/s

/gate/epoxyBox/attachPhantomSD
#/gate/CarbonCylinder/attachPhantomSD
/gate/layer2HorizontalFibreCylinder1/attachPhantomSD
/gate/layer1VerticalFibreCylinder1/attachPhantomSD
/gate/layer2HorizontalFibreCylinder2/attachPhantomSD
/gate/layer1VerticalFibreCylinder2/attachPhantomSD
/gate/layer4HorizontalFibreCylinder1/attachPhantomSD
/gate/layer3VerticalFibreCylinder1/attachPhantomSD
/gate/layer4HorizontalFibreCylinder2/attachPhantomSD
/gate/layer3VerticalFibreCylinder2/attachPhantomSD
/gate/layer6HorizontalFibreCylinder1/attachPhantomSD
/gate/layer5VerticalFibreCylinder1/attachPhantomSD
/gate/layer6HorizontalFibreCylinder2/attachPhantomSD
/gate/layer5VerticalFibreCylinder2/attachPhantomSD

#=====================================================
# PHYSICS
#=====================================================

/gate/physics/addProcess PhotoElectric
/gate/physics/processes/PhotoElectric/setModel StandardModel

/gate/physics/addProcess Compton
/gate/physics/processes/Compton/setModel StandardModel

/gate/physics/addProcess RayleighScattering
/gate/physics/processes/RayleighScattering/setModel PenelopeModel

/gate/physics/addProcess ElectronIonisation
/gate/physics/processes/ElectronIonisation/setModel StandardModel e-
/gate/physics/processes/ElectronIonisation/setModel StandardModel e+

/gate/physics/addProcess Bremsstrahlung
/gate/physics/processes/Bremsstrahlung/setModel StandardModel e-
/gate/physics/processes/Bremsstrahlung/setModel StandardModel e+

/gate/physics/addProcess eMultipleScattering e+
/gate/physics/addProcess eMultipleScattering e-

/gate/physics/addProcess XrayRefraction #decrement of real part
/gate/refractiveindex/setRefractionIndex Air 0.010 0.0
/gate/refractiveindex/setRefractionIndex Air 0.020 0.0
/gate/refractiveindex/setRefractionIndex Air 0.030 0.0
/gate/refractiveindex/setRefractionIndex Air 0.040 0.0

/gate/refractiveindex/setRefractionIndex Silicon 0.010 0.0 #0.0000171802239
/gate/refractiveindex/setRefractionIndex Silicon 0.020 0.0 #0.00000458362365
/gate/refractiveindex/setRefractionIndex Silicon 0.030 0.0 #0.00000206079153
```

```
/gate/refractiveindex/setRefractionIndex Silicon 0.040 0.0 #0.0000020607915З
```

```
/gate/refractiveindex/setRefractionIndex Epoxy 0.020000000 0.000000536910477000000
/gate/refractiveindex/setRefractionIndex Epoxy 0.020040588 0.000000534735705000000
/gate/refractiveindex/setRefractionIndex Epoxy 0.020081258 0.000000532569800000000
/gate/refractiveindex/setRefractionIndex Epoxy 0.020122010 0.000000530412763000000
/gate/refractiveindex/setRefractionIndex Epoxy 0.020162844 0.000000528264593000000
/gate/refractiveindex/setRefractionIndex Epoxy 0.020203764 0.000000526124893000000
/gate/refractiveindex/setRefractionIndex Epoxy 0.020244766 0.000000523993947000000
/gate/refractiveindex/setRefractionIndex Epoxy 0.020285850 0.000000521871641000000
/gate/refractiveindex/setRefractionIndex Epoxy 0.020327018 0.000000519757975000000
/gate/refractiveindex/setRefractionIndex Epoxy 0.020368268 0.000000517652950000000
/gate/refractiveindex/setRefractionIndex Epoxy 0.020409604 0.000000515556280000000
/gate/refractiveindex/setRefractionIndex Epoxy 0.020451022 0.000000513468194000000
/gate/refractiveindex/setRefractionIndex Epoxy 0.020492525 0.000000511388464000000
/gate/refractiveindex/setRefractionIndex Epoxy 0.020534113 0.000000509317147000000
/gate/refractiveindex/setRefractionIndex Epoxy 0.020575783 0.000000507254470000000
/gate/refractiveindex/setRefractionIndex Epoxy 0.020617539 0.000000505199978000000
/gate/refractiveindex/setRefractionIndex Epoxy 0.020659381 0.000000503153785000000
/gate/refractiveindex/setRefractionIndex Epoxy 0.020701307 0.000000501115835000000
/gate/refractiveindex/setRefractionIndex Epoxy 0.020743318 0.000000499086184000000
/gate/refractiveindex/setRefractionIndex Epoxy 0.020785412 0.000000497064946000000
/gate/refractiveindex/setRefractionIndex Epoxy 0.020827594 0.000000495051779000000
/gate/refractiveindex/setRefractionIndex Epoxy 0.020869863 0.000000493046571000000
/gate/refractiveindex/setRefractionIndex Epoxy 0.020912215 0.000000491049775000000
/gate/refractiveindex/setRefractionIndex Epoxy 0.020954654 0.000000489060938000000
/gate/refractiveindex/setRefractionIndex Epoxy 0.020997178 0.000000487080229000000
/gate/refractiveindex/setRefractionIndex Epoxy 0.021039791 0.000000485107421000000
/gate/refractiveindex/setRefractionIndex Epoxy 0.021082486 0.000000483142799000000
/gate/refractiveindex/setRefractionIndex Epoxy 0.021125272 0.000000481186021000000
/gate/refractiveindex/setRefractionIndex Epoxy 0.021168145 0.000000479237144000000
/gate/refractiveindex/setRefractionIndex Epoxy 0.021211102 0.000000477296339000000
/gate/refractiveindex/setRefractionIndex Epoxy 0.021254147 0.000000475363350000000
/gate/refractiveindex/setRefractionIndex Epoxy 0.021297281 0.000000473438035000000
/gate/refractiveindex/setRefractionIndex Epoxy 0.021340502 0.000000471520593000000
/gate/refractiveindex/setRefractionIndex Epoxy 0.021383809 0.000000469611024000000
/gate/refractiveindex/setRefractionIndex Epoxy 0.021427205 0.000000467709128000000
/gate/refractiveindex/setRefractionIndex Epoxy 0.021470688 0.000000465814992000000
/gate/refractiveindex/setRefractionIndex Epoxy 0.021514262 0.000000463928359000000
/gate/refractiveindex/setRefractionIndex Epoxy 0.021557920 0.000000462049570000000
/gate/refractiveindex/setRefractionIndex Epoxy 0.021601670 0.000000460178256000000
/gate/refractiveindex/setRefractionIndex Epoxy 0.021645508 0.000000458314531000000
/gate/refractiveindex/setRefractionIndex Epoxy 0.021689436 0.000000456458309000000
/gate/refractiveindex/setRefractionIndex Epoxy 0.021733451 0.000000454609733000000
/gate/refractiveindex/setRefractionIndex Epoxy 0.021777557 0.000000452768603000000
/gate/refractiveindex/setRefractionIndex Epoxy 0.021821752 0.000000450934976000000
/gate/refractiveindex/setRefractionIndex Epoxy 0.021866037 0.000000449108768000000
/gate/refractiveindex/setRefractionIndex Epoxy 0.021910412 0.000000447289949000000
/gate/refractiveindex/setRefractionIndex Epoxy 0.021954875 0.000000445478577000000
/gate/refractiveindex/setRefractionIndex Epoxy 0.021999430 0.000000443674509000000
/gate/refractiveindex/setRefractionIndex Epoxy 0.022044076 0.000000441877631000000
/gate/refractiveindex/setRefractionIndex Epoxy 0.022088811 0.000000440088201000000
/gate/refractiveindex/setRefractionIndex Epoxy 0.022133639 0.000000438305904000000
/gate/refractiveindex/setRefractionIndex Epoxy 0.022178557 0.000000436530883000000
/gate/refractiveindex/setRefractionIndex Epoxy 0.022223566 0.000000434762995000000
/gate/refractiveindex/setRefractionIndex Epoxy 0.022268664 0.000000433002413000000
/gate/refractiveindex/setRefractionIndex Epoxy 0.022313857 0.000000431248793000000
/gate/refractiveindex/setRefractionIndex Epoxy 0.022359141 0.000000429502393000000
/gate/refractiveindex/setRefractionIndex Epoxy 0.022404516 0.000000427763041000000
/gate/refractiveindex/setRefractionIndex Epoxy 0.022449982 0.000000426030738000000
/gate/refractiveindex/setRefractionIndex Epoxy 0.022495541 0.000000424305483000000
```

```
/gate/refractiveindex/setRefractionIndex Epoxy 0.022541193 0.000000422587220000000
/gate/refractiveindex/setRefractionIndex Epoxy 0.022586940 0.000000420875807000000
/gate/refractiveindex/setRefractionIndex Epoxy 0.022632775 0.000000419171499000000
/gate/refractiveindex/setRefractionIndex Epoxy 0.022678707 0.000000417473956000000
/gate/refractiveindex/setRefractionIndex Epoxy 0.022724731 0.000000415783347000000
/gate/refractiveindex/setRefractionIndex Epoxy 0.022770848 0.000000414099588000000
/gate/refractiveindex/setRefractionIndex Epoxy 0.022817059 0.000000412422651000000
/gate/refractiveindex/setRefractionIndex Epoxy 0.022863361 0.000000410752563000000
/gate/refractiveindex/setRefractionIndex Epoxy 0.022909760 0.000000409089125000000
/gate/refractiveindex/setRefractionIndex Epoxy 0.022956254 0.000000407432424000000
/gate/refractiveindex/setRefractionIndex Epoxy 0.023002842 0.000000405782430000000
/gate/refractiveindex/setRefractionIndex Epoxy 0.023049523 0.000000404139200000000
/gate/refractiveindex/setRefractionIndex Epoxy 0.023096299 0.000000402502593000000
/gate/refractiveindex/setRefractionIndex Epoxy 0.023143170 0.000000400872608000000
/gate/refractiveindex/setRefractionIndex Epoxy 0.023190137 0.000000399249245000000
/gate/refractiveindex/setRefractionIndex Epoxy 0.023237197 0.000000397632505000000
/gate/refractiveindex/setRefractionIndex Epoxy 0.023284354 0.000000396022358000000
/gate/refractiveindex/setRefractionIndex Epoxy 0.023331609 0.000000394418606000000
/gate/refractiveindex/setRefractionIndex Epoxy 0.023378957 0.000000392821505000000
/gate/refractiveindex/setRefractionIndex Epoxy 0.023426402 0.000000391230827000000
/gate/refractiveindex/setRefractionIndex Epoxy 0.023473941 0.000000389646686000000
/gate/refractiveindex/setRefractionIndex Epoxy 0.023521580 0.000000388068770000000
/gate/refractiveindex/setRefractionIndex Epoxy 0.023569315 0.000000386497334000000
/gate/refractiveindex/setRefractionIndex Epoxy 0.023617147 0.000000384932207000000
/gate/refractiveindex/setRefractionIndex Epoxy 0.023665076 0.000000383373418000000
/gate/refractiveindex/setRefractionIndex Epoxy 0.023713100 0.000000381820996000000
/gate/refractiveindex/setRefractionIndex Epoxy 0.023761223 0.000000380274827000000
/gate/refractiveindex/setRefractionIndex Epoxy 0.023809443 0.000000378734939000000
/gate/refractiveindex/setRefractionIndex Epoxy 0.023857760 0.000000377201332000000
/gate/refractiveindex/setRefractionIndex Epoxy 0.023906178 0.000000375673835000000
/gate/refractiveindex/setRefractionIndex Epoxy 0.023954691 0.000000374152592000000
/gate/refractiveindex/setRefractionIndex Epoxy 0.024003305 0.000000372637487000000
/gate/refractiveindex/setRefractionIndex Epoxy 0.024052020 0.000000371128493000000
/gate/refractiveindex/setRefractionIndex Epoxy 0.024100828 0.000000369625752000000
/gate/refractiveindex/setRefractionIndex Epoxy 0.024149738 0.000000368129008000000
/gate/refractiveindex/setRefractionIndex Epoxy 0.024198746 0.000000366638375000000
/gate/refractiveindex/setRefractionIndex Epoxy 0.024247856 0.000000365153710000000
/gate/refractiveindex/setRefractionIndex Epoxy 0.024297063 0.000000363675156000000
/gate/refractiveindex/setRefractionIndex Epoxy 0.024346373 0.000000362202428000000
/gate/refractiveindex/setRefractionIndex Epoxy 0.024395781 0.000000360735811000000
/gate/refractiveindex/setRefractionIndex Epoxy 0.024445289 0.000000359275134000000
/gate/refractiveindex/setRefractionIndex Epoxy 0.024494898 0.000000357820312000000
/gate/refractiveindex/setRefractionIndex Epoxy 0.024544606 0.000000356371515000000
/gate/refractiveindex/setRefractionIndex Epoxy 0.024594416 0.000000354928460000000
/gate/refractiveindex/setRefractionIndex Epoxy 0.024644330 0.000000353491259000000
/gate/refractiveindex/setRefractionIndex Epoxy 0.024694342 0.000000352059885000000
/gate/refractiveindex/setRefractionIndex Epoxy 0.024744455 0.000000350634338000000
/gate/refractiveindex/setRefractionIndex Epoxy 0.024794672 0.000000349214559000000
/gate/refractiveindex/setRefractionIndex Epoxy 0.024844990 0.000000347800579000000
/gate/refractiveindex/setRefractionIndex Epoxy 0.024895410 0.000000346392284000000
/gate/refractiveindex/setRefractionIndex Epoxy 0.024945932 0.000000344989701000000
/gate/refractiveindex/setRefractionIndex Epoxy 0.024996557 0.000000343592802000000
/gate/refractiveindex/setRefractionIndex Epoxy 0.025047283 0.000000342201560000000
/gate/refractiveindex/setRefractionIndex Epoxy 0.025098113 0.000000340815973000000
/gate/refractiveindex/setRefractionIndex Epoxy 0.025149047 0.000000339435985000000
/gate/refractiveindex/setRefractionIndex Epoxy 0.025200086 0.000000338061540000000
/gate/refractiveindex/setRefractionIndex Epoxy 0.025251227 0.000000336692665000000
/gate/refractiveindex/setRefractionIndex Epoxy 0.025302471 0.000000335329418000000
/gate/refractiveindex/setRefractionIndex Epoxy 0.025353818 0.000000333971684000000
/gate/refractiveindex/setRefractionIndex Epoxy 0.025405272 0.000000332619379000000
/gate/refractiveindex/setRefractionIndex Epoxy 0.025456828 0.000000331272616000000
/gate/refractiveindex/setRefractionIndex Epoxy 0.025508490 0.000000329931254000000
```

```
/gate/refractiveindex/setRefractionIndex Epoxy 0.025560258 0.000000328595348000000
/gate/refractiveindex/setRefractionIndex Epoxy 0.025612127 0.000000327264900000000
/gate/refractiveindex/setRefractionIndex Epoxy 0.025664106 0.000000325939766000000
/gate/refractiveindex/setRefractionIndex Epoxy 0.025716188 0.000000324620004000000
/gate/refractiveindex/setRefractionIndex Epoxy 0.025768375 0.000000323305613000000
/gate/refractiveindex/setRefractionIndex Epoxy 0.025820670 0.000000321996509000000
/gate/refractiveindex/setRefractionIndex Epoxy 0.025873070 0.000000320692749000000
/gate/refractiveindex/setRefractionIndex Epoxy 0.025925574 0.000000319394303000000
/gate/refractiveindex/setRefractionIndex Epoxy 0.025978190 0.000000318100973000000
/gate/refractiveindex/setRefractionIndex Epoxy 0.026030908 0.000000316813043000000
/gate/refractiveindex/setRefractionIndex Epoxy 0.026083734 0.000000315530286000000
/gate/refractiveindex/setRefractionIndex Epoxy 0.026136668 0.000000314252702000000
/gate/refractiveindex/setRefractionIndex Epoxy 0.026189709 0.000000312980319000000
/gate/refractiveindex/setRefractionIndex Epoxy 0.026242859 0.000000311713052000000
/gate/refractiveindex/setRefractionIndex Epoxy 0.026296115 0.000000310450957000000
/gate/refractiveindex/setRefractionIndex Epoxy 0.026349481 0.000000309193922000000
/gate/refractiveindex/setRefractionIndex Epoxy 0.026402953 0.000000307942031000000
/gate/refractiveindex/setRefractionIndex Epoxy 0.026456535 0.000000306695227000000
/gate/refractiveindex/setRefractionIndex Epoxy 0.026510225 0.000000305453511000000
/gate/refractiveindex/setRefractionIndex Epoxy 0.026564025 0.000000304216769000000
/gate/refractiveindex/setRefractionIndex Epoxy 0.026617932 0.000000302985114000000
/gate/refractiveindex/setRefractionIndex Epoxy 0.026671951 0.000000301758348000000
/gate/refractiveindex/setRefractionIndex Epoxy 0.026726078 0.000000300536612000000
/gate/refractiveindex/setRefractionIndex Epoxy 0.026780316 0.000000299319822000000
/gate/refractiveindex/setRefractionIndex Epoxy 0.026834664 0.000000298107892000000
/gate/refractiveindex/setRefractionIndex Epoxy 0.026889121 0.000000296900936000000
/gate/refractiveindex/setRefractionIndex Epoxy 0.026943691 0.000000295698811000000
/gate/refractiveindex/setRefractionIndex Epoxy 0.026998369 0.000000294501604000000
/gate/refractiveindex/setRefractionIndex Epoxy 0.027053158 0.000000293309256000000
/gate/refractiveindex/setRefractionIndex Epoxy 0.027108061 0.000000292121683000000
/gate/refractiveindex/setRefractionIndex Epoxy 0.027163072 0.000000290938971000000
/gate/refractiveindex/setRefractionIndex Epoxy 0.027218197 0.000000289761005000000
/gate/refractiveindex/setRefractionIndex Epoxy 0.027273434 0.000000288587785000000
/gate/refractiveindex/setRefractionIndex Epoxy 0.027328781 0.000000287419397000000
/gate/refractiveindex/setRefractionIndex Epoxy 0.027384242 0.000000286255670000000
/gate/refractiveindex/setRefractionIndex Epoxy 0.027439816 0.000000285096661000000
/gate/refractiveindex/setRefractionIndex Epoxy 0.027495502 0.000000283942342000000
/gate/refractiveindex/setRefractionIndex Epoxy 0.027551301 0.000000282792769000000
/gate/refractiveindex/setRefractionIndex Epoxy 0.027607213 0.000000281647800000000
/gate/refractiveindex/setRefractionIndex Epoxy 0.027663238 0.000000280507464000000
/gate/refractiveindex/setRefractionIndex Epoxy 0.027719377 0.000000279371790000000
/gate/refractiveindex/setRefractionIndex Epoxy 0.027775631 0.000000278240691000000
/gate/refractiveindex/setRefractionIndex Epoxy 0.027831998 0.000000277114196000000
/gate/refractiveindex/setRefractionIndex Epoxy 0.027888479 0.000000275992278000000
/gate/refractiveindex/setRefractionIndex Epoxy 0.027945074 0.000000274874935000000
/gate/refractiveindex/setRefractionIndex Epoxy 0.028001787 0.000000273762055000000
/gate/refractiveindex/setRefractionIndex Epoxy 0.028058613 0.000000272653693000000
/gate/refractiveindex/setRefractionIndex Epoxy 0.028115555 0.000000271549823000000
/gate/refractiveindex/setRefractionIndex Epoxy 0.028172611 0.000000270450414000000
/gate/refractiveindex/setRefractionIndex Epoxy 0.028229785 0.000000269355496000000
/gate/refractiveindex/setRefractionIndex Epoxy 0.028287074 0.000000268264984000000
/gate/refractiveindex/setRefractionIndex Epoxy 0.028344479 0.000000267178933000000
/gate/refractiveindex/setRefractionIndex Epoxy 0.028402002 0.000000266097203000000
/gate/refractiveindex/setRefractionIndex Epoxy 0.028459639 0.000000265019935000000
/gate/refractiveindex/setRefractionIndex Epoxy 0.028517395 0.000000263946987000000
/gate/refractiveindex/setRefractionIndex Epoxy 0.028575268 0.000000262878388000000
/gate/refractiveindex/setRefractionIndex Epoxy 0.028633258 0.000000261814080000000
/gate/refractiveindex/setRefractionIndex Epoxy 0.028691365 0.000000260754149000000
/gate/refractiveindex/setRefractionIndex Epoxy 0.028749592 0.000000259698453000000
/gate/refractiveindex/setRefractionIndex Epoxy 0.028807936 0.000000258647049000000
/gate/refractiveindex/setRefractionIndex Epoxy 0.028866398 0.000000257599908000000
/gate/refractiveindex/setRefractionIndex Epoxy 0.028924979 0.000000256557030000000
```

```
/gate/refractiveindex/setRefractionIndex Epoxy 0.028983680 0.000000255518330000000
/gate/refractiveindex/setRefractionIndex Epoxy 0.029042496 0.000000254483894000000
/gate/refractiveindex/setRefractionIndex Epoxy 0.029101436 0.000000253453578000000
/gate/refractiveindex/setRefractionIndex Epoxy 0.029160492 0.000000252427526000000
/gate/refractiveindex/setRefractionIndex Epoxy 0.029219670 0.000000251405567000000
/gate/refractiveindex/setRefractionIndex Epoxy 0.029278971 0.000000250387757000000
/gate/refractiveindex/setRefractionIndex Epoxy 0.029338389 0.000000249374068000000
/gate/refractiveindex/setRefractionIndex Epoxy 0.029397926 0.000000248364501000000
/gate/refractiveindex/setRefractionIndex Epoxy 0.029457586 0.000000247358997000000
/gate/refractiveindex/setRefractionIndex Epoxy 0.029517367 0.000000246357587000000
/gate/refractiveindex/setRefractionIndex Epoxy 0.029577270 0.000000245360155000000
/gate/refractiveindex/setRefractionIndex Epoxy 0.029637291 0.000000244366845000000
/gate/refractiveindex/setRefractionIndex Epoxy 0.029697438 0.000000243377485000000
/gate/refractiveindex/setRefractionIndex Epoxy 0.029757705 0.000000242392190000000
/gate/refractiveindex/setRefractionIndex Epoxy 0.029818094 0.000000241410845000000
/gate/refractiveindex/setRefractionIndex Epoxy 0.029878607 0.000000240433479000000
/gate/refractiveindex/setRefractionIndex Epoxy 0.029939242 0.000000239460093000000
/gate/refractiveindex/setRefractionIndex Epoxy 0.030000000 0.000000238490628000000

/gate/refractiveindex/setRefractionIndex Carbon 0.020000000 0.000001141153690
/gate/refractiveindex/setRefractionIndex Carbon 0.020040588 0.000001136532890
/gate/refractiveindex/setRefractionIndex Carbon 0.020081258 0.000001131930960
/gate/refractiveindex/setRefractionIndex Carbon 0.020122010 0.000001127348010
/gate/refractiveindex/setRefractionIndex Carbon 0.020162844 0.000001122783830
/gate/refractiveindex/setRefractionIndex Carbon 0.020203764 0.000001118237720
/gate/refractiveindex/setRefractionIndex Carbon 0.020244766 0.000001113710140
/gate/refractiveindex/setRefractionIndex Carbon 0.020285850 0.000001109200980
/gate/refractiveindex/setRefractionIndex Carbon 0.020327018 0.000001104710120
/gate/refractiveindex/setRefractionIndex Carbon 0.020368268 0.000001100237680
/gate/refractiveindex/setRefractionIndex Carbon 0.020409604 0.000001095782860
/gate/refractiveindex/setRefractionIndex Carbon 0.020451022 0.000001091346230
/gate/refractiveindex/setRefractionIndex Carbon 0.020492525 0.000001086927340
/gate/refractiveindex/setRefractionIndex Carbon 0.020534113 0.000001082526300
/gate/refractiveindex/setRefractionIndex Carbon 0.020575783 0.000001078143330
/gate/refractiveindex/setRefractionIndex Carbon 0.020617539 0.000001073778090
/gate/refractiveindex/setRefractionIndex Carbon 0.020659381 0.000001069430250
/gate/refractiveindex/setRefractionIndex Carbon 0.020701307 0.000001065100150
/gate/refractiveindex/setRefractionIndex Carbon 0.020743318 0.000001060787550
/gate/refractiveindex/setRefractionIndex Carbon 0.020785412 0.000001056492690
/gate/refractiveindex/setRefractionIndex Carbon 0.020827594 0.000001052215110
/gate/refractiveindex/setRefractionIndex Carbon 0.020869863 0.000001047954360
/gate/refractiveindex/setRefractionIndex Carbon 0.020912215 0.000001043711340
/gate/refractiveindex/setRefractionIndex Carbon 0.020954654 0.000001039485480
/gate/refractiveindex/setRefractionIndex Carbon 0.020997178 0.000001035276800
/gate/refractiveindex/setRefractionIndex Carbon 0.021039791 0.000001031084710
/gate/refractiveindex/setRefractionIndex Carbon 0.021082486 0.000001026910240
/gate/refractiveindex/setRefractionIndex Carbon 0.021125272 0.000001022752370
/gate/refractiveindex/setRefractionIndex Carbon 0.021168145 0.000001018611330
/gate/refractiveindex/setRefractionIndex Carbon 0.021211102 0.000001014487450
/gate/refractiveindex/setRefractionIndex Carbon 0.021254147 0.000001010380060
/gate/refractiveindex/setRefractionIndex Carbon 0.021297281 0.000001006289040
/gate/refractiveindex/setRefractionIndex Carbon 0.021340502 0.000001002214840
/gate/refractiveindex/setRefractionIndex Carbon 0.021383809 0.000000998157248
/gate/refractiveindex/setRefractionIndex Carbon 0.021427205 0.000000994115908
/gate/refractiveindex/setRefractionIndex Carbon 0.021470688 0.000000990091166
/gate/refractiveindex/setRefractionIndex Carbon 0.021514262 0.000000986082341
/gate/refractiveindex/setRefractionIndex Carbon 0.021557920 0.000000982090114
/gate/refractiveindex/setRefractionIndex Carbon 0.021601670 0.000000978113803
/gate/refractiveindex/setRefractionIndex Carbon 0.021645508 0.000000974153636
/gate/refractiveindex/setRefractionIndex Carbon 0.021689436 0.000000970209499
/gate/refractiveindex/setRefractionIndex Carbon 0.021733451 0.000000966281391
/gate/refractiveindex/setRefractionIndex Carbon 0.021777557 0.000000962369199
```

```
/gate/refractiveindex/setRefractionIndex Carbon 0.021821752 0.000000958472810
/gate/refractiveindex/setRefractionIndex Carbon 0.021866037 0.000000954592224
/gate/refractiveindex/setRefractionIndex Carbon 0.021910412 0.000000950727213
/gate/refractiveindex/setRefractionIndex Carbon 0.021954875 0.000000946878060
/gate/refractiveindex/setRefractionIndex Carbon 0.021999430 0.000000943044427
/gate/refractiveindex/setRefractionIndex Carbon 0.022044076 0.000000939226140
/gate/refractiveindex/setRefractionIndex Carbon 0.022088811 0.000000935423600
/gate/refractiveindex/setRefractionIndex Carbon 0.022133639 0.000000931636293
/gate/refractiveindex/setRefractionIndex Carbon 0.022178557 0.000000927864505
/gate/refractiveindex/setRefractionIndex Carbon 0.022223566 0.000000924107951
/gate/refractiveindex/setRefractionIndex Carbon 0.022268664 0.000000920366801
/gate/refractiveindex/setRefractionIndex Carbon 0.022313857 0.000000916640545
/gate/refractiveindex/setRefractionIndex Carbon 0.022359141 0.000000912929465
/gate/refractiveindex/setRefractionIndex Carbon 0.022404516 0.000000909233506
/gate/refractiveindex/setRefractionIndex Carbon 0.022449982 0.000000905552383
/gate/refractiveindex/setRefractionIndex Carbon 0.022495541 0.000000901886381
/gate/refractiveindex/setRefractionIndex Carbon 0.022541193 0.000000898234987
/gate/refractiveindex/setRefractionIndex Carbon 0.022586940 0.000000894598315
/gate/refractiveindex/setRefractionIndex Carbon 0.022632775 0.000000890976651
/gate/refractiveindex/setRefractionIndex Carbon 0.022678707 0.000000887369424
/gate/refractiveindex/setRefractionIndex Carbon 0.022724731 0.000000883776920
/gate/refractiveindex/setRefractionIndex Carbon 0.022770848 0.000000880198911
/gate/refractiveindex/setRefractionIndex Carbon 0.022817059 0.000000876635340
/gate/refractiveindex/setRefractionIndex Carbon 0.022863361 0.000000873086435
/gate/refractiveindex/setRefractionIndex Carbon 0.022909760 0.000000869551627
/gate/refractiveindex/setRefractionIndex Carbon 0.022956254 0.000000866031144
/gate/refractiveindex/setRefractionIndex Carbon 0.023002842 0.000000862524871
/gate/refractiveindex/setRefractionIndex Carbon 0.023049523 0.000000859032923
/gate/refractiveindex/setRefractionIndex Carbon 0.023096299 0.000000855555129
/gate/refractiveindex/setRefractionIndex Carbon 0.023143170 0.000000852091375
/gate/refractiveindex/setRefractionIndex Carbon 0.023190137 0.000000848641662
/gate/refractiveindex/setRefractionIndex Carbon 0.023237197 0.000000845206102
/gate/refractiveindex/setRefractionIndex Carbon 0.023284354 0.000000841784470
/gate/refractiveindex/setRefractionIndex Carbon 0.023331609 0.000000838376479
/gate/refractiveindex/setRefractionIndex Carbon 0.023378957 0.000000834982529
/gate/refractiveindex/setRefractionIndex Carbon 0.023426402 0.000000831602222
/gate/refractiveindex/setRefractionIndex Carbon 0.023473941 0.000000828235784
/gate/refractiveindex/setRefractionIndex Carbon 0.023521580 0.000000824882704
/gate/refractiveindex/setRefractionIndex Carbon 0.023569315 0.000000821543324
/gate/refractiveindex/setRefractionIndex Carbon 0.023617147 0.000000818217245
/gate/refractiveindex/setRefractionIndex Carbon 0.023665076 0.000000814904638
/gate/refractiveindex/setRefractionIndex Carbon 0.023713100 0.000000811605503
/gate/refractiveindex/setRefractionIndex Carbon 0.023761223 0.000000808319669
/gate/refractiveindex/setRefractionIndex Carbon 0.023809443 0.000000805047193
/gate/refractiveindex/setRefractionIndex Carbon 0.023857760 0.000000801788019
/gate/refractiveindex/setRefractionIndex Carbon 0.023906178 0.000000798541919
/gate/refractiveindex/setRefractionIndex Carbon 0.023954691 0.000000795309063
/gate/refractiveindex/setRefractionIndex Carbon 0.024003305 0.000000792089281
/gate/refractiveindex/setRefractionIndex Carbon 0.024052020 0.000000788882517
/gate/refractiveindex/setRefractionIndex Carbon 0.024100828 0.000000785688940
/gate/refractiveindex/setRefractionIndex Carbon 0.024149738 0.000000782508152
/gate/refractiveindex/setRefractionIndex Carbon 0.024198746 0.000000779340382
/gate/refractiveindex/setRefractionIndex Carbon 0.024247856 0.000000776185288
/gate/refractiveindex/setRefractionIndex Carbon 0.024297063 0.000000773043212
/gate/refractiveindex/setRefractionIndex Carbon 0.024346373 0.000000769913470
/gate/refractiveindex/setRefractionIndex Carbon 0.024395781 0.000000766796745
/gate/refractiveindex/setRefractionIndex Carbon 0.024445289 0.000000763692697
/gate/refractiveindex/setRefractionIndex Carbon 0.024494898 0.000000760601154
/gate/refractiveindex/setRefractionIndex Carbon 0.024544606 0.000000757522287
/gate/refractiveindex/setRefractionIndex Carbon 0.024594416 0.000000754455698
/gate/refractiveindex/setRefractionIndex Carbon 0.024644330 0.000000751401444
/gate/refractiveindex/setRefractionIndex Carbon 0.024694342 0.000000748359696
```

```
/gate/refractiveindex/setRefractionIndex Carbon 0.024744455 0.000000745330340
/gate/refractiveindex/setRefractionIndex Carbon 0.024794672 0.000000742312977
/gate/refractiveindex/setRefractionIndex Carbon 0.024844990 0.000000739307836
/gate/refractiveindex/setRefractionIndex Carbon 0.024895410 0.000000736314803
/gate/refractiveindex/setRefractionIndex Carbon 0.024945932 0.000000733334105
/gate/refractiveindex/setRefractionIndex Carbon 0.024996557 0.000000730365343
/gate/refractiveindex/setRefractionIndex Carbon 0.025047283 0.000000727408576
/gate/refractiveindex/setRefractionIndex Carbon 0.025098113 0.000000724463860
/gate/refractiveindex/setRefractionIndex Carbon 0.025149047 0.000000721531023
/gate/refractiveindex/setRefractionIndex Carbon 0.025200086 0.000000718610067
/gate/refractiveindex/setRefractionIndex Carbon 0.025251227 0.000000715700992
/gate/refractiveindex/setRefractionIndex Carbon 0.025302471 0.000000712803796
/gate/refractiveindex/setRefractionIndex Carbon 0.025353818 0.000000709918311
/gate/refractiveindex/setRefractionIndex Carbon 0.025405272 0.000000707044478
/gate/refractiveindex/setRefractionIndex Carbon 0.025456828 0.000000704182241
/gate/refractiveindex/setRefractionIndex Carbon 0.025508490 0.000000701331601
/gate/refractiveindex/setRefractionIndex Carbon 0.025560258 0.000000698492443
/gate/refractiveindex/setRefractionIndex Carbon 0.025612127 0.000000695665051
/gate/refractiveindex/setRefractionIndex Carbon 0.025664106 0.000000692848801
/gate/refractiveindex/setRefractionIndex Carbon 0.025716188 0.000000690044033
/gate/refractiveindex/setRefractionIndex Carbon 0.025768375 0.000000687250690
/gate/refractiveindex/setRefractionIndex Carbon 0.025820670 0.000000684468603
/gate/refractiveindex/setRefractionIndex Carbon 0.025873070 0.000000681697770
/gate/refractiveindex/setRefractionIndex Carbon 0.025925574 0.000000678938250
/gate/refractiveindex/setRefractionIndex Carbon 0.025978190 0.000000676189757
/gate/refractiveindex/setRefractionIndex Carbon 0.026030908 0.000000673452519
/gate/refractiveindex/setRefractionIndex Carbon 0.026083734 0.000000670726251
/gate/refractiveindex/setRefractionIndex Carbon 0.026136668 0.000000668011069
/gate/refractiveindex/setRefractionIndex Carbon 0.026189709 0.000000665306914
/gate/refractiveindex/setRefractionIndex Carbon 0.026242859 0.000000662613616
/gate/refractiveindex/setRefractionIndex Carbon 0.026296115 0.000000659931345
/gate/refractiveindex/setRefractionIndex Carbon 0.026349481 0.000000657259818
/gate/refractiveindex/setRefractionIndex Carbon 0.026402953 0.000000654599205
/gate/refractiveindex/setRefractionIndex Carbon 0.026456535 0.000000651949449
/gate/refractiveindex/setRefractionIndex Carbon 0.026510225 0.000000649310437
/gate/refractiveindex/setRefractionIndex Carbon 0.026564025 0.000000646682054
/gate/refractiveindex/setRefractionIndex Carbon 0.026617932 0.000000644064471
/gate/refractiveindex/setRefractionIndex Carbon 0.026671951 0.000000641457291
/gate/refractiveindex/setRefractionIndex Carbon 0.026726078 0.000000638860740
/gate/refractiveindex/setRefractionIndex Carbon 0.026780316 0.000000636274649
/gate/refractiveindex/setRefractionIndex Carbon 0.026834664 0.000000633699017
/gate/refractiveindex/setRefractionIndex Carbon 0.026889121 0.000000631133730
/gate/refractiveindex/setRefractionIndex Carbon 0.026943691 0.000000628578732
/gate/refractiveindex/setRefractionIndex Carbon 0.026998369 0.000000626034250
/gate/refractiveindex/setRefractionIndex Carbon 0.027053158 0.000000623500057
/gate/refractiveindex/setRefractionIndex Carbon 0.027108061 0.000000620975982
/gate/refractiveindex/setRefractionIndex Carbon 0.027163072 0.000000618462252
/gate/refractiveindex/setRefractionIndex Carbon 0.027218197 0.000000615958641
/gate/refractiveindex/setRefractionIndex Carbon 0.027273434 0.000000613465147
/gate/refractiveindex/setRefractionIndex Carbon 0.027328781 0.000000610981942
/gate/refractiveindex/setRefractionIndex Carbon 0.027384242 0.000000608508742
/gate/refractiveindex/setRefractionIndex Carbon 0.027439816 0.000000606045489
/gate/refractiveindex/setRefractionIndex Carbon 0.027495502 0.000000603592298
/gate/refractiveindex/setRefractionIndex Carbon 0.027551301 0.000000601148997
/gate/refractiveindex/setRefractionIndex Carbon 0.027607213 0.000000598715644
/gate/refractiveindex/setRefractionIndex Carbon 0.027663238 0.000000596292068
/gate/refractiveindex/setRefractionIndex Carbon 0.027719377 0.000000593878326
/gate/refractiveindex/setRefractionIndex Carbon 0.027775631 0.000000591474361
/gate/refractiveindex/setRefractionIndex Carbon 0.027831998 0.000000589080116
/gate/refractiveindex/setRefractionIndex Carbon 0.027888479 0.000000586695649
/gate/refractiveindex/setRefractionIndex Carbon 0.027945074 0.000000584320787
/gate/refractiveindex/setRefractionIndex Carbon 0.028001787 0.000000581955476
```

```
/gate/refractiveindex/setRefractionIndex Carbon 0.028058613 0.000000579599714
/gate/refractiveindex/setRefractionIndex Carbon 0.028115555 0.000000577253559
/gate/refractiveindex/setRefractionIndex Carbon 0.028172611 0.000000574917010
/gate/refractiveindex/setRefractionIndex Carbon 0.028229785 0.000000572589897
/gate/refractiveindex/setRefractionIndex Carbon 0.028287074 0.000000570272164
/gate/refractiveindex/setRefractionIndex Carbon 0.028344479 0.000000567963980
/gate/refractiveindex/setRefractionIndex Carbon 0.028402002 0.000000565664948
/gate/refractiveindex/setRefractionIndex Carbon 0.028459639 0.000000563375352
/gate/refractiveindex/setRefractionIndex Carbon 0.028517395 0.000000561094964
/gate/refractiveindex/setRefractionIndex Carbon 0.028575268 0.000000558823785
/gate/refractiveindex/setRefractionIndex Carbon 0.028633258 0.000000556561758
/gate/refractiveindex/setRefractionIndex Carbon 0.028691365 0.000000554308883
/gate/refractiveindex/setRefractionIndex Carbon 0.028749592 0.000000552064989
/gate/refractiveindex/setRefractionIndex Carbon 0.028807936 0.000000549830361
/gate/refractiveindex/setRefractionIndex Carbon 0.028866398 0.000000547604657
/gate/refractiveindex/setRefractionIndex Carbon 0.028924979 0.000000545388048
/gate/refractiveindex/setRefractionIndex Carbon 0.028983680 0.000000543180363
/gate/refractiveindex/setRefractionIndex Carbon 0.029042496 0.000000540981659
/gate/refractiveindex/setRefractionIndex Carbon 0.029101436 0.000000538791880
/gate/refractiveindex/setRefractionIndex Carbon 0.029160492 0.000000536611083
/gate/refractiveindex/setRefractionIndex Carbon 0.029219670 0.000000534438982
/gate/refractiveindex/setRefractionIndex Carbon 0.029278971 0.000000532275692
/gate/refractiveindex/setRefractionIndex Carbon 0.029338389 0.000000530121156
/gate/refractiveindex/setRefractionIndex Carbon 0.029397926 0.000000527975487
/gate/refractiveindex/setRefractionIndex Carbon 0.029457586 0.000000525838345
/gate/refractiveindex/setRefractionIndex Carbon 0.029517367 0.000000523709900
/gate/refractiveindex/setRefractionIndex Carbon 0.029577270 0.000000521589982
/gate/refractiveindex/setRefractionIndex Carbon 0.029637291 0.000000519478647
/gate/refractiveindex/setRefractionIndex Carbon 0.029697438 0.000000517375838
/gate/refractiveindex/setRefractionIndex Carbon 0.029757705 0.000000515281556
/gate/refractiveindex/setRefractionIndex Carbon 0.029818094 0.000000513195744
/gate/refractiveindex/setRefractionIndex Carbon 0.029878607 0.000000511118344
/gate/refractiveindex/setRefractionIndex Carbon 0.029939242 0.000000509049414
/gate/refractiveindex/setRefractionIndex Carbon 0.030000000 0.000000506988840


/gate/physics/processList Enabled
/gate/physics/processList Initialized

#=====================================================
# SIMULATION STATISTICS
#=====================================================

#/gate/actor/addActor   SimulationStatisticActor stat
#/gate/actor/stat/save  .../stat-wavefront.txt

/gate/processGate/enable
/gate/processGate/detectPerfectCrystalEnergy
/gate/processGate/detectFluorescence

/gate/processGate/setGridX 50000
/gate/processGate/setGridY 100
/gate/processGate/setPhysicalGridX 5.0
/gate/processGate/setPhysicalGridY 0.010
/gate/processGate/setOutputNameReal .../ProjReal_CFRPphantom125B
/gate/processGate/setOutputNameImag .../ProjImag_CFRPphantom125B
/gate/processGate/setOutputNameCounts .../ProjCounts_CFRPphantom125B
/gate/processGate/enableGrid


#=====================================================
# INITIALISATION
```

```
#=====================================================

/gate/run/initialize

#=====================================================
# DIGITIZER
#=====================================================

/gate/digitizer/Singles/insert adder
/gate/digitizer/Singles/insert readout
/gate/digitizer/Singles/readout/setDepth 2
/gate/digitizer/Singles/insert thresholder
/gate/digitizer/Singles/thresholder/setThreshold 10 keV

#=====================================================
# SOURCE
#=====================================================

# Xray source (defined using a histogram to define the energy distribution)

/gate/source/addSource xraygun
/gate/source/verbose 0
/gate/source/xraygun/gps/verbose 0
/gate/source/xraygun/gps/particle gamma
/gate/source/xraygun/gps/type Plane
/gate/source/xraygun/gps/shape Rectangle
/gate/source/xraygun/gps/halfx 2.5 mm
/gate/source/xraygun/gps/halfy 0.005 mm
/gate/source/xraygun/gps/centre 0. 0. -2.4 cm
/gate/source/xraygun/gps/mintheta 0.0 deg
/gate/source/xraygun/gps/maxtheta 0.0 deg
/gate/source/xraygun/gps/angtype iso
/gate/source/xraygun/gps/energytype Arb
/gate/source/xraygun/gps/histname arb
/gate/source/xraygun/gps/histpoint  0.025 7
/gate/source/xraygun/gps/histpoint  0.025001  4
/gate/source/xraygun/gps/arbint Lin
/gate/source/list

#=====================================================
# VISUALISATION
#=====================================================

#/control/execute .../visu_test.mac

#=====================================================
# OUTPUTS
#=====================================================

/gate/output/allowNoOutput

# ROOT output
#/gate/output/root/enable
#/gate/output/root/setFileName .../flatFiberPhantom10M
#/gate/output/root/setRootHitFlag 0
#/gate/output/root/setRootSinglesFlag 1
#/gate/output/root/setRootNtupleFlag 0
#/gate/output/verbose 1

# Specific CT Image output
#/gate/output/imageCT/enable
#/gate/output/imageCT/setFileName .../wavefront_projection_flatFiberPhantom675M
```

```
#/gate/output/imageCT/verbose 0
# VRT (variance reduction technique) for CT
# (the random seed is proper to the VRT module)
#/gate/output/imageCT/vrtFactor 5
#/gate/output/imageCT/setStartSeed 567489

#=====================================================
# START ACQUISITION
#=====================================================

# JamesRandom Ranlux64 MersenneTwister
/gate/random/setEngineName MersenneTwister
/gate/random/setEngineSeed 2134567

/gate/application/setTotalNumberOfPrimaries 125000000000

/gate/application/setTimeSlice     1. s
/gate/application/setTimeStart     0.  s
/gate/application/setTimeStop      500. s

/gate/application/start
```

Appendix B

Comparison of GATE EI simulations to experimental FleXCT data

---

This appendix contains a comparison between an experimental EI dataset of a beryllium cylinder acquired with the FleXCT system, equipped with the masks designed in Chapter 5, and the corresponding Monte Carlo simulation using the extended version of GATE described in Chapter 3 and Chapter 4. The presented results show a good agreement between simulation and experiment.

B.1 Methods

The experimental data was acquired with the FleXCT system of imec-Vision Lab (De Samber et al., 2021) after installation of the EI masks designed in Chapter 5. The experiment was performed with a tube voltage of 40 kVp and 50 W source power, acquiring 3 averages at 3 s exposure time for each image (150 μm detector pixel size). In total, 11 equally spaced sample mask steps were taken in the [-50 μm, 50 μm] interval relative to perfect sample and detector mask alignment and contrast retrieval (Eq. (2.70)) was performed to extract the transmission and refraction images. The source-to-detector distance was 1800 mm and the distance between source and sample mask was 1200 mm. The sample was a 8.9 mm diameter beryllium cylinder (see Fig. B.1) and was placed at a distance of 55 mm behind the sample mask. The experiment was originally performed by N. Francken from imec-Vision Lab (Francken et al., 2024b), and a small portion of the results is reproduced here to provide a reference for comparison to simulations.

Next, the FleXCT experiment was modeled in GATE with the same geometrical parameters as in the experiment and a Gaussian focal spot of 50 μm. The detector consisted of 101×101 Gadox pixels with a thickness of 208 μm (150 μm pixel size). In addition, a 750 μm carbon layer and a 250 μm plastic layer were added in front of the detector

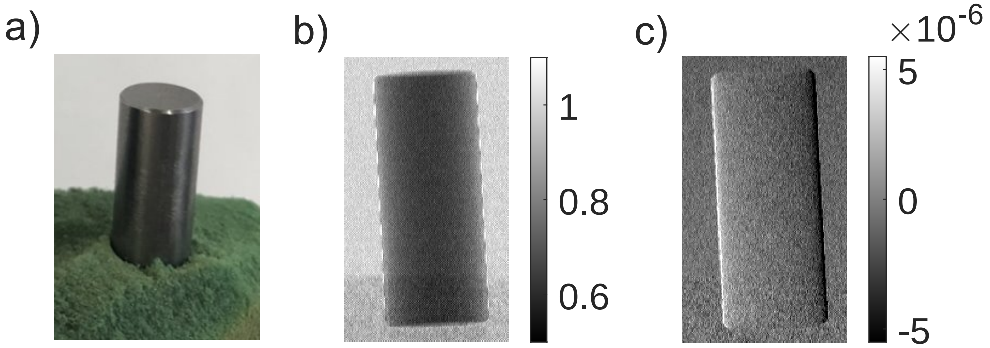

Figure B.1: a) Photograph of the 8.9 mm diameter beryllium cylinder used in the FleXCT experiment. b) Experimental EI transmission image of the cylinder. c) Experimental EI refraction image of the cylinder (in rad).

pixels, as well as a 200 μm amorphous silicon layer at the back. Detector electronics were not explicitly modeled in GATE and Gaussian blurring (0.5 pixel standard deviation) was applied to the images post simulation. The gratings were modeled explicitly as objects in the simulation and for each mask step 10^8 photons were simulated at the 40 kVp source. The slight tilt of the beryllium cylinder in the image plane was estimated from the experimental images and set to 2.9° relative to the vertical axis.

B.2 Results and discussion

The experimentally determined transmission and refraction images of the beryllium cylinder are shown in Fig. B.1. A slight tilt in the positioning of the cylinder can be perceived, which was estimated to be 2.9° from the transmission image. This tilt was subsequently applied to the digital phantom in the simulation. The simulation results after contrast retrieval are shown in Fig. B.2. Visual comparison of these results to the experimental images shown in Fig. B.1 shows a good qualitative agreement between experiment and simulation for both transmission and refraction.

Fig. B.3 shows a comparison of horizontal line profiles through the transmission and refraction images from Fig. B.1 and Fig. B.2. The plotted profiles are averages calculated from three adjacent central rows in the image, and the experimental profiles were calibrated such that the background signal was 100% for the transmission and 0 rad for the refraction, respectively. An excellent agreement is found for the transmission profiles. The refraction profiles show a good agreement between simulation and experiment as the refraction peaks show up that the expected positions, but some differences are also visible. First, the refraction is less pronounced in the experimental profile compared to the simulation. This can be explained by the tilt of the beryllium cylinder in the experimental data. Although an estimate of this tilt was included in the simulation, the estimation could

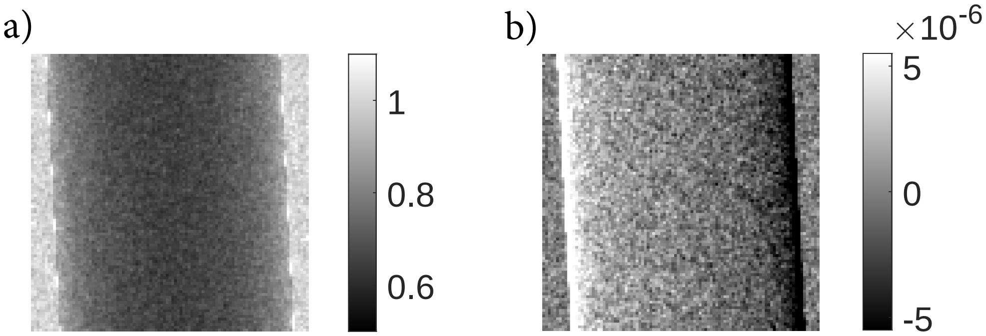

Figure B.2: a) Simulated EI transmission image of the 8.9 mm diameter beryllium cylinder. b) Simulated EI refraction image of the cylinder (in rad).

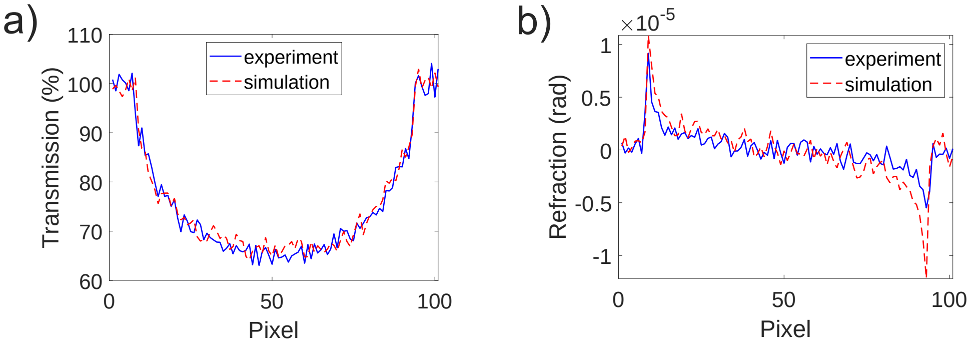

Figure B.3: Comparison of experimental and simulated (a) transmission profiles and (b) refraction profiles of the 8.9 mm diameter beryllium cylinder.

only be performed in the *xy*-plane. However, it is likely that the tilt in reality also had an out-of-plane component, which cannot be estimated from a single radiograph. Such an out-of-plane tilt will also affect the projected phase gradient, which can explain the difference between the simulated and experimental profiles. An additional factor potentially influencing the results is the fact that both the focal spot size and detector blurring are estimates of the unknown true values in the experiment. An experimental measurement of these values could further improve the accuracy of the simulation. In addition, it can be seen that the refraction peaks in the experimental profile are asymmetric, whereas the simulated profile shows the inversion symmetry expected from a symmetric cylinder sample. This discrepancy in the experimental data could be related to the tilt of the object or to the contrast retrieval procedure.

Overall, the results presented in this section indicate that the in-house version of GATE presented in this work is capable of realistically simulating EI X-ray phase contrast imaging experiments.

Appendix C

Effect of the virtual gratings approximation on the EI contrasts

This appendix contains a comparison between the contrasts retrieved from simulations with explicit and virtual gratings, as introduced in Chapter 4. The simulated setup, phantom, and acquisition scheme used for the explicit gratings simulation are identical to those used for the 2D virtual gratings simulation described in the main text (Section 4.3.2). The results presented in this section show good agreement between the contrasts retrieved from equivalent virtual and explicit grating simulations.

Fig. C.1, Fig. C.2, and Fig. C.3 show the difference maps between explicit and virtual grating results for all three contrasts retrieved from the 2D simulations with the beryllium sphere phantom (see 4.4.2), together with their corresponding histograms. The difference maps show no clear structure and the histograms of the differences appear to be centered around zero, implying that the differences exhibit a high degree of randomness. This indicates that the virtual and explicit grating simulation results are highly similar for all three contrast types, apart from statistical fluctuations. To illustrate the similarity between explicit and virtual gratings simulations results further, horizontal line profiles are taken along the central rows of the contrast images. These profiles are shown for all three contrasts in Fig. C.4, confirming that the virtual and explicit grating simulation results are matching. As can be seen from these plots, there is a difference between the two grating models in the magnitude of the statistical fluctuations, which is mostly apparent in the AC and DPC profiles. This is explained by the fact that the same set of photons is used for the generation of all the mask steps when using virtual gratings, whereas for the explicit grating simulations a separate MC simulation is performed for every mask step. This results in different noise properties in the stepping images, and therefore in the retrieved contrast images. Overall, the explicit and virtual grating simulations are in good agreement, confirming the validity of the virtual gratings approximation.

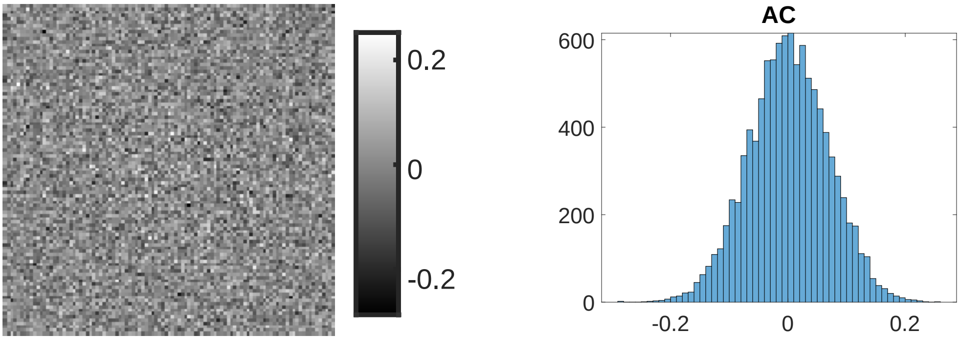

Figure C.1: Map and histogram of the pixelwise differences between the attenuation contrast retrieved from simulations with virtual and explicit gratings (arbitrary units).

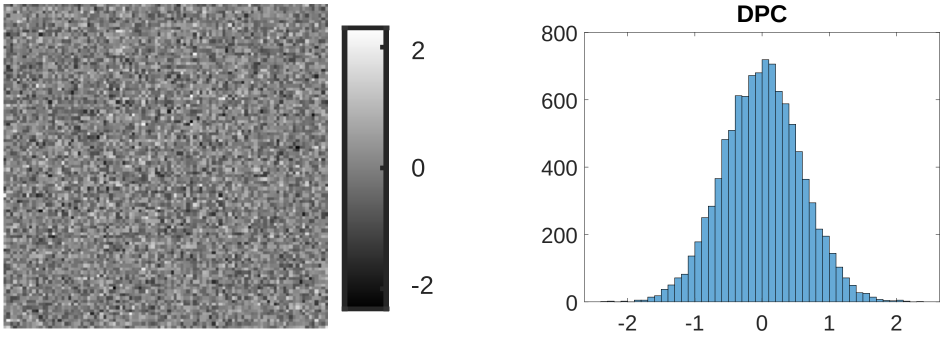

Figure C.2: Map and histogram of the pixelwise differences between the differential phase contrast retrieved from simulations with virtual and explicit gratings (arbitrary units).

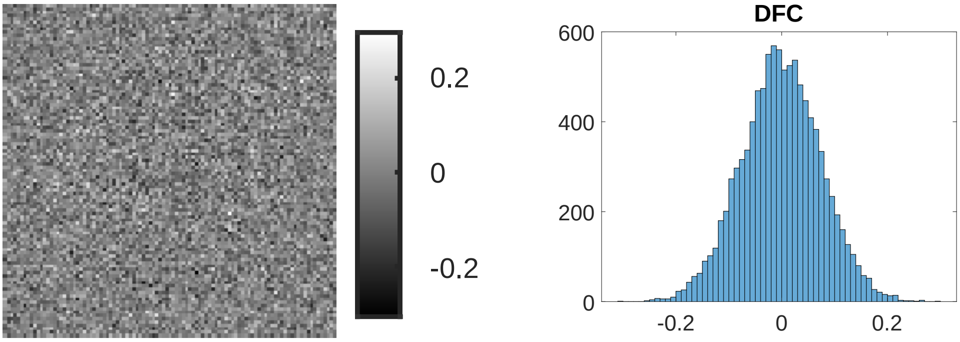

Figure C.3: Map and histogram of the pixelwise differences between the dark field contrast retrieved from simulations with virtual and explicit gratings (arbitrary units).

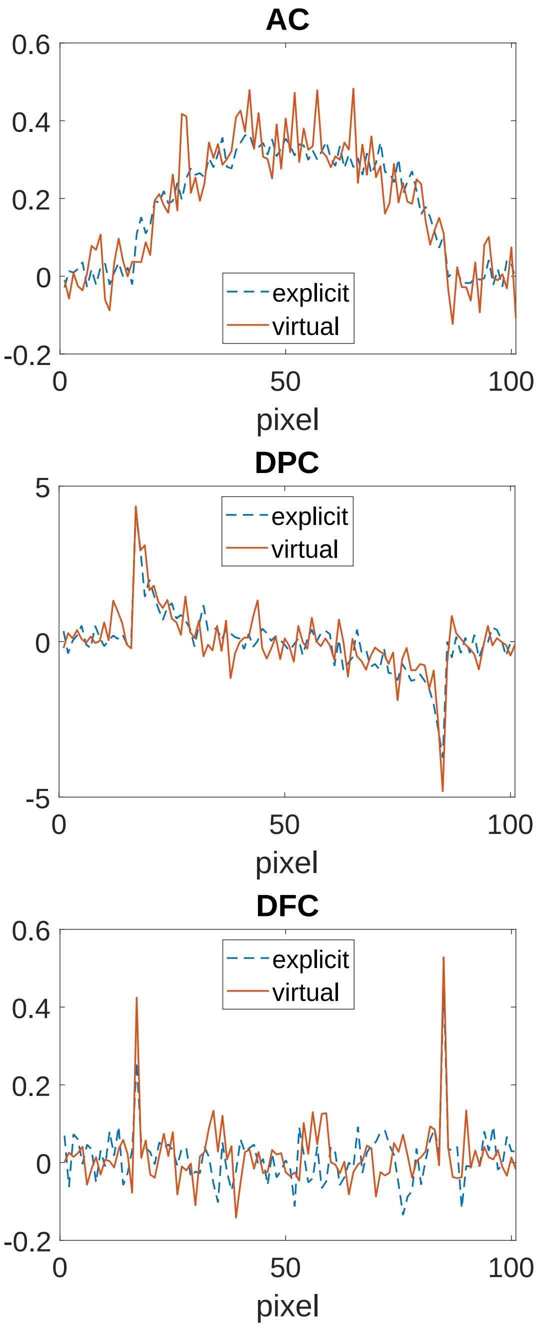

Figure C.4: Comparison between central horizontal profiles through the different contrast images of the beryllium sphere for both explicit and virtual gratings (arbitrary units).

Appendix D

Multi-contrast benchmarking of EI simulations: supporting tables

This appendix contains tables showing the spatially averaged dark field (σ^2) and transmission (T) signals for the CFRP phantoms with symmetric and eccentric fibers described in Chapter 6. The phase retrieval results and corresponding reference values are summarized in tables for which the row denotes the grating thickness and the column the aperture size. For the reference values, there is only a variation in aperture size. These values are indicated in the tables by the letter R in the first column. In addition to the the spatial averages, tables showing the corresponding standard deviations are provided as well.

Table D.1: **Average σ^2 (μrad^2): symmetric fibers**

Aperture size (μm) / Grating thickness (μm)	20	25	30	35	40
R	212.4	216.1	215.5	214.0	215.4
150	223.8	235.4	246.3	251.0	247.7
200	220.8	232.5	243.5	248.7	245.5
250	219.7	231.7	242.7	248.1	245.1
300	218.9	231.0	242.1	248.1	244.7
350	218.2	230.3	241.5	248.2	244.6

Table D.2: **Standard deviation σ^2 (μrad^2): symmetric fibers**

Aperture size (μm) Grating thickness (μm)	20	25	30	35	40
R	60.8	58.9	51.9	45.2	43.0
150	89.0	89.9	98.0	104.3	92.5
200	88.8	89.7	97.4	104.4	93.4
250	89.0	89.9	97.1	104.4	94.2
300	89.5	90.2	96.9	104.5	95.0
350	90.0	90.5	96.9	104.6	95.4

Table D.3: **Average T (%): symmetric fibers**

Aperture size (μm) Grating thickness (μm)	20	25	30	35	40
R	40.28	40.28	40.28	40.28	40.28
150	39.71	39.84	39.94	39.98	39.98
200	39.67	39.80	39.92	39.96	39.97
250	39.66	39.79	39.91	39.96	39.96
300	39.65	39.79	39.91	39.95	39.96
350	39.65	39.78	39.90	39.95	39.96

Table D.4: **Standard deviation T (%): symmetric fibers**

Aperture size (μm) Grating thickness (μm)	20	25	30	35	40
R	0.31	0.31	0.31	0.31	0.31
150	1.59	1.13	0.86	0.78	0.73
200	1.61	1.14	0.87	0.78	0.73
250	1.63	1.16	0.87	0.78	0.74
300	1.65	1.18	0.88	0.79	0.74
350	1.66	1.21	0.89	0.79	0.74

Table D.5: **Average σ^2 (μrad^2): eccentric fibers**

Aperture size (μm) Grating thickness (μm)	20	25	30	35	40
R	282.8	288.7	295.3	298.4	306.0
150	285.6	299.4	314.8	325.2	333.3
200	282.2	296.3	311.3	322.2	329.9
250	281.1	295.2	310.2	321.3	328.4
300	280.2	294.5	309.3	320.5	327.2
350	279.7	293.8	308.3	319.9	326.4

Table D.6: **Standard deviation σ^2 (μrad^2): eccentric fibers**

Aperture size (μm) Grating thickness (μm)	20	25	30	35	40
R	92.6	86.2	78.5	68.1	65.2
150	134.2	128.3	130.3	135.6	125.2
200	133.9	128.3	130.3	135.9	125.6
250	134.1	128.3	130.1	136.6	126.5
300	134.3	128.6	130.2	136.7	126.8
350	134.9	128.8	130.1	137.1	127.4

Table D.7: **Average T (%): eccentric fibers**

Aperture size (μm) Grating thickness (μm)	20	25	30	35	40
R	34.56	34.56	34.56	34.56	34.56
150	34.04	34.05	34.08	34.07	34.06
200	34.00	34.01	34.06	34.05	34.04
250	33.99	34.01	34.06	34.04	34.03
300	33.98	34.00	34.06	34.04	34.03
350	33.98	34.00	34.05	34.03	34.02

Table D.8: **Standard deviation T (%): eccentric fibers**

Aperture size (μm) / Grating thickness (μm)	20	25	30	35	40
R	0.37	0.37	0.37	0.37	0.37
150	2.10	1.67	1.35	1.13	0.94
200	2.12	1.69	1.36	1.13	0.95
250	2.14	1.70	1.37	1.14	0.96
300	2.16	1.71	1.38	1.15	0.97
350	2.18	1.73	1.39	1.16	0.97

Bibliography

Agostinelli, S., Allison, J., Amako, K., Apostolakis, J., Araujo, H., Arce, P., Asai, M., Axen, D., Banerjee, S., Barrand, G., Behner, F., Bellagamba, L., Boudreau, J., Broglia, L., Brunengo, A., Burkhardt, H., Chauvie, S., Chuma, J., Chytracek, R., Cooperman, G., Cosmo, G., Degtyarenko, P., Dell'Acqua, A., Depaola, G., Dietrich, D., Enami, R., Feliciello, A., Ferguson, C., Fesefeldt, H., Folger, G., Foppiano, F., Forti, A., Garelli, S., Giani, S., Giannitrapani, R., Gibin, D., Gomez Cadenas, J., Gonzalez, I., Gracia Abril, G., Greeniaus, G., Greiner, W., Grichine, V., Grossheim, A., Guatelli, S., Gumplinger, P., Hamatsu, R., Hashimoto, K., Hasui, H., Heikkinen, A., Howard, A., Ivanchenko, V., Johnson, A., Jones, F., Kallenbach, J., Kanaya, N., Kawabata, M., Kawabata, Y., Kawaguti, M., Kelner, S., Kent, P., Kimura, A., Kodama, T., Kokoulin, R., Kossov, M., Kurashige, H., Lamanna, E., Lampen, T., Lara, V., Lefebure, V., Lei, F., Liendl, M., Lockman, W., Longo, F., Magni, S., Maire, M., Medernach, E., Minamimoto, K., Mora de Freitas, P., Morita, Y., Murakami, K., Nagamatu, M., Nartallo, R., Nieminen, P., Nishimura, T., Ohtsubo, K., Okamura, M., O'Neale, S., Oohata, Y., Paech, K., Perl, J., Pfeiffer, A., Pia, M., Ranjard, F., Rybin, A., Sadilov, S., di Salvo, E., Santin, G., Sasaki, T., Savvas, N., Sawada, Y., Scherer, S., Sei, S., Sirotenko, V., Smith, D., Starkov, N., Stoecker, H., Sulkimo, J., Takahata, M., Tanaka, S., Tcherniaev, E., Safai Tehrani, E., Tropeano, M., Truscott, P., Uno, H., Urban, L., Urban, P., Verderi, M., Walkden, A., Wander, W., Weber, H., Wellisch, J., Wenaus, T., Williams, D., Wright, D., Yamada, T., Yoshida, H., and Zschiesche, D. (2003). GEANT4 - A simulation toolkit. *Nuclear Instruments and Methods in Physics Research Section A: Accelerators, Spectrometers, Detectors and Associated Equipment*, 506(3):250–303.

Allison, J., Amako, K., Apostolakis, J., Araujo, H., Arce Dubois, P., Asai, M., Barrand, G., Capra, R., Chauvie, S., Chytracek, R., Cirrone, G., Cooperman, G., Cosmo, G., Cuttone, G., Daquino, G., Donszelmann, M., Dressel, M., Folger, G., Foppiano, F., Generowicz, J., Grichine, V., Guatelli, S., Gumplinger, P., Heikkinen, A., Hrivnacova, I., Howard, A., Incerti, S., Ivanchenko, V., Johnson, T., Jones, F., Koi, T., Kokoulin, R., Kossov, M., Kurashige, H., Lara, V., Larsson, S., Lei, F., Link, O., Longo, F., Maire, M., Mantero, A., Mascialino, B., McLaren, I., Mendez Lorenzo, P., Minamimoto, K., Murakami, K., Nieminen, P., Pandola, L., Parlati, S., Peralta, L., Perl, J., Pfeiffer, A., Pia, M., Ribon, A., Rodrigues, P., Russo, G., Sadilov, S., Santin, G., Sasaki, T., Smith, D., Starkov, N., Tanaka, S., Tcherniaev, E., Tome, B., Trindade, A., Truscott, P., Urban, L., Verderi, M., Walkden, A., Wellisch, J., Williams, D., Wright, D., and Yoshida, H. (2006). Geant4 developments and applications. *IEEE Transactions on Nuclear Science*, 53(1):270–278.

Allison, J., Amako, K., Apostolakis, J., Arce, P., Asai, M., Aso, T., Bagli, E., Bagulya, A., Banerjee, S., Barrand, G., Beck, B., Bogdanov, A., Brandt, D., Brown, J., Burkhardt, H., Canal, P., Cano-Ott, D., Chauvie, S., Cho, K., Cirrone, G., Cooperman, G., Cortés-Giraldo, M., Cosmo, G., Cuttone, G., Depaola, G., Desorgher, L., Dong, X., Dotti, A., Elvira, V., Folger, G., Francis, Z., Galoyan, A., Garnier, L., Gayer, M., Genser, K., Grichine, V., Guatelli, S., Guèye, P., Gumplinger, P., Howard, A., Hřivnáčová, I., Hwang, S., Incerti, S., Ivanchenko, A., Ivanchenko, V., Jones, F., Jun, S., Kaitaniemi, P., Karakatsanis, N., Karamitros, M., Kelsey, M., Kimura, A., Koi, T., Kurashige, H., Lechner, A., Lee, S., Longo, F., Maire, M., Mancusi, D., Mantero, A., Mendoza, E., Morgan, B., Murakami, K., Nikitina, T., Pandola, L., Paprocki, P., Perl, J., Petrović, I., Pia, M., Pokorski, W., Quesada, J., Raine, M., Reis, M., Ribon, A., Ristić Fira, A., Romano, F., Russo, G., Santin, G., Sasaki, T., Sawkey, D., Shin, J., Strakovsky, I., Taborda, A., Tanaka, S., Tomé, B., Toshito, T., Tran, H., Truscott, P., Urban, L., Uzhinsky, V., Verbeke, J., Verderi, M., Wendt, B., Wenzel, H., Wright, D., Wright, D., Yamashita, T., Yarba, J., and Yoshida, H. (2016). Recent developments in Geant4. *Nuclear Instruments and Methods in Physics Research Section A: Accelerators, Spectrometers, Detectors and Associated Equipment*, 835:186–225.

Alloo, S. J., Paganin, D. M., Morgan, K. S., Kitchen, M. J., Stevenson, A. W., Mayo, S. C., Li, H. T., Kennedy, B. M., Maksimenko, A., Bowden, J. C., and Pavlov, K. M. (2022). Dark-field tomography of an attenuating object using intrinsic x-ray speckle tracking. *Journal of Medical Imaging*, 9(3):031502.

Als-Nielsen, J. and McMorrow, D. (2011). *Elements of Modern X-ray Physics*. John Wiley & Sons, Inc., Hoboken, NJ, USA.

Amako, K., Guatelli, S., Ivanchenko, V., Maire, M., Mascialino, B., Murakami, K., Nieminen, P., Pandola, L., Parlati, S., Pia, M., Piergentili, M., Sasaki, T., and Urban, L. (2005). Comparison of Geant4 electromagnetic physics models against the NIST reference data. *IEEE Transactions on Nuclear Science*, 52(4):910–918.

Ambrose, J. (1973). Computerized transverse axial scanning (tomography): Part 2. Clinical application. *The British Journal of Radiology*, 46(552):1023–1047.

Andersen, A. and Kak, A. C. (1984). Simultaneous Algebraic Reconstruction Technique (SART): A superior implementation of the ART algorithm. *Ultrasonic Imaging*, 6(1):81–94.

Arce, P., Lagares, J. I., Harkness, L., Desorgher, L., de Lorenzo, G., Abreu, Y., and Wang, Z. (2011). GAMOS: An easy and flexible way to use GEANT4. In *2011 IEEE Nuclear Science Symposium Conference Record*, pages 2230–2237. IEEE.

Astolfo, A., Buchanan, I., Partridge, T., Kallon, G. K., Hagen, C. K., Munro, P. R. T., Endrizzi, M., Bate, D., and Olivo, A. (2022). The effect of a variable focal spot size on the contrast channels retrieved in edge-illumination X-ray phase contrast imaging. *Scientific Reports*, 12(1):3354.

Astolfo, A., Endrizzi, M., Kallon, G., Millard, T. P., Vittoria, F. A., and Olivo, A. (2016). A first investigation of accuracy, precision and sensitivity of phase-based x-ray dark-field imaging. *Journal of Physics D: Applied Physics*, 49(48):485501.

Astolfo, A., Endrizzi, M., Vittoria, F. A., Diemoz, P. C., Price, B., Haig, I., and Olivo, A. (2017). Large field of view, fast and low dose multimodal phase-contrast imaging at high x-ray energy. *Scientific Reports*, 7(1):2187.

Auenhammer, R. M., Kim, J., Oddy, C., Mikkelsen, L. P., Marone, F., Stampanoni, M., and Asp, L. E. (2024). X-ray scattering tensor tomography based finite element modelling of heterogeneous materials. *npj Computational Materials*, 10(1):50.

Bartels, M. (2013). *Cone-beam x-ray phase contrast tomography of biological samples*. Universitatsverlag Gottingen.

Bartl, P., Durst, J., Haas, W., Michel, T., Ritter, A., Weber, T., and Anton, G. (2009). Simulation of X-ray phase-contrast imaging using grating-interferometry. In *2009 IEEE Nuclear Science Symposium Conference Record (NSS/MIC)*, pages 3577–3580.

Batenburg, K. J. and Sijbers, J. (2011). DART: A Practical Reconstruction Algorithm for Discrete Tomography. *IEEE Transactions on Image Processing*, 20(9):2542–2553.

Bayer, F. L., Hu, S., Maier, A., Weber, T., Anton, G., Michel, T., and Riess, C. P. (2014). Reconstruction of scalar and vectorial components in X-ray dark-field tomography. *Proceedings of the National Academy of Sciences*, 111(35):12699–12704.

Bech, M. (2022). Dual-binary phase gratings for x-ray interferometry. In Müller, B. and Wang, G., editors, *Proc. SPIE 12242, Developments in X-Ray Tomography XIV*, page 1224211. SPIE.

Bech, M., Bunk, O., Donath, T., Feidenhans'l, R., David, C., and Pfeiffer, F. (2010a). Quantitative x-ray dark-field computed tomography. *Physics in Medicine & Biology*, 55(18):5529–5539.

Bech, M., Jensen, T., Bunk, O., Donath, T., David, C., Weitkamp, T., Le Duc, G., Bravin, A., Cloetens, P., and Pfeiffer, F. (2010b). Advanced contrast modalities for X-ray radiology: Phase-contrast and dark-field imaging using a grating interferometer. *Zeitschrift für Medizinische Physik*, 20(1):7–16.

Beer, A. (1852). Bestimmung der Absorption des rothen Lichts in farbigen Flüssigkeiten. *Annalen der Physik und Chemie*, 162(5):78–88.

Bergbäck Knudsen, E., Prodi, A., Baltser, J., Thomsen, M., Kjær Willendrup, P., Sanchez del Rio, M., Ferrero, C., Farhi, E., Haldrup, K., Vickery, A., Feidenhans'l, R., Mortensen, K., Meedom Nielsen, M., Friis Poulsen, H., Schmidt, S., and Lefmann, K. (2013). McXtrace : a Monte Carlo software package for simulating X-ray optics, beamlines and experiments. *Journal of Applied Crystallography*, 46(3):679–696.

Berger, M. J., Hubbell, J. H., Seltzer, S. M., Chang, J., Coursey, J. S., Sukumar, R., Zucker, D. S., and Olsen, K. (2010). XCOM: Photon Cross Section Database (version 1.5). `http://physics.nist.gov/xcom`. Accessed: 2025-08-06.

Berry, M. V. and Klein, S. (1996). Integer, fractional and fractal Talbot effects. *Journal of Modern Optics*, 43(10):2139–2164.

Besson, G. (1999). CT image reconstruction from fan-parallel data. *Medical Physics*, 26(3):415–426.

Bielajew, A. F. (2020). *Fundamentals of the Monte Carlo method for neutral and charged particle transport*. The University of Michigan.

Bilderback, D. H., Elleaume, P., and Weckert, E. (2005). Review of third and next generation synchrotron light sources. *Journal of Physics B: Atomic, Molecular and Optical Physics*, 38(9):S773–S797.

Birnbacher, L., Braig, E.-M., Pfeiffer, D., Pfeiffer, F., and Herzen, J. (2021). Quantitative X-ray phase contrast computed tomography with grating interferometry. *European Journal of Nuclear Medicine and Molecular Imaging*, 48(13):4171–4188.

Bliznakova, K., Bliznakov, Z., and Dukov, N. (2022). Computational simulations and assessment of two approaches for x-ray phase contrast imaging. *Journal of Physics: Conference Series*, 2162(1):012013.

Bliznakova, K., Russo, P., Mettivier, G., Requardt, H., Popov, P., Bravin, A., and Buliev, I. (2015). A software platform for phase contrast x-ray breast imaging research. *Computers in Biology and Medicine*, 61:62–74.

Bonse, U. and Hart, M. (1965). An X-Ray Interferometer. *Applied Physics Letters*, 6(8):155–156.

Born, M. and Wolf, E. (1999). *Principles of optics: Electromagnetic theory of propagation, interference and diffraction of light*. Cambridge University Press, 7th edition.

Bracewell, R. N. (1956). Strip Integration in Radio Astronomy. *Australian Journal of Physics*, 9(2):198–217.

Braig, E.-M., Pfeiffer, D., Willner, M., Sellerer, T., Taphorn, K., Petrich, C., Scholz, J., Petzold, L., Birnbacher, L., Dierolf, M., Pfeiffer, F., and Herzen, J. (2020). Single spectrum three-material decomposition with grating-based x-ray phase-contrast CT. *Physics in Medicine & Biology*, 65(18):185011.

Bravin, A., Coan, P., and Suortti, P. (2013). X-ray phase-contrast imaging: from preclinical applications towards clinics. *Physics in Medicine & Biology*, 58(1):R1–R35.

Bricogne, G., Capelli, S. C., Evans, G., Mitschler, A., Pattison, P., Roversi, P., and Schiltz, M. (2005). X-ray absorption, refraction and resonant scattering tensors in selenated protein crystals: implications for data collection strategies in macromolecular crystallography. *Journal of Applied Crystallography*, 38(1):168–182.

Brombal, L., Arfelli, F., Brun, F., Di Trapani, V., Endrizzi, M., Menk, R. H., Perion, P., Rigon, L., Saccomano, M., Tromba, G., and Olivo, A. (2024). Edge-illumination spectral phase-contrast tomography. *Physics in Medicine & Biology*, 69(7):075027.

Brombal, L., Arfelli, F., Brun, F., Longo, F., Poles, N., and Rigon, L. (2022a). X-ray differential phase-contrast imaging simulations with Geant4. *Journal of Physics D: Applied Physics*, 55:045102.

Brombal, L., Arfelli, F., Menk, R. H., Rigon, L., and Brun, F. (2023). PEPI Lab: a flexible compact multi-modal setup for X-ray phase-contrast and spectral imaging. *Scientific Reports*, 13(1):4206.

Brombal, L., Rigon, L., Arfelli, F., Menk, R., and Brun, F. (2022b). A Geant4 tool for edge-illumination X-ray phase-contrast imaging. *Journal of Instrumentation*, 17(01):C01043.

Brun, R. and Rademakers, F. (1997). ROOT - An object oriented data analysis framework. *Nuclear Instruments and Methods in Physics Research Section A: Accelerators, Spectrometers, Detectors and Associated Equipment*, 389(1-2):81–86.

Buchanan, I., Kallon, G., Beckenbach, T., Schulz, J., Endrizzi, M., and Olivo, A. (2020). Effective modeling of high-energy laboratory-based x-ray phase contrast imaging utilizing absorption masks or gratings. *Journal of Applied Physics*, 128(21):214503.

Buzug, T. (2008). *Computed tomography: From photon statistics to modern cone-beam CT*. Springer-Verlag, Berlin/Heidelberg.

Chantler, C. T. (1995). Theoretical Form Factor, Attenuation, and Scattering Tabulation for Z =1–92 from E =1–10 eV to E =0.4–1.0 MeV. *Journal of Physical and Chemical Reference Data*, 24(1):71–643.

Chantler, C. T. (2000). Detailed Tabulation of Atomic Form Factors, Photoelectric Absorption and Scattering Cross Section, and Mass Attenuation Coefficients in the Vicinity of Absorption Edges in the Soft X-Ray (Z=30–36, Z=60–89, E=0.1 keV–10 keV), Addressing Convergence Issues . *Journal of Physical and Chemical Reference Data*, 29(4):597–1056.

Chantler, C. T., Olsen, K., Dragoset, R. A., Chang, J., Kishore, A. R., Kotochigova, S. A., and Zucker, D. S. (2005). X-Ray Form Factor, Attenuation and Scattering Tables (version 2.1). `http://physics.nist.gov/ffast`. Accessed: 2025-08-06.

Chapman, D., Thomlinson, W., Arfelli, F., Gmür, N., Zhong, Z., Menk, R., Johnson, R. E., Washburn, D., Pisano, E., and Sayers, D. (1996). Mammography imaging studies using a Laue crystal analyzer. *Review of Scientific Instruments*, 67(9):3360.

Chapman, D., Thomlinson, W., Johnston, R. E., Washburn, D., Pisano, E., Gmür, N., Zhong, Z., Menk, R., Arfelli, F., and Sayers, D. (1997). Diffraction enhanced x-ray imaging. *Physics in Medicine & Biology*, 42(11):2015–25.

Chen, Y., Guan, H., Hagen, C. K., Olivo, A., and Anastasio, M. A. (2017). Single-shot edge illumination x-ray phase-contrast tomography enabled by joint image reconstruction. *Optics Letters*, 42(3):619–622.

Cipiccia, S., Vittoria, F., Weikum, M., Olivo, A., and Jaroszynski, D. (2014). Inclusion of coherence in Monte Carlo models for simulation of x-ray phase contrast imaging. *Optics Express*, 22(19):23480–23488.

Cirauqui, D., García-March, M. Á., Guigó Corominas, G., Graß, T., Grzybowski, P. R., Muñoz-Gil, G., Saavedra, J. R. M., and Lewenstein, M. (2024). Comparing pseudo- and quantum-random number generators with Monte Carlo simulations. *APL Quantum*, 1(3):036125.

Clauser, J. F. and Reinsch, M. W. (1992). New theoretical and experimental results in Fresnel optics with applications to matter-wave and X-ray interferometry. *Applied Physics B: Photophysics and Laser Chemistry*, 54(5):380–395.

Cloetens, P., Barrett, R., Baruchel, J., Guigay, J.-P., and Schlenker, M. (1996). Phase objects in synchrotron radiation hard x-ray imaging. *Journal of Physics D: Applied Physics*, 29(1):133–146.

Cloetens, P., Guigay, J. P., De Martino, C., Baruchel, J., and Schlenker, M. (1997). Fractional Talbot imaging of phase gratings with hard x rays. *Optics Letters*, 22(14):1059–1061.

Cloetens, P., Ludwig, W., Baruchel, J., Guigay, J.-P., Pernot-Rejmánková, P., Salomé-Pateyron, M., Schlenker, M., Buffière, J.-Y., Maire, E., and Peix, G. (1999). Hard x-ray phase imaging using simple propagation of a coherent synchrotron radiation beam. *Journal of Physics D: Applied Physics*, 32(10A):A145–A151.

Compton, A. H. (1923). A Quantum Theory of the Scattering of X-rays by Light Elements. *Physical Review*, 21(5):483–502.

Cooley, J. W. and Tukey, J. W. (1965). An Algorithm for the Machine Calculation of Complex Fourier Series. *Mathematics of Computation*, 19(90):297.

Cormack, A. M. (1963). Representation of a Function by Its Line Integrals, with Some Radiological Applications. *Journal of Applied Physics*, 34(9):2722–2727.

Cormack, A. M. (1964). Representation of a Function by Its Line Integrals, with Some Radiological Applications. II. *Journal of Applied Physics*, 35(10):2908–2913.

Cowley, J. M. and Moodie, A. F. (1957). The scattering of electrons by atoms and crystals. I. A new theoretical approach. *Acta Crystallographica*, 10(10):609–619.

Creath, K. (1988). V phase-measurement interferometry techniques. In Wolf, E., editor, *Progress in Optics*, volume 26, pages 349–393. Elsevier.

Crowther, R., De Rosier, D., and Klug, A. (1970). The reconstruction of a three-dimensional structure from projections and its application to electron microscopy. *Proceedings of the Royal Society of London. A. Mathematical and Physical Sciences*, 317(1530):319–340.

Daillant, J. and Gibaud, A., editors (2009). *X-ray and Neutron Reflectivity*, volume 770 of *Lecture Notes in Physics*. Springer Berlin Heidelberg, Berlin, Heidelberg.

David, C., Nöhammer, B., Solak, H. H., and Ziegler, E. (2002). Differential x-ray phase contrast imaging using a shearing interferometer. *Applied Physics Letters*, 81(17):3287.

Davis, T. J., Gao, D., Gureyev, T. E., Stevenson, a. W., and Wilkins, S. W. (1995). Phase-contrast imaging of weakly absorbing materials using hard X-rays. *Nature*, 373(6515):595–598.

De Beenhouwer, J., Staelens, S., Kruecker, D., Ferrer, L., D'Asseler, Y., Lemahieu, I., and Rannou, F. R. (2007). Cluster computing software for GATE simulations. *Medical Physics*, 34(6):1926–1933.

De Beenhouwer, J., Staelens, S., Vandenberghe, S., and Lemahieu, I. (2008). Acceleration of GATE SPECT simulations. *Medical Physics*, 35(4):1476–1485.

De Beenhouwer, J., Staelens, S., Vandenberghe, S., Verhaeghe, J., Van Holen, R., Rault, E., and Lemahieu, I. (2009). Physics process level discrimination of detections for GATE: Assessment of contamination in SPECT and spurious activity in PET. *Medical Physics*, 36(4):1053–1060.

De Rosier, D. J. and Klug, A. (1968). Reconstruction of Three Dimensional Structures from Electron Micrographs. *Nature*, 217(5124):130–134.

De Samber, B., Renders, J., Elberfeld, T., Maris, Y., Sanctorum, J., Six, N., Liang, Z., De Beenhouwer, J., and Sijbers, J. (2021). FleXCT: a flexible X-ray CT scanner with 10 degrees of freedom. *Optics Express*, 29(3):3438–3457.

den Dekker, A., Gonnissen, J., De Backer, A., Sijbers, J., and Van Aert, S. (2013). Estimation of unknown structure parameters from high-resolution (S)TEM images: What are the limits? *Ultramicroscopy*, 134(2013):34–43.

Diemoz, P., Endrizzi, M., Hagen, C., Millard, T., Vittoria, F., and Olivo, A. (2015). Angular sensitivity and spatial resolution in edge illumination X-ray phase-contrast imaging. *Nuclear Instruments and Methods in Physics Research Section A: Accelerators, Spectrometers, Detectors and Associated Equipment*, 784:538–541.

Diemoz, P. C., Endrizzi, M., Zapata, C. E., Pešić, Z. D., Rau, C., Bravin, A., Robinson, I. K., and Olivo, A. (2013). X-Ray Phase-Contrast Imaging with Nanoradian Angular Resolution. *Physical Review Letters*, 110(13):138105.

Diemoz, P. C. and Olivo, A. (2014). On the origin of contrast in edge illumination X-ray phase-contrast imaging. *Optics Express*, 22(23):28199–28214.

Doherty, A., Massimi, L., Olivo, A., and Endrizzi, M. (2020). Optimal and automated mask alignment for use in edge illumination X-ray differential-phase and dark-field imaging techniques. *Nuclear Instruments and Methods in Physics Research Section A: Accelerators, Spectrometers, Detectors and Associated Equipment*, 984(May):164602.

Doherty, A., Savvidis, S., Navarrete-León, C., Gerli, M. F., Olivo, A., and Endrizzi, M. (2023). Edge-Illumination X-Ray Dark-Field Tomography. *Physical Review Applied*, 19(5):054042.

Dreier, E. S., Silvestre, C., Kehres, J., Turecek, D., Khalil, M., Hemmingsen, J. H., Hansen, O., Jakubek, J., Feidenhans'l, R., and Olsen, U. L. (2020). Single-shot, omni-directional x-ray scattering imaging with a laboratory source and single-photon localization. *Optics Letters*, 45(4):1021–1024.

du Plessis, A., Broeckhoven, C., Guelpa, A., and le Roux, S. G. (2017). Laboratory x-ray micro-computed tomography: a user guideline for biological samples. *GigaScience*, 6(6):1–11.

Einstein, A. (1905). Über einen die Erzeugung und Verwandlung des Lichtes betreffenden heuristischen Gesichtspunkt. *Annalen der Physik*, 322(6):132–148.

Elberfeld, T., De Beenhouwer, J., den Dekker, A. J., Heinzl, C., and Sijbers, J. (2018). Parametric Reconstruction of Glass Fiber-reinforced Polymer Composites from X-ray Projection Data—A Simulation Study. *Journal of Nondestructive Evaluation*, 37(3):62.

Elberfeld, T., Fröhler, B., Heinzl, C., Sijbers, J., and De Beenhouwer, J. (2023). cu-PARE: parametric reconstruction of curved fibres from glass fibre-reinforced composites. *Nondestructive Testing and Evaluation*, 38(4):648–667.

Endrizzi, M. (2018). X-ray phase-contrast imaging. *Nuclear Instruments and Methods in Physics Research Section A: Accelerators, Spectrometers, Detectors and Associated Equipment*, 878:88–98.

Endrizzi, M., Astolfo, A., Vittoria, F. A., Millard, T. P., and Olivo, A. (2016). Asymmetric masks for laboratory-based X-ray phase-contrast imaging with edge illumination. *Scientific Reports*, 6(1):25466.

Endrizzi, M., Basta, D., and Olivo, A. (2015). Laboratory-based X-ray phase-contrast imaging with misaligned optical elements. *Applied Physics Letters*, 107(12):124103.

Endrizzi, M., Diemoz, P. C., Millard, T. P., Louise Jones, J., Speller, R. D., Robinson, I. K., and Olivo, A. (2014). Hard X-ray dark-field imaging with incoherent sample illumination. *Applied Physics Letters*, 104(2):024106.

Endrizzi, M. and Olivo, A. (2014). Absorption, refraction and scattering retrieval with an edge-illumination-based imaging setup. *Journal of Physics D: Applied Physics*, 47(50):505102.

Endrizzi, M., Vittoria, F. A., Rigon, L., Dreossi, D., Iacoviello, F., Shearing, P. R., and Olivo, A. (2017). X-ray Phase-Contrast Radiography and Tomography with a Multiaperture Analyzer. *Physical Review Letters*, 118(24):243902.

Engelhardt, M., Kottler, C., Bunk, O., David, C., Schroer, C., Baumann, J., Schuster, M., and Pfeiffer, F. (2008). The fractional Talbot effect in differential x-ray phase-contrast imaging for extended and polychromatic x-ray sources. *Journal of Microscopy*, 232(1):145–157.

Esposito, M., Buchanan, I., Massimi, L., Ferrara, J. D., Shearing, P. R., Olivo, A., and Endrizzi, M. (2023). Laboratory-based x-ray dark-field microscopy. *Physical Review Applied*, 20(6):064039.

Evsevleev, S., Müller, B., Lange, A., and Kupsch, A. (2019). Refraction driven X-ray caustics at curved interfaces. *Nuclear Instruments and Methods in Physics Research Section A: Accelerators, Spectrometers, Detectors and Associated Equipment*, 916:275–282.

Faris, G. W. and Byer, R. L. (1988). Three-dimensional beam-deflection optical tomography of a supersonic jet. *Applied Optics*, 27(24):5202–5212.

Feldkamp, L. A., Davis, L. C., and Kress, J. W. (1984). Practical cone-beam algorithm. *Journal of the Optical Society of America A*, 1(6):612–619.

Ferguson, B., Wang, S., Gray, D., Abbot, D., and Zhang, X.-C. (2002). T-ray computed tomography. *Optics Letters*, 27(15):1312–1314.

Francken, N., Sanctorum, J., Huyge, B., Sijbers, J., and De Beenhouwer, J. (2025). Efficient X-ray dark field contrast simulations using a condensed history approach. *Optics Express*, 33(2):3562–3576.

Francken, N., Sanctorum, J., Paramonov, P., Sijbers, J., and De Beenhouwer, J. (2024a). Edge illumination x-ray phase contrast simulations using the CAD-ASTRA toolbox. *Optics Express*, 32(6):10005–10021.

Francken, N., Sanctorum, J., Renders, J., Paramonov, P., Sijbers, J., and De Beenhouwer, J. (2023). A Condensed History Approach to X-Ray Dark Field Effects in Edge Illumination Phase Contrast Simulations. In *45th Annual International Conference of the IEEE Engineering in Medicine and Biology Society*, pages 1–4.

Francken, N., Sanctorum, J., Sanctorum, J. G., Vanthienen, P.-J., Sijbers, J., and De Beenhouwer, J. (2024b). Inline edge illumination X-ray phase contrast imaging through mask misalignment. *Optics Express*, 32(18):32048–32061.

Fu, J., Shi, X., Guo, W., and Peng, P. (2019). Fast X-ray Differential Phase Contrast Imaging with One Exposure and without Movements. *Scientific Reports*, 9(1):1113.

Funk, P. (1913). Über Flächen mit lauter geschlossenen geodätischen Linien. *Mathematische Annalen*, 74:278–300.

Gassert, F. T., Urban, T., Frank, M., Willer, K., Noichl, W., Buchberger, P., Schick, R., Koehler, T., von Berg, J., Fingerle, A. A., Sauter, A. P., Makowski, M. R., Pfeiffer, D., and Pfeiffer, F. (2021). X-ray Dark-Field Chest Imaging: Qualitative and Quantitative Results in Healthy Humans. *Radiology*, 301(2):389–395.

Gilbert, P. (1972). Iterative methods for the three-dimensional reconstruction of an object from projections. *Journal of Theoretical Biology*, 36(1):105–117.

Glinz, J., Šleichrt, J., Kytýř, D., Ayalur-Karunakaran, S., Zabler, S., Kastner, J., and Senck, S. (2021). Phase-contrast and dark-field imaging for the inspection of resin-rich areas and fiber orientation in non-crimp vacuum infusion carbon-fiber-reinforced polymers. *Journal of Materials Science*, 56(16):9712–9727.

Goetz, K., Kalashnikov, M. P., Mikhaĭlov, Y. A., Sklizkov, G. V., Fedotov, S. I., Foerster, E., and Zaumseil, P. (1979). Measurements of the parameters of shell targets for laser thermonuclear fusion using an x-ray schlieren method. *Soviet Journal of Quantum Electronics*, 9(5):607–610.

Gommes, C. J., Jaksch, S., and Frielinghaus, H. (2021). Small-angle scattering for beginners. *Journal of Applied Crystallography*, 54(6):1832–1843.

Goodman, J. W. (1996). *Introduction to Fourier Optics*. McGraw-Hill.

Gordon, R., Bender, R., and Herman, G. T. (1970). Algebraic Reconstruction Techniques (ART) for three-dimensional electron microscopy and X-ray photography. *Journal of Theoretical Biology*, 29(3):471–481.

Greffier, J., Viry, A., Robert, A., Khorsi, M., and Si-Mohamed, S. (2025). Photon-counting CT systems: A technical review of current clinical possibilities. *Diagnostic and Interventional Imaging*, 106(2):53–59.

Gregor, J. and Benson, T. (2008). Computational Analysis and Improvement of SIRT. *IEEE Transactions on Medical Imaging*, 27(7):918–924.

Gullberg, G. T. (1979). The reconstruction of fan-beam data by filtering the back-projection. *Computer Graphics and Image Processing*, 10(1):30–47.

Gureyev, T. E., Mayo, S. C., Myers, D. E., Nesterets, Y., Paganin, D. M., Pogany, A., Stevenson, A. W., and Wilkins, S. W. (2009). Refracting Röntgen's rays: Propagation-based x-ray phase contrast for biomedical imaging. *Journal of Applied Physics*, 105(10):102005.

Gureyev, T. E., Paganin, D. M., Arhatari, B., Taba, S. T., Lewis, S., Brennan, P. C., and Quiney, H. M. (2020). Dark-field signal extraction in propagation-based phase-contrast imaging. *Physics in Medicine & Biology*, 65(21):215029.

Gustschin, A., Riedel, M., Taphorn, K., Petrich, C., Gottwald, W., Noichl, W., Busse, M., Francis, S. E., Beckmann, F., Hammel, J. U., Moosmann, J., Thibault, P., and Herzen, J. (2021). High-resolution and sensitivity bi-directional x-ray phase contrast imaging using 2D Talbot array illuminators. *Optica*, 8(12):1588–1595.

Hagen, C. K., Diemoz, P. C., Endrizzi, M., Rigon, L., Dreossi, D., Arfelli, F., Lopez, F. C. M., Longo, R., and Olivo, A. (2014a). Theory and preliminary experimental verification of quantitative edge illumination x-ray phase contrast tomography. *Optics Express*, 22(7):7989–8000.

Hagen, C. K., Munro, P. R. T., Endrizzi, M., Diemoz, P. C., and Olivo, A. (2014b). Low-dose phase contrast tomography with conventional x-ray sources. *Medical Physics*, 41(7):070701.

Hahn, D., Thibault, P., Fehringer, A., Bech, M., Koehler, T., Pfeiffer, F., and Noël, P. B. (2015). Statistical iterative reconstruction algorithm for X-ray phase-contrast CT. *Scientific Reports*, 5:10452.

Havariyoun, G., Vittoria, F. A., Hagen, C. K., Basta, D., Kallon, G. K., Endrizzi, M., Massimi, L., Munro, P., Hawker, S., Smit, B., Astolfo, A., Larkin, O. J., Waltham, R. M., Shah, Z., Duffy, S. W., Nelan, R. L., Peel, A., Suaris, T., Jones, J. L., Haig, I. G., Bate, D., and Olivo, A. (2019). A compact system for intraoperative specimen imaging based on edge illumination x-ray phase contrast. *Physics in Medicine & Biology*, 64(23):235005.

Hemberg, O., Otendal, M., and Hertz, H. M. (2003). Liquid-metal-jet anode electron-impact x-ray source. *Applied Physics Letters*, 83(7):1483–1485.

Henke, B., Gullikson, E., and Davis, J. (1993). X-Ray Interactions: Photoabsorption, Scattering, Transmission, and Reflection at E = 50-30,000 eV, Z = 1-92. *Atomic Data and Nuclear Data Tables*, 54(2):181 – 342.

Hentschel, M. P., Hosemann, R., Lange, A., Uther, B., and Brückner, R. (1987). Röntgenkleinwinkelbrechung an Metalldrähten, Glasfäden und hartelastischem Polyproplen. *Acta Crystallographica Section A: Foundations of Crystallography*, 43(4):506–513.

Hounsfield, G. N. (1973). Computerized transverse axial scanning (tomography): I. Description of system. *British Journal of Radiology*, 46(552):1016–1022.

How, Y. Y. and Morgan, K. S. (2022). Quantifying the x-ray dark-field signal in single-grid imaging. *Optics Express*, 30(7):10899–10918.

How, Y. Y., Paganin, D. M., and Morgan, K. S. (2023). On the quantification of sample microstructure using single-exposure x-ray dark-field imaging via a single-grid setup. *Scientific Reports*, 13(1):11001.

Hu, B. B. and Nuss, M. C. (1995). Imaging with terahertz waves. *Optics Letters*, 20(16):1716–1718.

Huang, Z.-F., Kang, K.-J., Zhang, L., Chen, Z.-Q., Ding, F., Wang, Z.-T., and Fang, Q.-G. (2009). Alternative method for differential phase-contrast imaging with weakly coherent hard x rays. *Physical Review A*, 79(1):013815.

Huyge, B., Francken, N., Sanctorum, J. G., Sanctorum, J., De Beenhouwer, J., and Sijbers, J. (2025). Edge illumination X-ray phase contrast imaging with continuous mask motion. *Optics Express*, 33(19):41271–41286.

Huyge, B., Sanctorum, J., Jeurissen, B., De Beenhouwer, J., and Sijbers, J. (2023a). Fiber Orientation Estimation from X-ray Dark Field Images of Fiber Reinforced Polymers Using Constrained Spherical Deconvolution. *Polymers*, 15(13):2887.

Huyge, B., Sanctorum, J., Six, N., De Beenhouwer, J., and Sijbers, J. (2021). Analysis Of Flat Fields In Edge Illumination Phase Contrast Imaging. In *2021 IEEE 18th International Symposium on Biomedical Imaging (ISBI)*, pages 1310–1313. IEEE.

Huyge, B., Vanthienen, P.-J., Six, N., Sijbers, J., and De Beenhouwer, J. (2023b). Adapting an XCT-scanner to enable edge illumination X-ray phase contrast imaging. *e-Journal of Nondestructive Testing*, 28(3):1–7.

Ilavsky, J., Zhang, F., Allen, A. J., Levine, L. E., Jemian, P. R., and Long, G. G. (2013). Ultra-Small-Angle X-ray Scattering Instrument at the Advanced Photon Source: History, Recent Development, and Current Status. *Metallurgical and Materials Transactions A*, 44(1):68–76.

James, F. (1990). A review of pseudorandom number generators. *Computer Physics Communications*, 60(3):329–344.

James, F. and Moneta, L. (2020). Review of High-Quality Random Number Generators. *Computing and Software for Big Science*, 4(1):2.

James, R. W. (1962). *The Optical Principles of the Diffraction of X-rays*. G. Bell and Sons Ltd., London, UK.

Jan, S., Benoit, D., Becheva, E., Carlier, T., Cassol, F., Descourt, P., Frisson, T., Grevillot, L., Guigues, L., Maigne, L., Morel, C., Perrot, Y., Rehfeld, N., Sarrut, D., Schaart, D., Stute, S., Pietrzyk, U., Visvikis, D., Zahra, N., and Buvat, I. (2011). GATE V6: A major enhancement of the GATE simulation platform enabling modelling of CT and radiotherapy. *Physics in Medicine & Biology*, 56(4):881–901.

Janssens, E. (2018). *Advances in X-ray reconstruction algorithms for limited data problems in conventional and non-conventional projection geometries*. PhD thesis, Universiteit Antwerpen.

Janssens, E., De Beenhouwer, J., Sanctorum, J., Senck, S., Heinzl, C., and Sijbers, J. (2017). Dual axis Dark Field Contrast Tomography for visualisation of scattering directions in a CFRP sample. In *4th Conference on X-ray and Neutron Phase Imaging with Gratings, Zurich, Switzerland.*

Jensen, T., Bech, M., Bunk, O., Donath, T., David, C., Feidenhans'L, R., and Pfeiffer, F. (2010a). Directional x-ray dark-field imaging. *Physics in Medicine & Biology*, 55(12):3317–3323.

Jensen, T. H., Bech, M., Zanette, I., Weitkamp, T., David, C., Deyhle, H., Rutishauser, S., Reznikova, E., Mohr, J., Feidenhans'l, R., and Pfeiffer, F. (2010b). Directional x-ray dark-field imaging of strongly ordered systems. *Physical Review B*, 82(21):214103.

Ji, X., Zhang, R., Li, K., and Chen, G.-H. (2020). Dual Energy Differential Phase Contrast CT (DE-DPC-CT) Imaging. *IEEE Transactions on Medical Imaging*, 39(11):3278–3289.

Kagias, M., Wang, Z., Villanueva-Perez, P., Jefimovs, K., and Stampanoni, M. (2016). 2D-Omnidirectional Hard-X-Ray Scattering Sensitivity in a Single Shot. *Physical Review Letters*, 116(9):093902.

Kak, A. C. and Slaney, M. (1988). *Principles of computerized tomographic imaging*. Society for Industrial and Applied Mathematics.

Kallmann, H. (1948). Neutron radiography. *Research*, 1(6):254–260.

Kallon, G. K., Vittoria, F. A., Buchanan, I., Endrizzi, M., and Olivo, A. (2020). An experimental approach to optimising refraction sensitivity for lab-based edge illumination phase contrast set-ups. *Journal of Physics D: Applied Physics*, 53(19):195404.

Katsuyama, K., Nagamine, T., Matsumoto, S.-i., and Sato, S. (2007). High energy X-ray CT study on the central void formations and the fuel pin deformations of FBR fuel assemblies. *Nuclear Instruments and Methods in Physics Research Section B: Beam Interactions with Materials and Atoms*, 255(2):365–372.

Kawrakow, I. (2000). Accurate condensed history Monte Carlo simulation of electron transport. I. EGSnrc, the new EGS4 version. *Medical Physics*, 27(3):485–498.

Keller, J. B. (1962). Geometrical Theory of Diffraction. *Journal of the Optical Society of America*, 52(2):116–130.

Khelashvili, G., Brankov, J. G., Chapman, D., Anastasio, M. A., Yang, Y., Zhong, Z., and Wernick, M. N. (2006). A physical model of multiple-image radiography. *Physics in Medicine & Biology*, 51(2):221–236.

Knoll, M. and Ruska, E. (1932). Das Elektronenmikroskop. *Zeitschrift für Physik*, 78:318–339.

Köhler, T., Engel, K. J., and Roessl, E. (2011). Noise properties of grating-based x-ray phase contrast computed tomography. *Medical Physics*, 38(S1):S106–S116.

Landweber, L. (1951). An Iteration Formula for Fredholm Integral Equations of the First Kind. *American Journal of Mathematics*, 73(3):615–624.

Lange, A., Kupsch, A., Müller, B. R., and Hentschel, M. P. (2012). Edge Artefacts of Radiographic Images by X-ray Refraction. *e-Journal of Nondestructive Testing*, 17(7):1–11.

Langer, M., Cen, Z., Rit, S., and Létang, J. M. (2020). Towards Monte Carlo simulation of X-ray phase contrast using GATE. *Optics Express*, 28(10):14522–14535.

Langer, M., Cloetens, P., Guigay, J.-P., and Peyrin, F. (2008). Quantitative comparison of direct phase retrieval algorithms in in-line phase tomography. *Medical Physics*, 35(10):4556–4566.

Leatham, T. A., Paganin, D. M., and Morgan, K. S. (2023). X-Ray Dark-Field and Phase Retrieval Without Optics, via the Fokker–Planck Equation. *IEEE Transactions on Medical Imaging*, 42(6):1681–1695.

L'Ecuyer, P. (1988). Efficient and portable combined random number generators. *Communications of the ACM*, 31(6):742–751.

Lewis, G. N. (1926). The Conservation of Photons. *Nature*, 118:874–875.

Liu, X., Liu, L., Huang, J., Lei, Y., and Li, J. (2023). Single-Shot Phase-Contrast Imaging with a Single Grating. *Photonics*, 10(9):968.

Ljungberg, M., Strand, S. E., and King, M. A. (1998). *Monte Carlo calculations in nuclear medicine: applications in diagnostic imaging*. Institute of Physics Publishing.

Lumbeeck, L.-P., Paramonov, P., Sijbers, J., and De Beenhouwer, J. (2023). Efficient iterative reconstruction with beam shape compensation for THz computed tomography. *Appl. Opt.*, 62(17):F31–F40.

Lüscher, M. (1994). A portable high-quality random number generator for lattice field theory simulations. *Computer Physics Communications*, 79(1):100–110.

Lynch, S. K., Pai, V., Auxier, J., Stein, A. F., Bennett, E. E., Kemble, C. K., Xiao, X., Lee, W.-K., Morgan, N. Y., and Wen, H. H. (2011). Interpretation of dark-field contrast and particle-size selectivity in grating interferometers. *Applied Optics*, 50(22):4310–4319.

Lyra, M. and Ploussi, A. (2011). Filtering in SPECT Image Reconstruction. *International Journal of Biomedical Imaging*, 2011:693795.

Ma, X., Yuan, X., Cao, Z., Qi, B., and Zhang, Z. (2016). Quantum random number generation. *npj Quantum Information*, 2(1):16021.

Magnin, C., Fernández Martínez, M., Mihai Cenda, D., Lantz, B., Barton, S., Faure, B., and Brun, E. (2025). How X-ray dark-field imaging relates to small-angle X-ray scattering measurements. *Journal of Applied Crystallography*, 58(4):1347–1354.

Magnin, C., Quénot, L., Bohic, S., Mihai Cenda, D., Fernández Martínez, M., Lantz, B., Faure, B., and Brun, E. (2023). Dark-field and directional dark-field on low-coherence x ray sources with random mask modulations: validation with SAXS anisotropy measurements. *Optics Letters*, 48(22):5839–5842.

Malecki, A., Potdevin, G., Biernath, T., Eggl, E., Grande Garcia, E., Baum, T., Noël, P. B., Bauer, J. S., and Pfeiffer, F. (2013). Coherent Superposition in Grating-Based Directional Dark-Field Imaging. *PLoS ONE*, 8(4):e61268.

Malecki, A., Potdevin, G., Biernath, T., Eggl, E., Willer, K., Lasser, T., Maisenbacher, J., Gibmeier, J., Wanner, A., and Pfeiffer, F. (2014). X-ray tensor tomography. *EPL (Europhysics Letters)*, 105(3):38002.

Malecki, A., Potdevin, G., and Pfeiffer, F. (2012). Quantitative wave-optical numerical analysis of the dark-field signal in grating-based X-ray interferometry. *EPL*, 99(4):48001.

Marsaglia, G. and Zaman, A. (1991). A New Class of Random Number Generators. *The Annals of Applied Probability*, 1(3):462–480.

Marsaglia, G., Zaman, A., and Wan Tsang, W. (1990). Toward a universal random number generator. *Statistics & Probability Letters*, 9(1):35–39.

Massimi, L., Suaris, T., Hagen, C. K., Endrizzi, M., Munro, P. R. T., Havariyoun, G., Hawker, P. M. S., Smit, B., Astolfo, A., Larkin, O. J., Waltham, R. M., Shah, Z., Duffy, S. W., Nelan, R. L., Peel, A., Jones, J. L., Haig, I. G., Bate, D., and Olivo, A. (2022). Volumetric High-Resolution X-Ray Phase-Contrast Virtual Histology of Breast Specimens With a Compact Laboratory System. *IEEE Transactions on Medical Imaging*, 41(5):1188–1195.

Matsumoto, G. and Krata, S. (1983). The neutron computer tomography. In Barton, J. P. and von der Hardt, P., editors, *Neutron Radiography*, pages 899–906, Dordrecht. Springer Netherlands.

Matsumoto, M. and Nishimura, T. (1998). Mersenne twister: A 623-Dimensionally Equidistributed Uniform Pseudo-Random Number Generator. *ACM Transactions on Modeling and Computer Simulation*, 8(1):3–30.

Matsunaga, N., Yano, K., Endrizzi, M., and Olivo, A. (2020). Detection of individual sub-pixel features in edge-illumination x-ray phase contrast imaging by means of the dark-field channel. *Journal of Physics D: Applied Physics*, 53(9):095401.

Maughan Jones, C. J., Vittoria, F. A., Olivo, A., Endrizzi, M., and Munro, P. R. T. (2018). Retrieval of weak x-ray scattering using edge illumination. *Optics letters*, 43(16):3874–3877.

Mayerhöfer, T. G., Pahlow, S., and Popp, J. (2020). The Bouguer-Beer-Lambert Law: Shining Light on the Obscure. *ChemPhysChem*, 21(18):2029–2046.

Metropolis, N. and Ulam, S. (1949). The Monte Carlo Method. *Journal of the American Statistical Association*, 44(247):335–341.

Meyer, S., Shi, S. Z., Shapira, N., Maidment, A. D. A., and Noël, P. B. (2021). Quantitative analysis of speckle-based X-ray dark-field imaging using numerical wave-optics simulations. *Scientific Reports*, 11(1):16113.

Millard, T. P., Endrizzi, M., Diemoz, P. C., Hagen, C. K., and Olivo, A. (2014). Monte Carlo model of a polychromatic laboratory based edge illumination x-ray phase contrast system. *Review of Scientific Instruments*, 85(5):053702.

Millard, T. P., Endrizzi, M., Rigon, L., Arfelli, F., Menk, R. H., Owen, J., Stride, E., and Olivo, A. (2013). Quantification of microbubble concentration through x-ray phase contrast imaging. *Applied Physics Letters*, 103(11):114105.

Miller, E. A., White, T. A., McDonald, B. S., and Seifert, A. (2013). Phase Contrast X-Ray Imaging Signatures for Security Applications. *IEEE Transactions on Nuclear Science*, 60(1):416–422.

Mittleman, D. M., Hunsche, S., Boivin, L., and Nuss, M. C. (1997). T-ray tomography. *Optics Letters*, 22(12):904–906.

Modregger, P., Kagias, M., Irvine, S. C., Brönnimann, R., Jefimovs, K., Endrizzi, M., and Olivo, A. (2017). Interpretation and Utility of the Moments of Small-Angle X-Ray Scattering Distributions. *Physical Review Letters*, 118(26):265501.

Momose, A. (2003). Phase-sensitive imaging and phase tomography using X-ray interferometers. *Optics Express*, 11(19):2303–2314.

Momose, A. (2020). X-ray phase imaging reaching clinical uses. *Physica Medica*, 79:93–102.

Momose, A. and Fukuda, J. (1995). Phase-contrast radiographs of nonstained rat cerebellar specimen. *Medical Physics*, 22(4):375–379.

Momose, A., Kawamoto, S., Koyama, I., Hamaishi, Y., Takai, K., and Suzuki, Y. (2003). Demonstration of X-Ray Talbot Interferometry. *Japanese Journal of Applied Physics*, 42(Part 2, No. 7B):L866–L868.

Momose, A., Kawamoto, S., Koyama, I., and Suzuki, Y. (2004). Phase tomography using an x-ray Talbot interferometer. In Bonse, U., editor, *Proc. SPIE 5535, Developments in X-Ray Tomography IV*, pages 352–360.

Momose, A., Takano, H., Wu, Y., Hashimoto, K., Samoto, T., Hoshino, M., Seki, Y., and Shinohara, T. (2020). Recent Progress in X-ray and Neutron Phase Imaging with Gratings. *Quantum Beam Science*, 4(1):9.

Momose, A., Ueda, R., Cai, M., Zhao, Z., Kalirai, S., Stan, M., Irwin, J., Kawakami, H., Zangi, P., Meyer, P., Börner, M., and Schulz, J. (2022). Recent progress in grating-based microscopic x-ray phase tomography. In Müller, B. and Wang, G., editors, *Proc. SPIE 12242, Developments in X-Ray Tomography XIV*, page 1224210. SPIE.

Momose, A., Yashiro, W., Takeda, Y., Suzuki, Y., and Hattori, T. (2006). Phase Tomography by X-ray Talbot Interferometry for Biological Imaging. *Japanese Journal of Applied Physics*, 45(6A):5254–5262.

Morgan, K. S., Paganin, D. M., and Siu, K. K. W. (2011). Quantitative single-exposure x-ray phase contrast imaging using a single attenuation grid. *Optics Express*, 19(20):19781–19789.

Morgan, K. S., Siu, K. K., and Paganin, D. M. (2010a). The projection approximation versus an exact solution for X-ray phase contrast imaging, with a plane wave scattered by a dielectric cylinder. *Optics Communications*, 283(23):4601–4608.

Morgan, K. S., Siu, K. K. W., and Paganin, D. M. (2010b). The projection approximation and edge contrast for x-ray propagation-based phase contrast imaging of a cylindrical edge. *Optics Express*, 18(10):9865–9878.

Munro, P. R., Ignatyev, K., Speller, R. D., and Olivo, A. (2010a). The relationship between wave and geometrical optics models of coded aperture type x-ray phase contrast imaging systems. *Optics Express*, 18(5):4103–4117.

Munro, P. R. T. (2019). Rigorous multi-slice wave optical simulation of x-ray propagation in inhomogeneous space. *Journal of the Optical Society of America A*, 36(7):1197–1208.

Munro, P. R. T., Ignatyev, K., Speller, R. D., and Olivo, A. (2010b). Limitations imposed by specimen phase gradients on the design of grating based x-ray phase contrast imaging systems. *Applied Optics*, 49(20):3860–3863.

Nazemi, E., Six, N., Iuso, D., De Samber, B., Sijbers, J., and De Beenhouwer, J. (2021). Monte-Carlo-Based Estimation of the X-ray Energy Spectrum for CT Artifact Reduction. *Applied Sciences*, 11(7).

Nesterets, Y. I. (2008). On the origins of decoherence and extinction contrast in phase-contrast imaging. *Optics Communications*, 281(4):533–542.

Nesterets, Y. I. and Gureyev, T. E. (2016). Partially coherent contrast-transfer-function approximation. *Journal of the Optical Society of America A*, 33(4):464–474.

Nguyen, V., Sanctorum, J. G., Van Wassenbergh, S., Dirckx, J. J. J., Sijbers, J., and De Beenhouwer, J. (2021). Geometry Calibration of a Modular Stereo Cone-Beam X-ray CT System. *Journal of Imaging*, 7(3):54.

Novotny, L. and Hecht, B. (2012). *Principles of Nano-Optics*. Cambridge University Press.

Olivo, A. (2021). Edge-illumination x-ray phase-contrast imaging. *Journal of Physics: Condensed Matter*, 33(36):363002.

Olivo, A., Arfelli, F., Cantatore, G., Longo, R., Menk, R. H., Pani, S., Prest, M., Poropat, P., Rigon, L., Tromba, G., Vallazza, E., and Castelli, E. (2001). An innovative digital imaging set-up allowing a low-dose approach to phase contrast applications in the medical field. *Medical Physics*, 28(8):1610–1619.

Olivo, A., Gkoumas, S., Endrizzi, M., Hagen, C. K., Szafraniec, M. B., Diemoz, P. C., Munro, P. R. T., Ignatyev, K., Johnson, B., Horrocks, J. A., Vinnicombe, S. J., Jones, J. L., and Speller, R. D. (2013). Low-dose phase contrast mammography with conventional x-ray sources. *Medical Physics*, 40(9):090701.

Olivo, A., Ignatyev, K., Munro, P., and Speller, R. (2009). Design and realization of a coded-aperture based X-ray phase contrast imaging for homeland security applications. *Nuclear Instruments and Methods in Physics Research Section A: Accelerators, Spectrometers, Detectors and Associated Equipment*, 610(2):604–614.

Olivo, A. and Speller, R. (2007a). A coded-aperture technique allowing x-ray phase contrast imaging with conventional sources. *Applied Physics Letters*, 91(7):074106.

Olivo, A. and Speller, R. (2007b). Modelling of a novel x-ray phase contrast imaging technique based on coded apertures. *Physics in Medicine & Biology*, 52(22):6555–6573.

Organista, C., Kagias, M., Tang, R., Shi, Z., Jefimovs, K., Boone, M. N., and Stampanoni, M. (2023). Optimization of the visibility of a tunable dual-phase x-ray grating interferometer. *Optics Continuum*, 2(1):232–248.

O'Shea, D. C., Suleski, T. J., Kathman, A. D., and Prather, D. W. (2003). *Diffractive Optics: Design, Fabrication, and Test*. SPIE - The International Society for Optical Engineering.

Paganin, D., Mayo, S. C., Gureyev, T. E., Miller, P. R., and Wilkins, S. W. (2002). Simultaneous phase and amplitude extraction from a single defocused image of a homogeneous object. *Journal of Microscopy*, 206(1):33–40.

Paganin, D. M. and Pelliccia, D. (2021). Chapter Two - X-ray phase-contrast imaging: a broad overview of some fundamentals. In Hÿtch, M. and Hawkes, P. W., editors, *Advances in Imaging and Electron Physics*, volume 218, pages 63–158. Elsevier.

Palenstijn, W. J., Batenburg, K. J., and Sijbers, J. (2011). Performance improvements for iterative electron tomography reconstruction using graphics processing units (GPUs). *Journal of Structural Biology*, 176(2):250–253.

Paramonov, P., Francken, N., Renders, J., Iuso, D., Elberfeld, T., De Beenhouwer, J., and Sijbers, J. (2024). CAD-ASTRA: a versatile and efficient mesh projector for X-ray tomography with the ASTRA-toolbox. *Optics Express*, 32(3):3425–3439.

Peter, S., Modregger, P., Fix, M., Volken, W., Frei, D., Manser, P., and Stampanoni, M. (2014). Combining Monte Carlo methods with coherent wave optics for the simulation of phase-sensitive X-ray imaging. *Journal of Synchrotron Radiation*, 21(3):613–622.

Pfeiffer, F., Bech, M., Bunk, O., Kraft, P., Eikenberry, E. F., Brönnimann, C., Grünzweig, C., and David, C. (2008). Hard-X-ray dark-field imaging using a grating interferometer. *Nature materials*, 7(2):134–137.

Pfeiffer, F., Bunk, O., Schulze-Briese, C., Diaz, A., Weitkamp, T., David, C., van der Veen, J. F., Vartanyants, I., and Robinson, I. K. (2005). Shearing Interferometer for Quantifying the Coherence of Hard X-Ray Beams. *Physical Review Letters*, 94(16):164801.

Pfeiffer, F., Herzen, J., Willner, M., Chabior, M., Auweter, S., Reiser, M., and Bamberg, F. (2013). Grating-based X-ray phase contrast for biomedical imaging applications. *Zeitschrift für Medizinische Physik*, 23(3):176–185.

Pfeiffer, F., Kottler, C., Bunk, O., and David, C. (2007). Hard X-Ray Phase Tomography with Low-Brilliance Sources. *Physical Review Letters*, 98(10):108105.

Pfeiffer, F., Weitkamp, T., Bunk, O., and David, C. (2006). Phase retrieval and differential phase-contrast imaging with low-brilliance X-ray sources. *Nature Physics*, 2(4):258–261.

Pfeiffer, H. G. and Liebhafsky, H. A. (1951). The origins of Beer's law. *Journal of Chemical Education*, 28(3):123–125.

Prade, F., Schaff, F., Senck, S., Meyer, P., Mohr, J., Kastner, J., and Pfeiffer, F. (2017). Nondestructive characterization of fiber orientation in short fiber reinforced polymer composites with X-ray vector radiography. *NDT & E International*, 86:65–72.

Prodi, A., Knudsen, E., Willendrup, P., Schmitt, S., Ferrero, C., Feidenhans'l, R., and Lefmann, K. (2011). A Monte Carlo approach for simulating the propagation of partially coherent x-ray beams. In Sanchez del Rio, M. and Chubar, O., editors, *Proc. SPIE 8141, Advances in Computational Methods for X-Ray Optics II*, volume 8141, page 814108.

Quenot, L., Bohic, S., and Brun, E. (2022). X-ray Phase Contrast Imaging from Synchrotron to Conventional Sources: A Review of the Existing Techniques for Biological Applications. *Applied Sciences*, 12(19):9539.

Quénot, L., Brun, E., Létang, J. M., and Langer, M. (2021). Evaluation of simulators for x-ray speckle-based phase contrast imaging. *Physics in Medicine & Biology*, 66(17):175027.

Radon, J. (1917). Über die Bestimmung von Funktionen durch ihre Integralwerte längs gewisser Mannigfaltigkeiten. *Berichte der Sächsischen Akademie der Wissenschaft*, 69:262–277.

Raeside, D. E. (1976). Monte Carlo principles and applications. *Physics in Medicine & Biology*, 21(2):181–197.

Renders, J., Mancini, L., De Beenhouwer, J., and Sijbers, J. (2024). Direct Reconstruction of Wet Foam from Sparse-View, Dynamic X-Ray CT Scans. *Advanced Engineering Materials*, 26(23):2400957.

Revol, V., Kottler, C., Kaufmann, R., Neels, A., and Dommann, A. (2012). Orientation-selective X-ray dark field imaging of ordered systems. *Journal of Applied Physics*, 112(11):114903.

Revol, V., Plank, B., Kaufmann, R., Kastner, J., Kottler, C., and Neels, A. (2013). Laminate fibre structure characterisation of carbon fibre-reinforced polymers by X-ray scatter dark field imaging with a grating interferometer. *NDT & E International*, 58:64–71.

Rigon, L., Arfelli, F., and Menk, R.-H. (2007). Three-image diffraction enhanced imaging algorithm to extract absorption, refraction, and ultrasmall-angle scattering. *Applied Physics Letters*, 90(11):114102.

Ritter, A., Bartl, P., Bayer, F., Gödel, K. C., Haas, W., Michel, T., Pelzer, G., Rieger, J., Weber, T., Zang, A., and Anton, G. (2014). Simulation framework for coherent and incoherent X-ray imaging and its application in Talbot-Lau dark-field imaging. *Optics Express*, 22(19):23276–23289.

Röntgen, W. C. (1898). Ueber eine neue Art von Strahlen. *Annalen der Physik*, 300(1):12–17.

Sakurai, J. J. and Napolitano, J. (2017). *Modern Quantum Mechanics*. Cambridge University Press.

Sanctorum, J., De Beenhouwer, J., and Sijbers, J. (2018). X-ray Phase-contrast Simulations of Fibrous Phantoms using GATE. In *2018 IEEE Nuclear Science Symposium and Medical Imaging Conference Proceedings (NSS/MIC)*, pages 1–5. IEEE.

Sanctorum, J., De Beenhouwer, J., and Sijbers, J. (2020). X-ray phase contrast simulation for grating-based interferometry using GATE. *Optics Express*, 28(22):33390–33412.

Sanctorum, J., De Beenhouwer, J., Weissenböck, J., Heinzl, C., Kastner, J., and Sijbers, J. (2019). Simulated grating-based x-ray phase contrast images of CFRP-like objects. *e-Journal of Nondestructive Testing*, 24(3):1–8.

Sanctorum, J., Sijbers, J., and De Beenhouwer, J. (2021a). Dark Field Sensitivity In Single Mask Edge Illumination Lung Imaging. In *2021 IEEE 18th International Symposium on Biomedical Imaging (ISBI)*, pages 775–778. IEEE.

Sanctorum, J., Sijbers, J., and De Beenhouwer, J. (2022a). Virtual grating approach for Monte Carlo simulations of edge illumination-based x-ray phase contrast imaging. *Optics Express*, 30(21):38695–38708.

Sanctorum, J., Sijbers, J., and De Beenhouwer, J. (2025). Multi-contrast benchmarking of edge illumination Monte Carlo simulations using virtual gratings. *Journal of Applied Physics*, 137(10):104904.

Sanctorum, J., Six, N., Sijbers, J., and De Beenhouwer, J. (2022b). Augmenting a conventional x-ray scanner with edge illumination-based phase contrast imaging: how to design the gratings. In Müller, B. and Wang, G., editors, *Proc. SPIE 12242, Developments in X-Ray Tomography XIV*, page 1224218. SPIE.

Sanctorum, J. G., Van Wassenbergh, S., Nguyen, V., De Beenhouwer, J., Sijbers, J., and Dirckx, J. J. J. (2021b). Extended imaging volume in cone-beam x-ray tomography using the weighted simultaneous iterative reconstruction technique. *Physics in Medicine & Biology*, 66(16):165008.

Santin, G., Strul, D., Lazaro, D., Simon, L., Krieguer, M., Martins, M., Breton, V., and Morel, C. (2003). GATE: A Geant4-Based Simulation Platform for PET and SPECT Integrating Movement and Time Management. *IEEE Transactions on Nuclear Science*, 50(5 II):1516–1521.

Sarrut, D., Arbor, N., Baudier, T., Borys, D., Etxebeste, A., Fuchs, H., Gajewski, J., Grevillot, L., Jan, S., Kagadis, G. C., Kang, H. G., Kirov, A., Kochebina, O., Krzemien, W., Lomax, A., Papadimitroulas, P., Pommranz, C., Roncali, E., Rucinski, A., Winterhalter, C., and Maigne, L. (2022). The OpenGATE ecosystem for Monte Carlo simulation in medical physics. *Physics in Medicine & Biology*, 67(18):184001.

Sauter, A. P., Andrejewski, J., Frank, M., Willer, K., Herzen, J., Meurer, F., Fingerle, A. A., Makowski, M. R., Pfeiffer, F., and Pfeiffer, D. (2021). Correlation of image quality parameters with tube voltage in X-ray dark-field chest radiography: a phantom study. *Scientific Reports*, 11(1):14130.

Scattarella, F., Tangaro, S., Modregger, P., Stampanoni, M., De Caro, L., and Bellotti, R. (2013). Post-detection analysis for grating-based ultra-small angle X-ray scattering. *Physica Medica*, 29(5):478–486.

Senck, S., Scheerer, M., Revol, V., Plank, B., Hannesschläger, C., Gusenbauer, C., and Kastner, J. (2018). Microcrack characterization in loaded CFRP laminates using quantitative two- and three-dimensional X-ray dark-field imaging. *Composites Part A: Applied Science and Manufacturing*, 115:206–214.

Sepehri, F., Hajivaliei, M., and Rajabi, H. (2020). Selection of random number generators in GATE Monte Carlo toolkit. *Nuclear Instruments and Methods in Physics Research Section A: Accelerators, Spectrometers, Detectors and Associated Equipment*, 973:164172.

Sharma, Y., Schaff, F., Wieczorek, M., Pfeiffer, F., and Lasser, T. (2017). Design of Acquisition Schemes and Setup Geometry for Anisotropic X-ray Dark-Field Tomography (AXDT). *Scientific Reports*, 7(1):3195.

Shepp, L. A. and Logan, B. F. (1974). The Fourier reconstruction of a head section. *IEEE Transactions on Nuclear Science*, 21(3):21–43.

Shoukroun, D., Doherty, A., Endrizzi, M., Bate, D., Fromme, P., and Olivo, A. (2022a). Post-acquisition mask misalignment correction for edge illumination x-ray phase contrast imaging. *Review of Scientific Instruments*, 93(5):053706.

Shoukroun, D., Massimi, L., Endrizzi, M., Bate, D., Fromme, P., and Olivo, A. (2022b). Edge illumination X-ray phase contrast imaging for impact damage detection in CFRP. *Materials Today Communications*, 31:103279.

Shoukroun, D., Massimi, L., Endrizzi, M., Nesbitt, A., Bate, D., Fromme, P., and Olivo, A. (2023). Quantification of porosity in composite plates using planar X-ray phase contrast imaging. *NDT & E International*, 139:102935.

Six, N., De Beenhouwer, J., and Sijbers, J. (2019). poly-DART: A discrete algebraic reconstruction technique for polychromatic X-ray CT. *Optics Express*, 27(23):33670–33682.

Six, N., Renders, J., De Beenhouwer, J., and Sijbers, J. (2024). Joint multi-contrast CT for edge illumination X-ray phase contrast imaging using split Barzilai-Borwein steps. *Optics Express*, 32(2):1135–1150.

Six, N., Renders, J., Sijbers, J., and De Beenhouwer, J. (2021). Gauss-Newton-Krylov for Reconstruction of Polychromatic X-Ray CT Images. *IEEE Transactions on Computational Imaging*, 7:1304–1313.

Slack, C. M. (1926). The Refraction of X-Rays in Prisms of Various Materials. *Physical Review*, 27(6):691–695.

Snigirev, A., Snigireva, I., Kohn, V., Kuznetsov, S., and Schelokov, I. (1995). On the possibilities of x-ray phase contrast microimaging by coherent high-energy synchrotron radiation. *Review of Scientific Instruments*, 66(12):5486–5492.

Spindler, S., Etter, D., Rawlik, M., Polikarpov, M., Romano, L., Shi, Z., Jefimovs, K., Wang, Z., and Stampanoni, M. (2023). The choice of an autocorrelation length in dark-field lung imaging. *Scientific Reports*, 13(1):2731.

Spindler, S., Pereira, A., Sommer, P., Rawlik, M., Romano, L., and Stampanoni, M. (2025). Simulation framework for X-ray grating interferometry optimization. *Optics Express*, 33(1):1345–1358.

Staelens, S. and Buvat, I. (2009). Chapter 5 - Monte Carlo Simulations in Nuclear Medicine Imaging. In Verdonck, P., editor, *Advances in Biomedical Engineering*, pages 177–209. Elsevier, Amsterdam.

Staelens, S., De Beenhouwer, J., Kruecker, D., Maigne, L., Rannou, F., Ferrer, L., D'Asseler, Y., Buvat, I., and Lemahieu, I. (2006). GATE: Improving the computational efficiency. *Nuclear Instruments and Methods in Physics Research Section A: Accelerators, Spectrometers, Detectors and Associated Equipment*, 569(2):341–345.

Strobl, M. (2014). General solution for quantitative dark-field contrast imaging with grating interferometers. *Scientific Reports*, 4(1):7243.

Strutt Rayleigh, J. W. (1881). XXV. On copying diffraction-gratings, and on some phenomena connected therewith. *Philosophical Magazine Series 5*, 11(67):196–205.

Suleski, T. J. (1997). Generation of Lohmann images from binary-phase Talbot array illuminators. *Applied Optics*, 36(20):4686–4691.

Sung, Y. and Barbastathis, G. (2013). Rytov approximation for x-ray phase imaging. *Optics Express*, 21(3):2674–2682.

Sung, Y., Segars, W. P., Pan, A., Ando, M., Sheppard, C. J. R., and Gupta, R. (2015). Realistic wave-optics simulation of X-ray phase-contrast imaging at a human scale. *Scientific Reports*, 5:12011.

Sung, Y., Sheppard, C. J. R., Barbastathis, G., Ando, M., and Gupta, R. (2013). Full-wave approach for x-ray phase imaging. *Optics Express*, 21(15):17547–17557.

Swank, R. K. (1973). Absorption and noise in x-ray phosphors. *Journal of Applied Physics*, 44(9):4199–4203.

Taguchi, K. and Iwanczyk, J. S. (2013). Vision 20/20: Single photon counting x-ray detectors in medical imaging. *Medical Physics*, 40(10):100901.

Talbot, H. (1836). LXXVI. Facts relating to optical science. No. IV. *Philosophical Magazine Series 3*, 9(56):401–407.

Tao, S., Tian, Z., Bai, L., Wang, W., Xu, Y., Kuang, C., and Liu, X. (2023). Tri-directional x-ray phase contrast multimodal imaging using one hexagonal mesh modulator. *Physics in Medicine & Biology*, 68(19):195017.

Taphorn, K., Kaster, L., Sellerer, T., Hötger, A., and Herzen, J. (2023). Spectral X-ray dark-field signal characterization from dual-energy projection phase-stepping data with a Talbot-Lau interferometer. *Scientific Reports*, 13(1):767.

Tessarini, S., Fix, M. K., Manser, P., Volken, W., Frei, D., Mercolli, L., and Stampanoni, M. (2022). Semi-classical Monte Carlo algorithm for the simulation of X-ray grating interferometry. *Scientific Reports*, 12(1):2485.

Tournier, J.-D., Calamante, F., and Connelly, A. (2007). Robust determination of the fibre orientation distribution in diffusion MRI: Non-negativity constrained super-resolved spherical deconvolution. *NeuroImage*, 35(4):1459–1472.

Urban, T., Gassert, F. T., Frank, M., Willer, K., Noichl, W., Buchberger, P., Schick, R. C., Koehler, T., Bodden, J. H., Fingerle, A. A., Sauter, A. P., Makowski, M. R., Pfeiffer, F., and Pfeiffer, D. (2022). Qualitative and Quantitative Assessment of Emphysema Using Dark-Field Chest Radiography. *Radiology*, 303(1):119–127.

van Aarle, W., Palenstijn, W. J., Cant, J., Janssens, E., Bleichrodt, F., Dabravolski, A., De Beenhouwer, J., Batenburg, K. J., and Sijbers, J. (2016). Fast and flexible X-ray tomography using the ASTRA toolbox. *Optics Express*, 24(22):25129–25147.

van Aarle, W., Palenstijn, W. J., De Beenhouwer, J., Altantzis, T., Bals, S., Batenburg, K. J., and Sijbers, J. (2015). The ASTRA Toolbox: A platform for advanced algorithm development in electron tomography. *Ultramicroscopy*, 157:35–47.

Van de Casteele, E., Van Dyck, D., Sijbers, J., and Raman, E. (2002). An energy-based beam hardening model in tomography. *Physics in Medicine & Biology*, 47(23):4181–4190.

Van Eyndhoven, G., Batenburg, K. J., Kazantsev, D., Van Nieuwenhove, V., Lee, P. D., Dobson, K. J., and Sijbers, J. (2015). An Iterative CT Reconstruction Algorithm for Fast Fluid Flow Imaging. *IEEE Transactions on Image Processing*, 24(11):4446–4458.

Vanthienen, P.-J., Sanctorum, J., Huyge, B., Six, N., Sijbers, J., and De Beenhouwer, J. (2023). Grating designs for cone beam edge illumination X-ray phase contrast imaging: a simulation study. *Optics Express*, 31(17):28051–28064.

Vignero, J., Marshall, N., Bliznakova, K., and Bosmans, H. (2018). A hybrid simulation framework for computer simulation and modelling studies of grating-based x-ray phase-contrast images. *Physics in Medicine & Biology*, 63(14):14NT03.

Vittoria, F., Endrizzi, M., Kallon, G., Hagen, C., Diemoz, P., Zamir, A., and Olivo, A. (2018). Beam tracking phase tomography with laboratory sources. *Journal of Instrumentation*, 13(4):C04008.

Vittoria, F. A., Diemoz, P. C., Endrizzi, M., Rigon, L., Lopez, F. C., Dreossi, D., Munro, P. R. T., and Olivo, A. (2013). Strategies for efficient and fast wave optics simulation of coded-aperture and other x-ray phase-contrast imaging methods. *Applied Optics*, 52(28):6940–6947.

Vittoria, F. A., Endrizzi, M., Diemoz, P. C., Wagner, U. H., Rau, C., Robinson, I. K., and Olivo, A. (2014). Virtual edge illumination and one dimensional beam tracking for absorption, refraction, and scattering retrieval. *Applied Physics Letters*, 104(13):134102.

Vittoria, F. A., Kallon, G. K. N., Basta, D., Diemoz, P. C., Robinson, I. K., Olivo, A., and Endrizzi, M. (2015). Beam tracking approach for single–shot retrieval of absorption, refraction, and dark–field signals with laboratory x–ray sources. *Applied Physics Letters*, 106(22):224102.

Voelz, D. G. and Roggemann, M. C. (2009). Digital simulation of scalar optical diffraction: revisiting chirp function sampling criteria and consequences. *Applied Optics*, 48(32):6132–6142.

Vogel, J., Schaff, F., Fehringer, A., Jud, C., Wieczorek, M., Pfeiffer, F., and Lasser, T. (2015). Constrained X-ray tensor tomography reconstruction. *Optics Express*, 23(12):15134–15151.

von Nardroff, R. (1926). Refraction of X-Rays by Small Particles. *Physical Review*, 28(2):240–246.

von Teuffenbach, M., Koehler, T., Fehringer, A., Viermetz, M., Brendel, B., Herzen, J., Proksa, R., Rummeny, E. J., Pfeiffer, F., and Noël, P. B. (2017). Grating-based phase-contrast and dark-field computed tomography: a single-shot method. *Scientific Reports*, 7(1):7476.

Wang, Z., Huang, Z., Zhang, L., Chen, Z., and Kang, K. (2009a). Implement X-ray refraction effect in Geant4 for phase contrast imaging. In *2009 IEEE Nuclear Science Symposium Conference Record (NSS/MIC)*, pages 2395–2398. IEEE.

Wang, Z. T., Kang, K. J., Huang, Z. F., and Chen, Z. Q. (2009b). Quantitative grating-based x-ray dark-field computed tomography. *Applied Physics Letters*, 95(9):2012–2015.

Weber, T., Bartl, P., Bayer, F., Durst, J., Haas, W., Michel, T., Ritter, A., and Anton, G. (2011). Noise in x-ray grating-based phase-contrast imaging. *Medical Physics*, 38(7):4133–4140.

Weitkamp, T. (2004). XWFP: an x-ray wavefront propagation software package for the IDL computer language. In Sanchez del Rio, M., editor, *Proc. SPIE 5536, Advances in Computational Methods for X-Ray and Neutron Optics*, pages 181–189.

Weitkamp, T., David, C., Kottler, C., Bunk, O., and Pfeiffer, F. (2006). Tomography with grating interferometers at low-brilliance sources. In Bonse, U., editor, *Proc. SPIE 6318, Developments in X-Ray Tomography V*, page 63180S.

Weitkamp, T., Diaz, A., David, C., Pfeiffer, F., Stampanoni, M., Cloetens, P., and Ziegler, E. (2005). X-ray phase imaging with a grating interferometer. *Optics Express*, 13(16):6296–6304.

Wen, H., Bennett, E., Hegedus, M., and Carroll, S. (2008). Spatial Harmonic Imaging of X-ray Scattering - Initial Results. *IEEE Transactions on Medical Imaging*, 27(8):997–1002.

Wen, H. H., Bennett, E. E., Kopace, R., Stein, A. F., and Pai, V. (2010). Single-shot x-ray differential phase-contrast and diffraction imaging using two-dimensional transmission gratings. *Optics Letters*, 35(12):1932–1934.

Wen, J., Zhang, Y., and Xiao, M. (2013). The Talbot effect: recent advances in classical optics, nonlinear optics, and quantum optics. *Advances in Optics and Photonics*, 5(1):83–130.

Wernick, M. N., Wirjadi, O., Chapman, D., Zhong, Z., Galatsanos, N. P., Yang, Y., Brankov, J. G., Oltulu, O., Anastasio, M. A., and Muehleman, C. (2003). Multiple-image radiography. *Physics in Medicine & Biology*, 48(23):3875–3895.

Wieczorek, M., Schaff, F., Jud, C., Pfeiffer, D., Pfeiffer, F., and Lasser, T. (2018). Brain Connectivity Exposed by Anisotropic X-ray Dark-field Tomography. *Scientific Reports*, 8(1):14345.

Wieczorek, M., Schaff, F., Pfeiffer, F., and Lasser, T. (2016). Anisotropic X-Ray Dark-Field Tomography: A Continuous Model and its Discretization. *Physical Review Letters*, 117(15):158101.

Wilde, J. P. and Hesselink, L. (2020). Modeling of an X-ray grating-based imaging interferometer using ray tracing. *Optics Express*, 28(17):24657–24681.

Wilde, J. P. and Hesselink, L. (2021a). Statistical optics modeling of dark-field scattering in X-ray grating interferometers: Part 1. Theory. *Optics Express*, 29(25):40891–40916.

Wilde, J. P. and Hesselink, L. (2021b). Statistical optics modeling of dark-field scattering in X-ray grating interferometers: Part 2. Simulation. *Optics Express*, 29(25):40917–40933.

Willer, K., Fingerle, A. A., Gromann, L. B., De Marco, F., Herzen, J., Achterhold, K., Gleich, B., Muenzel, D., Scherer, K., Renz, M., Renger, B., Kopp, F., Kriner, F., Fischer, F., Braun, C., Auweter, S., Hellbach, K., Reiser, M. F., Schroeter, T., Mohr, J., Yaroshenko, A., Maack, H.-I., Pralow, T., van der Heijden, H., Proksa, R., Koehler, T., Wieberneit, N., Rindt, K., Rummeny, E. J., Pfeiffer, F., and Noël, P. B. (2018). X-ray dark-field imaging of the human lung—A feasibility study on a deceased body. *PLOS ONE*, 13(9):e0204565.

Włodarczyk, B. and Pietrzak, J. (2015). Analytical reconstructions of intensity modulated x-ray phase-contrast imaging of human scale phantoms. *Biomedical Optics Express*, 6(11):4255–4272.

Włodarczyk, B. and Pietrzak, J. (2017). Hybrid framework for feasible modeling of an edge illumination X-ray phase-contrast imaging system at a human scale. *Physica Medica*, 40:1–10.

Wolter, H. (1952a). Spiegelsysteme streifenden Einfalls als abbildende Optiken für Röntgenstrahlen. *Annalen der Physik*, 445(1-2):94–114.

Wolter, H. (1952b). Verallgemeinerte Schwarzschildsche Spiegelsysteme streifender Reflexion als Optiken für Röntgenstrahlen. *Annalen der Physik*, 445(4-5):286–295.

Wong, M.-L. (1994). Polarizability and tensor ellipsoid in the Raman effect. *Vibrational Spectroscopy*, 7(2):197–199.

Wu, G., Ma, L., and Jiang, H. (2019). The roles of surface wettability and roughness of carbon fibers in interfacial enhancement of silicone resin composites. *Polymer Composites*, 40(1, SI):E255–E264.

Wu, Z., Wei, W. B., Gao, K., Liu, G., Liu, G. F., Sun, H. X., Jiang, J., Wang, Q. P., Lu, Y. L., and Tian, Y. C. (2021). Prototype system of noninterferometric phase-contrast computed tomography utilizing medical imaging components. *Journal of Applied Physics*, 129(7):074901.

Xiao, C., Létang, J. M., and Buffière, J.-Y. (2022). Characterization of internal fatigue cracks in aluminum alloys by simulation of phase contrast tomography. *Scientific Reports*, 12(1):5981.

Yan, A., Wu, X., and Liu, H. (2020). Predicting fringe visibility in dual-phase grating interferometry with polychromatic X-ray sources. *Journal of X-Ray Science and Technology*, 28(6):1055–1067.

Yao, Y. and Chen, S. (2013). The effects of fiber's surface roughness on the mechanical properties of fiber-reinforced polymer composites. *Journal of Composite Materials*, 47(23):2909–2923.

Yashiro, W., Terui, Y., Kawabata, K., and Momose, A. (2010). On the origin of visibility contrast in x-ray Talbot interferometry. *Optics Express*, 18(16):16890–16901.

Yoneyama, A. (2022). Three-dimensional x-ray thermography using crystal-based x-ray interferometer. In Müller, B. and Wang, G., editors, *Proc. SPIE 12242, Developments in X-Ray Tomography XIV*, page 122420X. SPIE.

Zaitsev, B. N., Baklanova, N. I., and Zima, T. M. (2008). Atomic force microscopy study of surface-modified carbon fibers. *Inorganic Materials*, 44(6):592–597.

Zamir, A., Hagen, C., Diemoz, P. C., Endrizzi, M., Vittoria, F., Chen, Y., Anastasio, M. A., and Olivo, A. (2017). Recent advances in edge illumination x-ray phase-contrast tomography. *Journal of Medical Imaging*, 4(4):040901.

Zanette, I., Zhou, T., Burvall, A., Lundström, U., Larsson, D. H., Zdora, M., Thibault, P., Pfeiffer, F., and Hertz, H. M. (2014). Speckle-Based X-Ray Phase-Contrast and Dark-Field Imaging with a Laboratory Source. *Physical Review Letters*, 112(25):253903.

Zernike, F. (1938). The concept of degree of coherence and its application to optical problems. *Physica*, 5(8):785–795.